

AD-A249 622



DTIC
ELECTE
MAY 7 1992
S C D

91-025 D (1)

SCATTERING FROM A FINITE COLLECTION OF
TRANSVERSE DIPOLE AND AXIAL SLOT ARRAYS WITH
EDGE EFFECTS

A Dissertation

Presented in Partial Fulfillment of the Requirements for
the Degree Doctor of Philosophy in the
Graduate School of the Ohio State University

by

J. Paul Skinner, B.S., M.S.E.E.

The Ohio State University

1991

Dissertation Committee:

Prof. B. A. Munk

Prof. E. H. Newman

Prof. R. C. Chou

Approved by:

[Signature]
Advisor
Department of Electrical
Engineering

DISTRIBUTION STATEMENT A
Approved for public release;
Distribution Unlimited

02 5 01 008

92-11970



REPORT DOCUMENTATION PAGE

Form Approved
OMB No. 0704-0188

Public reporting burden for this collection of information is estimated to average 1 hour per response, including the time for reviewing instructions, searching existing data sources, gathering and maintaining the data needed, and completing and reviewing the collection of information. Send comments regarding this burden estimate or any other aspect of this collection of information, including suggestions for reducing this burden, to Washington Headquarters Services, Directorate for Information Operations and Reports, 1215 Jefferson Davis Highway, Suite 1204, Arlington, VA 22202-4302, and to the Office of Management and Budget, Paperwork Reduction Project (0704-0188), Washington, DC 20503.

1. AGENCY USE ONLY (Leave blank)		2. REPORT DATE 1991	3. REPORT TYPE AND DATES COVERED XXXXX DISSERTATION	
4. TITLE AND SUBTITLE Scattering From a Finite Collection of Transverse Dipole and Axial Slot Arrays with Edge Effects			5. FUNDING NUMBERS	
6. AUTHOR(S) J. Paul Skinner, Captain				
7. PERFORMING ORGANIZATION NAME(S) AND ADDRESS(ES) AFIT Student Attending: Ohio State University			8. PERFORMING ORGANIZATION REPORT NUMBER AFIT/CI/CIA-91-025D	
9. SPONSORING / MONITORING AGENCY NAME(S) AND ADDRESS(ES) AFIT/CI Wright-Patterson AFB OH 45433-6583			10. SPONSORING / MONITORING AGENCY REPORT NUMBER	
11. SUPPLEMENTARY NOTES				
12a. DISTRIBUTION / AVAILABILITY STATEMENT Approved for Public Release IAW 190-1 Distributed Unlimited ERNEST A. HAYGOOD, Captain, USAF Executive Officer			12b. DISTRIBUTION CODE	
13. ABSTRACT (Maximum 200 words)				
14. SUBJECT TERMS			15. NUMBER OF PAGES 258	
			16. PRICE CODE	
17. SECURITY CLASSIFICATION OF REPORT		18. SECURITY CLASSIFICATION OF THIS PAGE	19. SECURITY CLASSIFICATION OF ABSTRACT	
			20. LIMITATION OF ABSTRACT	

Scattering from a Finite Collection of Transverse
Dipole and Axial Slot Arrays with Edge Effects

By

J. Paul Skinner, Ph.D.

The Ohio State University, 1991

Advisor: Professor Benedikt A. Munk

Accession For	
NTIS GR&I	<input checked="" type="checkbox"/>
EPIC TAB	<input type="checkbox"/>
Unannounced	<input type="checkbox"/>
Justification	
By _____	
Distribution/	
Availability Codes	
Dist	Avail and/or Special
A-1	

A moment method based solution for the electromagnetic radiation and scattering from geometries composed of transverse dipole column arrays and a finite collection of axial slot arrays is developed. Each "array" is an infinite column of periodic elements, with transverse referring to a dipole orientation perpendicular to the infinite axis and axial denoting that thin linear slots are directed along the infinite axis. The slots are mounted in infinite ground planes, which may be surrounded by an arbitrary stack of infinite lossless dielectric slabs, simulating a hybrid frequency selective radome (i.e., periodic surface) in one linear polarization, which is infinite in one dimension and finite in another. Transverse dipole arrays are used to simulate phased array antennas in a similar "finite by infinite" model. Independent modes in scattering current expansions are defined along single columns of periodic elements, with Floquet's theorem governing the current fluctuation along the infinite axis. A coupling matrix is developed with nine sub-blocks, representing mutual admittances, mutual impedances, unitless voltage gains, and unitless current gains. Efficient methods for calculating coupling terms are developed, using both spatial and spectral domain methods (transformable via the Poisson sum formula)

in free space, and using the Array Scanning Method to circumvent the application of Sommerfeld integrals with planar dielectric interfaces. Summation acceleration techniques, such as Shanks' transformation, are used to enhance efficiency. Asymptotic solutions are also developed for coupling between widely separated columns of elements. Coupling calculations are validated by spatially adding a large number of column-to-column terms to simulate the coupling from a doubly-infinite array of elements to a test element, which may be found directly in a plane wave expansion. Validation of the entire moment method procedure is also provided by comparing far zone field calculations with those expected from using solution currents from doubly-infinite arrays with the approximation of using physical optics to correct for the finite aperture width.

DEDICATION

To my loving wife Melinda, and my son Alex.

ACKNOWLEDGEMENTS

Many people and organizations are due thanks for helping me accomplish this work. To my advisor, Prof. Benedikt Munk, a sincere thanks for helping guide me into an interesting topic which I found to be a pleasant mixture of theoretical and practical work. To the Air Force Institute of Technology, a gracious thanks for both selecting me for a Ph.D. assignment and funding my tuition. To the ElectroScience Laboratory of the Ohio State University, a thank you for providing me a place to accomplish my research and for giving me the computer support I needed. I also wish to thank the many fellow graduate students at the ElectroScience Lab, from whom I learned much through technical discussions. In particular, I express thanks to Steve Schneider, Roger Hill, Gary Somers, and Bob Mariano for the many fruitful suggestions and ideas they presented to me. Dr. Lee Henderson provided assistance at many times in the research, and in particular gave invaluable help in discussions on convergence and the inner workings of his PMM code. I am also pleased to thank Profs. Edward Newman and Ri-Chee Chou for being on my reading committee and for their helpful suggestions. A special thanks is given to my mother and deceased father, for giving me a sense of pride in accomplishment and a desire for knowledge. Finally, I must express my heartfelt thanks to my wife and family for enduring the long hours required in my doctoral studies and research. Without their support, I surely could not have accomplished this.

- Paul Skinner

VITA

- March 11, 1961 Born in Beaumont, Texas
- December 1982 B.S.E.E., Summa Cum Laude
Texas A&M University,
College Station, Texas
- Jan. 1983 - Apr. 1983 U.S. Air Force Officer Training School,
Lackland Air Force Base, Texas
- April 22, 1983 Commissioned as a 2nd Lieutenant
in the U. S. Air Force
- December 1984 M.S.E.E.
Air Force Institute of Technology,
Wright-Patterson Air Force Base, Ohio
- Dec. 1984 - Dec. 1988 Radar Cross Section Reduction Engineer,
Avionics Laboratory, Wright-Patterson
Air Force Base, Ohio
- April 22, 1987 Promotion to Captain, USAF
- Jan. 1989 - present Air Force Institute of Technology
Research Fellow, ElectroScience
Laboratory, The Ohio State
University, Columbus, Ohio

PUBLICATIONS

- "A Moment Method Solution to Spiral Antenna Radiation," Proc. of the Antenna Applications Symposium, Robert Allerton Park, University of Illinois, 1984.
- "Radiation and Scattering of Spiral Antennas," M.S. Thesis, Air Force Institute of Technology, December 1984.

"On RCS Reduction of Finite Arrays," co-authors B. Munk, J. Ustoff, S. Schneider, and L. Henderson, Technical Report 723669-1, ElectroScience Laboratory, Ohio State University, generated under Grant No. NSG-1613 from NASA Langley Research Center, April 1991.

FIELDS OF STUDY

Major Field: Electrical Engineering

Major Area:

Electromagnetics Prof. B. A. Munk (Advisor)
Prof. R. G. Kouyoumjian

Minor areas:

Communication Systems Prof. D. T. Davis

Mathematics Prof. J. T. Scheick

TABLE OF CONTENTS

DEDICATION	ii
ACKNOWLEDGEMENTS	iii
VITA	iv
LIST OF FIGURES	ix
CHAPTER	PAGE
I. INTRODUCTION	1
1.1 BACKGROUND AND PROBLEM STATEMENT	1
1.2 OVERALL SOLUTION APPROACH	7
1.3 OVERVIEW OF REMAINING CHAPTERS	17
II. SLOT-TO-SLOT COUPLING	19
2.1 HOMOGENEOUS REGIONS OF SPACE	19
2.1.1 Outer Zone Coupling	19
2.1.2 Inner Zone Coupling	38
2.2 STRATIFIED MEDIA	50
2.2.1 Outer Zone Coupling	50
2.2.2 Inner Zone Coupling	86

III.	DIPOLE-TO-DIPOLE COUPLING	106
3.1	HOMOGENEOUS REGIONS OF SPACE	106
3.1.1	Spectral Domain Solution	106
3.1.2	Spatial Domain Solution	118
3.2	DIPOLES NEAR A DIELECTRIC CLAD GROUND PLANE .	128
IV.	DIPOLE-TO-SLOT COUPLING	147
4.1	COUPLING IN FREE SPACE	148
4.2	COUPLING THROUGH A STRATIFIED MEDIA	157
V.	EXCITATION SOURCES AND FAR ZONE FIELDS	178
5.1	INDUCED CURRENT IN A SLOT FROM AN EXTERNAL PLANE WAVE SOURCE	179
5.2	FAR ZONE SCATTERED FIELDS	192
VI.	RESULTS	204
6.1	RADOME EXAMPLES	205
6.2	ANTENNA WITH RADOME EXAMPLES	228
VII.	CONCLUSIONS	242
 APPENDICES		
A.	CONVERGENCE ACCELERATION OF INFINITE SUMS	244
A.1	THE FEJER KERNEL	245
A.2	THE SPIRAL AVERAGE METHOD	246
A.3	SHANKS' TRANSFORMATION	250
B.	THE ARRAY SCANNING METHOD FOR A SINGLE COLUMN OF PERIODIC SOURCES	252

BIBLIOGRAPHY 256

LIST OF FIGURES

FIGURE		PAGE
1	Generalized Geometry of a Finite Collection of Transverse Dipole and Axial Slot Arrays which are Embedded in an Infinite Stratified Media - View from the Infinite Axis	5
2	Perspective View of a Finite Collection of Transverse Dipole and Axial Slot Arrays in a Single Ground Plane in Free Space	6
3	Two Ground Planes with Single Axial Slots in the Presence of a Single Transverse Dipole	8
4	Equivalent Scattering Geometry	9
5	Geometry of Outer Zone Coupling between Slot Modes in a Homogeneous Half-Space; View from the Infinite Axis	20
6	Side View of a Single Column of Periodic \hat{z} -Directed Hertzian Magnetic Current Sources	21
7	Comparison of Calculation Times by Four Solution Methods for Mutual Admittance to Converge to 0.1% Error - Piecewise Sinusoidal Axial Slot Modes in Free Space with $L = 0.4\lambda$, $D_z = 0.6\lambda$, $z = 0$	33
8	Mutual Admittance Between Piecewise Sinusoidal Axial Slot Modes in Region I with Free Space and $L = 0.4\lambda$, $D_z = 0.6\lambda$, $z = 0$, $s_z = 0$	35
9	Mutual Admittance Between Piecewise Sinusoidal Axial Slot Modes in Region I with Free Space and $L = 0.5\lambda$, $D_z = 0.6\lambda$, $z = 0$	36
10	Mutual Admittance Between Piecewise Sinusoidal Axial Slot Modes in Region I with Free Space and $L = 0.599\lambda$, $D_z = 0.6\lambda$, $z = 0$	37
11	Geometry of Inner Zone Coupling in a Homogeneous Medium	38
12	Equivalent Geometry of Inner Zone Coupling in a Homogeneous Medium with a Doubly-Infinite Array	39
13	Contours of Relative Evanescent Mode Strength in Plane Wave Expansion for Self-Admittance of \hat{z} -Directed Slots Inside Ground Planes: $L = 0.4\lambda$, $D_z = 0.6\lambda$, $d = 0.3\lambda$, $z = 0$, $W = 0.02\lambda$	42

14	Comparison of Calculation Times by Two Solution Methods for Mutual Admittance in a Homogeneous Inner Zone - Case A: $L = 0.4\lambda$, $D_z = 0.6\lambda$, $d = 0.3\lambda$, $z = 0$	45
15	Comparison of Calculation Times by Two Solution Methods for Mutual Admittance in a Homogeneous Inner Zone - Case B: $L = 0.4\lambda$, $D_z = 0.6\lambda$, $d = 0.3\lambda$, $z = 0$	46
16	Mutual Admittance Between Piecewise Sinusoidal Axial Slot Modes in Region II (Case A) with Free Space and $L = 0.4\lambda$, $D_z = 0.6\lambda$, $d = 0.3\lambda$, $z = 0$	47
17	Mutual Admittance Between Piecewise Sinusoidal Axial Slot Modes in Region II (Case B) with Free Space and $L = 0.4\lambda$, $D_z = 0.6\lambda$, $d = 0.3\lambda$, $z = 0$	48
18	Geometry of Outer Zone Coupling between Slot Modes in a Stratified Dielectric Medium	50
19	T_{\perp} in the Neighborhood of a Surface Wave Singularity for $k = n = 0$ term, $\epsilon_1 = 2\epsilon_2$, $d_1 = 0.3\lambda_1$, loss tangent = 0.01	63
20	T_{\perp} in the Neighborhood of a Surface Wave Singularity for $k = n = 0$ term, $\epsilon_1 = 2\epsilon_2$, $d_1 = 0.3\lambda_1$, loss tangent = 0.001	64
21	T_{\perp} in the Neighborhood of a Surface Wave Singularity for $k = n = 0$ term, $\epsilon_1 = 2\epsilon_2$, $d = 0.3\lambda_1$, loss tangent = 0.0001	65
22	"One Sided" Mutual Admittance between Axial Modes for $\epsilon_1 = \epsilon_2$, $D_z = 0.75\lambda_1$, $L = 0.5\lambda_1$	68
23	Direct and First Two Bounce Terms in Geometrical Optics Approximation	69
24	"One Sided" Mutual Admittance between Axial Modes for $\epsilon_1 = 0.5\epsilon_2$, $D_z = 0.75\lambda_1$, $L = 0.5\lambda_1$	71
25	"One Sided" Mutual Admittance between Axial Modes for $\epsilon_1 = 2\epsilon_2$, $D_z = 0.75\lambda_1$, $L = 0.5\lambda_1$	72
26	"One Sided" Mutual Admittance between Axial Modes for $\epsilon_1 = 2\epsilon_2$ by Array Scanning Method, $D_z = 0.75\lambda_1$, $L = 0.5\lambda_1$	73
27	Magnitudes of "One Sided" Mutual Admittances for the Three Categories	74
28	"One Sided" Scan Admittance of a Doubly-Infinite Array of Slots, $D_z = 0.45\lambda_1$, $\epsilon_e = \epsilon_1 = 2\epsilon_2$	75
29	Fresnel Reflection Coefficients Inside a Stratified Medium	77

30	Comparison of Numerical Integration and Analytical Singularity Removal with the ASM in Getting "One Sided" Mutual Admittance between Axial Modes for $\epsilon_1 = 4\epsilon_0$, $\epsilon_2 = 2\epsilon_0$, $d_1 = 0.4\lambda_1$, $D_z = 0.75\lambda_1$, $L = 0.5\lambda_1$	79
31	f_{00} Term for the Single Slab Example	80
32	"One Sided" Mutual Admittance using Numerical Implementation of the ASM with $\epsilon_1 = 4\epsilon_0$, $\epsilon_2 = 2\epsilon_0$, $\epsilon_3 = \epsilon_0$, $d_1 = 0.4\lambda_1$, $d_2 = 0.3\lambda_2$, $D_z = 0.75\lambda_1$, $L = 0.5\lambda_1$	81
33	f_{00} Term for the Double Slab Example	82
34	"One Sided" Scan Admittance of a Doubly-Infinite Array of Slots, $D_x = 0.45\lambda_1$, $\epsilon_e = \epsilon_1$, Double Slab Example Geometry, Spatial Domain with the Fejer Kernel	83
35	"One Sided" Scan Admittance of a Doubly-Infinite Array of Slots, $D_x = 0.45\lambda_1$, $\epsilon_e = \epsilon_1$, Double Slab Example Geometry, Spatial Domain with Shanks' Transformation	84
36	Geometry of Inner Zone Coupling in a Stratified Medium	87
37	Mutual Admittance Between Piecewise Sinusoidal Axial Slot Modes in Region II (Case A) with Free Space and $L = 0.4\lambda$, $D_z = 0.6\lambda$, $d = 0.3\lambda$, $z = 0$, using the Array Scanning Method	89
38	"One Sided" Mutual Admittance using Numerical Implementation of the ASM with Double Slab Inner Zone Example Geometry, Effective Dielectric Constant of $\epsilon_e = \epsilon_1$	90
39	f_{00} Term at $x = 0$ for the Inner Zone Double Slab Example	92
40	"One Sided" Scan Admittance for the Inner Zone Double Slab Example, $D_x = 0.45\lambda_1$	93
41	"One Sided" Mutual Admittance using Numerical Implementation of the ASM with Triple Slab Inner Zone Example Geometry, Effective Dielectric Constant of $\epsilon_e = \epsilon_1$, Case A Testing	95
42	f_{00} Term at $x = 0$ for the Inner Zone Triple Slab Example, Case A Testing	96
43	"One Sided" Scan Admittance for the Inner Zone Triple Slab Example Geometry, $D_x = 0.3\lambda_1$, Case A Testing	97
44	Mutual Admittance using Numerical Implementation of the ASM with Triple Slab Inner Zone Example Geometry, Case B Testing	102
45	f_{00} Term at $x = 0$ for the Inner Zone Triple Slab Example, Case B Testing	103

46	Mutual Scan Admittance between Doubly-Infinite Slot Modes on Opposite Ground Planes for the Inner Zone Triple Slab Example Geometry, $D_x = 0.3\lambda_1$	104
47	Side View of a Single Column of Periodic \hat{x} -Directed Hertzian Electric Current Sources	107
48	Top View of a Displaced \hat{x} -Directed Hertzian Dipole Array	110
49	Top View of Far Zone Geometry for a Radiating Column of Periodic Transverse Dipoles	111
50	Error in Asymptotic Solution of E_x from Example Dipole Array in Free Space along an Axial Path - $L = D_z = \lambda/3$, $z = 0$, $s_z = 0$. . .	114
51	Error in Asymptotic Solution of E_x from Example Dipole Array in Free Space along a Transverse Path - $L = D_z = \lambda/3$, $z = 0$, $s_z = 0$.	115
52	Error in Asymptotic Solution of E_x and E_y from Example Dipole Array in Free Space along a Circumferential Path at $\rho = 2.5\lambda$, $L = D_z = \lambda/3$, $z = 0$, $s_z = 0$	116
53	Transverse Dipole Array Coupling Geometry in Free Space	117
54	Single Dipole-to-Dipole Coupling Geometry - Top View	119
55	Comparison of Calculation Times by Four Solution Methods for Mutual Impedance versus Separation Distance y - Piecewise Sinusoidal Transverse Dipole Modes in Free Space with $L = D_z = \lambda/3$, $z = 0$, $s_z = 0$	122
56	Comparison of Calculation Times by Four Solution Methods for Mutual Impedance versus Separation Distance x - Piecewise Sinusoidal Transverse Dipole Modes in Free Space with $L = D_z = \lambda/3$, $z = 0$, $y = L/40$, $s_z = 0$	123
57	Mutual Impedance Between Piecewise Sinusoidal Transverse Dipole Modes in Free Space along a \hat{y} Axis Cut with $L = D_z = \lambda/3$, $z = 0$, $s_z = 0$	124
58	Mutual Impedance Between Piecewise Sinusoidal Transverse Dipole Modes in Free Space along an \hat{x} Axis Cut with $L = D_z = \lambda/3$, $z = 0$, $y = L/40$, $s_z = 0$	125
59	Scan Impedance of a Doubly-Infinite Array of \hat{x} -Directed Dipoles in Free Space - $L = D_z = \lambda/3$, $D_x = 0.4\lambda$, Wire Radius = $L/40$. .	126
60	Geometry of Transverse Dipole Mode Coupling in the Vicinity of a Dielectric Clad Ground Plane	128

61	Geometry of "Artificially Created" Doubly-Infinite Array of Transverse Dipoles Used for the ASM Calculation of the Reflected Impedance Component near a Dielectric Clad Ground Plane	130
62	Reflected Component of Self-Impedance from a Bare Ground Plane using the ASM - $L = D_z = \lambda/3, \phi_t = \phi_r = 0, s_z = 0$	136
63	Reflected Component of Mutual Impedance from a Bare Ground Plane using the ASM - $L = D_z = \lambda/3, z = 0, \phi_t = \phi_r = 0, d = \lambda, s_z = 0$	137
64	Reflected Component of Self-Impedance with a Bare Ground Plane using the ASM - $L = D_z = \lambda/3, \phi_t = \phi_r = 30^\circ, s_z = 0$	138
65	Integrand from the ASM Computation of the Reflected Component of Self-Impedance with a Bare Ground Plane - $L = D_z = \lambda/3, \phi_t = \phi_r = 30^\circ, d = \lambda/4, s_z = 0$	139
66	Integrand from the ASM Computation of the Reflected Component of Self-Impedance with a Bare Ground Plane - $L = D_z = \lambda/3, \phi_t = \phi_r = 30^\circ, d = 2\lambda, s_z = 0$	141
67	Comparison of Rigorous and Asymptotically Based ASM Solutions for Reflected Component of Self-Impedance from a Dielectric Coated Ground Plane - $L = D_z = \lambda/3, \phi_t = \phi_r = 30^\circ, s_z = 0$	143
68	Reflected Component of Scan Impedance of a Doubly-Infinite Array of \hat{x} -Directed Dipoles near a Ground Plane Coated with Two Dielectrics	145
69	Total Scan Impedance of a Doubly-Infinite Array of \hat{x} -Directed Dipoles near a Ground Plane Coated with Two Dielectrics	146
70	Geometry of Transverse Dipole Mode with Image Source Radiating to a Receive Axial Slot Mode in Free Space - Top View	149
71	Dipole-to-Slot Coupling in Free Space with Dipoles Parallel to the Ground Plane - $L_s = L_d = 0.4\lambda, D_z = 0.6\lambda, z_c = 0, s_z = 0$	152
72	Dipole-to-Slot Coupling in Free Space with Dipoles 45° from Ground Plane - $L_s = L_d = 0.4\lambda, D_z = 0.6\lambda, z_c = 0, s_z = 0$	153
73	Dipole-to-Slot Coupling in Free Space with Dipoles Perpendicular to the Ground Plane - $L_s = L_d = 0.4\lambda, D_z = 0.6\lambda, z_c = 0, s_z = 0$	154
74	Scanning Current Gain between a Doubly-Infinite Array of Transmitting Dipoles and a Receiving Slot Spaced 0.1λ Away - Skinner Solution Overlays PMM Solution Almost Perfectly	156
75	Geometry of Slot-to-Dipole Coupling through a Stratified Medium	157

76	Slot-to-Dipole Coupling with the Dipole Parallel to a Styrofoam Coated Ground Plane - $L_s = L_d = 0.4\lambda_0$, $D_z = 0.6\lambda_0$, $s_z = 0$, $d_1 = \lambda_0/30$, $\epsilon_1 = 1.05\epsilon_0$	163
77	Slot-to-Dipole Coupling with the Dipole 45° to a Styrofoam Coated Ground Plane - $L_s = L_d = 0.4\lambda_0$, $D_z = 0.6\lambda_0$, $s_z = 0$, $d_1 = \lambda_0/30$, $\epsilon_{1r} = 1.05$	164
78	Slot-to-Dipole Coupling with the Double Slab Example Geometry and Dipoles Tilted to 45° from \hat{x} , $y - d_{tot} = 1\lambda_0$, $\epsilon_{1r} = 4$, $\epsilon_{2r} = 2$, $d_1 = 0.2\lambda_1$, $d_2 = 0.2\lambda_2$, $L_s = L_d = 0.5\lambda_1$, $D_z = 0.75\lambda_1$, $s_z = 0$	166
79	Slot-to-Dipole Coupling with the Double Slab Example Geometry and Dipoles Parallel to the Ground Plane, $y - d_{tot} = 0.2\lambda_0$	167
80	Integrand for Previous ASM Solution at $x = 0$	168
81	Slot-to-Dipole Coupling with the Double Slab Example Geometry and Dipoles Parallel to the Ground Plane, $y - d_{tot} = 0.7\lambda_0$	170
82	Integrand for Previous ASM Solution at $x = 0$	171
83	Scanning Voltage Gain between a Doubly-Infinite Array of Transmitting Slots and a Receiving Dipole with the Double Slab Example Geometry - $y - d_{tot} = 0.2\lambda_0$	172
84	Integrand for ASM Solution with the Double Slab Geometry and the Dipole at $(0, 5\lambda_0, 0)$	173
85	Comparison of Numerically Integrated ASM Solution and Stationary Phase Solution for Slot-to-Dipole Coupling with the Double Slab Example Geometry vs. y at $x = z = 0$	175
86	Comparison of Numerically Integrated ASM Solution and Stationary Phase Solution for Slot-to-Dipole Coupling with the Double Slab Example Geometry vs. x at $y = 2\lambda_0$ and $z = 0$	176
87	Bottom View of Plane Wave Excitation of a Slot	180
88	Propagation Direction and Orthogonal Polarization States for an Incident Plane Wave	181
89	Excitation Current for a Slot in a Ground Plane with No Dielectrics - $L = 1\text{cm}$, $\lambda_0 = 3\text{cm}$, $x_c = 15\text{cm}$, $\alpha = 0$, TE_z source	188
90	Excitation Current for a Slot at the Origin in a Double Slab Coated Ground Plane - $f = 10\text{GHz}$, $L = 0.75\text{cm}$, $\epsilon_e = \epsilon_1 = 4\epsilon_0$, $\epsilon_2 = 2\epsilon_0$, $d_1 = 0.2\lambda_1$, $d_2 = 0.2\lambda_2$, $\alpha = 0$, TE_z source	189
91	Excitation Current for a Slot at $x_c = 15\text{cm}$ in a Double Slab Coated Ground Plane - $f = 10\text{GHz}$, $L = 0.75\text{cm}$, $\epsilon_e = \epsilon_1 = 4\epsilon_0$, $\epsilon_2 = 2\epsilon_0$, $d_1 = 0.2\lambda_1$, $d_2 = 0.2\lambda_2$, $\alpha = 0$, TE_z source	191

92	Cone of Bistatic Scatter Directions for a Periodic Column of Slots Illuminated at an Arbitrary Incident Angle	193
93	Integrand from ASM Solution for Fields from a Slot Mode in the Double Slab Example Geometry - $\bar{R} = -20\lambda_0\hat{y}$, $\bar{R}_m = 0$	200
94	Electric Fields Radiated by a Single Slot Mode in the Example Double Slab Geometry at an Observation Radius of $10\lambda_0$	202
95	Transmission Through a Radome Composed of Doubly-Infinite Slot Arrays Embedded in Dielectrics which Give Near Scan Independence using the PMM Code	207
96	Top View of the Truncated Hybrid Radome - 21 Columns of Slots on Each Infinite Ground Plane with Infinite Dielectrics - Asterisks Designate Each Column of Periodic Slots	207
97	Front View of the Truncated Hybrid Radome - 21 Columns of Slots on Each Infinite Ground Plane	208
98	Currents on the 21 Column Truncated Hybrid Radome vs. Currents on an Infinite Radome - 100 V/m Normal Incidence Source, TE_z , 10 GHz	210
99	Backscatter from 21 Column Truncated Hybrid Radome at 10 GHz, TE_z	211
100	Bistatic Transmission Pattern of 21 Column Truncated Hybrid Radome at 10 GHz, TE_z , Normal Incidence - Data Normalized to Physical Optics	213
101	Bistatic Transmission Pattern of 21 Column Truncated Hybrid Radome at 10 GHz TE_z , $\eta = 30^\circ$ Incidence - Data Normalized to Physical Optics	214
102	Bistatic Transmission Pattern of 21 Column Truncated Hybrid Radome at 10 GHz, TE_z , $\eta = 60^\circ$ Incidence - Data Normalized to Physical Optics	215
103	Bistatic Transmission Pattern of 21 Column Truncated Metal Radome (No Dielectrics) at 8 GHz, TE_z , Normal Incidence - Data Normalized to Physical Optics	216
104	Bistatic Transmission Pattern of 21 Column Truncated Metal Radome (No Dielectrics) at 8 GHz, TE_z , $\eta = 60^\circ$ Incidence - Data Normalized to Physical Optics	217
105	Currents on the 41 Column Truncated Hybrid Radome vs. Currents on an Infinite Radome - 100 V/m Normal Incidence Source, 10 GHz, TE_z	219
106	Backscatter from 41 Column Truncated Hybrid Radome at 10 GHz, TE_z	221

107	Bistatic Transmission Pattern of 41 Column Truncated Hybrid Radome at 10 GHz, TE_z , Normal Incidence - Data Normalized to Physical Optics	222
108	Bistatic Transmission Pattern of 41 Column Truncated Hybrid Radome at 10 GHz, TE_z , $\eta = 30^\circ$ Incidence - Data Normalized to Physical Optics	223
109	Bistatic Transmission Pattern of 41 Column Truncated Hybrid Radome at 10 GHz, TE_z , $\eta = 60^\circ$ Incidence - Data Normalized to Physical Optics	224
110	Front View of 41 Column of Slots with Edge Loadings Provided by Shunt Resistances	226
111	Bistatic Transmission Pattern of Edge Treated and Ordinary Truncated 41 Column Hybrid Radomes at 10 GHz, TE_z , Normal Incidence - Data Normalized to Physical Optics	227
112	Transmission Through a Doubly-Infinite Array of Passive Inductively Loaded Dipoles in Resonance from the PMM Code	230
113	Top View of Finite Phased Array Antenna Near the 21 Column Truncated Hybrid Radome - Antenna to Radome Space = $0.5875\lambda_0$	231
114	Transmission Patterns for the Antenna/Radome Geometry in Figure 113 and the Antenna in Free Space with Uniform In-Phase Excitation, 10 GHz, TE_z	232
115	Top View of Test Geometry with One Radiating Column of Transverse Dipoles placed $\lambda_0/4$ from the 21 Column Truncated Hybrid Radome	233
116	Transmission Patterns for the Single Dipole Column in Figure 115 both Through the Radome and Without the Radome, 10 GHz, TE_z	234
117	Top View of Test Geometry with One Radiating Column of Transverse Dipoles placed $1.5875\lambda_0$ from the 21 Column Truncated Hybrid Radome	235
118	Transmission Patterns for the Single Dipole Column in Figure 117 both Through the Radome and Without the Radome	236
119	Input Impedances for Each Column in the Dipole Antenna Array in Figure 113 along with Similar Input Impedances for the Antenna in Free Space, 10 GHz	238
120	Top View of Finite Phased Array Antenna Near the 21 Column Truncated Hybrid Radome - Antenna to Radome Space = $2.5875\lambda_0$	239
121	Input Impedances for Each Column in the Antenna Array in Figure 120 along with Similar Input Impedances for the Antenna in Free Space, 10 GHz	240

122	Transmission Patterns for the Antenna/Radome Geometry in Figure 120 and the Antenna in Free Space with Uniform In-Phase Excitation, 10 GHz, TE_z	241
123	Array of Point Sources	247
124	Spiral Average Method for Free Space Periodic Green's Function - $D_z = \lambda/3, \rho = 0.2\lambda, z = 0.1\lambda$	248
125	Doubly-Infinite Array of Hertzian Dipole Sources	253

CHAPTER I

INTRODUCTION

1.1 BACKGROUND AND PROBLEM STATEMENT

Over the last several years, much effort has been devoted to developing the theory of radiation and scattering from frequency selective surfaces (FSS). This theory has been used in many antenna and radome designs. Several computer codes have been developed at The Ohio State University, which use the plane wave expansion method, developed by Munk and others [1, 2], to get a very efficient expression for fields from doubly infinite arrays (i.e., periodic in two orthogonal directions). A particularly useful code is the Periodic Moment Method (PMM) code from Henderson [3], which can be used to model bent wire and slot arrays in a stratified medium, where all elements are fully contained in the plane(s) of the array(s). The application of this code and others has helped to mature the doubly infinite FSS theory.

The PMM code may be used as a first order design tool for many practical antennas and radomes. However, it fails to predict edge termination or diffraction effects inherent in actual designs. Measured data from radiating finite phased arrays have demonstrated that sidelobe levels change dramatically when edge termination effects change the "sensed" impedance from that which occurs within an infinite array [4].

The designer of a radome panel or antenna array which is to be mounted in a metallic body cannot design the transition between the FSS and the surrounding surface with the present version of the PMM code. In addition, the PMM code

must be used to design antennas and radomes separately¹. Therefore, no mutual interaction effects between the antenna and radome, which in some locations are in close proximity, can be analyzed.

Practical FSS designs contain finite arrays in two dimensions. To fully analyze them, it is tempting to use a brute force method which is time consuming and taxing on computer storage. Such a method would account for all of the scattering mechanisms in the finite array. The primary effect from finiteness can be viewed as edge scattering, which is similar to an edge diffraction from a solid surface. Important secondary effects include the scattering from the junction of two edges (similar to corner diffraction) and the multiple interactions between edges and corners. The transmission and reflection properties of FSS also tend to change slightly from that predicted with infinite FSS theory as the finite size shrinks. For this reason, researchers outside of the Ohio State community have recently noted the need to model the finite scattering effects [5].

Although a brute force solution is usually too expensive, a solution to FSS scattering with the primary edge termination mechanism (and multiple edge interactions between parallel edges) is possible with an array which is finite in one dimension and infinite in another. With such a geometry, infinite array theory may be used to fully characterize one dimension, and the moment method may be used for the other.

A few attempts have been made recently to model scattering from FSS which are finite in one dimension and infinite in another. Shubert [6] developed a Fourier series based method which extended doubly-infinite array theory to analyze finite arrays in the presence of an infinite stratified medium. His approach is not easily transferable to arrays which are designed with different elements or impedance loadings near the edges, which is a likely approach for modifying the edge scattering effect. His

¹Assuming the antenna array plane is not parallel to the radome plane.

approach also becomes computationally burdensome when examining an array at near grazing incidence.

Researchers outside of Ohio State [7, 8] have recently attempted to model truncated and curved arrays by assuming the equivalent currents at any particular column are the same as those which would exist on an infinite array. This approach is the array analog to physical optics, and like its solid surface cousin, gives poor results near grazing angles of incidence. These solutions also do not include the modeling of dielectric materials.

Hughes [9] modeled the scattering from a finite collection of \hat{z} directed dipoles which were infinitely periodic in z as well. His work included the development of a code which models a collection of these dipole "strings" either in free space or in the presence of a conducting circular cylinder (also infinite in z). Simon [10] extended Hughes work to embed dipoles which were conformal to a helix in a dielectric-clad circular cylinder. In his work, the dipoles could be \hat{z} directed, $\hat{\phi}$ directed, or in any combination of these two helical directions.

Strickler [11] used the code developed by Hughes to model an antenna mounted over a finite width ground plane in free space. He modeled the ground plane with a carefully tuned passive dipole array. His work explored the usefulness of designing practical FSS using the "finite by infinite array" approach.

Finally, Hayes [12] attempted to model the scattering from individual strings of dipoles in free space where each dipole was perpendicular to the infinite array axis. His attempt failed to get the self impedance of an individual dipole string or the mutual impedance between two closely spaced strings. His field expressions also proved to be too computationally intense to be implemented into a practical computer code.

The code created by Hughes has been a great help for designing FSS composed of vertically oriented elements with radiation and scattering primarily desired in a horizontal plane. This situation is often denoted the TM polarization. Since the work of Hayes failed to be practical, a similar analysis capability is needed for transverse dipoles (i.e., the TE case). Such an analysis capability is necessary to design treatments on the edges of an array without expensive "trial and error" hardware experiments. The analysis needs to also include the effects of near zone coupling and truncation with a finite array of slots in a ground plane, which can act as a radome. Since such radomes often are designed with two slotted planes sandwiched between dielectrics, these types of geometries must be accommodated in the analysis.

This dissertation concentrates on the development of an analysis technique which handles the case of transverse dipoles and axial slots in a "finite by infinite" array. Transverse dipoles are defined as being oriented in some direction which is perpendicular to the infinite axis. The dipole orientations in various columns, however, do not necessarily stay parallel to each other. Axial slots are defined to be oriented only in the direction of the infinite axis, which makes them polarization compatible with transverse dipoles. To clarify this geometry, Figure 1 depicts a view from the infinite axis at a generalized set of transverse dipole and axial slot arrays, as can be analyzed by the methods in this dissertation. Note that only the slot arrays are embedded in a dielectric medium.

Figure 2 gives a perspective view of a set of transverse dipole array columns in the presence of a set of axial slot array columns in a single ground plane with no dielectrics. Note that the infinite axis is designated by \hat{z} and that each column array (dipole or slot) has a common multiple inter-element spacing, D_z . Also note that

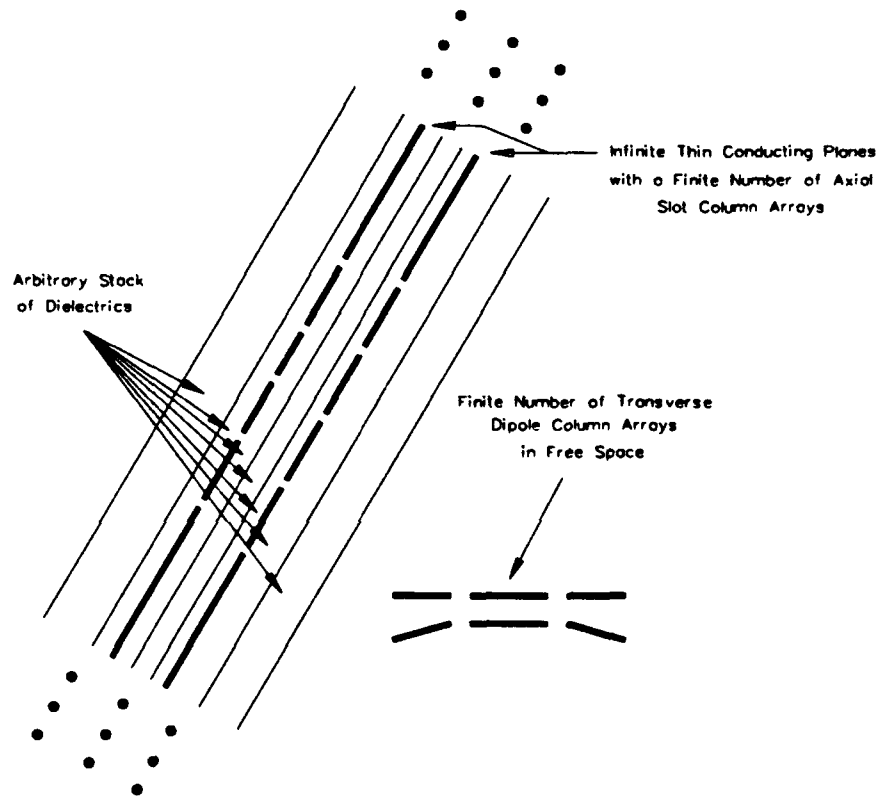


Figure 1: Generalized Geometry of a Finite Collection of Transverse Dipole and Axial Slot Arrays which are Embedded in an Infinite Stratified Media - View from the Infinite Axis

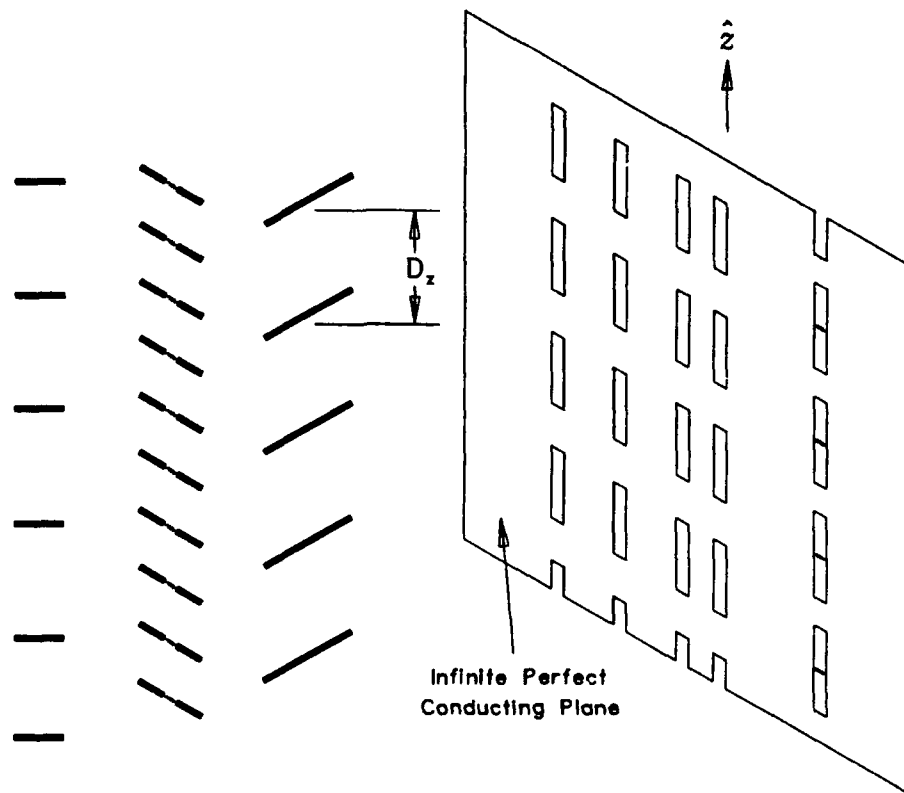


Figure 2: Perspective View of a Finite Collection of Transverse Dipole and Axial Slot Arrays in a Single Ground Plane in Free Space

the dipoles may be loaded with lumped impedances at their terminals and the slots may have lumped shunt admittance loads.

Two types of problems shall be examined with these geometries. The first is that of a radiating set of dipoles, which forms a phased array antenna. In such an application, a finite width ground plane for the antenna may be simulated by a set of resonating passive dipole array columns, at some particular frequency and angle. The radiation pattern of the antenna through the radome is of interest, as well as the input impedances of various dipoles and the effects of truncation.

The second problem is that of passive scattering by the radome and antenna dipoles. For this problem, the excitation comes from a plane wave which impinges

on the radome from the half-space not containing the dipoles. Both bistatic and backscatter echo is of interest for this excitation.

1.2 OVERALL SOLUTION APPROACH

The solution approach adopted in this dissertation is to form integral equations based on equivalent scattering currents for both the dipoles and slots, then solve for the unknown currents using the method of moments [13]. With the equivalent currents found, all other quantities such as input impedances and scattered fields may be determined. This section presents the general moment method procedure which is employed, with the details of forming the solution left for the remainder of the dissertation.

The governing integral equations may be developed from the perspective of the geometry shown in Figure 3, which depicts two ground planes, each of which having a single axial slot, and a single transverse dipole. The extension to a multiple number of slots, including infinite column arrays, will follow by a modal definition with Floquet's theorem, as will be described later. The addition of dielectric slabs around the slotted planes will be handled by the proper choice of Green's functions in the integral equations.

The electromagnetic equivalence theorem [14] is employed by filling the slots with a perfect conductor and replacing the dipole with free space. Magnetic currents become equivalent scattering sources at the former slot locations on both sides of the planes, and electric currents become an equivalent scattering source along the former surface of the thin cylindrical dipole. These currents are of the form,

$$\overline{M} = \overline{E} \times \hat{n} \quad (1.1)$$

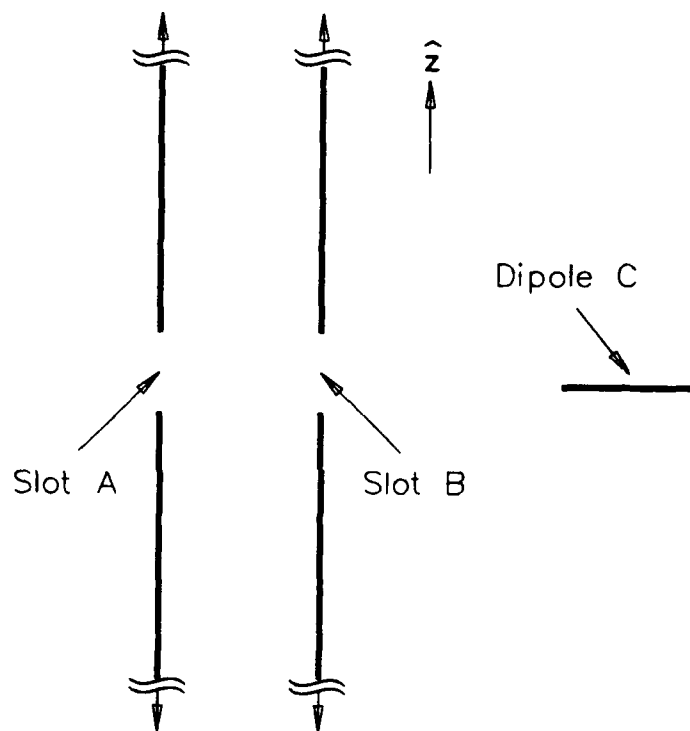


Figure 3: Two Ground Planes with Single Axial Slots in the Presence of a Single Transverse Dipole

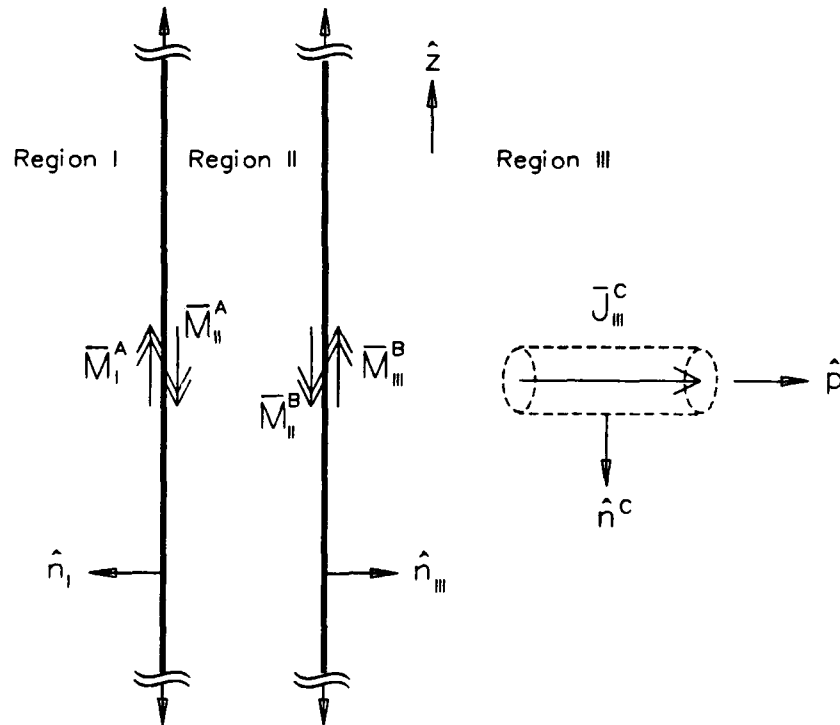


Figure 4: Equivalent Scattering Geometry

and

$$\bar{J} = \hat{n} \times \bar{H} \quad (1.2)$$

where \bar{E} is the total electric field which exists in the slot and \bar{H} is the total magnetic field which exists on the dipole surface in the original problem. The unit vector, \hat{n} is the outward normal direction for each equivalent surface. The new geometry with the equivalent surfaces and equivalent scattering currents is depicted in Figure 4.

The superscripts for the currents in Figure 4 indicate the scattering object and the subscripts donate the region of space in which the current is applicable. Using a thin wire assumption, the equivalent electric scattering current for the dipole is axial (for the dipole) directed and uniformly distributed about the circumference. It is

then compressed into a single filament of current, which exists along the center axis of the former dipole. The magnetic currents for the slots are depicted as being removed from the perfect conductors, but are actually located an infinitesimal distance away.

Using the boundary condition that the electric field in the slots is continuous across each region from the original problem, the opposite signs of the outward normals implies that

$$\overline{M}_I^A = -\overline{M}_{II}^A \quad (1.3)$$

and

$$\overline{M}_{II}^B = -\overline{M}_{III}^B. \quad (1.4)$$

One other independent boundary condition must be used to form the integral equations for the slots. It is the continuity of the tangential components of the magnetic field across the slots in the original problem. Thus the total tangential magnetic field at the slots from each region must be identical.

For now, assume the excitation source is an externally provided plane wave which exists in Region I. A magnetic field equation may be written for field location points within slot A. It is:

$$\begin{aligned} \hat{n}_I \times \left[\overline{H}_I^{inc} + \overline{H}_I^{ref} + \overline{H}_I^{scat}(\overline{M}_I^A) \right] \\ = \hat{n}_I \times \left[\overline{H}_{II}^{scat}(-\overline{M}_I^A) + \overline{H}_{II}^{scat}(-\overline{M}_{III}^B) \right] \end{aligned} \quad (1.5)$$

where Equations (1.3) and (1.4) have been used to remove all explicit references to \overline{M}_{II} . The field \overline{H}^{inc} is from the incident plane wave and \overline{H}^{ref} is the corresponding reflected plane wave from the complete conducting plane. They may be combined to form a generalized incident field, which is

$$\overline{H}_I^{ginc} = \overline{H}_I^{inc} + \overline{H}_I^{ref}. \quad (1.6)$$

A magnetic field equation may also be written for field locations within slot B.

It is:

$$\begin{aligned}\hat{n}_{III} \times & \left[\overline{H}_{II}^{scat}(-\overline{M}_I^A) + \overline{H}_{II}^{scat}(-\overline{M}_{III}^B) \right] \\ & = \hat{n}_{III} \times \left[\overline{H}_{III}^{scat}(\overline{M}_{III}^B) + \overline{H}_{III}^{scat}(\overline{J}_{III}^C) \right].\end{aligned}\quad (1.7)$$

Finally, an electric field equation may be written for the former dipole surface locations by noting that the tangential components of the electric field must vanish in the original problem. It is:

$$\hat{n}^C \times \left[\overline{E}_{III}^{scat}(\overline{M}_{III}^B) + \overline{E}_{III}^{scat}(\overline{J}_{III}^C) \right] = 0. \quad (1.8)$$

Equations (1.5), (1.7), and (1.8) are vector equations involving two surface vector components. In general, they can be decomposed into six scalar equations. Using the thin wire and thin slot assumptions, the dominating currents will be directed along the major axes of the slots and dipoles. Removing the other direction of current flow, the currents of the two slots and one dipole are of the form of three scalar unknowns. There is no need to use all six scalar equations for the three unknowns. Therefore, we may select only the three scalar equations corresponding to fields along the major axes, which are \hat{z} for the slots and \hat{p} for the dipole. With this scalar reduction, and rearranging terms in a standard format², the governing equations become:

$$\hat{z} \cdot \overline{H}_I^{ginc} = -\hat{z} \cdot \left[\overline{H}_I^{scat}(\overline{M}_I^A) + \overline{H}_{II}^{scat}(\overline{M}_I^A) + \overline{H}_{II}^{scat}(\overline{M}_{III}^B) \right], \quad (1.9)$$

$$0 = -\hat{z} \cdot \left[\overline{H}_{II}^{scat}(\overline{M}_I^A) + \overline{H}_{II}^{scat}(\overline{M}_{III}^B) + \overline{H}_{III}^{scat}(\overline{M}_{III}^B) + \overline{H}_{III}^{scat}(\overline{J}_{III}^C) \right], \quad (1.10)$$

²Using the linearity of the radiation operator, $\overline{F}(-\overline{K}) = -\overline{F}(\overline{K})$, where \overline{F} is either an electric or magnetic field and \overline{K} is either an electric or magnetic current.

$$0 = -\hat{p} \cdot \left[\bar{E}_{III}^{scat}(\bar{M}_{III}^B) + \bar{E}_{III}^{scat}(\bar{J}_{III}^C) \right]. \quad (1.11)$$

Equation (1.11) is valid anywhere on the surface of the original dipole, but we will constrict its application to a thin filament along the major axis at some yet to be specified circumferential position. By the complementary nature of slots and dipoles, the admittance of a thin rectangular slot strip should behave like the impedance of a corresponding thin rectangular metal strip. A thin metal strip can be approximated by a thin wire, which has a radius of one-fourth of the original strip width [15]. Therefore, the equivalent magnetic currents may be concentrated into thin filaments located at the center of the slots and the application of Equations (1.9) and (1.10) may be done on thin filaments (\hat{z} directed) located an "equivalent wire radius" from the radiating currents at slots A and B, respectively. For reasons which will be discussed later, the best choice of circumferential position for these "testing filaments" is as far from the perfect conducting planes as possible.

Equations (1.9) through (1.11) are linked integral equations with the scattering currents, \bar{M}_I^A , \bar{M}_{III}^B , and \bar{J}_{III}^C as the unknown quantities. The fields from these currents may be expressed by the following radiation integrals, which are generically given in terms of appropriate dyadic Green's functions as [16]:

$$\bar{H}(\bar{M}) = j\omega\epsilon \int \bar{\Gamma}(\bar{R}, \bar{R}') \cdot \bar{M}(\bar{R}') d\bar{R}' \quad (1.12)$$

$$\bar{H}(\bar{J}) = - \int [\nabla \times \bar{\Gamma}(\bar{R}, \bar{R}')] \cdot \bar{J}(\bar{R}') d\bar{R}' \quad (1.13)$$

$$\bar{E}(\bar{J}) = j\omega\mu \int \bar{\Gamma}(\bar{R}, \bar{R}') \cdot \bar{J}(\bar{R}') d\bar{R}' \quad (1.14)$$

$$\bar{E}(\bar{M}) = \int [\nabla \times \bar{\Gamma}(\bar{R}, \bar{R}')] \cdot \bar{M}(\bar{R}') d\bar{R}' \quad (1.15)$$

where \bar{R}' and \bar{R} represent position vectors to source and observation points, respectively. Equations (1.12) through (1.15) are presented for completeness as the general procedure for finding the fields. The dyadic Green's function must be chosen for the

region in which the source and field observation point are located. For cases where stratified dielectric layers are included, the dyadic Green's function which satisfies the appropriate dielectric boundary conditions must be chosen. For the remainder of this dissertation, however, we shall not explicitly identify either dyadic or scalar Green's functions, though they shall be inherent in the solutions.

We use the moment method to solve Equations (1.9) through (1.11) simultaneously in an approximate sense. First, we choose a set of basis functions which we believe can represent the unknown currents fairly well when weighted with unknown expansion coefficients. That is, we choose

$$\overline{M}_I^A \approx \hat{z} \sum_{n=1}^{N_A} V_n^A \phi_n^A(\overline{R}'), \quad (1.16)$$

$$\overline{M}_{III}^B \approx \hat{z} \sum_{n=1}^{N_B} V_n^B \phi_n^B(\overline{R}'), \quad (1.17)$$

and

$$\overline{J}_{III}^C \approx \hat{p} \sum_{n=1}^{N_C} I_n^C \phi_n^C(\overline{R}'). \quad (1.18)$$

The functions $\phi_n(\overline{R}')$ are the chosen dimensionless basis functions. The unknown expansion coefficients, V_n and I_n^C , have dimensions of volts and amperes, respectively.

Since the assumed current expansions contain an approximation, they create an error function when substituted back into the governing integral equations. Using linearity of the radiation integral and ϵ to define the errors, we get

$$\begin{aligned} \hat{z} \cdot \overline{H}_I^{ginc} &= -\hat{z} \cdot \sum_{n=1}^{N_A} V_n^A [\overline{H}_{II}^{scat}(\hat{z}\phi_n^A) + \overline{H}_{III}^{scat}(\hat{z}\phi_n^A)] - \hat{z} \cdot \sum_{n=1}^{N_B} V_n^B \overline{H}_{II}^{scat}(\hat{z}\phi_n^B) \\ &+ \epsilon^A(\overline{R}, V_1^A, V_2^A, \dots, V_{N_A}^A, V_1^B, V_2^B, \dots, V_{N_B}^B), \end{aligned} \quad (1.19)$$

$$0 = -\hat{z} \cdot \sum_{n=1}^{N_A} V_n^A \overline{H}_{II}^{scat}(\hat{z}\phi_n^A) - \hat{z} \cdot \sum_{n=1}^{N_B} V_n^B [\overline{H}_{II}^{scat}(\hat{z}\phi_n^B) + \overline{H}_{III}^{scat}(\hat{z}\phi_n^B)]$$

$$\begin{aligned}
& - \hat{z} \cdot \sum_{n=1}^{N_C} I_n^C \bar{H}_{III}^{scat}(\hat{p}\phi_n^C) \\
& + \epsilon^B(\bar{R}, V_1^A, V_2^A, \dots, V_{N_A}^A, V_1^B, V_2^B, \dots, V_{N_B}^B, I_1^C, I_2^C, \dots, I_{N_C}^C), \quad (1.20)
\end{aligned}$$

and

$$\begin{aligned}
0 & = -\hat{p} \cdot \sum_{n=1}^{N_B} V_n^B \bar{E}_{III}^{scat}(\hat{z}\phi_n^B) - \hat{p} \cdot \sum_{n=1}^{N_C} I_n^C \bar{E}_{III}^{scat}(\hat{p}\phi_n^C) \\
& + \epsilon^C(\bar{R}, V_1^B, V_2^B, \dots, V_{N_B}^B, I_1^C, I_2^C, \dots, I_{N_C}^C). \quad (1.21)
\end{aligned}$$

As seen in the above equations, the value of the error is a function of the expansion coefficients which will be used. By the method of Harrington [13], we choose the errors to vanish in the weighted sense of being integrated with some testing functions. That is, we choose some testing functions of the form, θ_m , and force the condition that

$$\int \epsilon^i(\bar{R}) \cdot \theta_m^i(\bar{R}) d\bar{R} = 0 \quad (1.22)$$

where $i = A, B$, or C . This condition is essentially governing the outcome of the expansion coefficients which will eliminate the error in this weighted sense. Thus, by introducing an equal number of testing functions as basis functions (for each slot and dipole), we produce a system of linear equations. The equations may be represented by the following matrix expression, of which the entries are actually sub-matrices and sub-column arrays.

$$\begin{bmatrix} I_m^A \\ 0 \\ 0 \end{bmatrix} = \begin{bmatrix} Y_{mn_{II}}^{AA} + Y_{mn_{III}}^{AA} & Y_{mn}^{AB} & 0 \\ Y_{mn}^{BA} & Y_{mn_{II}}^{BB} + Y_{mn_{III}}^{BB} & G_{mn}^{BC} \\ 0 & G_{mn}^{CB} & Z_{mn}^{CC} \end{bmatrix} \begin{bmatrix} V_n^A \\ V_n^B \\ I_n^C \end{bmatrix} \quad (1.23)$$

In the index pairs, the first index denotes both a matrix row and a receiving, or testing mode. The second index corresponds to a matrix column and a transmitting (basis) mode.

The entries of the coupling matrix are of the forms:

$$Y_{mnI}^{AA} = - \int \hat{z} \cdot \bar{H}_I^{scat}(\hat{z}\phi_n^A) \cdot \theta_m^A(\bar{R}) d\bar{R} \quad (1.24)$$

$$Y_{mnII}^{AA} = - \int \hat{z} \cdot \bar{H}_{II}^{scat}(\hat{z}\phi_n^A) \cdot \theta_m^A(\bar{R}) d\bar{R} \quad (1.25)$$

$$Y_{mn}^{AB} = - \int \hat{z} \cdot \bar{H}_{II}^{scat}(\hat{z}\phi_n^B) \cdot \theta_m^A(\bar{R}) d\bar{R} \quad (1.26)$$

$$Y_{mn}^{BA} = - \int \hat{z} \cdot \bar{H}_{II}^{scat}(\hat{z}\phi_n^A) \cdot \theta_m^B(\bar{R}) d\bar{R} \quad (1.27)$$

$$Y_{mnII}^{BB} = - \int \hat{z} \cdot \bar{H}_{II}^{scat}(\hat{z}\phi_n^B) \cdot \theta_m^B(\bar{R}) d\bar{R} \quad (1.28)$$

$$Y_{mnIII}^{BB} = - \int \hat{z} \cdot \bar{H}_{III}^{scat}(\hat{z}\phi_n^B) \cdot \theta_m^B(\bar{R}) d\bar{R} \quad (1.29)$$

$$G_{mn}^{BC} = - \int \hat{z} \cdot \bar{H}_{III}^{scat}(\hat{p}\phi_n^C) \cdot \theta_m^B(\bar{R}) d\bar{R} \quad (1.30)$$

$$G_{mn}^{CB} = - \int \hat{p} \cdot \bar{E}_{III}^{scat}(\hat{z}\phi_n^B) \cdot \theta_m^C(\bar{R}) d\bar{R} \quad (1.31)$$

$$Z_{mn}^{CC} = - \int \hat{p} \cdot \bar{E}_{III}^{scat}(\hat{p}\phi_n^C) \cdot \theta_m^C(\bar{R}) d\bar{R} \quad (1.32)$$

The Y s have the interpretation of mutual and self-admittances, with units of mhos³ The Z s are of the form of mutual and self-impedances, with units of ohms. The V s and I s in Equation (1.23) have units of volts and amperes, respectively. Entries in the sub-block G^{BC} are unitless current gains and entries of G^{CB} are unitless voltage gains. By manipulating the equations so that each entry in the coupling matrix is defined with a minus sign, the admittances and impedances agree with the physical meaning attached by Schelkunoff [17]. With this arrangement, it is relatively easy to add the effects of lumped impedance loads at the dipole terminals

³Units for the coupling matrix terms arise by normalizing all basis functions used in generating Equations (1.24) through (1.32). For the magnetic scattering current basis functions, ϕ_n^A and ϕ_n^B , this normalization involves a hidden $1/volt$ factor. For the electric scattering current basis functions, ϕ_n^C , there is a hidden $1/amp$ factor. This is identical to the normalization procedure used by Schelkunoff [17].

or lumped admittance loads across the centers of the slots, as they contribute directly to the self-coupling terms of appropriate modes.

The expressions, $Y_{mn_I}^{AA}$ and $Y_{mn_{II}}^{AA}$ (and similar for Y^{BB}), are merely "one sided" mutual admittances, which are added in parallel to form the total mutual admittances used in the coupling matrix.

To complete the generalized solution approach, the entries of the non-zero sub-array in the excitation vector are:

$$I_m^A = \int \hat{z} \cdot \bar{H}_I^{ginc}(\bar{R}) \cdot \theta_m^A(\bar{R}) d\bar{R}. \quad (1.33)$$

In a problem where the dipole is radiating, the top two sub-arrays in the excitation vector are zero and the bottom sub-array contains the coefficients of delta-gap voltage generators placed at the terminals of the basis functions [18].

With the use of the electromagnetic reciprocity theorem [14], some symmetries may be found in the coupling matrix. The entire matrix is absolutely symmetric, except for entries corresponding to the G^{BC} and G^{CB} sub-blocks. For these blocks, an anti-symmetry is formed with the entries obeying

$$G_{mn}^{CB} = -G_{nm}^{BC} \quad (1.34)$$

for any particular integer value of n between 1 and N_B and m between 1 and N_C .

The scattering or radiation problem is completed by solving for the unknown expansion coefficients of the scattering currents, then using these currents in the radiation integral. Usually, the fields of interest are in Region I, so only the currents for slot A and the radiation integral for Region I are required. The unknown current coefficients are normally found by getting the inverse of the coupling matrix or solving Equation (1.23) with a Gaussian elimination routine.

The solution thus far has been presented in terms of two single slots and a single dipole. The extension to "finite by infinite" arrays does not change the basic moment

method procedure. This extension only involve the definition of basis functions which are single infinite arrays. Each mode (slot or dipole) must have a common inter-element spacing, D_z (see Figure 2). If a particular column of elements is denser in z than the others (e.g., see the middle column of dipoles in Figure 2, which are twice as dense in z as the other columns), the problem can still be handled with an interlacing of modes in z , as long as there is a common integral number of inter-element spacings between all arrays, which can serve as D_z ⁴. The current on each element of a basis function is identical, except for a possible linear phase progression along \hat{z} , which is governed by Floquet's theorem.

Often in the moment method, the testing functions are chosen to be identical to the basis functions, which is dubbed Galerkin's method. For the case of an infinite column mode, the strict use of Galerkin's method must be avoided since it will result in infinite values in the entries of the excitation vector and coupling matrix⁵. A "quasi-Galerkin" method of truncating the testing function to be non-zero only on a single element of the column, denoted the reference element, can be used by making the testing current shapes identical to the basis currents on this reference element. The "quasi-Galerkin" method assures that the excitation vector and coupling matrix entries are finite, and this approach is adopted in this dissertation.

1.3 OVERVIEW OF REMAINING CHAPTERS

In the chapters to follow, the solution to the moment method problem is developed specifically for "finite by infinite" arrays involving two conducting planes of

⁴For the dipoles depicted in Figure 2, four periodic transverse dipole modes may be used - one each for the first and third columns, and two interlaced modes for the middle column. Each mode uses the D_z spacing shown in the figure.

⁵This occurs even with the wire radius displacement between testing and basis functions.

axial slots surrounded by dielectrics and in the neighborhood of a "finite by infinite" array of transverse dipoles. Chapter II provides the derivation of slot-to-slot mode coupling, which form the self and mutual admittances in the coupling matrix. Chapter III gives the corresponding dipole-to-dipole self and mutual impedance derivations. The current and voltage gains in the coupling matrix are evaluated in Chapter IV. To complete the moment method solution, Chapter V presents the derivation of excitation vector entries and far zone fields after the scattering currents are known. Finally, Chapter VI gives some numerical results of complete moment method solutions and Chapter VII summarizes the dissertation and concludes.

CHAPTER II

SLOT-TO-SLOT COUPLING

In this chapter, we shall develop expressions for the self and mutual admittances used in the coupling matrix in Equation (1.23). Several solutions are developed, with the goal of each to be as efficient as possible for the region of space in which it is applied (see Figure 4) and the dielectric composition of that region. Thus, a "mixed bag of tricks" is presented such that a computer algorithm can choose the most efficient solution for the situation in a particular application.

This chapter is divided into two main sections, which concentrate on homogeneous regions of space and regions which included planar dielectric interfaces. Each of these sections is further subdivided into solutions for "outer zone" coupling (i.e., Regions I or III) and "inner zone" coupling (Region II).

2.1 HOMOGENEOUS REGIONS OF SPACE

2.1.1 Outer Zone Coupling

The problem of "outer zone" coupling between slot modes is depicted in Figure 5, which shows a radiating basis function of the form of a \hat{z} -directed periodic filamentary magnetic current on a ground plane, and a testing function displaced some distance in \hat{x} from the radiating current and an "equivalent wire radius" in \hat{y} from the ground plane. The environment is a homogeneous half-space.

To derive the radiated fields from the axial periodic magnetic current mode, first we examine how a column of \hat{z} -directed Hertzian magnetic currents radiates in

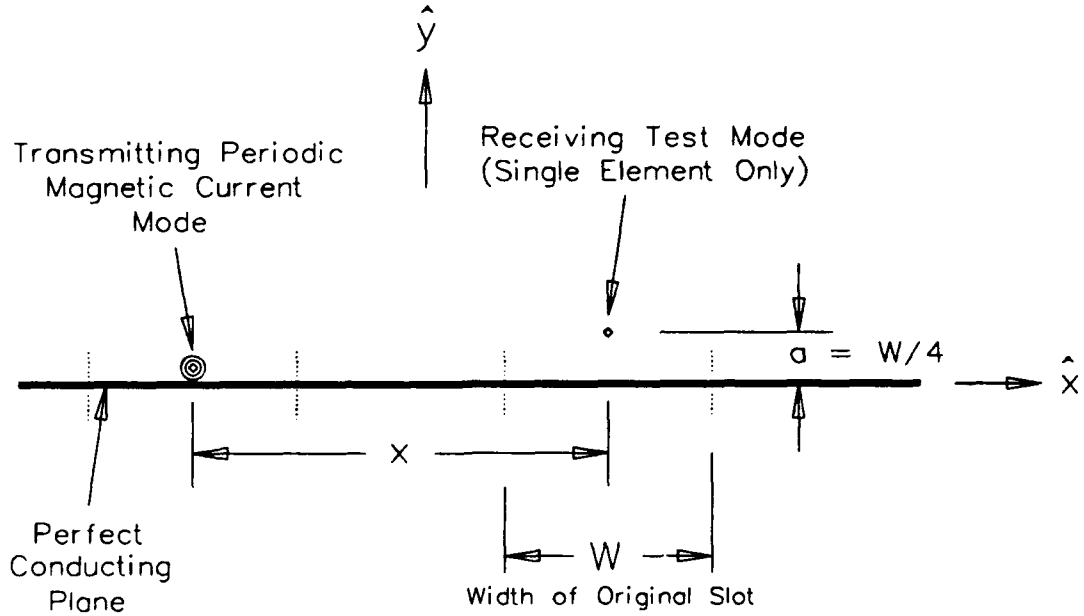


Figure 5: Geometry of Outer Zone Coupling between Slot Modes in a Homogeneous Half-Space; View from the Infinite Axis

free space. The appropriate geometry, in a transverse or side view, is given in Figure 6. Without loss of generality, the “reference element”, denoted by $m = 0$, is located at the origin and the field observation point is arbitrary.

From classical radiation theory [14], the electric vector potential at the field observation point from the m th Hertzian element is

$$d\bar{F}_m = \hat{z} \frac{\epsilon I_m dz'}{4\pi} \frac{e^{-j\beta R_m}}{R_m}, \quad (2.1)$$

where I_m is the constant magnetic current level over the infinitesimal source length and R_m is the slant path defined by

$$R_m = \sqrt{x^2 + y^2 + (mD_z - z)^2}. \quad (2.2)$$

By the superposition of the entire array of sources, the total vector potential at the observation point is

$$d\bar{F} = \sum_{m=-\infty}^{\infty} d\bar{F}_m. \quad (2.3)$$

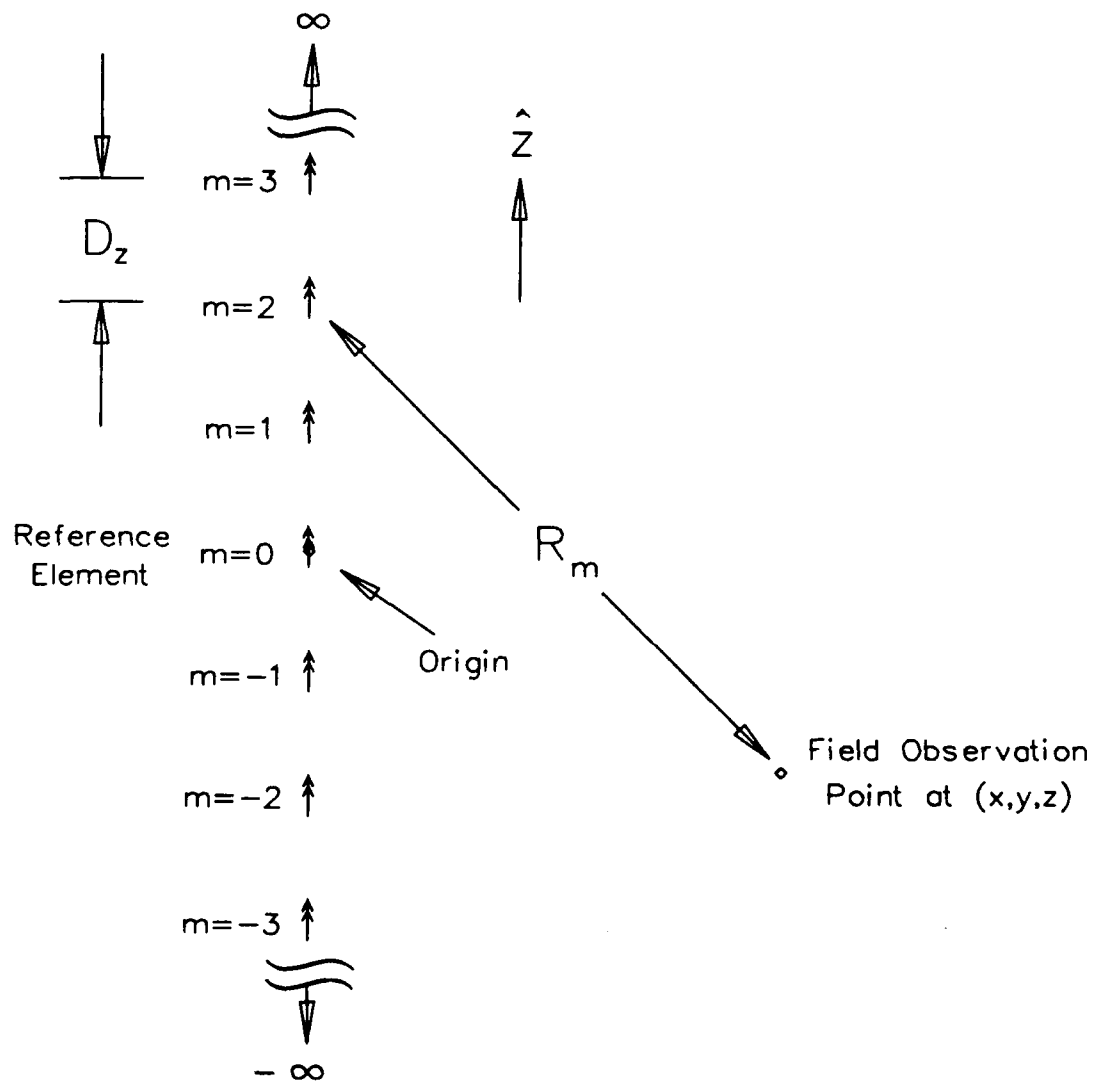


Figure 6: Side View of a Single Column of Periodic \hat{z} -Directed Hertzian Magnetic Current Sources

Next, we assume that the currents on these Hertzian elements are induced by an incoming plane wave having the propagation direction,

$$\hat{s} = \hat{x}s_x + \hat{y}s_y + \hat{z}s_z. \quad (2.4)$$

By Floquet's theorem [19], the induced current on the m th element will have the form

$$I_m = I_0 e^{-j\beta m D_z s_z}, \quad (2.5)$$

where I_0 is the current induced on the reference element. The total electric vector potential may now be rewritten as

$$d\bar{F} = \hat{z} \frac{\epsilon I_0 dz'}{4\pi} \sum_{m=-\infty}^{\infty} e^{-j\beta m D_z s_z} \frac{e^{-j\beta R_m}}{R_m}. \quad (2.6)$$

Now we introduce the Poisson Sum Formula [20], which is:

$$\sum_{m=-\infty}^{\infty} e^{jm\omega_0 t} F(m\omega_0) = T \sum_{n=-\infty}^{\infty} f(t + nT) \quad (2.7)$$

where $T = 2\pi/\omega_0$ and $F(\omega)$ is the Fourier transform of $f(t)$, as defined below,

$$F(\omega) = \int_{-\infty}^{\infty} f(t) e^{-j\omega t} dt, \quad (2.8)$$

with the inverse transform,

$$f(t) = \frac{1}{2\pi} \int_{-\infty}^{\infty} F(\omega) e^{j\omega t} d\omega. \quad (2.9)$$

Here and in most equations in this dissertation, the summation index m is used for spatial domain expressions and n is used for spectral domain expressions.

The Poisson Sum Formula is often useful in transforming a slowly converging infinite sum into a much faster converging sum. In the present case, the sum in Equation (2.6) is slowly converging for most observation points, and can benefit from the transformation. To make this transformation, we define the following:

$$\begin{aligned}\omega_0 &= D_z \\ t &= -\beta s_z \\ F(m\omega_0) &= \frac{e^{-j\beta R_m}}{R_m}.\end{aligned}$$

We also make use of the following Fourier transform pair [21],

$$\mathcal{F} \left[\frac{e^{jzt}}{j^2} H_0^{(2)}(\rho\sqrt{\beta^2 - t^2}) \right] = \frac{e^{-j\beta\sqrt{\rho^2 + (\omega - z)^2}}}{\sqrt{\rho^2 + (\omega - z)^2}} \quad (2.10)$$

where \mathcal{F} denotes the forward Fourier transform operation. With this transform pair, the Poisson Sum Formula changes Equation (2.6) into

$$d\bar{F} = \hat{z} \frac{\epsilon I_0 dz'}{j4D_z} \sum_{n=-\infty}^{\infty} e^{-j\beta z r_z} H_0^{(2)}(\beta r_\rho \rho), \quad (2.11)$$

where we have defined

$$r_z = s_z + \frac{n\lambda}{D_z}, \quad (2.12)$$

$$r_\rho = \sqrt{1 - r_z^2}, \quad (2.13)$$

and

$$\rho = \sqrt{x^2 + y^2}. \quad (2.14)$$

When the absolute value of r_z is less than or equal to one, the argument of the Hankel function in Equation (2.11) is real, and the corresponding term represents the vector potential of a propagating cylindrical wave mode. Typically, only one propagating mode term will exist, corresponding to the $n = 0$ term, though beam steering (or the incident plane wave direction) and inter-element spacing may combine to allow a finite number of other propagating modes (grating lobes) to exist.

The infinite number of other modes are evanescent cylindrical wave modes, which decrease in amplitude rapidly both as the mode number and distance (ρ) from the array increase. To make the evanescent modes behave according to the radiation condition, a choice of $-j$ must be made in taking the square root which

defines r_ρ . The evaluation of the Hankel function with this negative imaginary argument becomes equivalent to the evaluation of a modified Bessel function with a real argument.

The total electric field radiated by the Hertzian array is

$$d\bar{E} = -\frac{1}{\epsilon} \nabla \times d\bar{F}. \quad (2.15)$$

Substituting the expression in Equation (2.11) and using the irrotational property of \hat{z} , we get

$$d\bar{E} = \frac{I_0 dz'}{j4D_z} \hat{z} \times \sum_{n=-\infty}^{\infty} \nabla \left[e^{-j\beta z r_z} H_0^{(2)}(\beta r_\rho \rho) \right]. \quad (2.16)$$

The gradient in Equation (2.16) is best performed in cylindrical coordinates, which gives the result of

$$d\bar{E} = -\hat{\phi} \frac{\beta I_0 dz'}{j4D_z} \sum_{n=-\infty}^{\infty} r_\rho e^{-j\beta z r_z} H_1^{(2)}(\beta r_\rho \rho), \quad (2.17)$$

where $\hat{\phi}$ is the cylindrical coordinate vector which "encircles" the z axis in the counterclockwise sense when looking "down" from $+\infty$.

The radiated magnetic field is obtained from Faraday's law, which gives

$$\begin{aligned} d\bar{H} &= -\frac{1}{j\omega\mu} \nabla \times d\bar{E} \\ &= -\frac{\omega\epsilon I_0 dz'}{4D_z} \sum_{n=-\infty}^{\infty} e^{-j\beta z r_z} \left[\hat{\rho} j r_\rho r_z H_1^{(2)}(\beta r_\rho \rho) + \hat{z} r_\rho^2 H_0^{(2)}(\beta r_\rho \rho) \right] \end{aligned} \quad (2.18)$$

after several steps of algebra.

Now suppose the elements of the array are no longer infinitesimal in length. Instead, assume the magnetic current on the reference element is finite has a total length, L (centered about the origin), with a current shape given by $I(z')$. The radiated fields from this new array may be obtained by integrating the fields from a collection of Hertzian arrays. We also may assume that the array of magnetic currents is located on the surface of a perfect conducting plane, which is the case for

the admittance calculations that are desired. By image theory [14], the tangential magnetic currents double after removing the plane and using a homogeneous medium equivalence. The total fields radiated by the finite length element magnetic current array are:

$$\bar{E} = -\hat{\phi} \frac{\beta}{j2D_z} \sum_{n=-\infty}^{\infty} e^{-j\beta z r_z} r_\rho P^t H_1^{(2)}(\beta r_\rho) \quad (2.19)$$

and

$$\bar{H} = -\frac{\omega\epsilon}{2D_z} \sum_{n=-\infty}^{\infty} e^{-j\beta z r_z} P^t \cdot \left[\hat{\rho} j r_\rho r_z H_1^{(2)}(\beta r_\rho) + \hat{z} r_\rho^2 H_0^{(2)}(\beta r_\rho) \right] \quad (2.20)$$

where a transmitting pattern factor has been defined by

$$P^t = \int_{-L/2}^{L/2} I(z') e^{j\beta z' r_z} dz' \quad (2.21)$$

Noting that the cylindrical wave modes may be assigned directions of

$$\hat{r} = \hat{\rho} r_\rho + \hat{z} r_z, \quad (2.22)$$

the transmitting pattern factor may be rewritten as

$$P^t = \int_{-L/2}^{L/2} I(l) e^{j\beta l \hat{p} \cdot \hat{r}} dl, \quad (2.23)$$

where \hat{p} is the orientation of the element, which equals \hat{z} for the slot modes. Equation (2.23) agrees with the pattern factor definition used by Munk [1, 2] in the plane wave expansion of the fields from doubly-infinite arrays.

It is interesting to note that the fields radiated by the axial slot mode are omni-directional in the cylindrical coordinate, ϕ .

From Equations (1.24) through (1.29), it is seen that to compute the admittance terms of the coupling matrix, only the \hat{z} component of the radiated magnetic field is required. The electric field will be used in slot-to-dipole coupling, and is retained for future reference.

The computation of "outer zone" coupling for the homogeneous half-space is completed with the integration of the magnetic field multiplied by a testing function at the receiving filament. From Figure 5, we consider the centers of the slots of the two modes to be separated by the distance x along the conducting plane. Thus, the total separation distance is $\rho = \sqrt{x^2 + a^2}$. Using the function $I^{test}(z)$ to represent the testing current shape, the "one sided" admittance for the homogeneous half-space is:

$$Y = \frac{\omega\epsilon}{2D_z} \sum_{n=-\infty}^{\infty} \tau_{\rho}^2 P^t P^r H_0^{(2)}(\beta r_{\rho} \sqrt{x^2 + a^2}), \quad (2.24)$$

where a receiving pattern factor is defined by

$$P^r = \int I^{test}(z) e^{-j\beta z r_z} dz, \quad (2.25)$$

which is integrated over the test filament. This receiving pattern factor may also be written in the form of Equation (2.23), except with a sign change in the exponential.

The transmitting and receiving pattern factors may be evaluated in closed form for many commonly used basis and testing functions. Some examples of normalized mode shapes which have closed form pattern factors include the following:

Constant Functions (CON)

$$I(z) = 1 \quad (2.26)$$

Piecewise Sinusoids (PWS)

$$I(z) = \frac{\sin[\beta(\frac{L}{2} - |z|)]}{\sin(\frac{\beta L}{2})} \quad (2.27)$$

Piecewise Cosinusoids (PWC)

$$I(z) = \frac{\cos(\beta z) - \cos(\frac{\beta L}{2})}{1 - \cos(\frac{\beta L}{2})} \quad (2.28)$$

Rooftop Functions (TRI)

$$I(z) = -\frac{2}{L}|z| + 1 \quad (2.29)$$

Full Period Cosines (FPC)

$$I(z) = \frac{1}{2} \cos\left(\frac{2\pi z}{L}\right) + \frac{1}{2}. \quad (2.30)$$

Each of the above modes was defined for a total element length of L , centered about $z = 0$. Assuming that the modes are shifted so that the reference element is centered at $z = z_c$, the following pattern factors result (in order):

$$P(CON) = \frac{2}{\beta r_z} \sin\left(\frac{\beta L r_z}{2}\right) e^{\pm j\beta z_c r_z} \quad (2.31)$$

$$P(PWS) = \frac{2}{\beta \sin\left(\frac{\beta L}{2}\right)} \frac{[\cos\left(\frac{\beta L r_z}{2}\right) - \cos\left(\frac{\beta L}{2}\right)]}{1 - r_z^2} e^{\pm j\beta z_c r_z} \quad (2.32)$$

$$P(PWC) = \frac{2}{\beta - \beta \cos\left(\frac{\beta L}{2}\right)} \left[\frac{\sin\left(\frac{\beta L}{2}\right) \cos\left(\frac{\beta L r_z}{2}\right) - \frac{1}{r_z} \cos\left(\frac{\beta L}{2}\right) \sin\left(\frac{\beta L r_z}{2}\right)}{1 - r_z^2} \right] e^{\pm j\beta z_c r_z} \quad (2.33)$$

$$P(TRI) = \frac{4}{L\beta^2 r_z^2} \left[1 - \cos\left(\frac{\beta L r_z}{2}\right) \right] e^{\pm j\beta z_c r_z} \quad (2.34)$$

$$P(FPC) = \frac{16\pi^2 \sin\left(\frac{\beta L r_z}{2}\right)}{L^2 \beta r_z \left[\frac{16\pi^2}{L^2} - 4\beta^2 r_z^2 \right]} e^{\pm j\beta z_c r_z} \quad (2.35)$$

where the plus sign is used for transmitting pattern factors and the minus sign is used for receiving patterns.

It is interesting to note the asymptotic characteristics of the pattern factors, which affects the convergence of the spectral domain sum in Equation (2.24). The pattern factor series for the constant current mode goes as $1/n$ for increasing n . Note that this current has an abrupt discontinuity at the endpoints of the mode, which cannot occur without a charge accumulation for an actual dipole or slot. The

pattern factors for the piecewise sinusoid/cosinusoids and rooftop functions go as $1/n^2$. Each of these current shapes go to zero at the endpoints, but with slope discontinuities. Finally, the pattern factor series for the full period cosine goes as $1/n^3$. This current not only goes to zero at the endpoints, but also with a first derivative of zero.

Although the current for a slot of reasonable length (e.g. $\lambda/2$) may be represented fairly well by a large number of constant pulse modes defined in subdomains, such a solution is not usually implemented with periodic surfaces due to the desire to limit the total number of modes¹ and the slow convergence yielded by the asymptotic behavior of the pattern factors.

Piecewise sinusoids/cosinusoids are typically used for basis and testing functions of linear slot and dipole elements in periodic arrays [3]. Experience with moment method solutions using a large number of basis functions on a single dipole shows that the current induced in a scattering mode is nearly the shape of a single piecewise cosinusoid and the current produced by a radiating dipole is nearly the shape of a single piecewise sinusoid, as long as the total length of the dipole is less than about 0.6λ . Each of these modes lead to reasonably fast convergence in the cylindrical wave sums. Faster convergence can be achieved with full period cosine modes, but since the true currents are usually not closely represented by these modes, they are not good candidates for most circumstances.

When a slot is sufficiently long or the solution accuracy requires the use of more than one mode to model a slot array, an overlapping set of piecewise sinusoids

¹Limiting the number of periodic modes benefits primarily in the reduction of expensive calculations to fill a coupling matrix, unlike in ordinary moment method applications where the inversion of a large impedance matrix may dominate CPU time.

or rooftop functions form a good basis set. The rooftop functions have a slight advantage in not producing "cusps" in the overall current shape, when combined.

A final mention must be made of the special advantage offered by piecewise sinusoidal basis functions. This advantage is that the radiated field from such a current function on a single element (not a periodic array) may be expressed in closed form, even in the near zone. Thus, the mutual admittance between periodic slot modes could have been expressed in the spatial domain without numerical integrations, and avoiding the Poisson Sum transformation.

To express the mutual admittance in the spatial domain, one must first find the fields radiated by a piecewise sinusoid current on a single element. Carter [22] first derived the radiated fields from a half wavelength dipole with a sinusoidal distribution. Brown [23] extended his work to get a closed form expression for the electric field from a dipole of arbitrary length with one piecewise sinusoidal mode. Brown's result has the form of spherical wave sources at each endpoint and the center of the piecewise sinusoid. Applying duality to his result, the radiating from a single piecewise sinusoid magnetic current in a homogeneous medium (no ground plane), which is \hat{z} -directed, has total length L , and is centered at the origin includes the following \hat{z} component of the magnetic field:

$$H_z = \frac{-jY_0}{4\pi \sin(\frac{\beta L}{2})} \left[\frac{e^{-j\beta R_1}}{R_1} + \frac{e^{-j\beta R_2}}{R_2} - 2 \cos(\frac{\beta L}{2}) \frac{e^{-j\beta R}}{R} \right], \quad (2.36)$$

where the distances are

$$R = \sqrt{x^2 + y^2 + z^2}, \quad (2.37)$$

$$R_1 = \sqrt{x^2 + y^2 + (z - \frac{L}{2})^2}, \quad (2.38)$$

$$R_2 = \sqrt{x^2 + y^2 + (z + \frac{L}{2})^2}, \quad (2.39)$$

and Y_0 is the intrinsic admittance of the homogeneous medium. The magnetic field component in Equation (2.36) is in units of amperes/meter with a hidden 1 volt

factor understood in the numerator to account for the normalization of the magnetic current.

Now consider a second magnetic piecewise sinusoidal current of equal length and parallel to the first. Recalling the first current is centered at the origin, the second current may be centered at $\bar{R} = \rho\hat{\rho} + z\hat{z}$. Without loss of generality, we may assume that its position z is greater than zero. By applying the testing procedure given in Equations (1.24) through (1.29) with the radiated field in Equation (2.36), the following expression is obtained for the mutual admittance (ignoring any ground plane) in the spatial domain:

$$\begin{aligned}
Y_{12} = & \frac{Y_0}{8\pi \sin^2(\frac{\beta L}{2})} \left[(2 + 4 \cos^2(\frac{\beta L}{2})) (e^{j\beta z} E_i(X_1) + e^{-j\beta z} E_i(X_2)) \right. \\
& - 4 \cos(\frac{\beta L}{2}) (e^{j\beta(z+\frac{L}{2})} E_i(X_3) + e^{-j\beta(z+\frac{L}{2})} E_i(X_4)) \\
& - 4 \cos(\frac{\beta L}{2}) (e^{j\beta|z-\frac{L}{2}|} E_i(X_5) + e^{-j\beta|z-\frac{L}{2}|} E_i(X_6)) \\
& + e^{j\beta(z+L)} E_i(X_7) + e^{-j\beta(z+L)} E_i(X_8) \\
& \left. + e^{j\beta|z-L|} E_i(X_9) + e^{-j\beta|z-L|} E_i(X_{10}) \right], \tag{2.40}
\end{aligned}$$

where the following functions and arguments are defined:

$$E_i(X) = C_i(X) - jS_i(X) \tag{2.41}$$

$$C_i(X) = - \int_X^\infty \frac{\cos(\tau)}{\tau} d\tau \tag{2.42}$$

$$S_i(X) = \int_0^X \frac{\sin(\tau)}{\tau} d\tau \tag{2.43}$$

$$X_1 = \beta \left[\sqrt{\rho^2 + z^2} + z \right] \tag{2.44}$$

$$X_2 = \frac{(\beta\rho)^2}{X_1} \tag{2.45}$$

$$X_3 = \beta \left[\sqrt{\rho^2 + \left(z + \frac{L}{2}\right)^2} + z + \frac{L}{2} \right] \quad (2.46)$$

$$X_4 = \frac{(\beta\rho)^2}{X_3} \quad (2.47)$$

$$X_5 = \beta \left[\sqrt{\rho^2 + \left(z - \frac{L}{2}\right)^2} - z + \frac{L}{2} \right] \quad (2.48)$$

$$X_6 = \frac{(\beta\rho)^2}{X_5} \quad (2.49)$$

$$X_7 = \beta \left[\sqrt{\rho^2 + (z + L)^2} + z + L \right] \quad (2.50)$$

$$X_8 = \frac{(\beta\rho)^2}{X_7} \quad (2.51)$$

$$X_9 = \beta \left[\sqrt{\rho^2 + (z - L)^2} - z + L \right] \quad (2.52)$$

$$X_{10} = \frac{(\beta\rho)^2}{X_9} \quad (2.53)$$

Since the sine and cosine integrals can be tabulated or approximated with simple functions, the mutual admittance in Equation (2.40) is said to be in closed form.

With both spectral and spatial domain solutions available for the slot coupling with PWS basis functions, the question which must be answered is which approach leads to an accurate solution with the best speed? To answer this, a typical case is chosen with the lengths of the radiating and receiving modes both at 0.4λ , an inter-element spacing of $D_z = 0.6\lambda$, and no z offset between the two modes. The inter-modal spacing, ρ , is varied from very low values, which typically correspond to self-admittance calculations, to 10λ . At each value of ρ , a reference solution for the admittance was obtained by summing in the spectral domain (Equation (2.24)) up to $n = 10,000$, which is well beyond what is required for convergence. Four methods were then used to form the sums, until 0.1% accuracy was obtained by the formula,

$$Error = \left| \frac{Y_{sum} - Y_{ref}}{Y_{ref}} \right|. \quad (2.54)$$

The CPU time² for getting such accuracy was noted in the four methods, which were:

1. An unassisted spectral domain sum.
2. A spatial domain sum with the Fejer kernel acceleration.
3. A spatial domain sum with spiral average acceleration.
4. A spatial domain sum with Shanks' transformation.

The latter three methods involve acceleration techniques which are described in Appendix A. These acceleration techniques work well with series which oscillate about the convergence point, which is the case in the spatial domain. For the spectral domain, which approaches convergence in a "monotonic" manner, none of these techniques improves convergence.

The result of the convergence experiment is plotted in Figure 7, which shows the CPU time for a given spacing ρ with each solution method.

The data shows that for $\rho > 0.007\lambda$, the unassisted spectral domain sum is superior to all of the methods involving the spatial domain. This is expected since the evanescent modes of the spectral domain sum die out as ρ is increased, thus the sum becomes dominated by the finite number (in this case, one) of propagating cylindrical wave modes. Of the spatial domain techniques, the Shanks' algorithm, which is the most difficult to program, is decidedly the fastest.

The crossover point between the spectral domain and the Shanks' method corresponds to a self-admittance calculation for a slot mode which has an aspect ratio of $L/W \approx 14$. Although the Shanks' algorithm is faster for applications of higher

²All CPU times in this dissertation are based on the VAX 8550 machine at the Ohio State University ElectroScience Laboratory. Accuracy of the data is only about $\pm 10\%$, depending on the time-sharing load conditions on the computer when the data is being run.

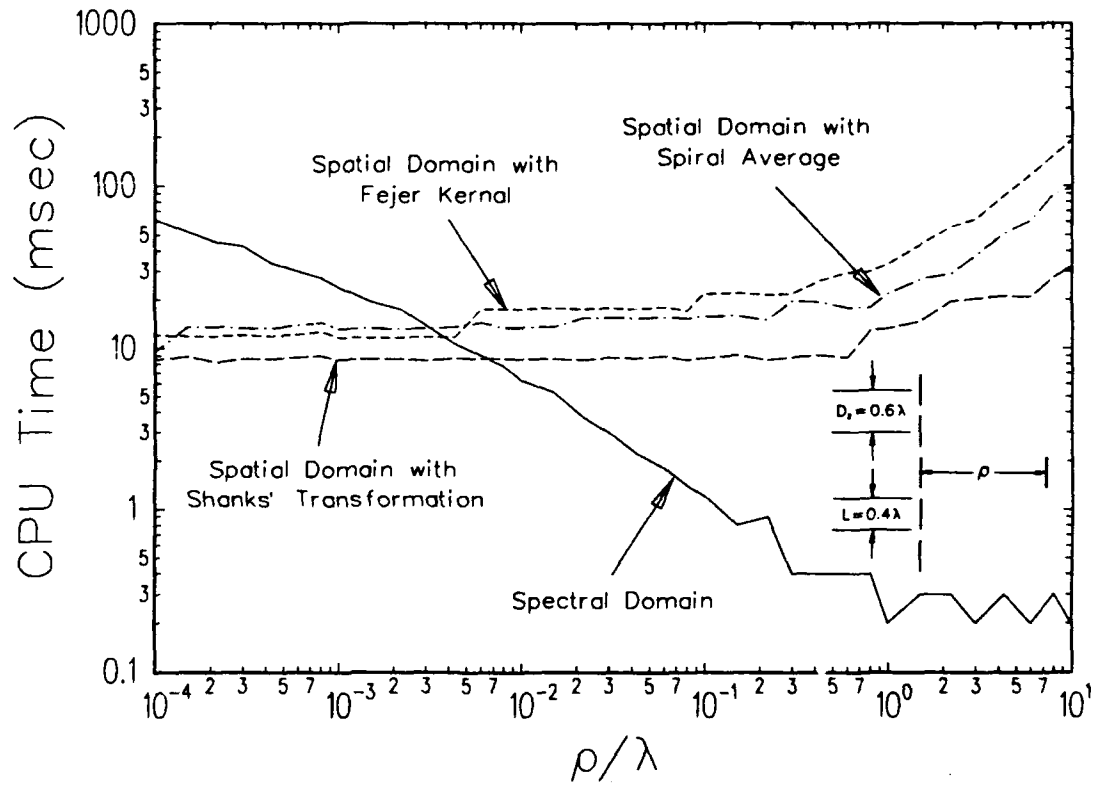


Figure 7: Comparison of Calculation Times by Four Solution Methods for Mutual Admittance to Converge to 0.1% Error - Piecewise Sinusoidal Axial Slot Modes in Free Space with $L = 0.4\lambda$, $D_z = 0.6\lambda$, $z = 0$

aspect ratios, the CPU savings is not substantial enough (unless extremely high aspect ratios are used) for the relatively few self-admittance calculations in a coupling matrix fill to warrant the programming of the spatial domain sum for the slot-to-slot coupling.

The spatial domain sums tend to be slower as the inter-modal spacing, ρ , is increased. This is explained physically with the spiral average method in that more pairs of slots must be added before the phase changes become nearly linear, producing the well behaved spiral. It is interesting to note that the Shanks' transformation and Fejer kernel methods behave similarly.

To conclude this section, we present some mutual admittance data for the "one-sided" homogeneous half-space coupling, as computed with Equation (2.24), the preferred method. First, we show admittance data versus modal separation distance ρ for the case of element lengths of $L = 0.4\lambda$ (both modes), inter-element spacings of $D_z = 0.6\lambda$, and no offset in z between the modes. The s_z parameter for this example is set to zero. Piecewise sinusoidal currents are assumed for both the transmitting and receiving modes. The data is plotted in Figure 8. Note the complicated behavior of the mutual susceptance (imaginary component) for $\rho < 1\lambda$, in which case many evanescent modes in the cylindrical wave expansion are contributing. Beyond one wavelength, the admittance data behaves like the single propagating mode, which is a simple Hankel function, decaying in magnitude as $1/\sqrt{\rho}$.

Next, we repeat the mutual admittance calculations for $D_z = 0.6\lambda$ and slot lengths of $L = 0.5\lambda$ and $L = 0.599\lambda$ (for both transmit and receive modes). Again, the s_z parameter is set to zero. The calculated results are plotted in Figures 9 and 10, respectively. Note that the susceptance for the $L = 0.5\lambda$ case approaches a finite value with a finite slope as ρ approaches zero. This is because the elements are at a

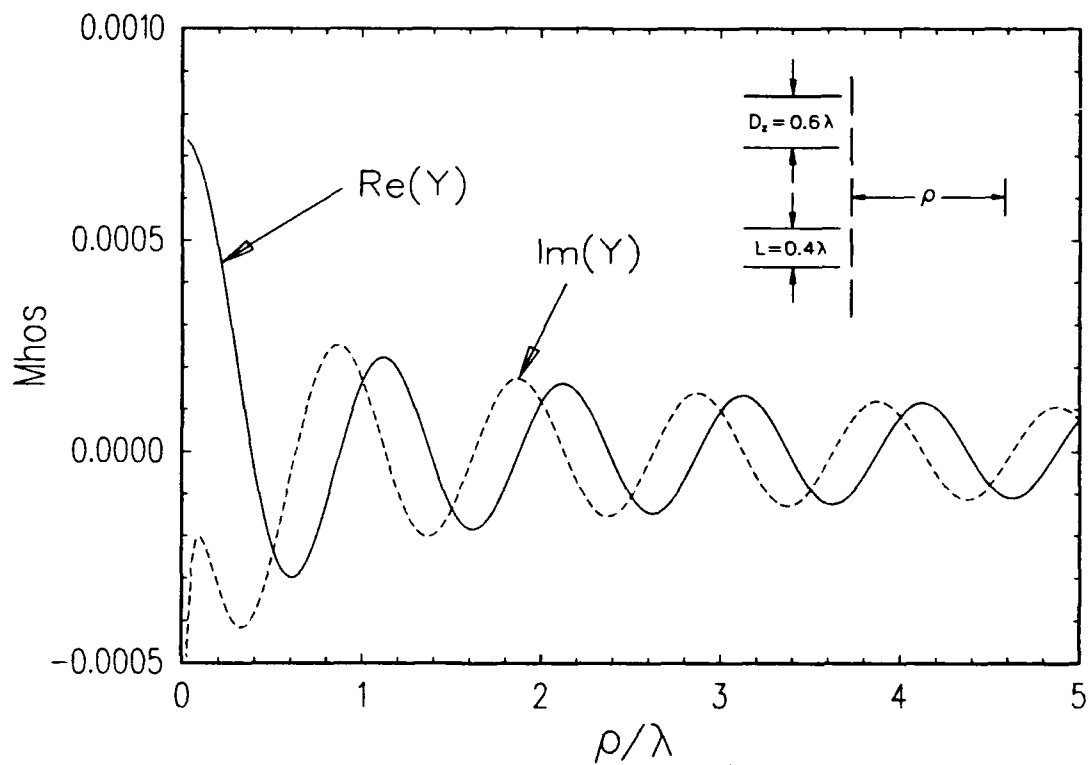


Figure 8: Mutual Admittance Between Piecewise Sinusoidal Axial Slot Modes in Region I with Free Space and $L = 0.4\lambda$, $D_z = 0.6\lambda$, $z = 0$, $s_z = 0$

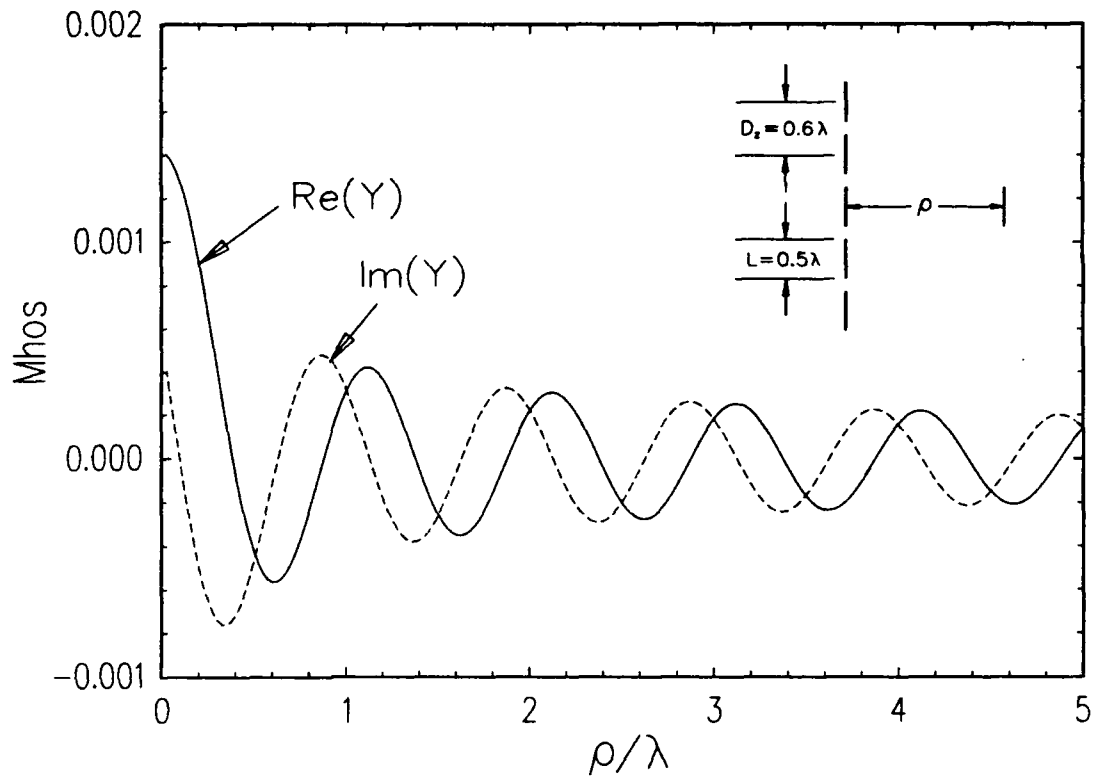


Figure 9: Mutual Admittance Between Piecewise Sinusoidal Axial Slot Modes in Region I with Free Space and $L = 0.5\lambda$, $D_z = 0.6\lambda$, $z = 0$

resonant length. For the $L = 0.599\lambda$ case, the susceptance goes to $+\infty$ as ρ goes to zero, which is expected with the elements longer than the first resonant length.

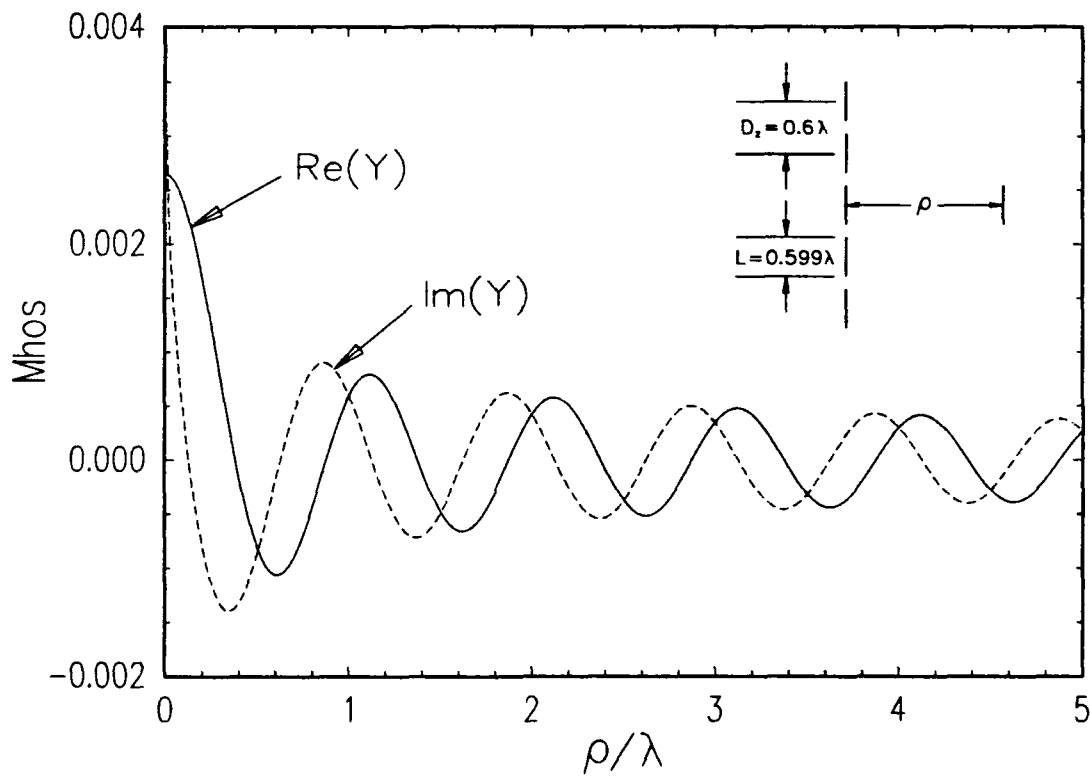


Figure 10: Mutual Admittance Between Piecewise Sinusoidal Axial Slot Modes in Region I with Free Space and $L = 0.599\lambda$, $D_z = 0.6\lambda$, $z = 0$

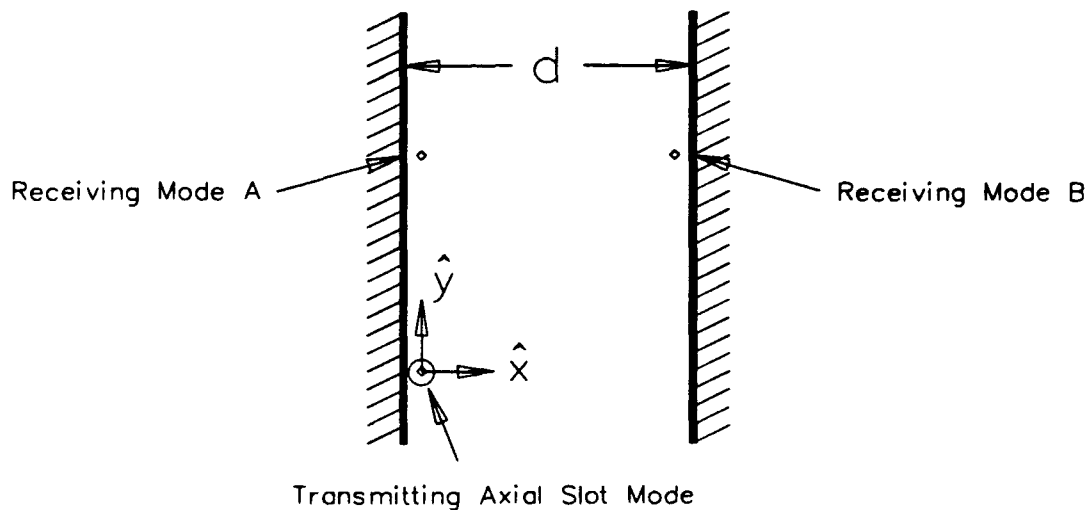


Figure 11: Geometry of Inner Zone Coupling in a Homogeneous Medium

2.1.2 Inner Zone Coupling

In this section, we consider the coupling between slot modes in Region II (ref. Figure 4) for a homogeneous medium. That is, we wish to get efficient solutions to Equations (1.25) through (1.28) with no dielectric interfaces between the conducting planes. The geometry to be considered is shown in Figure 11. It depicts receiving mode locations on both the same conducting plane as the transmitting mode and the opposite conducting plane. Note that the origin is located at the center of the reference element in the transmitting mode.

By successive applications of image theory [14], the conducting planes may be moved out to $\pm\infty$ in the \hat{x} axis. This creates the effect of making the transmitting column array into a doubly-infinite planar array, of which each current element has double the magnitude of the original magnetic currents. The columns of the equivalent doubly-infinite array are spaced at

$$D_x = 2d \quad (2.55)$$

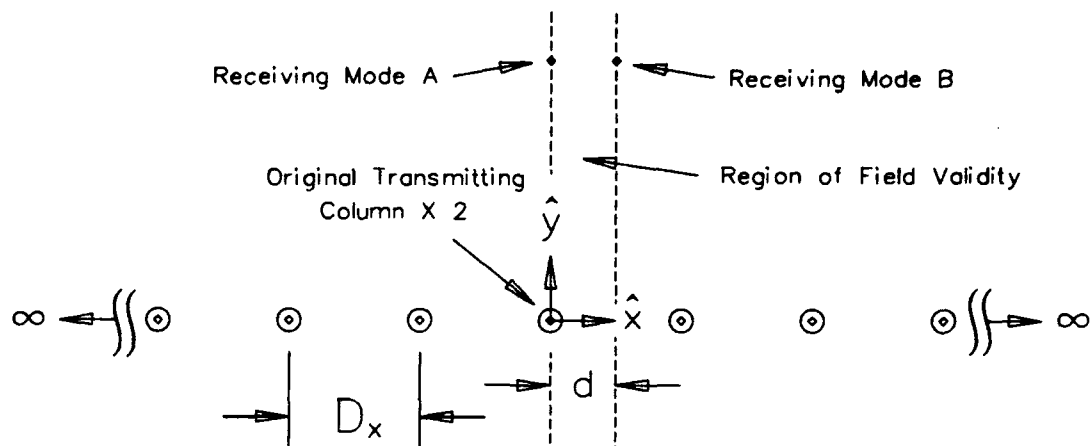


Figure 12: Equivalent Geometry of Inner Zone Coupling in a Homogeneous Medium with a Doubly-Infinite Array

apart, and the inter-element spacing in \hat{z} , D_z , remains the same as the original problem. The new transmitting array columns are of similar form as the original current mode (times 2), with same amplitudes and equal phases. In the equivalent problem, the radiated fields from the transmitting planar array are only valid for the region $0 \leq x \leq d$, which corresponds to the original region between the conducting planes. This equivalent geometry is depicted in Figure 12. Note that the receiving element is located an infinitesimal distance from either Plane A or Plane B.

An almost endless number of solutions may be formed for the mutual coupling from the transmitting doubly-infinite array in Figure 12 to the receiving element on either Plane A or Plane B. Different solutions may be obtained by transforming between spectral and spatial domains (for either or both sums), changing the order of the sums, and applying different acceleration techniques to enhance numerical convergence, such as the methods described in Appendix A. Because space does not permit a total exhaustion of the solution possibilities, the author has selected to demonstrate the convergence characteristics of only two solutions, which with the experience and intuition of the author, provide excellent results for either near

or far zone coupling. These methods are the plane wave expansion method and a "spatial-spectral method" which uses Shanks' transformation.

The plane wave expansion solution was derived by Monk and others for the mutual impedance between doubly-infinite arrays of dipoles [1, 2]. It is derived by forming a vector potential from a Hertzian array as a doubly-infinite sum in the spatial domain, using the Poisson Sum Formula to convert each sum to the spectral domain (giving the form of a plane wave expansion), performing curls to get the fields, then integrating to get the fields from modes of a finite length and the impedance with a testing function. In performing the latter steps, the basic plane wave expansion form is preserved.

Applying duality to the result in [2] and doubling the result to account for the doubled sources in Figure 12, the plane wave expansion solution is:

$$Y = \frac{Y_0}{D_x D_z} \sum_{k=-\infty}^{\infty} \sum_{n=-\infty}^{\infty} \frac{e^{-j\beta \bar{R} \cdot \hat{r}}}{r_y} [P_{\perp}^t P_{\perp}^r + P_{\parallel}^t P_{\parallel}^r], \quad (2.56)$$

where Y_0 is the intrinsic admittance of the medium. Several additional parameters in Equation (2.56) need explanation. The vector \bar{R} refers to the position of the center of the receiving element. The unit vector \hat{r} represents the direction of the plane waves, and is given by

$$\hat{r} = \frac{k\lambda}{D_x} \hat{x} + r_y \hat{y} + \frac{n\lambda}{D_z} \hat{z}, \quad (2.57)$$

where r_y normalizes the unit vector and is chosen with the $-j$ square root for evanescent plane waves. The P functions are merely pattern factors for single elements of the transmit and receive modes for different polarizations. They are given by:

$$P_{\perp}^{t,r} = \hat{p} \cdot \hat{n}_{\perp} P^{t,r}, \quad (2.58)$$

and

$$P_{\parallel}^{t,r} = \hat{p} \cdot \hat{n}_{\parallel} P^{t,r}, \quad (2.59)$$

where the element direction here is $\hat{p} = \hat{z}$ and we have defined

$$\hat{n}_{\perp} = -\frac{\hat{y} \times \hat{r}}{|\hat{y} \times \hat{r}|}, \quad (2.60)$$

$$\hat{n}_{\parallel} = \frac{\hat{n}_{\perp} \times \hat{r}}{|\hat{n}_{\perp} \times \hat{r}|}, \quad (2.61)$$

and the total pattern factor is

$$P^{t,r} = \int_{\text{element}} I(l) e^{\pm j\beta l \hat{p} \cdot \hat{r}} dl \quad (2.62)$$

with the plus sign chosen for the transmitting mode and the minus sign for the receiving mode.

For the \hat{z} -directed elements, the polarized pattern factors become:

$$P_{\perp}^{t,r} = \frac{r_x P^{t,r}}{\sqrt{r_x^2 + r_z^2}} \quad (2.63)$$

$$P_{\parallel}^{t,r} = -\frac{r_y r_z P^{t,r}}{\sqrt{r_x^2 + r_z^2}} \quad (2.64)$$

where r_x and r_z are the \hat{x} and \hat{z} components of \hat{r} in Equation (2.57).

In forming the plane wave expansion, the summation indices are changed from q and m , which correspond to spatial directions of \hat{x} and \hat{z} (see Figure 125 in Appendix B), to the spectral indices of k and n , respectively. Because the axial slot currents are \hat{z} -directed, the pattern factors force preferential convergence conditions on the spectral sum in n versus that of k . The pattern factors will decay while moving off normal in the YZ plane, which corresponds to moving to higher order spectral modes in n (with $k = 0$). In contrast, the pattern factors are omni-directional in the XY plane, which corresponds to the sum in k .

To illustrate the convergence characteristics of the plane wave modes in kn space, an example has been chosen with the lengths of the transmitting and receive elements at $L = 0.4\lambda$, an inter-element spacing of $D_z = 0.6\lambda$, ground plane spacing of

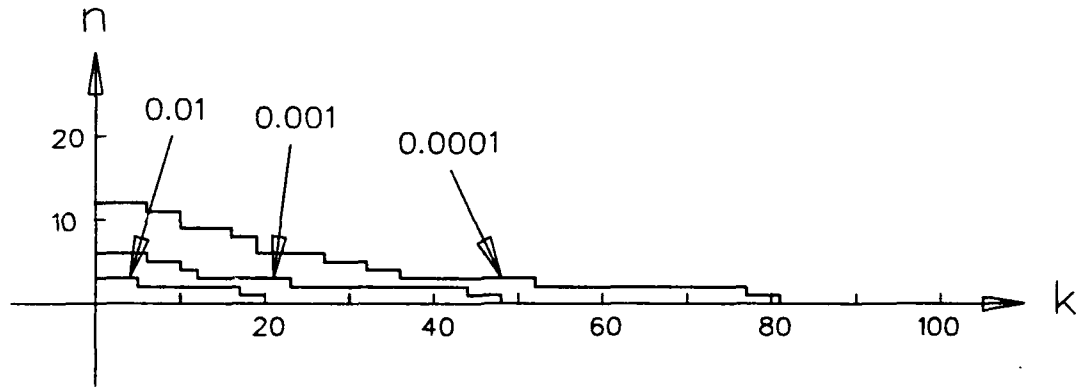


Figure 13: Contours of Relative Evanescent Mode Strength in Plane Wave Expansion for Self-Admittance of \hat{z} -Directed Slots Inside Ground Planes: $L = 0.4\lambda$, $D_z = 0.6\lambda$, $d = 0.3\lambda$, $z = 0$, $W = 0.02\lambda$

$d = 0.3\lambda$, no offset in z between modes, and a test separation distance of $y = 0.005\lambda$ with the test filament on the same ground plane as the transmitting mode (i.e., the Case A). The columns of currents are of equal phase. The relatively close testing location corresponds to a self-admittance calculation for a slot width of $W = 0.02\lambda$, which is a slot of aspect ratio $L/W = 20$. For this typical self-admittance calculation, the convergence of the plane wave expansion is taxed, since many evanescent modes must be included. Since the D_z and D_x spacings in this example are each less than one wavelength and the array is equally phased, only one propagating plane wave mode exists, corresponding to the $k = n = 0$ term. The relative amplitudes of the evanescent modes can be compared to that of this propagating mode. Such a calculation was performed, and Figure 13 depicts contours which define boundaries in kn space on the evanescent terms which have magnitudes more than 0.01, 0.001, and 0.001 of the magnitude of the propagating term in Equation (2.56). Only the first quadrant is shown, with symmetry understood about the k and n axes. The figure clearly shows the convergence in n is faster than the convergence in k , as expected by the nature of the pattern factors.

The contours in Figure 13 provide a clue to how the double summations should be carried out, maintaining computational efficiency. The following technique was selected by the researcher. First, the $k = n = 0$ term is found. Next, separate sums are formed along the k axis and the n axis, excluding the $k = n = 0$ term. These sums are formed with successive terms comprising of \pm term pairs on each index. Each of these axis sums are carried until three successive terms provide marginal changes in the sum's magnitude of less than 0.00001 times the previous magnitude of the sum. This establishes an upper limit on k and n which are stored. Next, the quadrant areas are summed (excluding the axes) with the procedure of starting with $n = 1$, then summing from $k = 1, 2, 3, \dots$, until convergence is found with three successive terms changing the partial sums by a relative magnitude of less than 0.00001 of the previous sum. As this quadrant sum is made, symmetric terms are also added in the other three quadrants. The procedure is then followed at $n = 2$, $n = 3$, and so forth until the upper limit on n found on the axis sum is reached. This procedure was found to provide similar speed and accuracy to the method used in Henderson's Periodic Moment Method Code (PMM), when the default accuracy parameter in PMM is used [3].

The plane wave expansion method is slow when a lot of evanescent modes are relatively strong, which occurs when y is electrically small. On the other hand, when y is larger than about one wavelength, the contribution from the evanescent modes is so insignificant that the double sum convergence procedure described above does not need to be carried out. Assuming that $D_x < 1\lambda$ and $d < 0.5\lambda$ (i.e., $D_x < 1\lambda$), which is typically the case, and assuming $y > 1\lambda$, the single propagating plane wave term from Equation (2.56) gives:

$$Y \approx \frac{Y_0 P^t P^r e^{-j\beta y}}{D_x D_z}. \quad (2.65)$$

With the spectral plane wave expansion solution developed, we now turn our attention to an alternative "spatial-spectral" solution. This method is based on the spectral solution to the radiation from a single column of \hat{z} -directed elements, which in the previous section proved to be very fast. Specifically, the mutual admittance problem in Figure 12 may be decomposed into a single infinite sum of mutual admittances between separate column modes and the same testing element, where all of the columns are in-phase. The mutual admittance for a single column to the test element is found spectrally with the cylindrical wave expansion in Equation (2.24). The series of columns are then added spatially, making the total double sum a combination of spectral and spatial domain manipulation. To accelerate the spatial domain sum, Shanks' transformation (ref. Appendix A) is applied.

Examples were used to compare the pure spectral domain solution of the plane wave expansion with the mixed "spatial-spectral" domain approach. Each example used element lengths of $L = 0.4\lambda$, inter-element spacings of $D_z = 0.6\lambda$, ground plane spacing of $d = 0.3\lambda$, and no offset in z between the transmitting and receiving modes. Examples were made with the test element at various y positions on each of the two ground planes (i.e., Case A of $x = 0$ and Case B of $x = d$). The plane wave expansion method was used with the convergence criteria defined above for $y < 1\lambda$, and with Equation (2.65) for $y \geq 1\lambda$. The spatial-spectral method was carried out with similar convergence checks, and the resulting calculations matched the spectral domain calculations within 0.1% almost always (including cases where the single plane approximation in Equation (2.65) is used).

For Case A, the two solutions were run for conditions of $0.001\lambda \leq y \leq 10\lambda$. Piecewise sinusoidal modes were used for transmitting and receiving. The calculation time for each admittance data was noted and is plotted in Figure 14. Note that the

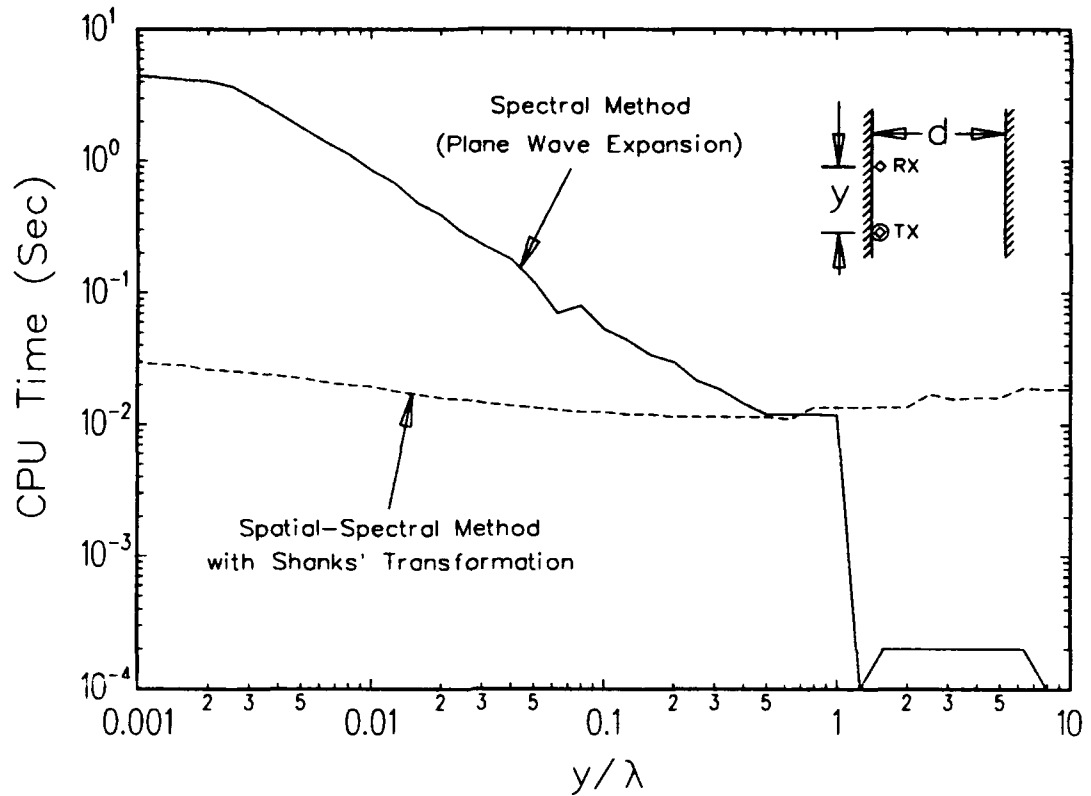


Figure 14: Comparison of Calculation Times by Two Solution Methods for Mutual Admittance in a Homogeneous Inner Zone - Case A: $L = 0.4\lambda$, $D_z = 0.6\lambda$, $d = 0.3\lambda$, $z = 0$

spectral method becomes faster than the mixed domain method only when the single propagating plane wave approximation is used.

The experiment was repeated for Case B, with all of the parameters as defined before except the test element being located on the opposite ground plane from the transmitting mode. Again, piecewise sinusoidal current shapes were assumed. The calculation time were noted and are plotted in Figure 15. Again, the spectral method is only faster when the single propagating plane wave approximation is used, which is for $y > 1\lambda$. Note that the curves in Figure 15 are very similar to those in Figure 14. Thus, the conclusion is that regardless of if the receiving mode is on the

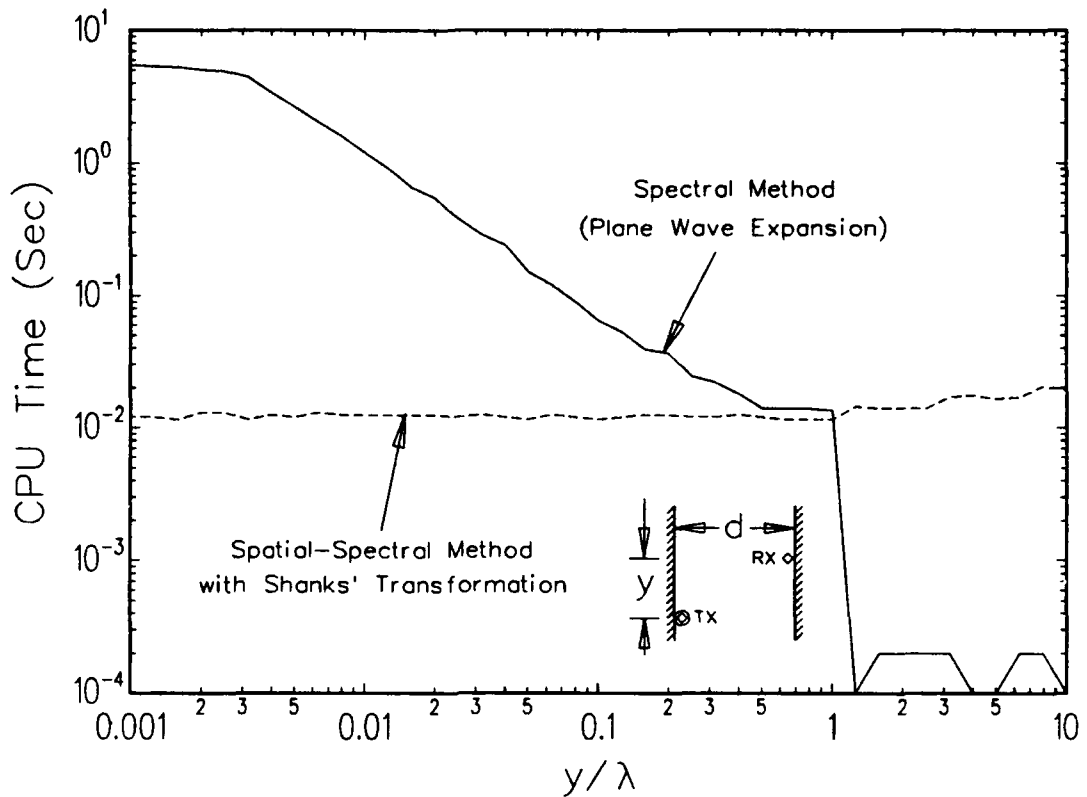


Figure 15: Comparison of Calculation Times by Two Solution Methods for Mutual Admittance in a Homogeneous Inner Zone - Case B: $L = 0.4\lambda$, $D_z = 0.6\lambda$, $d = 0.3\lambda$, $z = 0$

same plane as the transmitting mode, the preferred calculation method is to use the spatial-spectral method (based on Equation (2.24) for each of the radiating columns in Figure 12) with acceleration from Shanks' transformation when $y < 1\lambda$ and using Equation (2.65) when $y > 1\lambda$.

To conclude this section, we present the mutual admittance data which was calculated in the process of obtaining the CPU data in Figures 14 and 15. Specifically, this data is for testing on both planes using the spatial-spectral method when $y < 1\lambda$ and the single propagating plane wave approximation when $y > 1\lambda$. Figure 16 shows the mutual admittance for testing on the same plane as the radiating mode

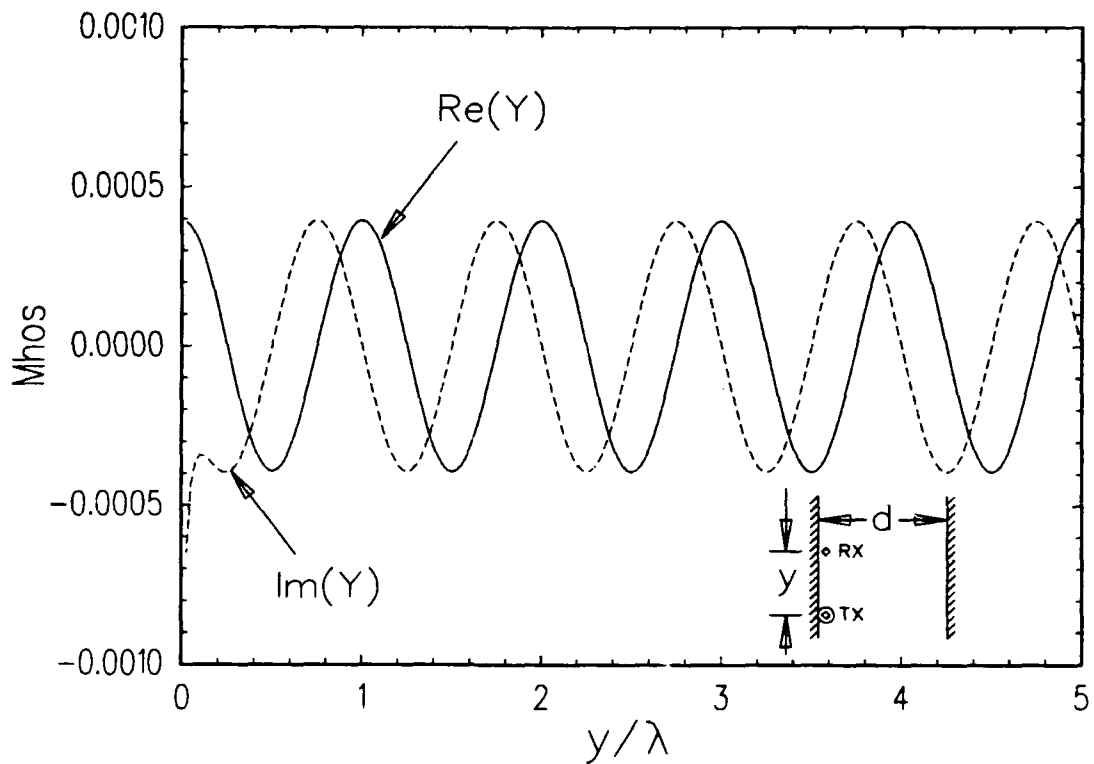


Figure 16: Mutual Admittance Between Piecewise Sinusoidal Axial Slot Modes in Region II (Case A) with Free Space and $L = 0.4\lambda$, $D_z = 0.6\lambda$, $d = 0.3\lambda$, $z = 0$

(Case A) and Figure 17 shows similar data for testing on the opposite plane (Case B). Piecewise sinusoidal current shapes were assumed.

Several interesting things are noted from Figures 16 and 17. First, the mutual susceptance in Case A as y approaches zero goes to $-\infty$, which fundamentally is caused by the fact that the element lengths are less than $\lambda/2$. The susceptance in Case B does not have such a singularity, though, since the testing is never infinitely close to a radiating element. For both cases, the susceptance displays a somewhat complicated behavior for the first wavelength, then follows the mutual conductance (real component) in a simple non-decaying plane wave fashion for $y > 1\lambda$. This plane wave is merely the propagating waveguide mode inside the original structure

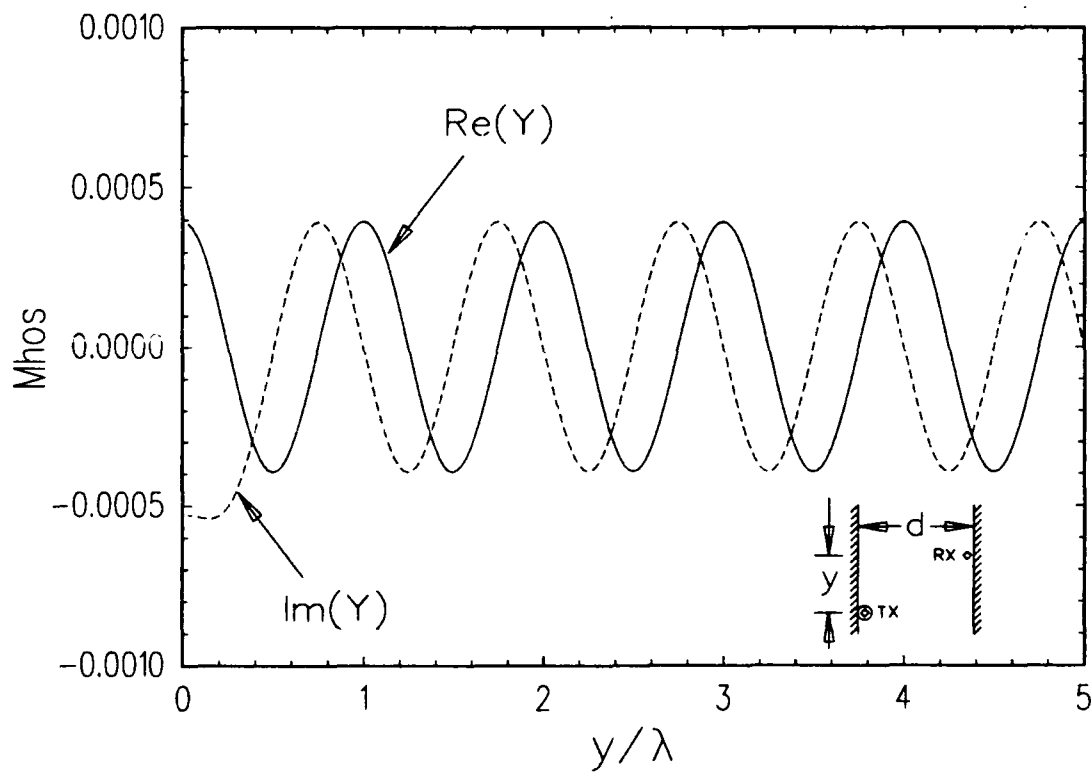


Figure 17: Mutual Admittance Between Piecewise Sinusoidal Axial Slot Modes in Region II (Case B) with Free Space and $L = 0.4\lambda$, $D_z = 0.6\lambda$, $d = 0.3\lambda$, $z = 0$

(see Figure 11). The mutual conductance data is almost exactly the same for Case A and Case B testing. Finally, note that there is no discernable discontinuity in the data in each plot at $y = 1\lambda$, which is where the method of calculation changes.

If the ground plane spacing is expanded to $d > \lambda/2$, then more propagating waveguide modes will appear. This corresponds to more propagating plane wave modes in Equation (2.56), which must be included to alter the solution in Equation (2.65) when $y > 1\lambda$. The spatial-spectral method with Shanks' acceleration would not change for the near zone calculations, though.

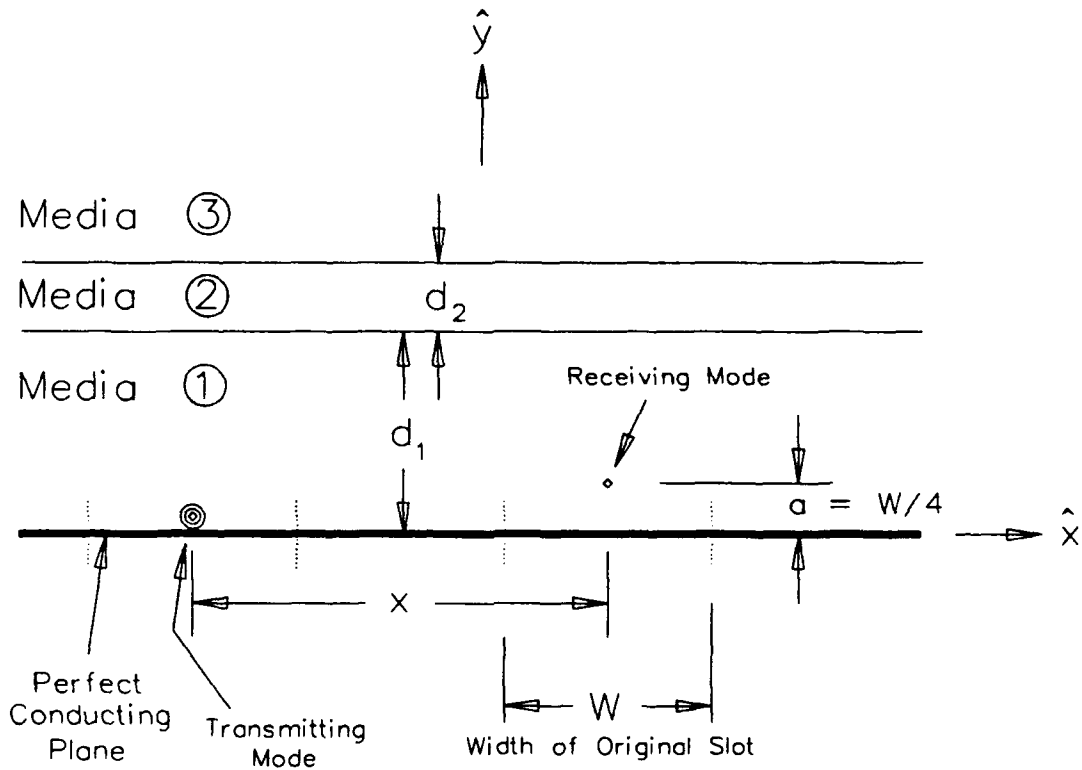


Figure 18: Geometry of Outer Zone Coupling between Slot Modes in a Stratified Dielectric Medium

2.2 STRATIFIED MEDIA

2.2.1 Outer Zone Coupling

The geometry of “outer zone” coupling between slot modes in a stratified dielectric medium is depicted in Figure 18. The radiating basis function is a periodic \hat{z} -directed thin filament located directly on the ground plane surface. The testing function occupies a thin filament for just a single element, located an “equivalent wire radius” away from the ground plane, as previously discussed.

Although Figure 18 shows two dielectric layers and a third dielectric half-space, the number of layers is completely arbitrary. Layers may be thin or thick, with the exception of the first layer, which must be thick enough so that $d_1 \gg a$, in

order to preserve the thin slot assumptions which are used. As with the case of the homogeneous half-space, we will assume the center of the reference element in the transmitting mode is located at the origin, and that the center of the receiving element is located at the position vector,

$$\bar{R} = x\hat{x} + ay\hat{y} + z\hat{z}. \quad (2.66)$$

The "traditional" way to solve for the radiation from the transmitting periodic mode is to find the Green's function which enforces the boundary conditions at each dielectric interface, and at the ground plane. This Green's function will have integrals of the Sommerfeld form, which are difficult to evaluate due to highly oscillatory integrands. To circumvent the need to evaluate such integrals, the array scanning method (ASM) is adopted here, which is also a completely rigorous method. This method was reported for use in calculating the self impedance of a single dipole near a single planar dielectric interface [24]. The application of the method in the present research is much different, however, in that it involves a scan in only a single plane, but with a more complicated geometry.

Although the array scanning method avoids the formulation of Sommerfeld integrals, it does produce an integral with singularities associated with surface wave formation. These singularities may be removed with an analytical approximation, leaving a well behaved integrand which can be numerically evaluated. The integral may also be interpreted as a Fourier transform involving the separation distance x between the modes. Since the formulation of the coupling matrix often requires similar mutual coupling geometries with the only difference being a change in the value of x , Fast Fourier Transforms (FFTs) may be used to accelerate the overall moment method solution.

The basis for the array scanning method, as it is applied to calculate field and coupling quantities from a radiating mode of singly-periodic sources, is given in Appendix B. By extension of Equation (B.9), the admittance between the modes depicted in Figure 18 is

$$Y = \frac{D_x}{\lambda} \int_{-\frac{\lambda}{2D_x}}^{\frac{\lambda}{2D_x}} Y_A ds_x, \quad (2.67)$$

where Y_A is the admittance between a radiating artificially created doubly-infinite array of periodic sources and the original receive element and D_x is the inter-column spacing of the artificial array, as discussed in Appendix B. The λ s in Equation (2.67) may be for either the dielectric slab nearest the ground plane (Media 1), free space (Media 0), or any of the other dielectrics. However, the chosen λ must be for the same region for which the s_x scan parameter is applied. For convenience and to avoid confusion, the dielectric slab in which the sources are embedded (Media 1) will be used for both the λ and s_x parameters for ASM applications throughout this dissertation.

The admittance from the full planar array, Y_A , may be found in a plane wave expansion, as derived by Munk [1, 2] for the similar case of mutual impedance between doubly-infinite dipole arrays. Applying duality to Munk's result, we get:

$$Y_A = \frac{Y_1}{2D_x D_z} \sum_{k=-\infty}^{\infty} \sum_{n=-\infty}^{\infty} \frac{e^{-j\beta_1 \bar{R} \cdot \hat{r}_1}}{r_{y_1}} [P_{\perp}^t P_{\perp}^r T_{\perp} + P_{\parallel}^t P_{\parallel}^r T_{\parallel}]. \quad (2.68)$$

Several parameters in Equation (2.68) need explanation. The variables Y_1 and β_1 refer to the intrinsic admittance and wavenumber of the dielectric slab nearest to the ground plane (i.e., media 1). The position vector \bar{R} is defined by Equation (2.66). The unit vector \hat{r}_1 represents the direction of the plane waves in media 1, and is given by

$$\hat{r}_1 = (s_x + \frac{k\lambda_1}{D_x})\hat{x} + r_{y_1}\hat{y} + \frac{n\lambda_1}{D_z}\hat{z}, \quad (2.69)$$

where r_{y1} normalizes the unit vector and is chosen with the $-j$ square root for evanescent plane waves. Note that the parameter s_x is a directional cosine for the steering of the propagating plane wave direction, as discussed in Appendix B.

The P functions in Equation (2.68) are merely pattern factors for single elements of the transmit and receive modes in media 1 for different polarizations. They are defined in Equations (2.63) and (2.64) for the \hat{z} -directed slot modes, with the only modification being the components of \hat{r} coming from Equation (2.69). It should be noted, though, that when the dielectric constants of the neighboring slabs nearest and on each side of the slotted plane differ, an effective dielectric constant ϵ_e and corresponding effective wavenumber β_e governs the piecewise sinusoidal or cosinusoidal current shapes in Equations (2.27) and (2.28). A procedure for getting ϵ_e which is "sensed" by the slot is described by Kornbau, using a static capacitance argument [25]. Although not an exact solution, he concluded that a good approximation under most circumstances is to declare ϵ_e to be the arithmetic average of the dielectric constants immediately on each side of the slotted plane. Regardless of how the effective dielectric constant is chosen, when it is applied to an axial current mode in which the immediate environment has a dielectric constant of ϵ_1 , Equations (2.32) and (2.33) change to the following:

$$P(PWS) = \frac{2\beta_e}{\sin(\frac{\beta_e L}{2})} \left[\frac{\cos(\frac{\beta_1 r_z L}{2}) - \cos(\frac{\beta_e L}{2})}{\beta_e^2 - \beta_1^2 r_z^2} \right] \cdot e^{\pm j\beta_1 z c r_z} \quad (2.70)$$

$$P(PWC) = \frac{2\beta_e}{\beta_1 r_z} \left[\frac{\beta_1 r_z \sin(\frac{\beta_e L}{2}) \cos(\frac{\beta_1 r_z L}{2}) - \beta_e \cos(\frac{\beta_e L}{2}) \sin(\frac{\beta_1 r_z L}{2})}{(1 - \cos(\frac{\beta_e L}{2}))(\beta_e^2 - \beta_1^2 r_z^2)} \right] \cdot e^{\pm j\beta_1 z c r_z} \quad (2.71)$$

Throughout this dissertation, when the effective dielectric constant is not specifically given for "one sided" admittance calculations, it is assumed to be the same dielectric constant as that of the dielectric slab nearest to the ground plane.

The final clarification due to Equation (2.68) are the T factors, which encompass the effect of the media interfaces, accounting for the infinite geometric series of plane wave bounces within the dielectric slab nearest to the ground plane. Assume for now that a single dielectric slab exists on the ground plane such that media 2 is an infinite half-space. From [1, 2], and using the fact that the transmitting mode is at the ground plane and the receive mode has the coordinate $y = a$, we find the T factors to have the form,

$$T = \frac{[1 + \Gamma_{10}] [1 + \Gamma_{12} e^{-j2\beta_1(d_1-a)r_{y1}}]}{1 - \Gamma_{10}\Gamma_{12} e^{-j2\beta_1 d_1 r_{y1}}}, \quad (2.72)$$

where parallel and perpendicular polarization subscripts have been suppressed on T and all Γ s. The reflection coefficients are merely the Fresnel coefficients for magnetic fields in plane waves going from media 1 to either the infinite half-space (media 2) or the ground plane ("media 0"). The reflection coefficients at the media 1-2 interface are:

$$\Gamma_{12\perp} = \frac{Y_2 r_{y1} - Y_1 r_{y2}}{Y_2 r_{y1} + Y_1 r_{y2}} \quad (2.73)$$

and

$$\Gamma_{12\parallel} = \frac{Y_2 r_{y2} - Y_1 r_{y1}}{Y_2 r_{y2} + Y_1 r_{y1}}, \quad (2.74)$$

where Y_i refers to the intrinsic admittance of the i th media. The y component of the plane wave direction in media 2 is given by

$$r_{y2} = \sqrt{1 - r_{x2}^2 - r_{z2}^2} \quad (2.75)$$

with a $-j$ chosen for evanescent plane waves. Finally, phase matching at the boundary gives

$$\beta_2 r_{x2} = \beta_1 r_{x1} \quad (2.76)$$

and

$$\beta_2 r_{z_2} = \beta_1 r_{z_1}. \quad (2.77)$$

Since the ground plane is a perfect electrical conductor, the other reflection coefficients are simply

$$\Gamma_{10\perp} = \Gamma_{10\parallel} = 1. \quad (2.78)$$

Thus, Equation (2.72) may be simplified to the form,

$$T = 2 \frac{1 + \Gamma_{12} e^{-j2\beta_1(d_1-a)r_{y_1}}}{1 - \Gamma_{12} e^{-j2\beta_1 d_1 r_{y_1}}}. \quad (2.79)$$

Further simplification occurs if one assumes that $d_1 - a \approx d_1$, but such an approximation does not need to be made, and will only limit the usefulness of the results.

It should be noted that the T factors are functions of the plane wave space indices k and n , as well as the scan direction parameter s_x . This dependence is buried inside r_{y_1} and Γ_{12} for each polarization.

We choose the inter-column spacing D_x for the "artificial" transmitting doubly infinite array to be a half wavelength inside media 1. This choice is not necessary for the method, but leads to both a convenience in isolating possible singularities and a physical interpretation of the array scanning. These features will be explained later in the development of the solution.

With this inter-column spacing, and using Equations (2.66), (2.68), and (2.69), substitutions may be made into Equation (2.67), which yield:

$$Y = \frac{Y_1}{2\lambda_1 D_x} \sum_{k=-\infty}^{\infty} e^{-j2k\beta_1 x} \sum_{n=-\infty}^{\infty} \int_{-1}^1 f_{kn}(s_x) e^{-j\beta_1 x s_x} ds_x, \quad (2.80)$$

where we have defined the functions,

$$f_{kn}(s_x) = \frac{e^{-j\beta_1(ar_{y_1} + \frac{nz\lambda_1}{D_x})}}{r_{y_1}} [P_{\perp}^t P_{\perp}^r T_{\perp} + P_{\parallel}^t P_{\parallel}^r T_{\parallel}], \quad (2.81)$$

for $-1 < s_x < 1$ and $f_{kn}(s_x) = 0$ for all other values of s_x .

Using the Fourier transform definition of

$$F(\omega) = \int_{-\infty}^{\infty} f(t)e^{-j\omega t} dt, \quad (2.82)$$

it is easily seen that the mutual admittance may be expressed as:

$$Y = \frac{Y_1}{2\lambda_1 D_z} \sum_{k=-\infty}^{\infty} e^{-j2k\beta_1 x} \sum_{n=-\infty}^{\infty} F_{kn}(\beta_1 x). \quad (2.83)$$

This expression may be further simplified by using the linearity of the Fourier transform. That is,

$$Y = \frac{Y_1}{2\lambda_1 D_z} \sum_{k=-\infty}^{\infty} e^{-j2k\beta_1 x} F_{k\Sigma}(\beta_1 x), \quad (2.84)$$

where we have defined

$$F_{k\Sigma}(\beta_1 x) = \int_{-\infty}^{\infty} f_{k\Sigma}(s_x) e^{-j\beta_1 x s_x} ds_x \quad (2.85)$$

and

$$f_{k\Sigma}(s_x) = \sum_{n=-\infty}^{\infty} f_{kn}(s_x). \quad (2.86)$$

For most applications involving truncated periodic surfaces, a large number of columns of periodic slots will occur, with most columns having similar slot elements. Thus, for the computation of the coupling matrix, most mutual admittances calculated with the array scanning method will have similar pattern factors, and certainly will have the same T factors. The only difference in the calculations will involve the separation distance, x , which is in the argument of the Fourier transforms. Fast Fourier Transforms (FFTs) may be used to accelerate the overall solution, by providing an array of information on the $F_{k\Sigma}$ functions over a wide range of $\beta_1 x$ values. The series of functions, $f_{k\Sigma}$, need only to be sample once, then given to an FFT algorithm. The output of the algorithm provides $F_{k\Sigma}$ at a large number of discrete values of $\beta_1 x$. Linear interpolation of this data can be used to get the transform

at almost any particular $\beta_1 x$. This procedure is faster than performing the integral in Equation (2.85) separately for each x spacing. For this reason, Equation (2.84) expresses the array scanning method result in a convenient form.

The result of Equation (2.84) is applicable to slot column coupling in stratified media where the shape of the slot elements are arbitrary (i.e., not confined to simple \hat{z} -directed thin slots). Using concepts such as Munk's composite pattern factors [1, 2], the extension is easily made. However, one must be careful not to use the polarized pattern decompositions in Equations (2.63) and (2.64), which are valid only for \hat{z} -directed elements. Instead, one should rely on the more general forms of Equations (2.58) through (2.62).

Computation of the Fourier transforms in the array scanning method is fairly straight-forward, except in a few particular terms where singularities occur in f_{kn} . These particular k and n term combinations may be removed from the definitions of $f_{k\Sigma}$ and the associated transforms, $F_{k\Sigma}$. That is, their integrals in the array scanning method may be added separately. The singularities can occur as r_{y_1} goes to zero, or in the case of "surface wave poles", the denominators of the T factors go to zero. Fortunately, the integration in the neighborhood of these singularities may be removed with analytical approximations. The procedure to do this is discussed as follows.

Assuming all permeabilities are identical to free space and the dielectrics are lossless, the application of the array scanning method (ASM) for the "one sided" mutual admittance between pairs of infinite column modes of axial oriented slots may be divided into the following three categories:

- I. $\epsilon_1 = \epsilon_2$ (i.e., homogeneous half-space)
- II. $\epsilon_1 < \epsilon_2$ (i.e., the relatively dense outside space)

III. $\epsilon_1 > \epsilon_2$ (i.e., the relatively dense slab)

With the inter-column spacing (D_x) chosen to be $\lambda_1/2$ in the ASM, and assuming the element spacing (D_z) is less than a wavelength in media 1, the $k = n = 0$ term in the plane wave expansion is the only source of propagating plane waves, which are launched at all angles (perpendicular to \hat{z}) in media 1 as the integration on s_x is performed. All other combinations of k and n imply evanescent plane wave excitation in the dielectric slab.

Two types of singularities can occur in the ASM integrands. The first is a simple pole when r_{y_1} goes to zero. The second is a much more complicated singularity associated with the resonant excitation of a surface wave when the denominator of the T factors goes to zero. We shall examine each type of singularity as they occur for the three dielectric categories.

First, consider the case of the homogeneous half-space. Although this case was solved efficiently with the development of Equation (2.24) in a previous section, it is presented here to help validate the ASM. For applications with homogeneous half-spaces, a simple singularity associated with r_{y_1} approaching zero occurs at four locations in the ASM integrands. They are at s_x approaching both $+1$ and -1 for the $k = n = 0$ term, and for s_x approaching -1 for the $k = 1, n = 0$ term, and s_x approaching $+1$ for the $k = -1, n = 0$ term. For the $k = n = 0$ term, the entire integral may be performed in closed form with the approximation that the "equivalent wire radius" (a) is negligible for the propagating plane waves. Also note that the T factor for any k, n combination and polarization is always exactly equal to 2 for the homogeneous half-space. Using axial slots and piecewise sinusoidal current shapes, the Fourier transform of the $k = n = 0$ term may be approximated as:

$$F_{00}(\beta_1 x) \approx \int_{-1}^1 \frac{8}{\beta_1^2 \sin^2(\frac{\beta_1 L}{2})} \left[1 - \cos(\frac{\beta_1 L}{2}) \right]^2 \frac{e^{-j\beta_1 x s_x}}{\sqrt{1 - s_x^2}} ds_x$$

$$\approx \frac{8\pi}{\beta_1^2 \sin^2(\frac{\beta_1 L}{2})} \left[1 - \cos(\frac{\beta_1 L}{2}) \right]^2 J_0(\beta_1 x). \quad (2.87)$$

Note that since only the $n = 0$ term in Equation (2.24) and the $k = n = 0$ term in Equation (2.87) have non-zero real components, the two formulas are in agreement (neglecting a) when the constants from Equation (2.84) and the pattern factors from Equation (2.32) are included.

For the $k = \pm 1, n = 0$ terms, the integrand cannot be approximated well over the entire region of integration. However, an analytic approximation can be made in the neighborhood of the singularities. This approximation involves noting that the numerator in the integrand is almost a constant in the neighborhood of the singularity, and that integrals of the form $\int \frac{C}{-j\sqrt{u^2-1}} du$ may be evaluated in closed form. The process yields:

$$F_{1,0}(\beta_1 x) \approx \frac{8}{\beta_1^2 \sin^2(\frac{\beta_1 L}{2})} \left[1 - \cos(\frac{\beta_1 L}{2}) \right]^2 \left[j e^{j\beta_1 x} \ln(1 + \Delta + \sqrt{2\Delta + \Delta^2}) + \int_{-1+\Delta}^1 \frac{e^{-j\beta_1 a \sqrt{1-(s_x+2)^2}}}{\sqrt{1-(s_x+2)^2}} e^{-j\beta_1 x s_x} ds_x \right] \quad (2.88)$$

and

$$F_{-1,0}(\beta_1 x) \approx \frac{8}{\beta_1^2 \sin^2(\frac{\beta_1 L}{2})} \left[1 - \cos(\frac{\beta_1 L}{2}) \right]^2 \left[j e^{-j\beta_1 x} \ln(1 + \Delta + \sqrt{2\Delta + \Delta^2}) + \int_{-1}^{1-\Delta} \frac{e^{-j\beta_1 a \sqrt{1-(s_x-2)^2}}}{\sqrt{1-(s_x-2)^2}} e^{-j\beta_1 x s_x} ds_x \right] \quad (2.89)$$

The remaining integrals in Equations (2.88) and (2.89) are well behaved and may be evaluated numerically. The analytical approximation in removing the integral in the neighborhood of these singularities degrades as Δ becomes larger.

Because of these singularities, when applying the ASM for homogeneous half-spaces, it is best to separate the $k = -1, 0, 1$ and $n = 0$ terms from the expansion in

Equation (2.84), and evaluate them separately at each x value of interest. The rest of the k, n terms may be put through an FFT algorithm as mentioned previously.

Now consider the category of a relatively dense outside space (i.e., $\epsilon_1 < \epsilon_2$). In this case, there are no singularities which hinder the FFT operations in Equation (2.84). Although it is true that r_{y_1} approaches zero at similar locations as in the homogeneous half-space, the T_{\perp} factor also approach zero in these same locations³. This is caused by the reflection coefficient $\Gamma_{12\perp}$ approaching -1 at these "end-fire" angles, which makes the numerator in T_{\perp} go to zero. The ratio, T_{\perp}/r_{y_1} , is found to be numerically stable and finite at arbitrarily close positions from the suspected singularity - thus, there is no singularity. In practice, the integrand may be sampled at a slight offset from the r_{y_1} locations and given to the FFT algorithm.

No singularity exists in the T factors for the relatively dense outside space category.

Now consider the final category, that of the relatively dense slab (i.e., $\epsilon_1 > \epsilon_2$). This case is perhaps the most interesting since it is the only one which supports surface waves and it is more likely to occur in practical applications. As with the case of the relatively dense outside space, there is no true singularity when r_{y_1} goes to zero because T_{\perp} also approaches zero in the same locations. L'Hopital's rule may be used to show that the ratio T_{\perp}/r_{y_1} approaches $j2d_1\beta_1$ as r_{y_1} goes to zero.

The much more interesting phenomena with this category is the existence of singularities in T_{\perp} as surface waves become excited in the dielectric slab⁴. With the chosen "artificial" inter-column spacing of $D_x = \lambda_1/2$, these singularities are confined to exist between the scan direction associated with the critical angle and

³Note that T_{\parallel} is irrelevant since the parallel components of the pattern factors go to zero for all $n = 0$ terms with the \hat{z} -directed elements.

⁴Again, T_{\parallel} is irrelevant in this phenomena since the parallel components of the pattern factors vanish in the term which supports the surface waves.

the end-fire scan direction for the $k = n = 0$ term only. That is, defining a critical scan direction⁵ of $s_{x_c} = \sqrt{\epsilon_2/\epsilon_1}$, the locations of the surface wave singularities are at $s_x = s_{x_p}$, where

$$s_{x_c} < |s_{x_p}| < 1. \quad (2.90)$$

For all values of s_x in this range, the magnitude of the dielectric reflection coefficients for the $k = n = 0$ is exactly one.

We define a polar angle ϕ such that

$$e^{j\phi} = \Gamma_{12\perp} e^{-j2\beta_1 d_1 r_{y_1}}. \quad (2.91)$$

From Equation (2.79), and neglecting the equivalent wire radius a , the T factor for the $k = n = 0$ term can be written as

$$T_{\perp} = 2 \frac{1 + e^{j\phi}}{1 - e^{j\phi}} = j2 \cot\left(\frac{\phi}{2}\right). \quad (2.92)$$

Obviously, the surface wave singularities occur when ϕ is either zero or a multiple of 2π . Note that the T factor is an odd function of ϕ around the singularity. Since the rest of the $k = n = 0$ integrand is fairly constant in the neighborhood of a singularity, the effect of the singularity can be removed if one defines symmetric limits of ϕ about the singularity and translates the result back to corresponding limits on s_x . That is, the integral of the $k = n = 0$ term from $\phi = -\Delta$ to $+\Delta$ is zero, as long as Δ is chosen small enough so that the remaining factors in the integrand (i.e., r_{y_1} and the pattern factors) are roughly constant. Thus, the region from $\phi = -\Delta$ to $+\Delta$ can be excluded from the scan integration of the imaginary component of the $k = n = 0$ term.

⁵This is in agreement with the critical angle of plane wave incidence which just allows transmission into the outside space, from Snell's law.

The new ϕ variable is related to the scan parameter s_x in a non-linear equation. The values of s_x which correspond to $\phi = \pm\Delta$ are solutions to the equation:

$$g(s_x) = \pm\Delta + j \ln \left[\frac{s_{x_c} \sqrt{1 - s_x^2} + \frac{j}{s_{x_c}} \sqrt{s_x^2 - s_{x_c}^2}}{s_{x_c} \sqrt{1 - s_x^2} - \frac{j}{s_{x_c}} \sqrt{s_x^2 - s_{x_c}^2}} \right] + 2d_1\beta_1\sqrt{1 - s_x^2} = 0. \quad (2.93)$$

The roots may be found by the Newton-Raphson iteration method [26], which is to form the next guess for the root from the existing guess by the operation

$$s_{x_{n+1}} = s_{x_n} - \frac{g(s_{x_n})}{g'(s_{x_n})}, \quad (2.94)$$

where the prime designates the derivative of g with respect to s_x , which is

$$g'(s_x) = \frac{-2s_x(1 - s_{x_c}^2)}{\sqrt{1 - s_x^2} \sqrt{s_x^2 - s_{x_c}^2} \left[s_{x_c}^2 - s_x^2 s_{x_c}^2 + \frac{s_x^2}{s_{x_c}^2} - 1 \right]} - \frac{2d_1\beta_1 s_x}{\sqrt{1 - s_x^2}}. \quad (2.95)$$

At first inspection, the T factor appears to be purely imaginary in the region past the critical angle for the $k = n = 0$ term. This makes physical sense because no radiated energy can escape the dielectric slab for these scan angles. However, one must be careful because the derivation of the T factor from Munk [1, 2] assumed that multiple plane wave bounces in the slab have the form of a geometric series, which is expressed in closed form. When scanning beyond the critical angle, the ratio between terms in the bounce series has a magnitude of exactly one, which does not permit the use of the closed form sum. The T factor is perfectly valid, though, if a slight amount of loss is inserted for propagation in the \hat{y} direction.

To see more clearly what happens in the neighborhood of a surface wave singularity, take for example the geometry of a dielectric slab of twice the permittivity as the outside space with a thickness of $0.3\lambda_1$. For this case, the critical angle corresponds to a scan parameter of $s_{x_c} \approx \pm 0.7071$ and a single surface wave singularity exists at $s_{x_p} \approx \pm 0.8385$. In Figures 19 through 21, we have plotted the real and

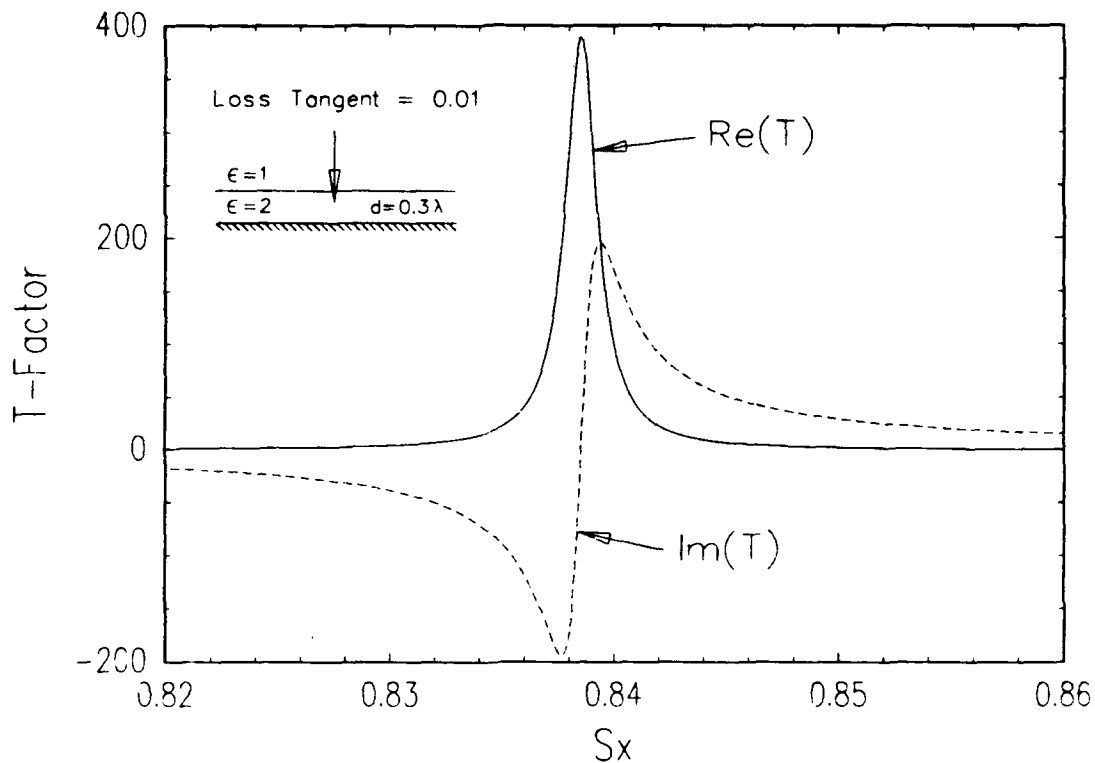


Figure 19: T_{\perp} in the Neighborhood of a Surface Wave Singularity for $k = n = 0$ term, $\epsilon_1 = 2\epsilon_2$, $d_1 = 0.3\lambda_1$, loss tangent = 0.01

imaginary components of the $k = n = 0$ T factor in the neighborhood of this singularity for loss tangents (of ϵ_1) of 0.01, 0.001, and 0.0001 in the \hat{y} direction. The imaginary components clearly converge to the expected cotangent behavior about the singularity as loss is decreased. The real component, though, approaches a single impulse function located at the singularity. Numerical experiments confirm that the area under the real component is independent of the loss.

For a more elegant solution, we wish to express the T factor as the sum of the imaginary component (from Equation (2.79)) and an impulse function with a real weight at the surface wave singularity under lossless conditions. That is, we wish to express the T factor as the sum of the expression in Equation (2.79) for s_x outside

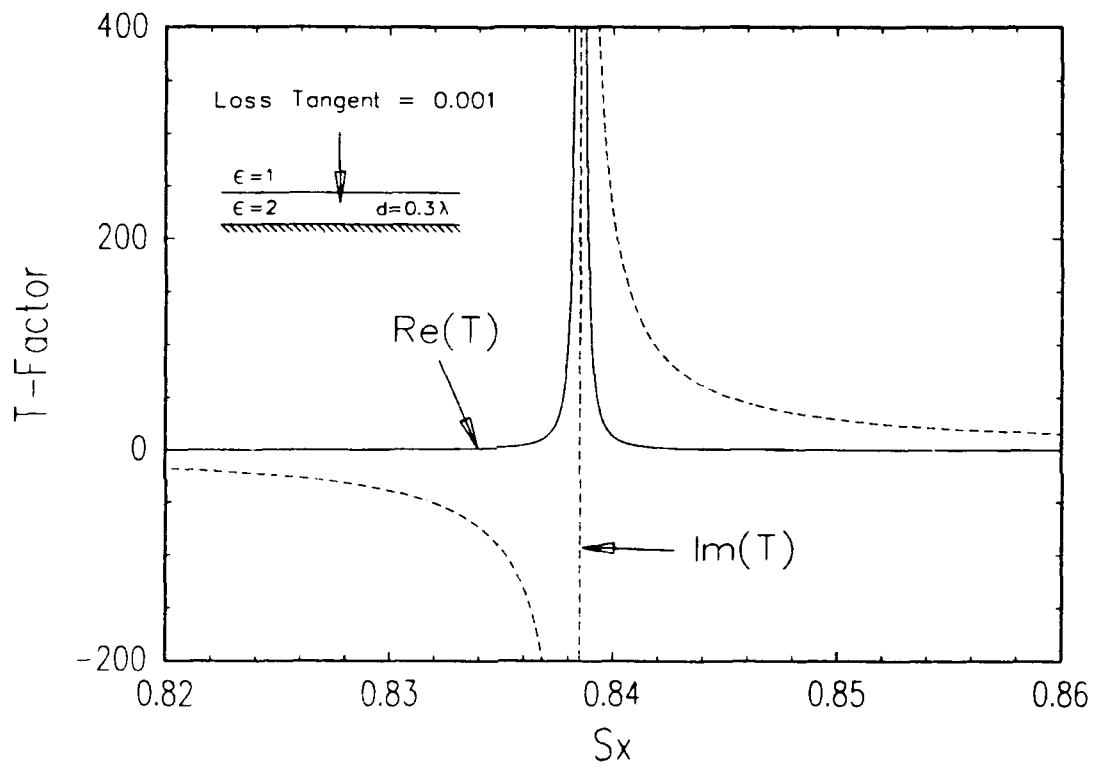


Figure 20: T_{\perp} in the Neighborhood of a Surface Wave Singularity for $k = n = 0$ term, $\epsilon_1 = 2\epsilon_2$, $d_1 = 0.3\lambda_1$, loss tangent = 0.001

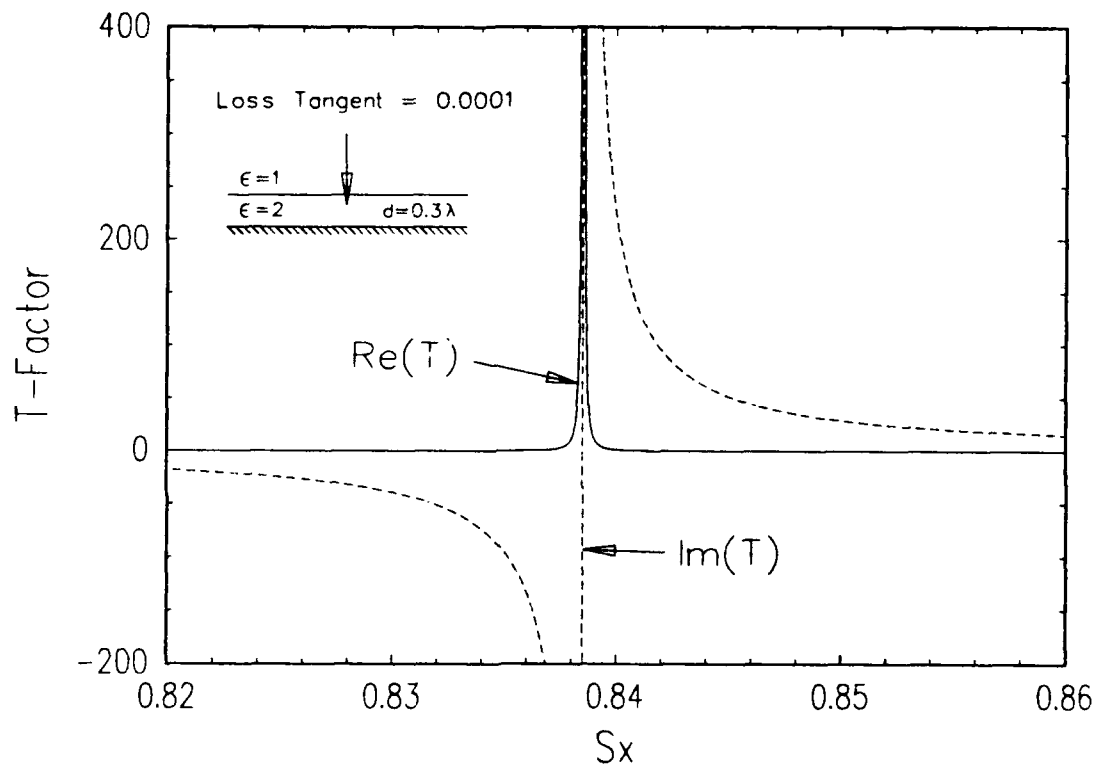


Figure 21: T_{\perp} in the Neighborhood of a Surface Wave Singularity for $k = n = 0$ term, $\epsilon_1 = 2\epsilon_2$, $d = 0.3\lambda_1$, loss tangent = 0.0001

some small neighborhood around the singularity, and

$$T_{\perp} = C [\delta(s_x + s_{xp}) + \delta(s_x - s_{xp})] \quad (2.96)$$

for s_x within the neighborhood of the singularity. Once the weight of the impulse functions is determined, it is easy to find the Fourier transforms for implementation of the ASM.

The weight of the impulse functions is derived as follows. With a small amount of loss, the area under the real part of the T factor around the singularity may be written as

$$C \approx \int \text{Re} \left[2 \frac{1 + \alpha e^{j\phi}}{1 - \alpha e^{j\phi}} \right] ds_x, \quad (2.97)$$

where we have used the same definition of a polar angle ϕ as Equation (2.91) and we include the real constant α as a number slightly less than one to represent loss. The limits of integration are some neighborhood in s_x about the singularity, which does not need to be specified yet. Since the denominator changes much more rapidly than the numerator, the weight can be approximated as

$$C \approx \int \text{Re} \left[\frac{4}{1 - \alpha e^{j\phi}} \right] ds_x. \quad (2.98)$$

Multiplying the numerator and denominator by the complex conjugate of the latter and taking the real part yields

$$C \approx \int \frac{4 - 4\alpha \cos \phi}{1 + \alpha^2 - 2\alpha \cos \phi} ds_x \approx \int 2 \left(\frac{ds_x}{d\phi} \right) d\phi \quad (2.99)$$

where we have applied the limit as α approaches one. With a little bit of faith, we assert that in order to completely capture the singularity, one complete rotation in ϕ is required. Furthermore, the value of $\frac{ds_x}{d\phi}$ is nearly constant around the singularity. Thus, we find the weight of the impulse function to be

$$C = 4\pi \frac{ds_x}{d\phi} \quad (2.100)$$

evaluated at $s_x = s_{x_p}$ or $\phi = 0$. We note that $\frac{ds_x}{d\phi} = -1/g'(s_x)$ where $g'(s_x)$ is given in Equation (2.95). The value of C in Equation (2.100) agrees with the area under real part of the T factor in numerical experiments, confirming that the singularity is indeed captured by the one complete rotation in ϕ .

Now some example computations using the ASM can be made to compute the “one sided” mutual admittance between pairs of infinite column axial slot modes. For each example which follows, the following parameters are chosen:

$$D_z = 0.75\lambda_1$$

$$L = 0.5\lambda_1 = \text{total lengths of transmit and receive slots}$$

$$W = L/10 = \text{slot widths}$$

$$z = 0$$

$$d_1 = 0.4\lambda_1$$

$$\epsilon_1 = 2\epsilon_0 \text{ where } \epsilon_0 \text{ is that of free space}$$

Only one dielectric slab.

Both ϵ_1 and ϵ_2 are lossless.

Piecewise sinusoidal current shapes for both modes, with an effective dielectric constant of $\epsilon_e = \epsilon_1$.

The first case investigated in the Category I geometry, with $\epsilon_2 = \epsilon_1 = 2\epsilon_0$. For this case, the solution in Equation (2.24), developed for a homogeneous half-space, forms a reference for checking the ASM result. This reference solution is referred to as a geometrical optics (GO) solution, which will become clear later when it is applied in stratified media computations. Figure 22 shows a comparison of the ASM and GO solutions for the “one sided” mutual admittance between the axial modes, as a function of separation distance. The agreement between the solutions gives confidence in the ASM implementation.

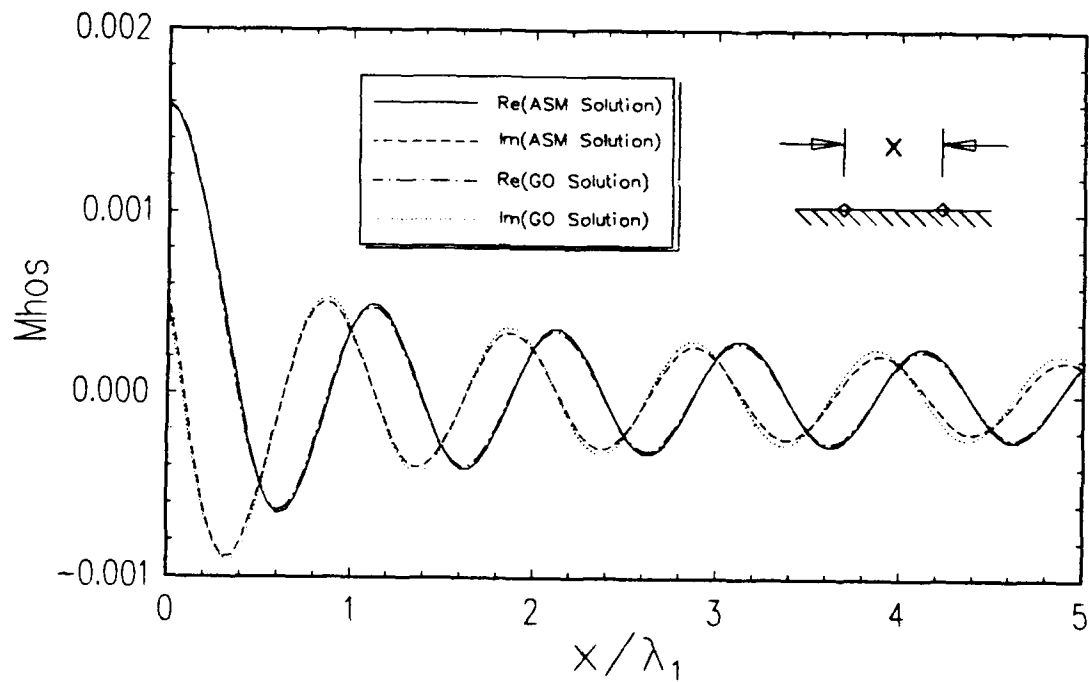


Figure 22: "One Sided" Mutual Admittance between Axial Modes for $\epsilon_1 = \epsilon_2$, $D_z = 0.75\lambda_1$, $L = 0.5\lambda_1$

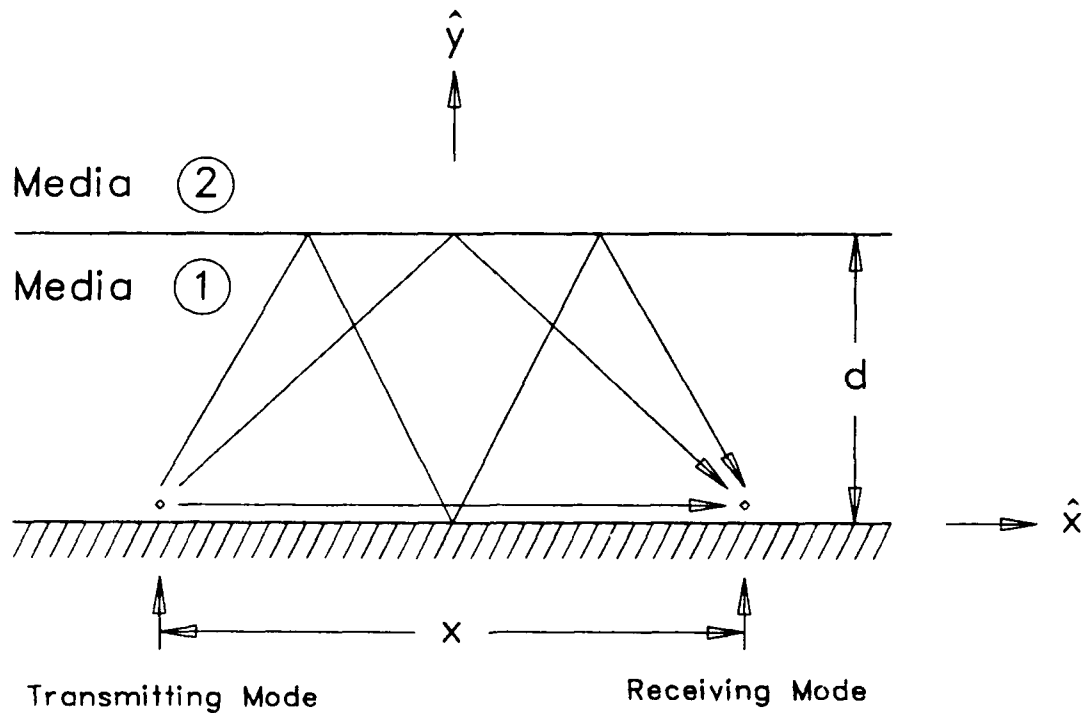


Figure 23: Direct and First Two Bounce Terms in Geometrical Optics Approximation

For stratified media, a GO reference solution is formed by using the result in Equation (2.24) for direct and bounce ray terms, as depicted in Figure 23. The infinite bundle of cylindrical waves from Equation (2.24) are assumed to be initially launched as if they were in a homogeneous half-space. The bundle then reaches the receive mode in a direct path and an infinite series of bounce paths. For the bounce terms, the contribution to the mutual admittance is assumed to be as if it is from the Hankel functions in Equation (2.24) with the distance ρ being the total bounce path length instead of the direct length, $\sqrt{x^2 + a^2}$. Fresnel reflection coefficients corresponding to propagating plane waves at the appropriate ray angles are used.

The geometrical optics approximation can be evaluated very fast, since only a few bounce modes are needed for convergence in most cases. However, the characterization of a cylindrical wavefront reflecting on a planar interface with Fresnel reflection coefficients is fairly crude, so the accuracy is not expected to be good, particularly as the dielectric slab becomes thin and as important ray contributions are near grazing incidence to the boundaries. To improve the accuracy, the Hankel functions can be spectrally decomposed and the Fresnel reflection coefficients may be applied with rigor. However, this only leads to integrals of the Sommerfeld type, which are cumbersome to evaluate. We wish to avoid the requirement to evaluate Sommerfeld integrals, so we choose to use the geometrical optics approximation as an easy checking method for gaining confidence in the ASM.

A Category II geometry is tested by letting $\epsilon_2 = 2\epsilon_1 = 4\epsilon_0$. A comparison of the ASM and GO solutions for "one sided" mutual admittance is given in Figure 24. The agreement of the methods is fairly good for small separation distances, but decays (in percentage terms) as the columns spread apart. This is not unexpected since the characterization of bounces by Fresnel coefficients for the cylindrical wavefronts is not very good at high angles of incidence.

For a typical representative of the dense slab category (III), the case of $\epsilon_1 = 2\epsilon_2$ is chosen. Figure 25 shows a comparison of the ASM and GO solutions for this case for separation distances up to one wavelength in the slab. Beyond this distance, the GO solution behaves erratically and does not come close to matching the ASM solution. This is no doubt explained by both the Fresnel reflection approximation breakdown and the GO solution's failure to adequately characterize the formation of trapped surface waves, which behave as non-decaying plane waves. The ASM solution is expanded to $5\lambda_1$ separation in Figure 26, which clearly shows the plane wave behavior of the surface wave. Note that the near equal amplitudes of the

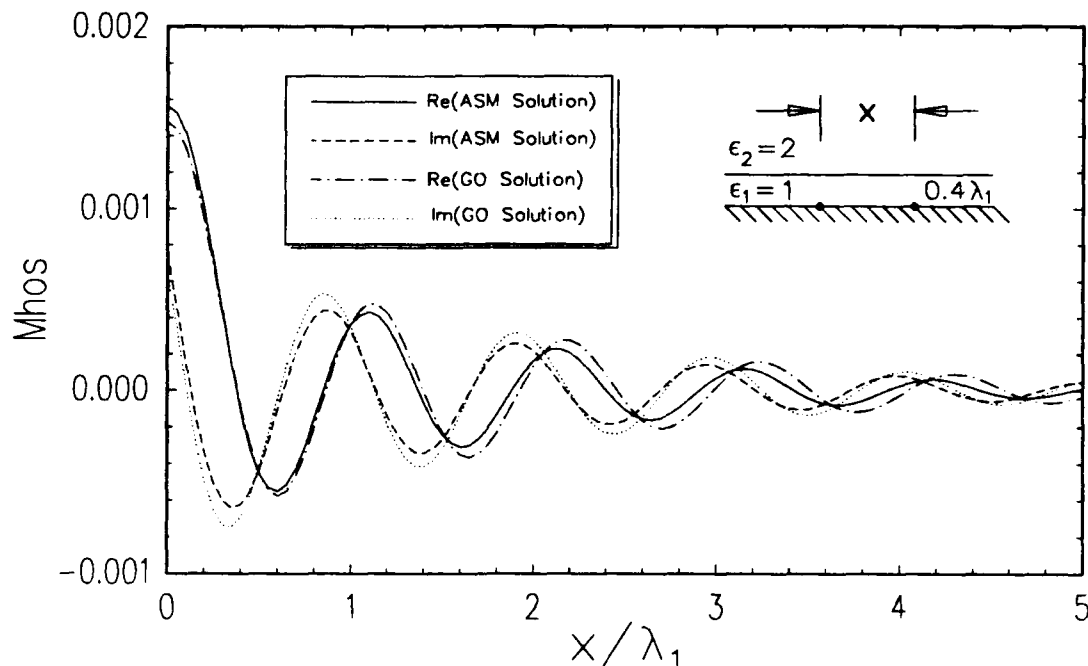


Figure 24: "One Sided" Mutual Admittance between Axial Modes for $\epsilon_1 = 0.5\epsilon_2$, $D_z = 0.75\lambda_1$, $L = 0.5\lambda_1$

real and imaginary components of the mutual admittance give confidence in the analytically determined impulse function weight (ref. Equation (2.100)) for the surface wave singularity.

This example proved to be the most computationally intense, as careful numerical integrations had to be performed near the surface wave singularity. The generation of the data plotted in Figure 26 took approximately two minutes of CPU time on a VAX 8550 machine. The other examples took about one CPU minute.

In Figure 27, the total magnitude of the complex "one sided" mutual admittances is plotted for the three previous cases. It is seen that the homogeneous half-space case gives a coupling proportional to $1/\sqrt{x}$, while the denser half-space has a faster roll-off. The case of the denser slab, however, tends to have approach a

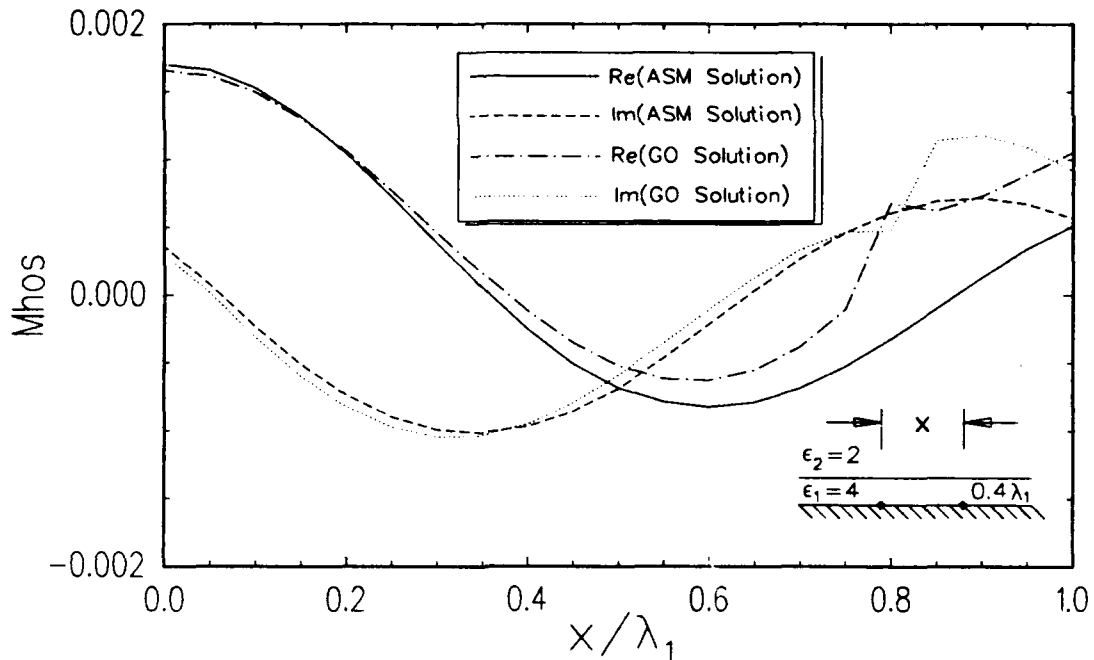


Figure 25: "One Sided" Mutual Admittance between Axial Modes for $\epsilon_1 = 2\epsilon_2$, $D_z = 0.75\lambda_1$, $L = 0.5\lambda_1$

constant amplitude of coupling as distance is increased. This is because the coupling is dominated by a single surface wave which is not decaying.

It is interesting to note that the coupling between the modes in the dense slab case does not monotonically decrease with distance. There is a "partial shadow zone" around $0.5\lambda_1 < x < 2\lambda_1$, in which the surface wave has not fully formed. This may also be explained by geometrical optics, in that single bounce rays before the critical angle have reflection coefficients less than one, but beyond the critical angle have magnitudes of exactly one. This change in reflection coefficient can overcome the decrease in amplitude from a slightly longer ray path.

Since the ASM and GO solutions diverge so quickly in Figure 25, one may be skeptical that the "partial shadow zone" phenomena in Figure 27 is correct. To check this, the data in Figure 26 is used to simulate the "one sided" scan admittance

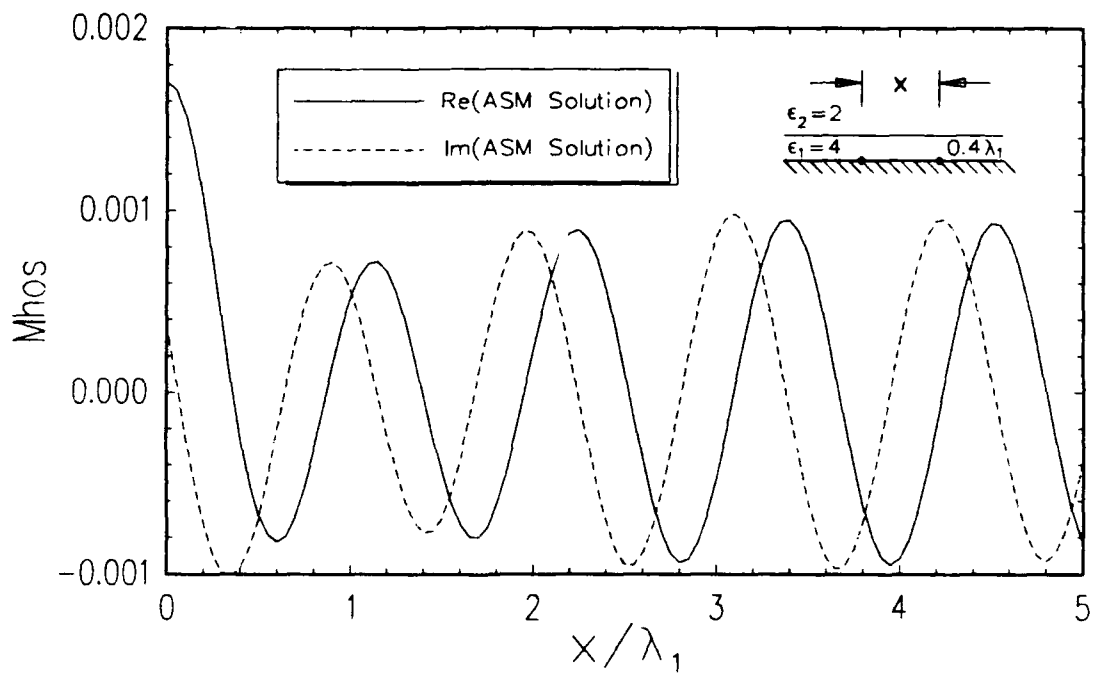


Figure 26: "One Sided" Mutual Admittance between Axial Modes for $\epsilon_1 = 2\epsilon_2$ by Array Scanning Method, $D_z = 0.75\lambda_1$, $L = 0.5\lambda_1$

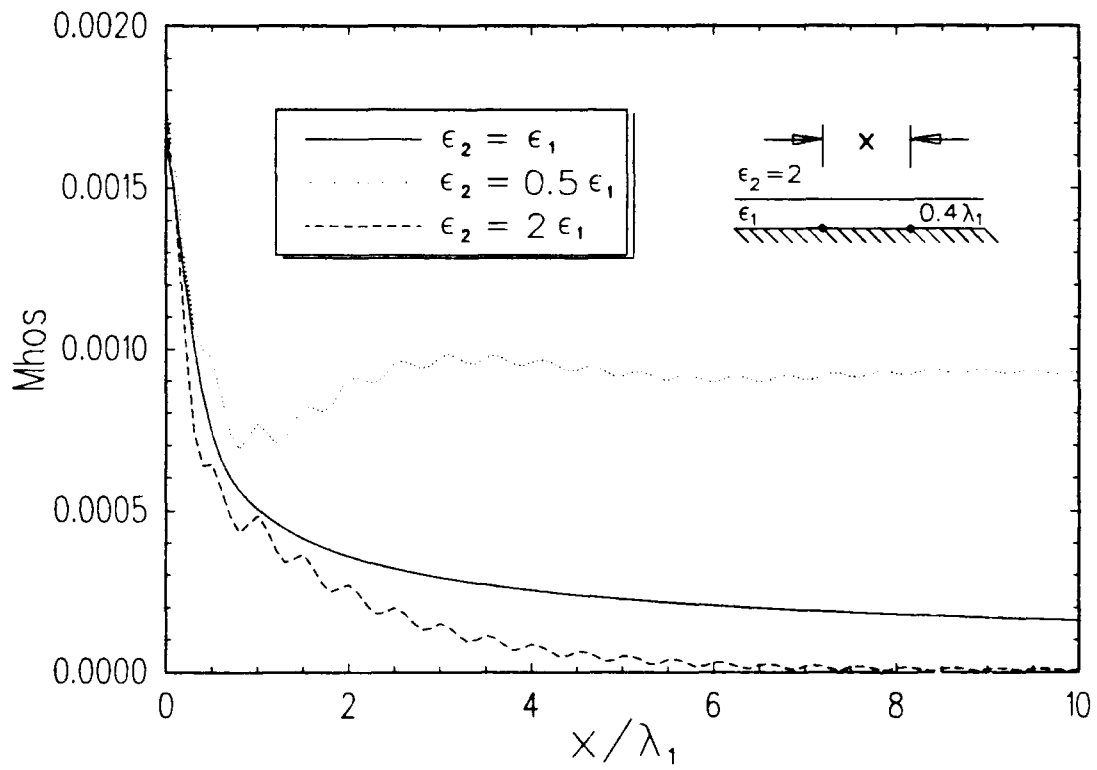


Figure 27: Magnitudes of "One Sided" Mutual Admittances for the Three Categories

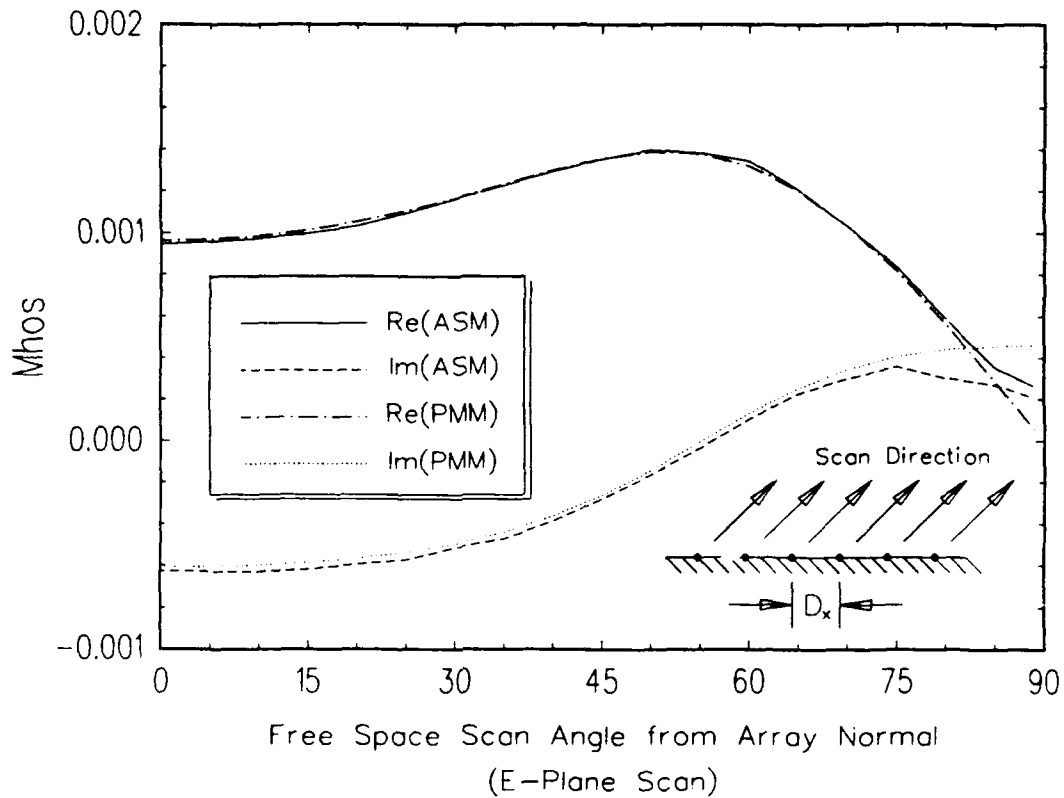


Figure 28: "One Sided" Scan Admittance of a Doubly-Infinite Array of Slots, $D_x = 0.45\lambda_1$, $\epsilon_e = \epsilon_1 = 2\epsilon_2$

of a doubly infinite slot array in the dielectric. One hundred column-to-column admittances are added spatially with Floquet phasing factors in \hat{x} with a Fejer kernel (see Appendix A) used to accelerate convergence. An inter-column spacing of $0.45\lambda_1$ is chosen for the simulated doubly infinite array. This guarantees that several of the data points from the "shadow zone" will be represented. As a comparison the Periodic Moment Method (PMM) code is used to compute the "one sided" self-admittance of a single doubly infinite slot mode [3]. The two predictions of the "one sided" self admittance are plotted in Figure 28 for a complete sweep of free space scan angles in the XY plane. The agreement is excellent, except at high scan angles (attributed to the Fejer kernel), which gives confidence in the data in Figure 26.

The extension of this solution to problems involving multiple layers of dielectrics comes from a relatively easy change in the T factors. The change in the formulation is a substitution for an effective reflection coefficient at the media 1-2 interface for the Fresnel coefficient. Recall that the Fresnel coefficient is derived on the assumption that medias 1 and 2 are unbounded half-spaces. The procedure of "walking through the dielectrics" from the outer interface to the 1-2 interface, in order to find the effective reflection coefficient, is described by Munk [2] in his Appendix D. This procedure is summarized as follows.

Consider the stratified medium shown in Figure 29. The picture shows a set of four dielectrics, which can be part of an arbitrary number of dielectrics. Fresnel reflection coefficients are identified with subscripts denoting the dielectric in which a plane wave is located, and the abutting dielectric at the interface.

Assuming Region $m + 1$ is an infinite half-space, an effective reflection coefficient may be formed at the $m - 1, m$ interface for the aggregate effect of a plane wave hitting this interface in the presence of both Regions m and $m + 1$. This coefficient, distinguished from the Fresnel coefficient by the superscript e , is

$$\Gamma_{m-1,m}^e = \frac{\Gamma_{m-1,m} + \Gamma_{m,m+1} e^{-j2\beta_m d_m r_{ym}}}{1 - \Gamma_{m,m+1} \Gamma_{m,m-1} e^{-j2\beta_m d_m r_{ym}}}. \quad (2.101)$$

Thus, the simple Fresnel coefficients, which are based on two materials in infinite half-spaces, are used to "cascade" the reflection at the $m, m + 1$ interface to the $m - 1, m$ interface. Further cascading to the "left" (as in Figure 29), is done by using the newly found effective reflection as follows:

$$\Gamma_{m-2,m-1}^e = \frac{\Gamma_{m-2,m-1} + \Gamma_{m-1,m}^e e^{-j2\beta_{m-1} d_{m-1} r_{y_{m-1}}}}{1 - \Gamma_{m-1,m-2} \Gamma_{m-1,m}^e e^{-j2\beta_{m-1} d_{m-1} r_{y_{m-1}}}}. \quad (2.102)$$

These formulas hold for both electric and magnetic field reflections, and for each polarization.

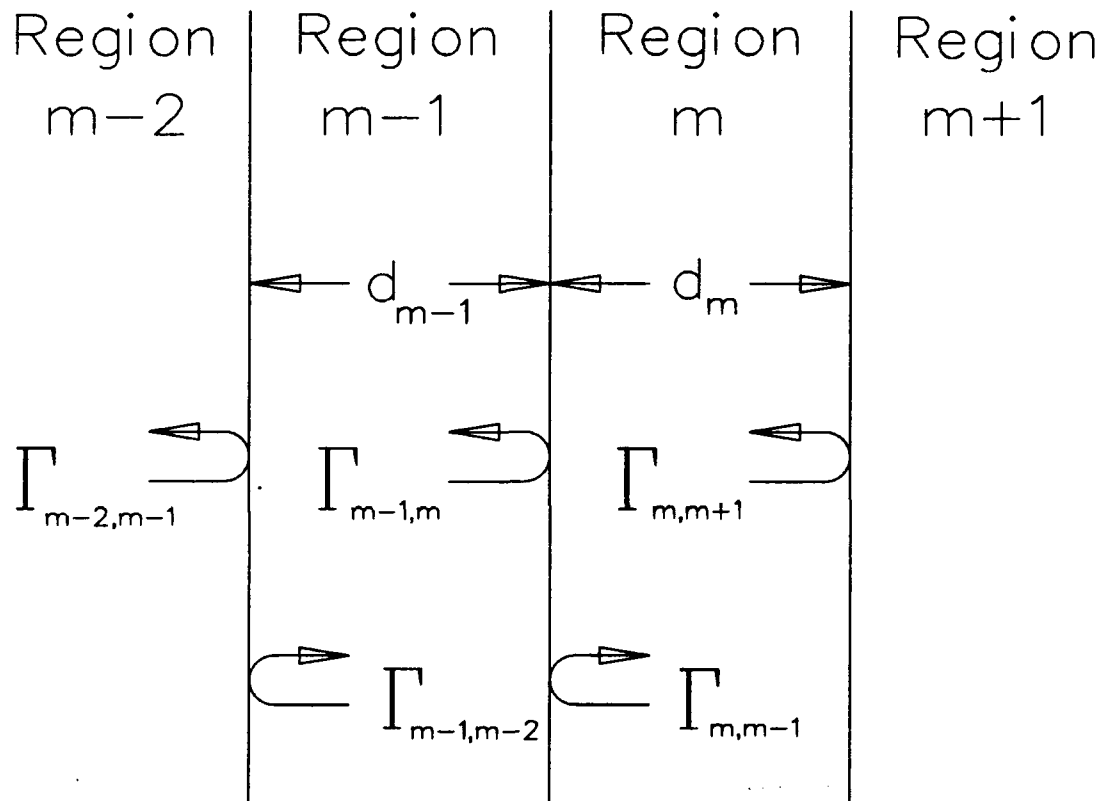


Figure 29: Fresnel Reflection Coefficients Inside a Stratified Medium

In the case of multiple dielectric layers, the phenomena of surface wave formation becomes very complex. Although transcendental equations exist which describe the locations of the surface wave poles, s_{zp} , they are much more complicated than Equation (2.95), which works for the single layer. Therefore, the removal of surface wave contributions by identifying the strengths of the singularities in an analytical sense is not practical for the case of an arbitrary number of layers. Instead, we adopt the approach of inserting a slight loss tangent for propagation in the \hat{y} direction for each dielectric layer, and integrate the $k = n = 0$ term numerically with fine sampling to capture the sharp bell shaped portion of the real part of T_{\perp} around each surface wave singularity. This process can also be used for the single layer case, producing the same results as using Equation (2.100) (which produced Figure 26, i.e., an identical figure is produced when integrating numerically with a small loss tangent), but it is much slower than the analytical solution. Therefore, the careful numerical integration approach with small loss tangents is reserved for use with multiple dielectric layers only.

The numerical integration approach is tested for the case of a single and double slab geometry with the following parameters:

frequency = 10 GHz

$D_z = 0.75\lambda_1$

$L = 0.5\lambda_1 =$ total lengths of transmit and receive slots

$W = L/10 =$ slot widths

$z = 0$

$d_1 = 0.4\lambda_1$, for both one and two slab examples

$\epsilon_1 = 4\epsilon_0$, for both one and two slab examples

$d_2 = 0.3\lambda_2$, for two slab example only

$\epsilon_2 = 2\epsilon_0$ for second slab in two slab case or half-space in one slab case

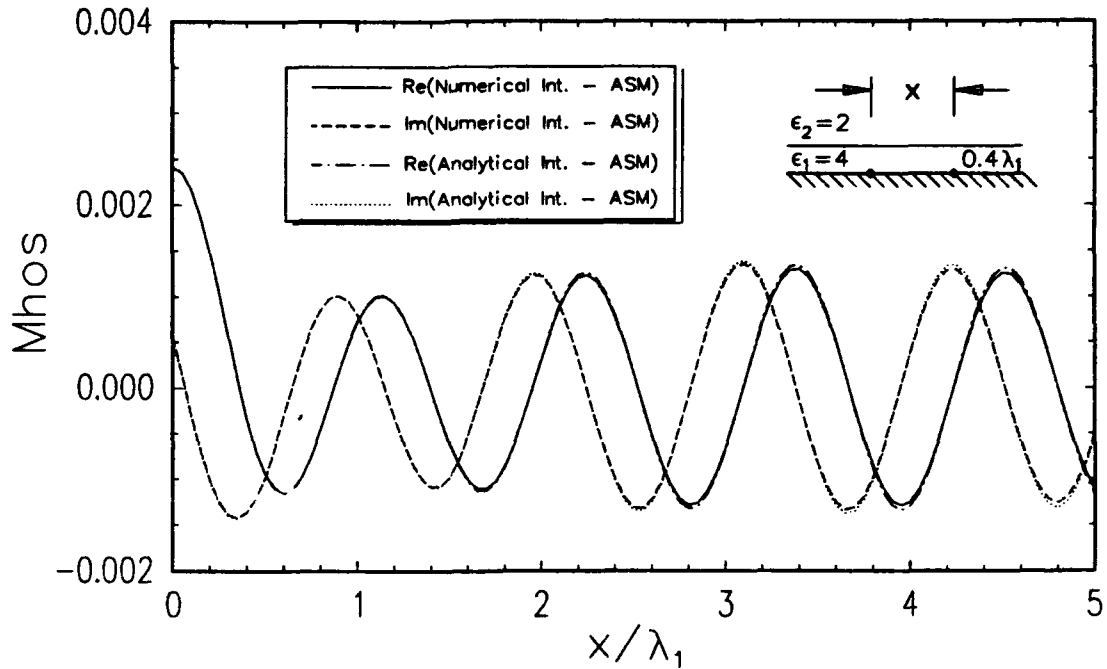


Figure 30: Comparison of Numerical Integration and Analytical Singularity Removal with the ASM in Getting "One Sided" Mutual Admittance between Axial Modes for $\epsilon_1 = 4\epsilon_0$, $\epsilon_2 = 2\epsilon_0$, $d_1 = 0.4\lambda_1$, $D_z = 0.75\lambda_1$, $L = 0.5\lambda_1$

$\epsilon_3 = \epsilon_0$ for two slab example only

Piecewise sinusoidal current shapes for both modes, with the effective dielectric constant of $\epsilon_e = \epsilon_1$.

The case of "one sided" mutual admittance for the single slab case was computed with both the analytical removal of the surface wave singularity and a careful numerical integration with a loss tangent of 0.01 in the slab for \hat{y} -directed propagation.. The result of each method is plotted in Figure 30. Note that the methods match very closely, as expected, and that each curve is approximately $\sqrt{2}$ times the data plotted in Figure 26, which is expected by the scaling of the geometry. The numerically integrated data took approximately five times as much computation time as the analytical singularity removal, after adding the overhead from the FFTs on all other k and n terms.

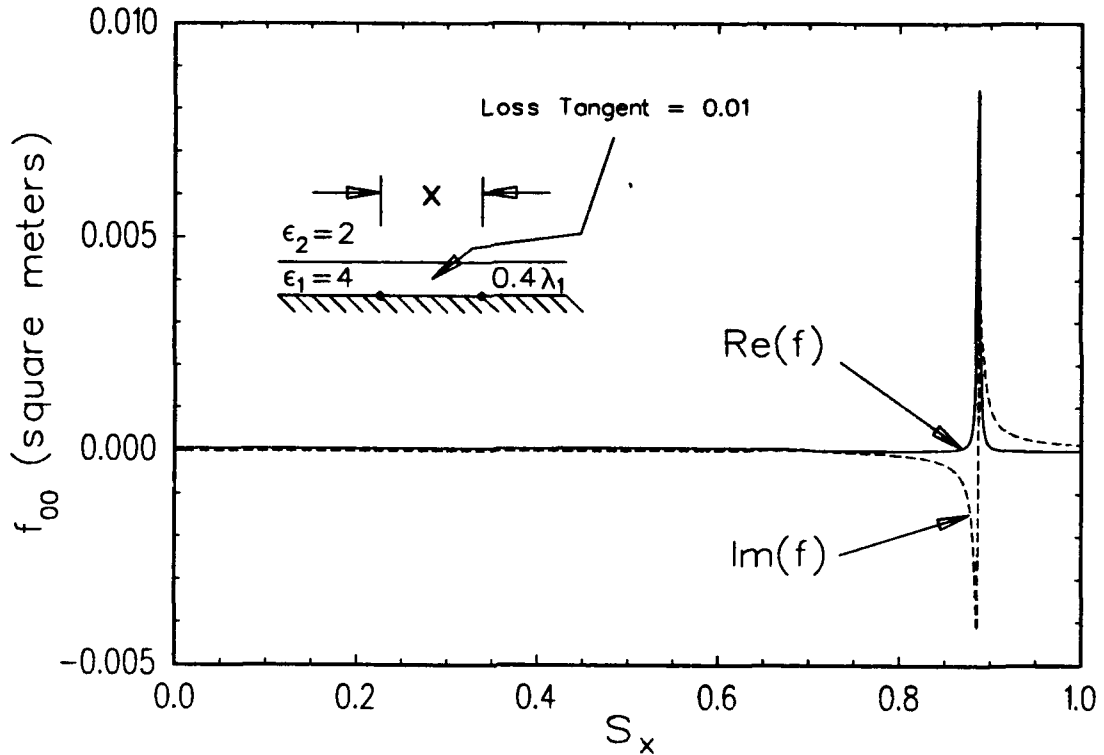


Figure 31: f_{00} Term for the Single Slab Example

With the loss tangent of 0.01 in the dielectric slab, the integrand for the $k = n = 0$ term of the expansion in Equation (2.82) is examined with $x = 0$. That is, f_{00} is examined and plotted in Figure 31. It shows the resonant behavior of a surface wave singularity at $s_{xp} \approx 0.8385$.

The double slab case was also computed with the numerical integration implementation of the ASM with loss tangents of 0.01 in each slab. The “one sided” mutual admittance in this case is plotted in Figure 32.

The corresponding $k = n = 0$ integrand (for $x = 0$) for the double slab case is plotted in Figure 33. Note that there are now two surface wave singularities - a strong one at $s_{xp} \approx 0.8840$ and a weak one at $s_{xp} \approx 0.5105$. The effect of the two surface waves is a “slower” weak plane wave adding with a “faster” (but still slower

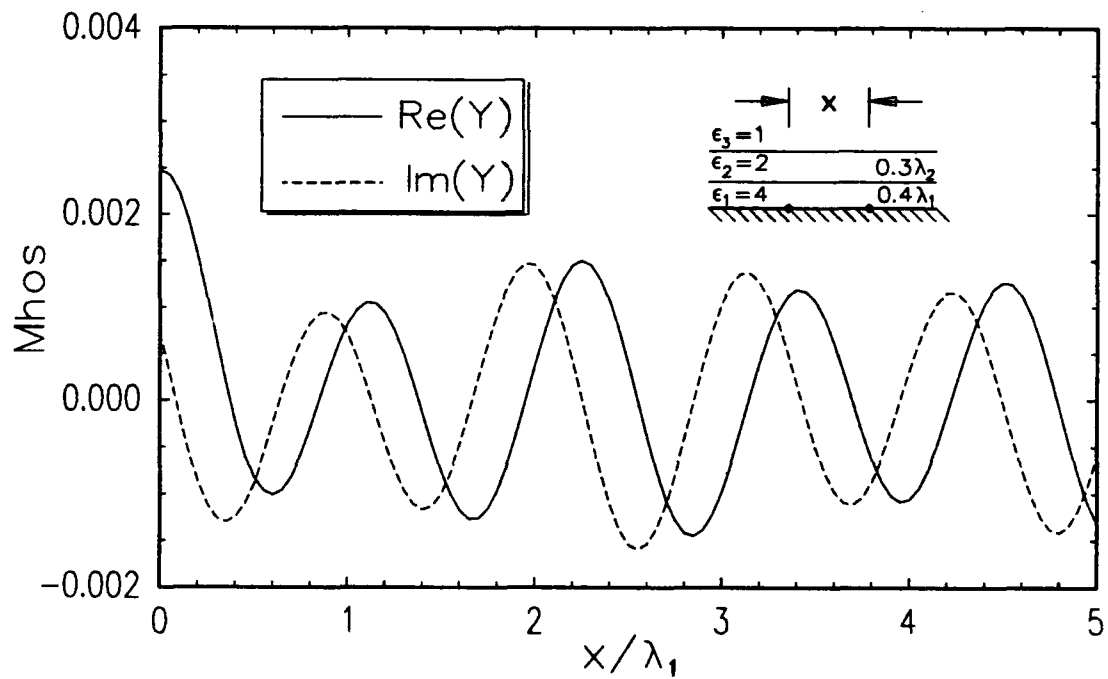


Figure 32: "One Sided" Mutual Admittance using Numerical Implementation of the ASM with $\epsilon_1 = 4\epsilon_0$, $\epsilon_2 = 2\epsilon_0$, $\epsilon_3 = \epsilon_0$, $d_1 = 0.4\lambda_1$, $d_2 = 0.3\lambda_2$, $D_z = 0.75\lambda_1$, $L = 0.5\lambda_1$

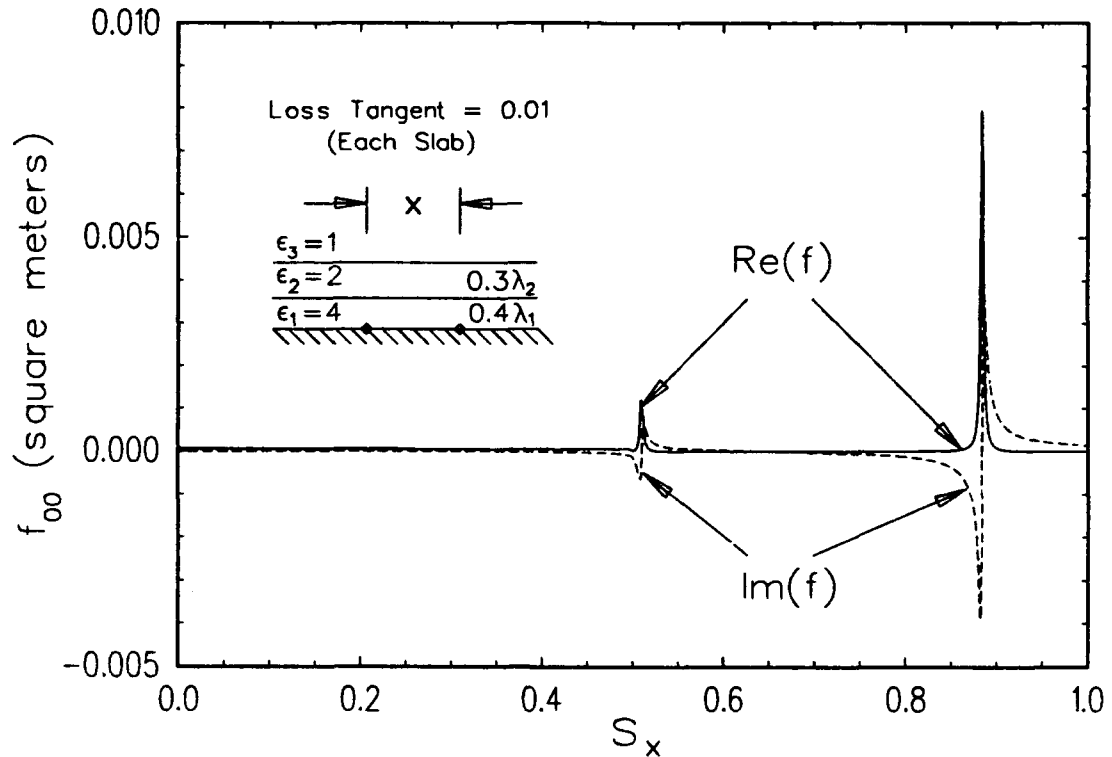


Figure 33: f_{00} Term for the Double Slab Example

than free space propagation) strong plane wave. The result is seen in the admittance data in Figure 32, which shows the beginning of the two “wobbling” plane waves which continue forever without attenuation as x increases.

To verify that the data plotted in Figure 32 is reasonable, we again use the concept of spatial addition of column-to-column mode admittances with Floquet phasing factors in \hat{x} to simulate the full planar array “one sided” scan admittance. This admittance is checked against the PMM code [3], which uses the direct plane wave expansion solution from Munk [1, 2]. The spatial domain sum of the ASM data was formed from 201 slot column modes spaced at $D_x = 0.45\lambda_1$ apart, with the assistance of a Fejer kernel. The comparison of the scan admittance data from

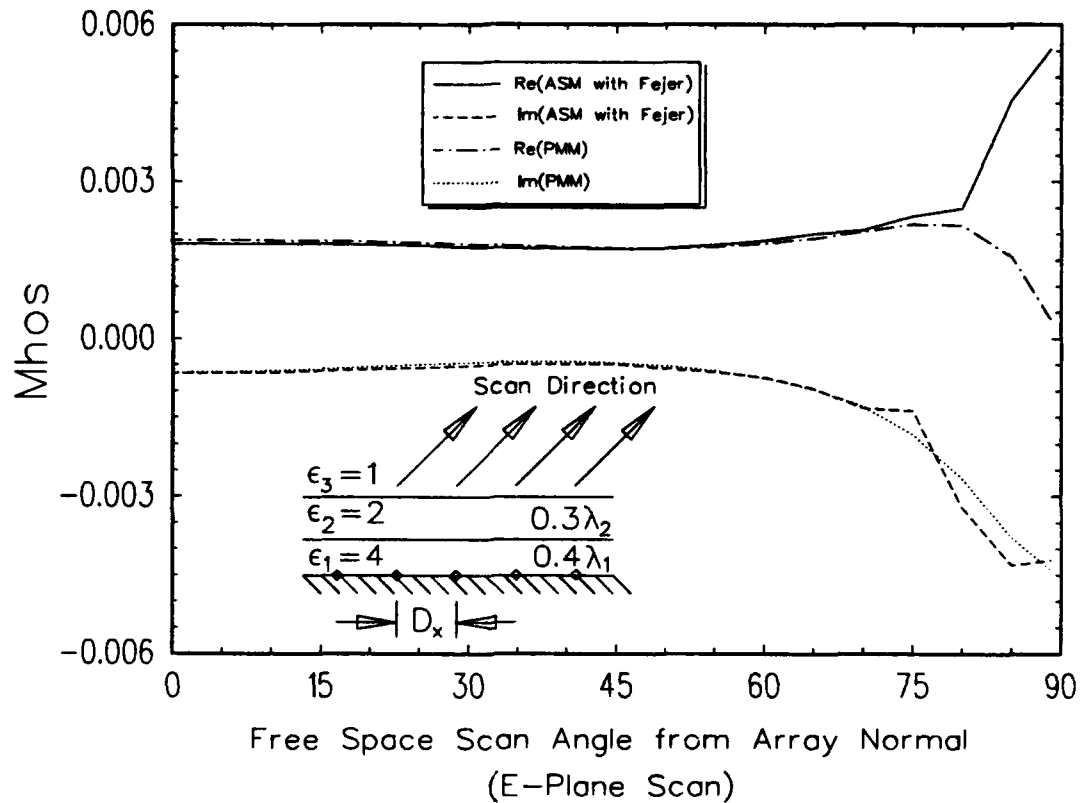


Figure 34: "One Sided" Scan Admittance of a Doubly-Infinite Array of Slots, $D_x = 0.45\lambda_1$, $\epsilon_e = \epsilon_1$, Double Slab Example Geometry, Spatial Domain with the Fejer Kernel

each method is shown in Figure 34. The comparison is good except at high scan angles, which as in Figure 28, is attributed to the Fejer kernel.

To see if the column-to-column coupling data actually supports good planar scan data at high scan angles, the same spatial domain sum was performed with Shanks' transformation used instead of the Fejer kernel. The results of this and the PMM predictions are plotted in Figure 35. The excellent agreement at even high scan angles gives a strong indication that the column mode coupling data in Figure 32 is good.

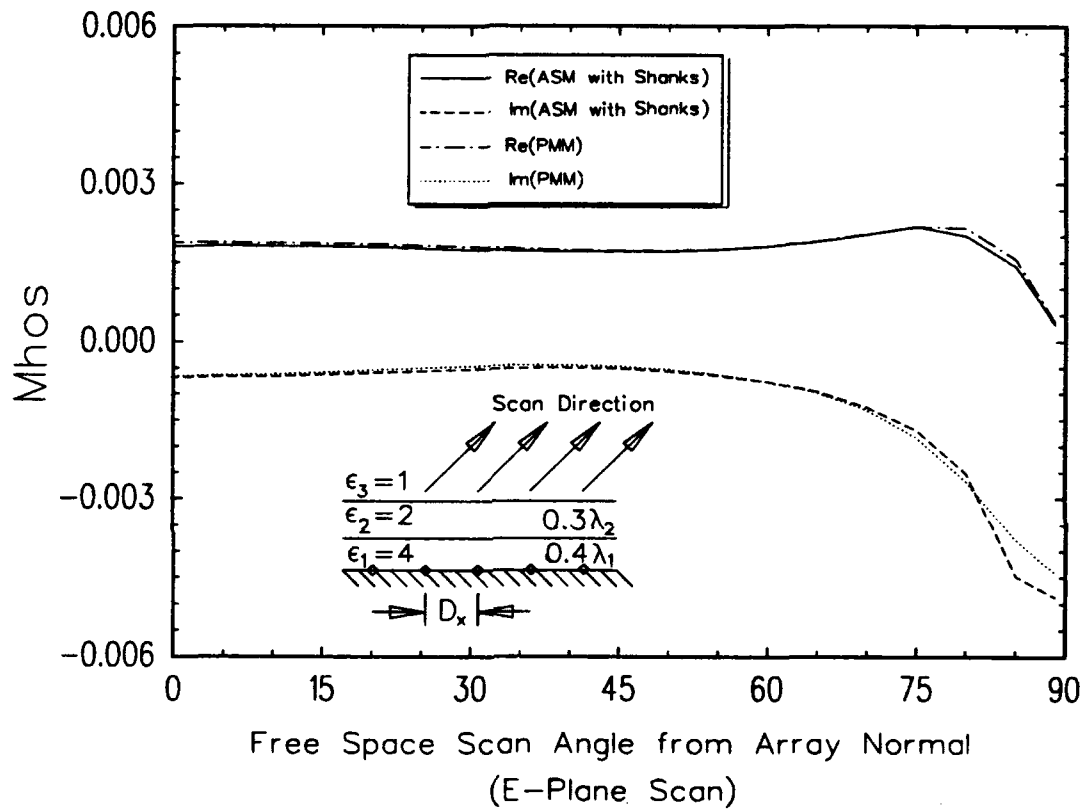


Figure 35: "One Sided" Scan Admittance of a Doubly-Infinite Array of Slots, $D_x = 0.45\lambda_1$, $\epsilon_e = \epsilon_1$, Double Slab Example Geometry, Spatial Domain with Shanks' Transformation

As seen in Figures 34 and 35, the scan admittance of a doubly-infinite array of slots in the given double slab geometry is relatively constant over free space scan angles between 0 and 60 degrees from normal in the E-plane. Such is not the case in the single slab example plotted in Figure 28. This illustrates the concept of scan independence, which may be achieved in an approximate sense over wide angular sectors with an intelligent choice of dielectrics, as demonstrated by Munk and others [27]. Thus it is seen that in addition to mechanical and structural reasons, there is an important electrical reason to analyze and design periodic surfaces with dielectric coatings.

2.2.2 Inner Zone Coupling

In this section, we consider the coupling between slot modes in a stratified version of Region II (ref. Figure 4). An example of the geometry to be considered is shown in Figure 36. It depicts receiving mode locations for both conducting planes. Note that the origin is located at the center of the reference element in the transmitting mode, and that when the receiving mode is for a slotted array column on the same ground plane as the transmitting mode, the test point is offset an "equivalent wire radius" from the ground plane, as discussed previously. Also note that the coordinate system has been changed from that used in the homogeneous case (see Figure 11, for the convenience of the expressions which will be used. Although Figure 36 depicts three dielectric layers, the number of such layers is considered arbitrary.

The problem of inner zone coupling is again divided into two cases. Case A is that where the receiving mode is for a slot on the same ground plane as the transmitting mode. Case B is for a receiving mode on the opposite ground plane as the transmitting mode. We shall first devote our attention to Case A.

The solution to the stratified inner zone coupling problem for Case A is just as described for the stratified (multi-layer) outer zone coupling problem, using the Array Scanning Method (ASM). The only modification is that the "outermost" boundary, which corresponds to Ground Plane B, gives rise to magnetic field reflection coefficients of +1 for every plane wave mode, no matter what the scan angle. The transferring of the reflection coefficient to the media 1-2 interface is accomplished by successive applications of Equation (2.102). Because multiple dielectric layers are involved, the surface wave poles are integrated numerically with a slight loss tangent (for \hat{y} -directed propagation only) inserted for each layer.

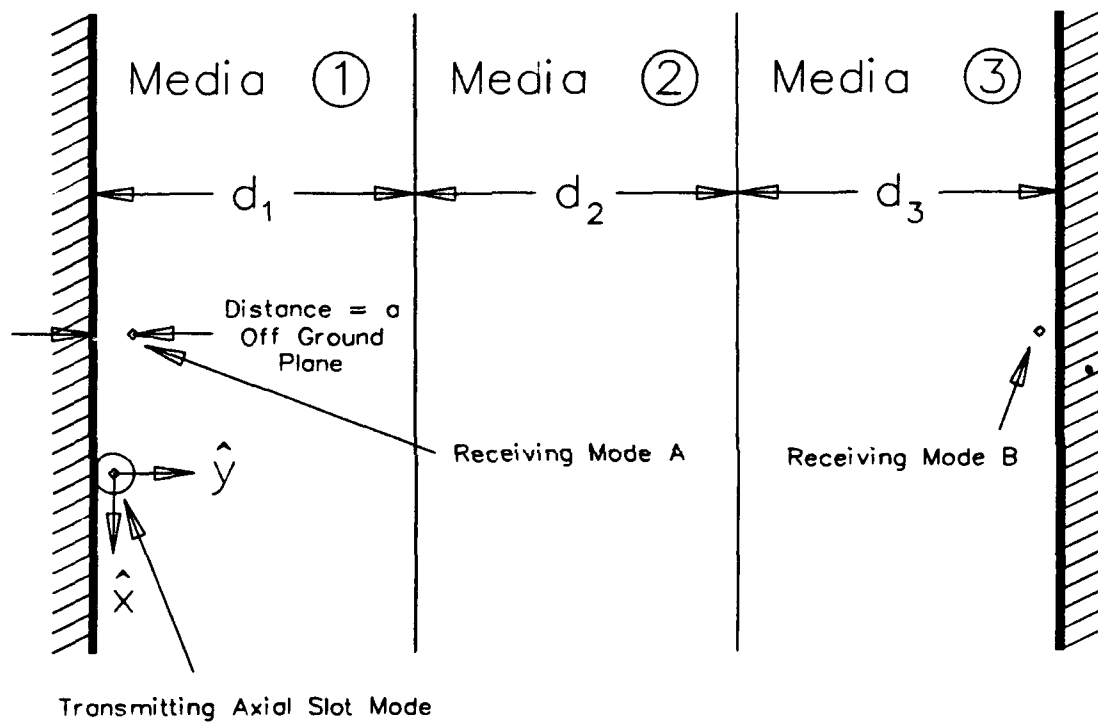


Figure 36: Geometry of Inner Zone Coupling in a Stratified Medium

The ASM was first applied to an inner zone coupling problem with only one dielectric slab, which is merely a homogeneous inner zone. Specifically, an example was chosen with slot lengths of $L = 0.4\lambda$, inter-element spacings of $D_z = 0.6\lambda$, thickness of $d = 0.3\lambda$, dielectric constant of $\epsilon_1 = \epsilon_0$, and no offset in z between the transmit and receive modes. This corresponds to the homogeneous inner zone (Case A) problem used in Figure 16. When employing the ASM with this problem with +1 reflection coefficients at both ground plane surfaces, a surface wave pole becomes excited at $s_x = \pm 1$ for the $k = n = 0$ term. This corresponds to the excitation of a TEM waveguide mode. To complicate matters, the $1/r_y$ singularity exists at the same location in the ASM integrands, which makes it very difficult to analytically remove the pole. Therefore, an approximation was made by replacing the second ground plane (B) with a semi-infinite media with dielectric constant of $10,000\epsilon_0$. This interface reflects almost exactly like a ground plane, and shifts the surface wave pole just enough from the $1/r_y$ pole so that each may be integrated numerically with a slight loss added in the slab. This procedure produced the mutual admittance data shown in Figure 37, which is fairly close to the data found by more exact methods (for the homogeneous inner zone) in Figure 16. Again, this provides further evidence that the ASM is a valid calculation technique.

The ASM was next applied to an inner zone geometry with two dielectric slabs. In this case, the parameters chosen were $\epsilon_e = \epsilon_1 = 4\epsilon_0$, $\epsilon_2 = 2\epsilon_0$, $d_1 = 0.2\lambda_1$, $d_2 = 0.35\lambda_2$, $L = 0.5\lambda_1$, $W = L/10$, $D_z = 0.75\lambda_1$, and $z = 0$. This geometry is referred to as the double slab inner zone example with $d_2 = 0.35\lambda_2$. Case A testing was examined at 10 GHz using the ASM, and the resulting "one sided" mutual admittance is plotted in Figure 38.

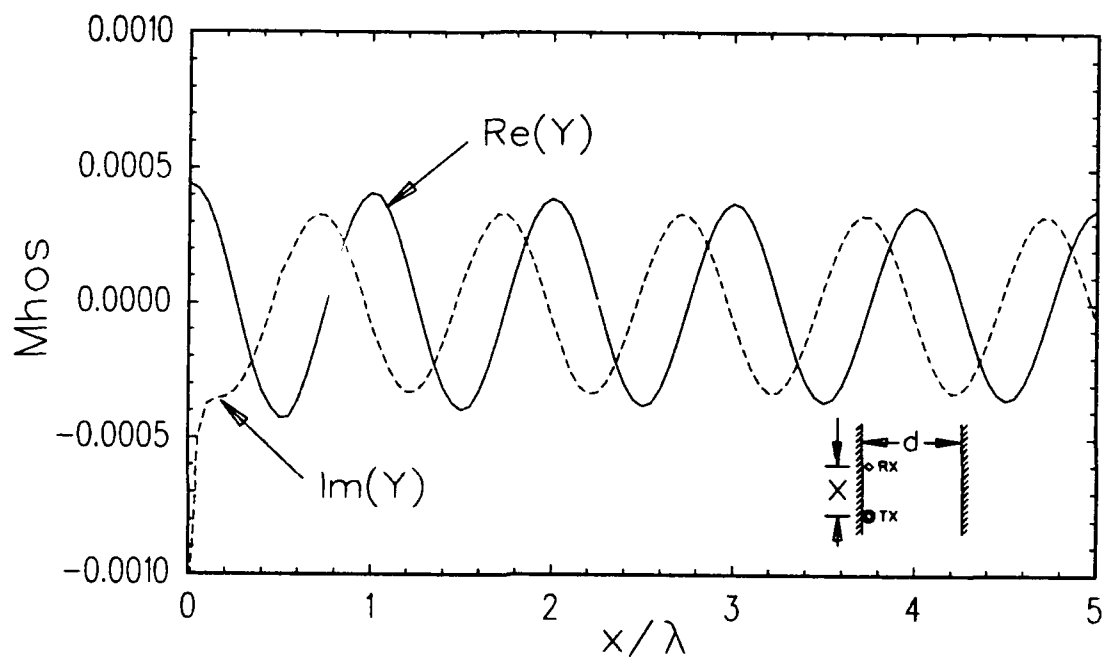


Figure 37: Mutual Admittance Between Piecewise Sinusoidal Axial Slot Modes in Region II (Case A) with Free Space and $L = 0.4\lambda$, $D_z = 0.6\lambda$, $d = 0.3\lambda$, $z = 0$, using the Array Scanning Method

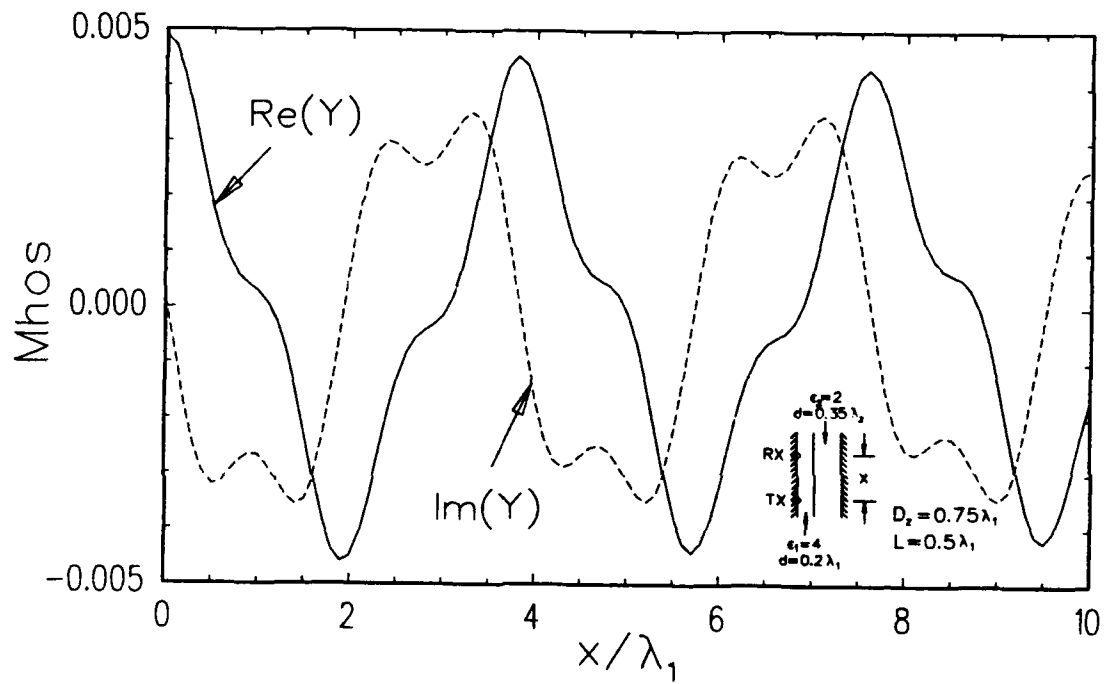


Figure 38: "One Sided" Mutual Admittance using Numerical Implementation of the ASM with Double Slab Inner Zone Example Geometry, Effective Dielectric Constant of $\epsilon_e = \epsilon_1$

The admittance data in Figure 38 appears to be dominated by two surface wave components. These terms form a large amplitude plane wave of “wavelength”⁶ approximately equal to $3.8\lambda_1$ added with a much smaller amplitude plane wave of much shorter “wavelength” (but still longer than λ_1). This interpretation of the data is borne out by the $k = n = 0$ (propagating) integrand in the ASM, which is plotted in Figure 39 for the case where $x = 0$. This integrand is computed using loss tangents of 0.01 in each dielectric slab. Note that a strong surface wave pole is located at $s_{xp} \approx 0.794$ and a weaker surface wave pole is located at $s_{xp} \approx 0.262$. As a pole moves to $s_{xp} = 1$, a TEM mode would become excited (which has a “wavelength” of λ_1), so the pole at 0.794 corresponds to the larger amplitude and longer “wavelength” surface wave. This makes sense with the admittance data in Figure 38.

To verify that the column-to-column admittance data plotted in Figure 38 is probably correct, discrete data points from receive modes at integral multiples of $D_x = 0.45\lambda_1$ were added spatially with Floquet phase factors and with the Fejer kernel. This produces a simulation of the “one sided” scan admittance of a doubly-infinite array of slots, which can be compared with computations from the PMM code, which use the direct plane wave expansion method. This was done with the Floquet phase factors referenced to a free space scan angle, and the results are plotted in Figure 40.

There are a number of interesting features in Figure 40. The data indicates a resonance is reached at a free space scan angle of about 31.6 degrees from normal. From Snell’s Law, this corresponds to an angle of 15.2 degrees inside the first dielectric slab ($\epsilon_1 = 4\epsilon_0$), which translates to a scan parameter of $s_x = 0.262$. This

⁶“Wavelength” in this discussion refers to the effective wavelength as seen in the waveguide formed by the ground planes.

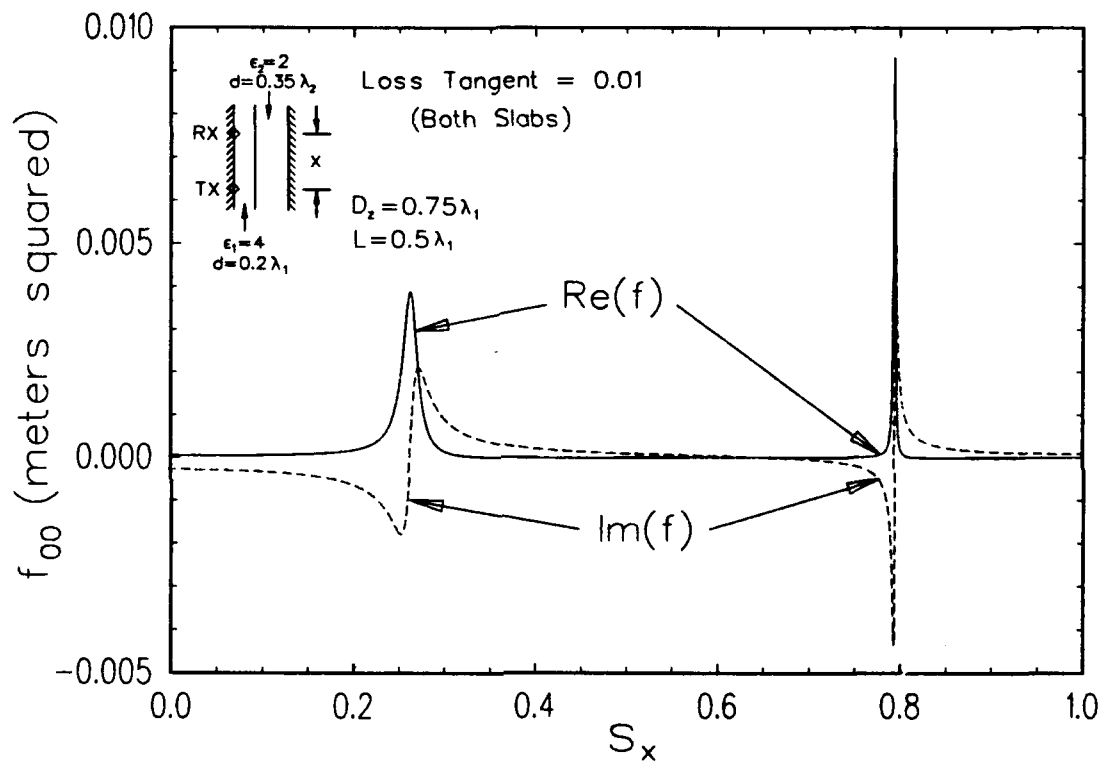


Figure 39: f_{00} Term at $x = 0$ for the Inner Zone Double Slab Example

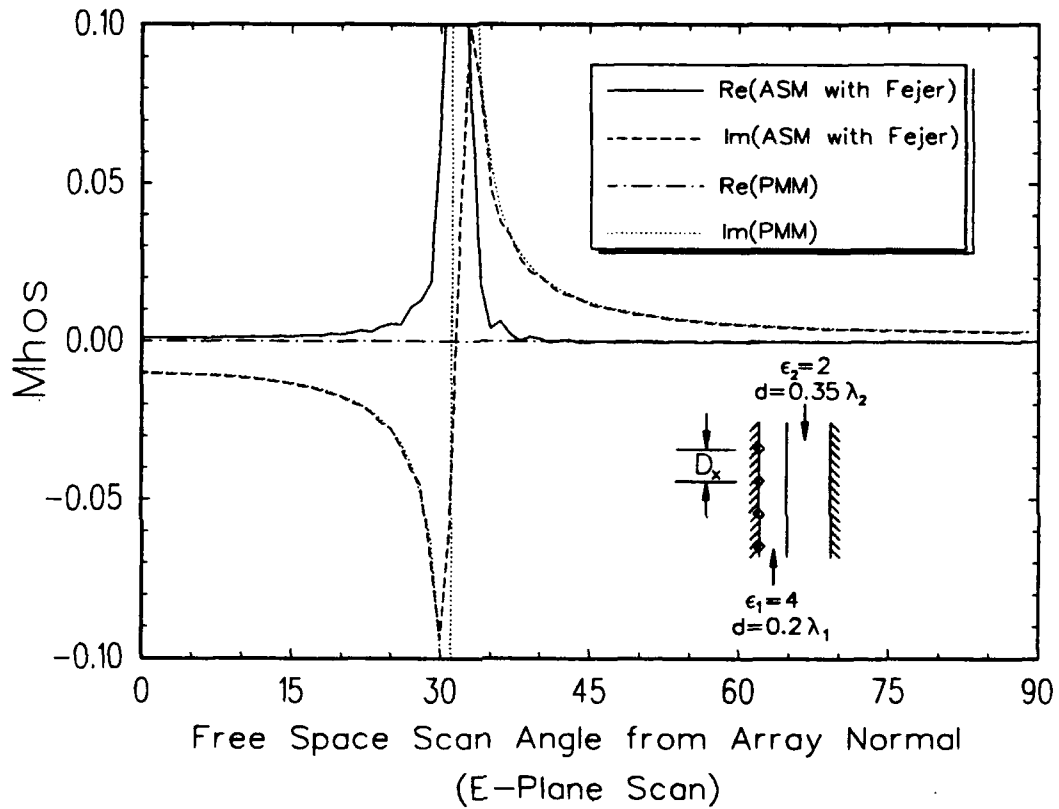


Figure 40: "One Sided" Scan Admittance for the Inner Zone Double Slab Example, $D_x = 0.45 \lambda_1$

resonance is therefore attributed to the first surface wave pole seen in Figure 39. Another surface wave is excited in the slab at $s_x = 0.794$, but this corresponds to an angle of 52.6 degrees in the slab, which is beyond the critical angle (30 degrees) for emergence into the real angles in free space. Therefore, the second resonance is not visible in the free space scan.

Ideally, the real part of the scan admittance produced by the ASM data in Figure 40 should be zero for all scans, except for an impulse function at the surface wave excitation. This is caused by the inability of the transmitting mode to radiate real energy away from the array. In the plotted data, however, the impulse function at the resonance location is opened up due to the slight loss tangent used in the T factors. Such a loss tangent is not included in the PMM reference data. Discounting this notable exception, the simulated scan data from the ASM computed column-to-column admittance compares very well with the direct PMM computations, giving more confidence in the ASM data in Figure 38.

Typically, double slab inner zone geometries are avoided in periodic surface designs since they are not symmetric. Instead, a more likely geometry contains an inner zone with three symmetric dielectric slabs. For example, we choose a first slab (nearest the transmitting and receiving modes' ground plane) to have $\epsilon_1 = 4\epsilon_0$ with a thickness of $d_1 = 0.2\lambda_1$. A middle slab is chosen with $\epsilon_2 = 2\epsilon_0$ and thickness $d_2 = 0.33\lambda_2$. A third slab identical to the first and an accompanying ground plane (B) completes the sandwich. The slot modes were defined with $D_z = 0.6\lambda_1$, $L = 0.5\lambda_1$, $W = L/10$, and $z = 0$. Using piecewise sinusoidal currents with the effective dielectric constant of $\epsilon_e = \epsilon_1$, the "one sided" mutual admittance between the two periodic slot columns on ground plane A were computed using the numerical integration implementation of the ASM. The result is plotted in Figure 41.

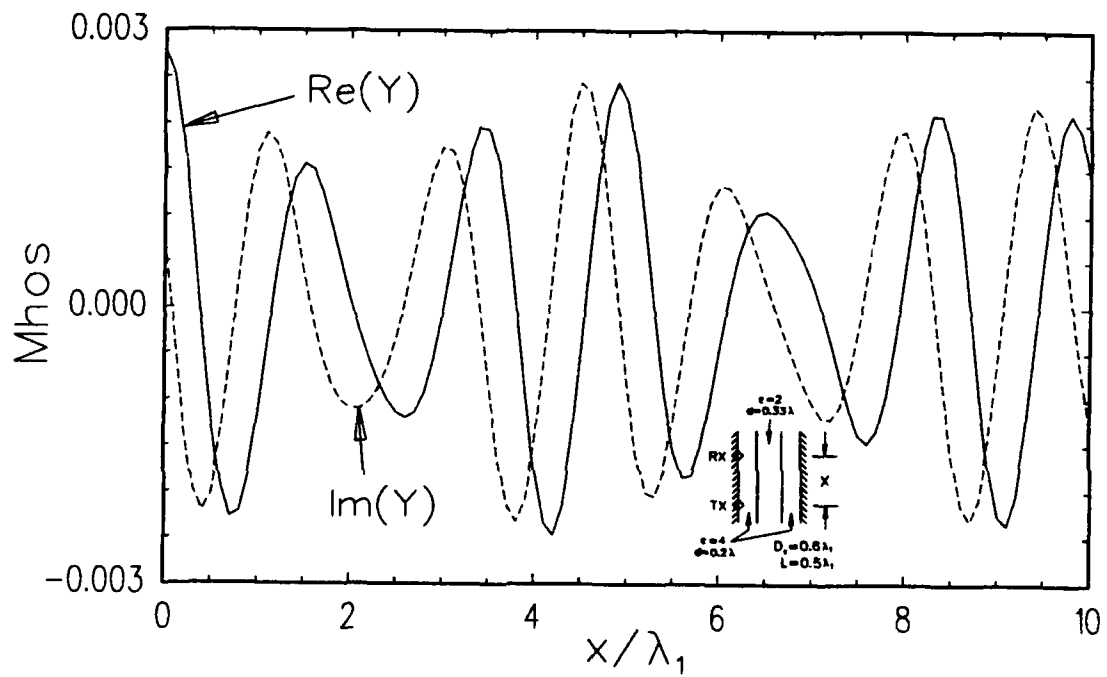


Figure 41: "One Sided" Mutual Admittance using Numerical Implementation of the ASM with Triple Slab Inner Zone Example Geometry, Effective Dielectric Constant of $\epsilon_e = \epsilon_1$, Case A Testing

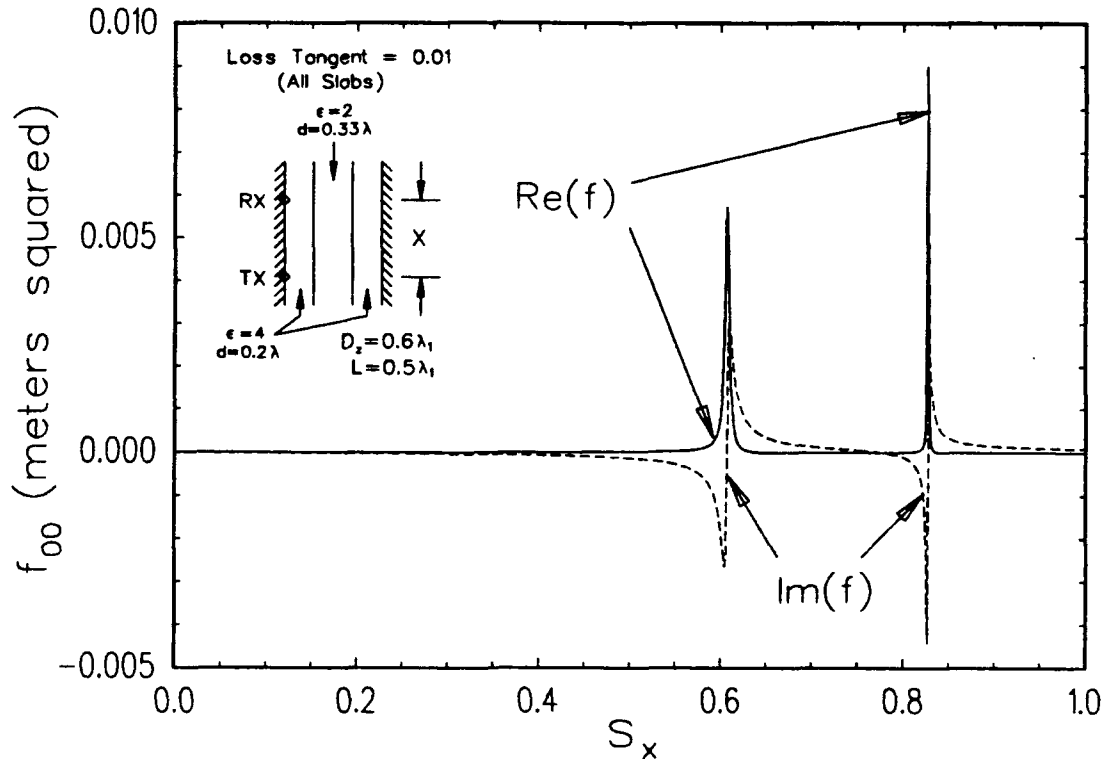


Figure 42: f_{00} Term at $x = 0$ for the Inner Zone Triple Slab Example, Case A Testing

The admittance data in Figure 41 is dominated by the interaction of more than one surface wave. This is seen more clearly in Figure 42, which shows the integrand for the $k = n = 0$ term in the ASM. There are two distinct resonances which are caused by surface wave generation.

Again, to verify that the ASM data in Figure 41 is correct, we spatially add column-to-column admittances with Floquet phase factors and a Fejer kernel to simulate the “one sided” scan admittance for a full doubly-infinite slot array. Using separation distances of multiples of $D_x = 0.3\lambda_1$, the simulated scan admittance from the ASM data was computed and is plotted in Figure 43. Also plotted is a reference solution from the PMM code.

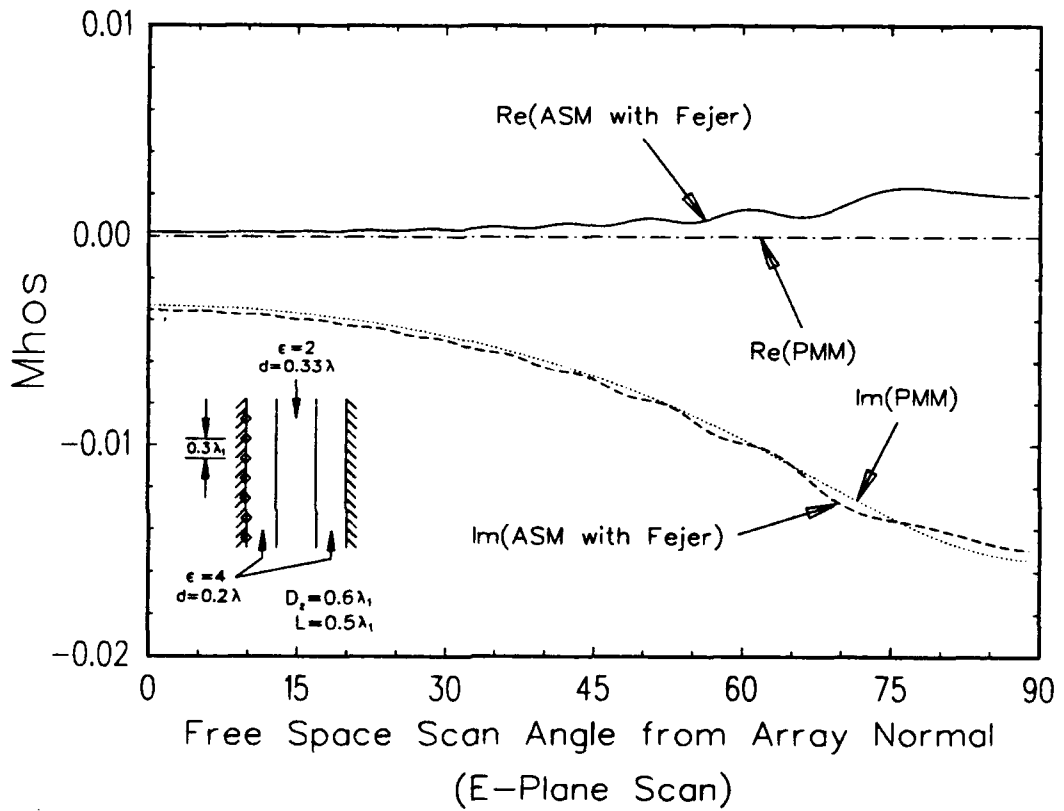


Figure 43: "One Sided" Scan Admittance for the Inner Zone Triple Slab Example Geometry, $D_x = 0.3\lambda_1$, Case A Testing

Since the surface waves are excited beyond $s_x = 0.5$ (corresponding to the critical angle in the first dielectric - compared to free space), there are no resonances in the scan admittance in Figure 43 over the free space scan angles. Such a condition is necessary (but not sufficient) when attempting to design a periodic surface with scan independence. As seen in the data, though, scan independence is not achieved with the triple slab example with the gradual change in the scan susceptance.

As with any inner zone example, the real component of the scan admittance in Figure 43 should be zero over all scan angles. The reconstructed ASM data shows a drift off zero, though, which is partially due to numerical errors in the complicated procedure to produce the data. It may also be due to a nearing of the shoulder of a surface wave resonance for the singularity at $s_x \approx 0.6$ in Figure 42, with the slight loss tangents used in the ASM calculations.

Now we shall consider the stratified inner zone coupling with Case B testing, where the receiving slot element is on the different ground plane from the transmitting slot column mode. The implementation of the ASM now changes, with fundamentally different T factors describing the transmission of plane wave through the dielectric layers. As before, though, Equation (2.67) describes the basis of the ASM. The mutual admittance from a full planar (doubly-infinite) slot array radiating to a receiving slot element on the opposite ground plane is found by applying duality to Munk's result [2], and reducing the result with ground plane reflection coefficients and mode locations, for the geometry depicted in Figure 36. Without loss of generality and for convenience, we declare the the center of the reference element in the transmitting array to be located at

$$\bar{R}_t = x\hat{x} + z\hat{z} \quad (2.103)$$

and the receiving slot located at

$$\bar{R}_r = d_{tot}\hat{y}, \quad (2.104)$$

where d_{tot} is the total distance between the ground planes. This gives the full planar admittance to be:

$$Y_A = \frac{Y_1}{2D_x D_z} \sum_{k=-\infty}^{\infty} \sum_{n=-\infty}^{\infty} \frac{e^{+j\beta_1 \bar{R}_t \cdot \hat{r}_1}}{r_{y_1}} \phi_{1m} \left[P_{\perp,1}^t P_{\perp,m}^r T_{\perp,1m} + \frac{r_{y_1}}{r_{y_m}} P_{\parallel,1}^t P_{\parallel,m}^r T_{\parallel,1m} \right]. \quad (2.105)$$

Several parameters in Equation (2.105) require explanation. As before, Y_1 and β_1 refer to the intrinsic admittance and wavenumber of the dielectric slab nearest to the transmitting mode. The unit vector \hat{r}_1 represents the direction of the plane waves in the first slab, and is given by Equation (2.69). Propagation directions in the other layers are found by successive applications of Equations (2.75) through (2.77). The parameter, ϕ_{1m} , gives the phase delay from one ground plane to the other through the m layers of dielectric, and is given by

$$\phi_{1m} = \prod_{i=1}^m \phi_i = \prod_{i=1}^m e^{-j\beta_i d_i r_{y_i}}. \quad (2.106)$$

The pattern factors are found from Equations (2.62) through (2.64), except the receiving mode pattern, being located in the m th dielectric slab, uses the associated β_m and \hat{r}_m in its evaluation. Thus, the extra subscripts 1 and m in Equation (2.105) remind the reader where the pattern factors are found.

The final clarification for Equation (2.105) are the T factors, which describe the complete transition through the layers (without the phase delay). Simplifying Munk's expressions [2] for the present geometry, the T factors are:

$$T_{1m} = \frac{4 \prod_{i=1}^{m-1} [1 + \Gamma_{i,i+1}]}{\prod_{i=1}^m [1 - \Gamma_{i,i-1} \Gamma_{i,i+1}^e e^{-j2\beta_i d_i r_{y_i}}]}, \quad (2.107)$$

where parallel and perpendicular polarization subscripts have been suppressed on T and all Γ s. Also note that the superscript e denotes an effective reflection coefficient (ref. Equation (2.102)) while the lack of the superscript denotes the use of the Fresnel coefficients in Equations (2.73) and (2.74).

As with earlier implementations of the ASM, the chosen inter-column spacing for the "artificial" transmitting array is $D_x = \lambda_1/2$. Using this spacing, and substituting Equation (2.105) into Equation (2.67), we get:

$$Y = \frac{Y_1}{2\lambda_1 D_z} \sum_{k=-\infty}^{\infty} e^{+j2k\beta_1 x} \sum_{n=-\infty}^{\infty} \int_{-1}^1 f_{kn}(s_x) e^{+j\beta_1 x s_x} ds_x, \quad (2.108)$$

where we have defined the functions,

$$f_{kn}(s_x) = \frac{e^{+j\beta_1 \frac{nz\lambda_1}{D_z}}}{r_{y1}} \phi_{1m} \left[P_{\perp,1}^t P_{\perp,m}^r T_{\perp,1m} + \frac{r_{y1}}{r_{ym}} P_{\parallel,1}^t P_{\parallel,m}^r T_{\parallel,1m} \right], \quad (2.109)$$

for $-1 < s_x < 1$ and $f_{kn}(s_x) = 0$ for all other values of s_x .

Using the alternative Fourier transform definition of

$$F(\omega) = \int_{-\infty}^{\infty} f(t) e^{+j\omega t} dt, \quad (2.110)$$

it is easily seen that the mutual admittance may be expressed as:

$$Y = \frac{Y_1}{2\lambda_1 D_z} \sum_{k=-\infty}^{\infty} e^{+j2k\beta_1 x} \sum_{n=-\infty}^{\infty} F_{kn}(\beta_1 x). \quad (2.111)$$

Using the linearity of the Fourier transform, we simplify the expression to

$$Y = \frac{Y_1}{2\lambda_1 D_z} \sum_{k=-\infty}^{\infty} e^{+j2k\beta_1 x} F_{k\Sigma}(\beta_1 x), \quad (2.112)$$

where we have defined

$$F_{k\Sigma}(\beta_1 x) = \int_{-\infty}^{\infty} f_{k\Sigma}(s_x) e^{+j\beta_1 x s_x} ds_x \quad (2.113)$$

and $f_{k\Sigma}$ is given by Equation (2.86) with the functions f_{kn} coming from Equation (2.109).

As with the previous applications of the ASM, we can employ Fast Fourier Transforms (FFTs) to accelerate the overall moment method solution in most cases, since the application of Equation (2.112) will be repeated several times under similar conditions, except for a change in the value of x .

To demonstrate the ASM with Case B testing, a triple slab geometry is chosen, similar to that used in producing Figures 41 through 43 using Case A testing. Specifically, the following parameters are chosen: $\epsilon_1 = 4\epsilon_0$, $\epsilon_2 = 2\epsilon_0$, $\epsilon_3 = 4\epsilon_0$, $d_1 = 0.2\lambda_1$, $d_2 = 0.33\lambda_2$, $d_3 = 0.2\lambda_3$, $D_z = 0.6\lambda_1$, $L = 0.5\lambda_1$, $z = 0$. The slot width W do not enter into the calculations for Case B testing. Piecewise sinusoidal currents are assumed with effective dielectric constants equal to ϵ_1 for the transmitting mode and ϵ_3 for the receiving mode. As with the Case A testing, a slight loss tangent (in this case, 0.02) is used for the \hat{y} -directed propagation in each layer for calculating the T factors. Note that this loss is not included in the phase delay term, ϕ_{1m} .

The mutual admittance between the slot column modes on opposite ground planes separated by the three dielectric layers is calculated via the numerical integration implementation of the ASM. The result is plotted in Figure 44.

Figure 44 depicts the complicated interaction of multiple surface waves, similar to that from Case A testing (ref. Figure 41). Note that the data in Case B testing is also on the same order of magnitude of that in Case A testing.

The surface wave excitation for the Case B testing is also shown in Figure 45, which plots the integrand for the $k = n = 0$ term in the ASM. It shows surface wave resonances at the same s_x values as those in the Case A testing (ref. Figure 42), but with different resonant characteristics. Unlike the Case A testing, the evanescent plane wave modes (k, n not both zero) in the ASM were almost negligible in Case B testing, so the Fourier transform of the data plotted in Figure 45 dominated the admittance calculations.

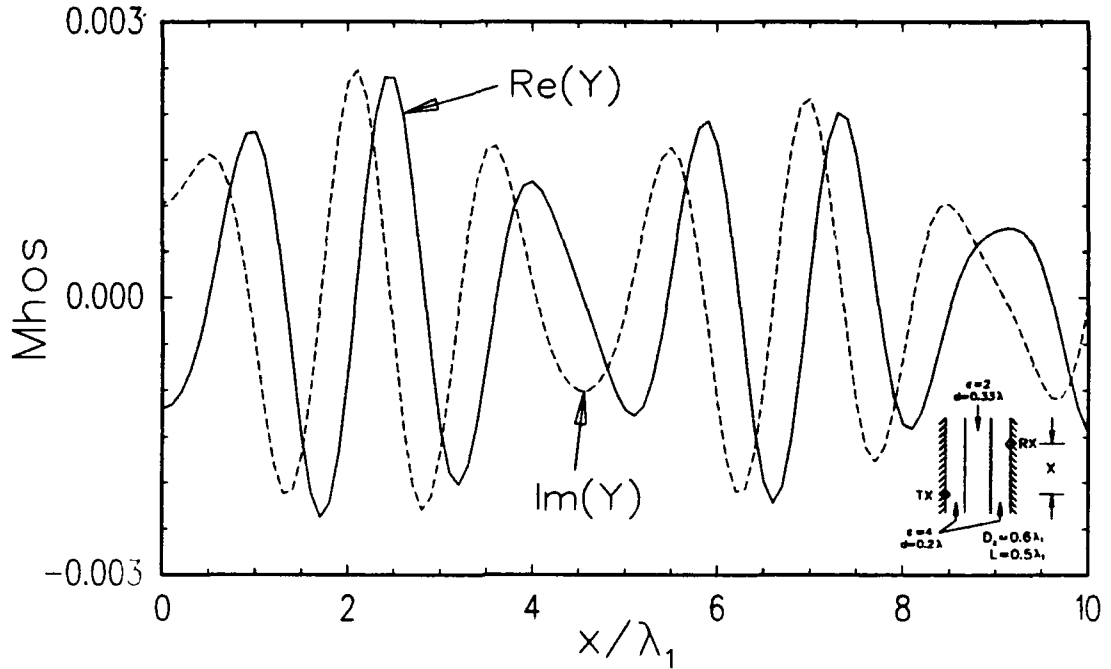


Figure 44: Mutual Admittance using Numerical Implementation of the ASM with Triple Slab Inner Zone Example Geometry, Case B Testing

Finally, to verify that the ASM data in Figure 44 is correct, we again use the technique of spatially adding column-to-column admittance with Floquet phase factors and a Fejer kernel to simulate the mutual scan admittance between two doubly-infinite slot arrays on the opposite ground planes. Using column separation distances of multiples of $D_x = 0.3\lambda_1$, the simulated scan admittance from the ASM data was computed and is plotted in Figure 46. Also plotted is a reference solution from the PMM code, which is adjusted by a factor of -1 to account for the sign convention Henderson used in defining the equivalent scattering currents on two ground planes [3], which is the opposite of the current directions adopted here in Figure 4.

As with the Case A testing scan (rel. Figure 43, since the surface waves are excited beyond $s_x = 0.5$, no resonances in the scan admittance in Figure 46 emerge

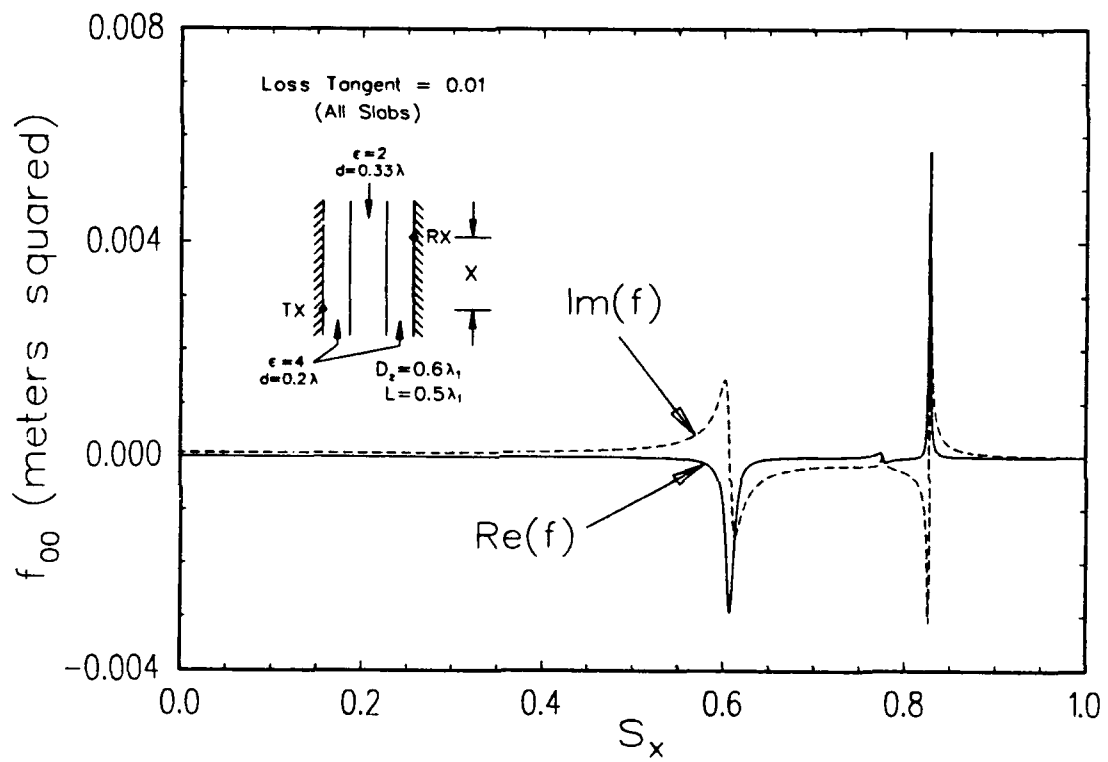


Figure 45: f_{00} Term at $x = 0$ for the Inner Zone Triple Slab Example, Case B Testing

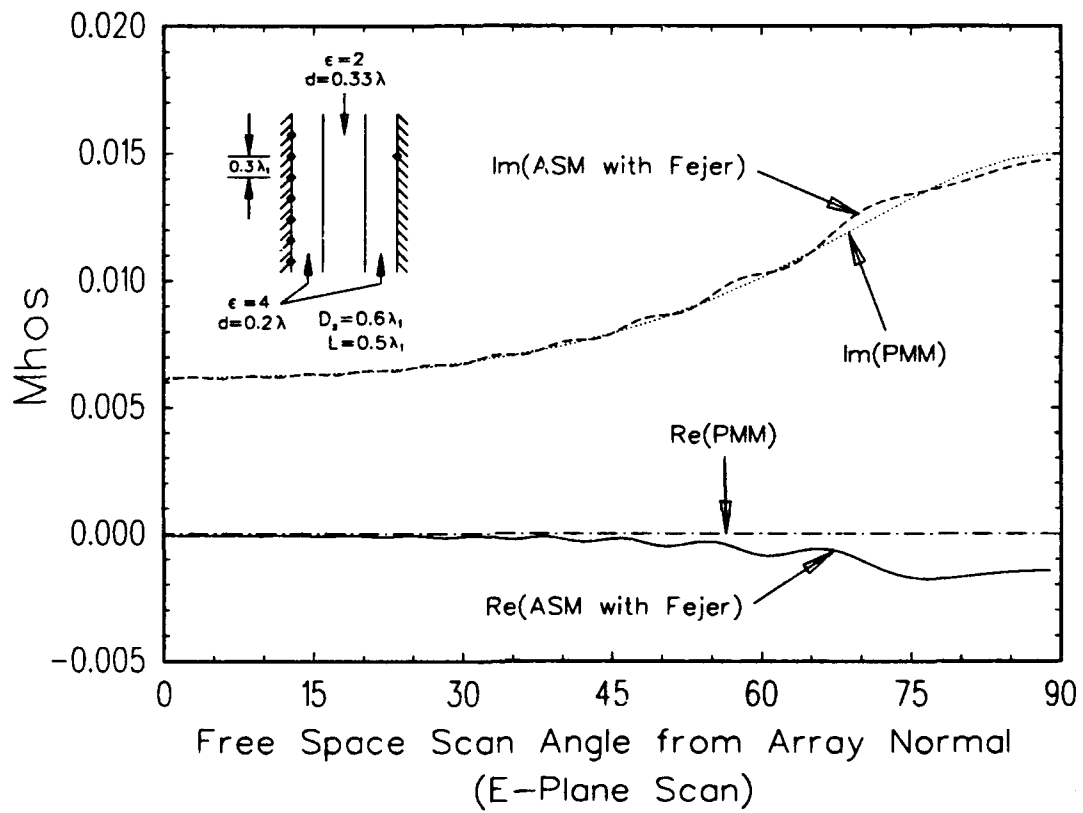


Figure 46: Mutual Scan Admittance between Doubly-Infinite Slot Modes on Opposite Ground Planes for the Inner Zone Triple Slab Example Geometry, $D_z = 0.3\lambda_1$

past the critical angle into the free space scan angles. Also note that the agreement of the scan susceptance between the ASM and PMM calculations is excellent. The scan conductance with the ASM data drifts off zero again, though, due to the loss tangent used and the numerical errors in going through a fairly complicated series of calculations.

CHAPTER III

DIPOLE-TO-DIPOLE COUPLING

In this chapter, we will develop expressions for the self and mutual impedances used in the coupling matrix in Equation (1.23). Specifically, we shall solve Equation (1.32) for transverse dipole column modes. Several solutions will be developed, each of which having regions of applicability and efficiency.

This chapter is divided into two main sections, which concentrate on solutions in a homogeneous space, and solutions for dipole modes located near a ground plane or a dielectric coated ground plane.

3.1 HOMOGENEOUS REGIONS OF SPACE

The first problem considered is that of self or mutual impedances between transverse dipole modes in a homogeneous space. Solutions are developed in both the spectral and spatial domains. The spectral domain solution is generally preferred, though the spatial domain solution offers efficiency advantages for most self impedance and some mutual impedances between closely spaced modes.

3.1.1 Spectral Domain Solution

Consider a column of periodic \hat{x} -directed Hertzian electric current sources, as depicted in Figure 47. Without loss of generality, the "reference element", denoted by the index $m = 0$, is located at the origin. The field observation point is arbitrary.

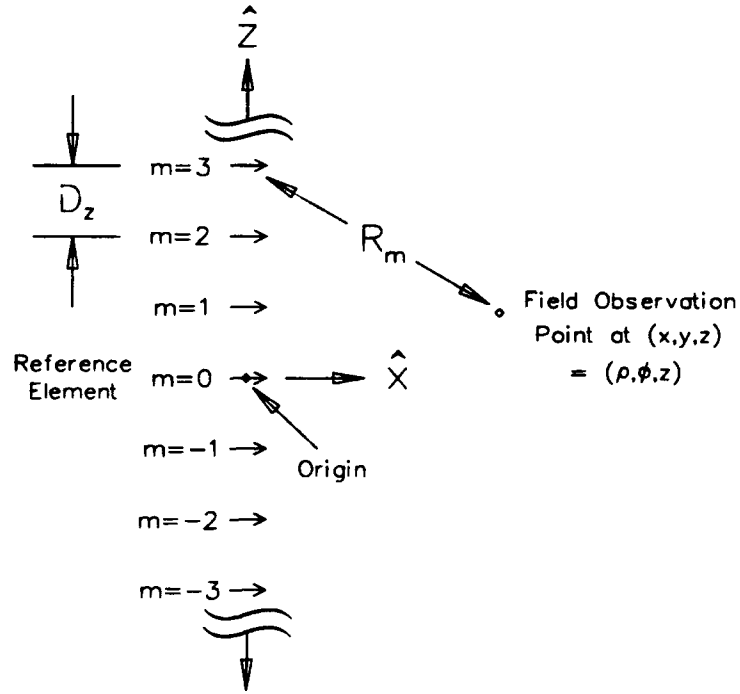


Figure 47: Side View of a Single Column of Periodic \hat{x} -Directed Hertzian Electric Current Sources

The Hertzian sources have equal amplitudes, and a possible linear phase progression governed by Floquet's theorem.

The spectral representation of the total magnetic vector potential at the field observation point is derived by a process similar to that used with \hat{z} -directed magnetic current sources in Equations (2.1) through (2.11). This results in

$$d\bar{A} = \hat{x} \frac{\mu I_0 dx'}{j4D_z} \sum_{n=-\infty}^{\infty} e^{-j\beta z r_z} H_0^{(2)}(\beta r_\rho \rho), \quad (3.1)$$

where r_z and r_ρ are defined by Equations (2.12) and (2.13), and I_0 is the current on the reference element.

The total magnetic field at the observation point is found from the curl [14],

$$d\bar{H} = \frac{1}{\mu} \nabla \times d\bar{A}. \quad (3.2)$$

Substituting the expression in Equation (3.1) and using the irrotational property of \hat{x} , we get

$$d\bar{H} = -\hat{x} \frac{I_0 dx'}{j4D_z} \times \sum_{n=-\infty}^{\infty} \nabla \left[e^{-j\beta z r_z} H_0^{(2)}(\beta r_{\rho\rho}) \right]. \quad (3.3)$$

The gradient in Equation (3.3) is easily performed in cylindrical coordinates. The resulting vector components in $\hat{\rho}$ and $\hat{\phi}$ are then changed to equivalent \hat{x} and \hat{y} components, which are easily crossed with the leading \hat{x} term in Equation (3.3). The convenience of eventually using rectangular components is also noted when fields are to be dotted with the linear directions of testing dipoles in impedance integrals (ref. Equation (1.32)). Thus, the total magnetic field at the field observation point reduces to

$$d\bar{H} = -\frac{\beta I_0 dx'}{j4D_z} \sum_{n=-\infty}^{\infty} e^{-j\beta z r_z} \left[\hat{y} j r_z H_0^{(2)}(\beta r_{\rho\rho}) - \hat{z} r_{\rho}(\sin \phi) H_1^{(2)}(\beta r_{\rho\rho}) \right]. \quad (3.4)$$

The radiated electric field is obtained from Ampere's Law, which is

$$d\bar{E} = \frac{1}{j\omega\epsilon} \nabla \times d\bar{H}. \quad (3.5)$$

This yields

$$d\bar{E} = -\frac{\eta I_0 dx'}{4D_z} \sum_{n=-\infty}^{\infty} \left(\hat{y} \times \nabla \left[j r_z e^{-j\beta z r_z} H_0^{(2)}(\beta r_{\rho\rho}) \right] - \hat{z} \times \nabla \left[r_{\rho}(\sin \phi) e^{-j\beta z r_z} H_1^{(2)}(\beta r_{\rho\rho}) \right] \right) \quad (3.6)$$

where η is the intrinsic impedance of the medium.

Performing the gradients in cylindrical coordinates, and changing the vectors to rectangular directions results in the following rectangular field components:

$$dE_x = \frac{-\eta I_0 dl}{4D_z} \sum_{n=-\infty}^{\infty} e^{-j\beta z r_z} \left[\beta(r_z^2 + r_{\rho}^2 \sin^2 \phi) H_0^{(2)}(\beta r_{\rho\rho}) + \frac{r_{\rho}}{\rho} (\cos 2\phi) H_1^{(2)}(\beta r_{\rho\rho}) \right], \quad (3.7)$$

$$dE_y = \frac{-\eta I_0 dl}{4D_z} \sum_{n=-\infty}^{\infty} e^{-j\beta z r_z} (\sin \phi \cos \phi) \left[\frac{2r_\rho}{\rho} H_1^{(2)}(\beta r_\rho \rho) - \beta r_\rho^2 H_0^{(2)}(\beta r_\rho \rho) \right], \quad (3.8)$$

and

$$dE_z = \frac{-\eta I_0 dl}{4D_z} \sum_{n=-\infty}^{\infty} j\beta r_\rho r_z (\cos \phi) e^{-j\beta z r_z} H_1^{(2)}(\beta r_\rho \rho). \quad (3.9)$$

Now assume the Hertzian dipole array is translated to some point away from the origin, as shown in the XY plane view in Figure 48. The electric field that this translated Hertzian array provides to the observation point is found by simply replacing the ρ and ϕ in Equations (3.7) through (3.9) with ρ_d and ϕ_d , respectively, which are new cylindrical coordinates localized to the displaced Hertzian source. Note that the Hertzian dipoles are still \hat{x} -directed and the z coordinate of the reference element in the displaced array is now arbitrary. Thus, we also have a displacement variable, $z_d = z - z'$, which can be substituted for z in Equations (3.7) through (3.9). Also note that although the \hat{z} component of the electric field is not needed for Equation (1.32), it is presented here for completeness.

Now suppose the elements of the radiating dipole array are of finite length, but still \hat{x} -directed. The total field from the array at the observation point is found by integrating the contributions from an infinite number of Hertzian arrays, weighted by the current shape assumed for the finite length dipoles. Denoting the endpoints of the finite length dipoles by $x' = a$ and $x' = b$, the electric field components are:

$$E_x = -\frac{\eta}{4D_z} \sum_{n=-\infty}^{\infty} e^{-j\beta z_d r_z} \left[\beta r_z^2 p_1 + \beta r_\rho^2 p_2 + r_\rho p_3 \right] \quad (3.10)$$

$$E_y = -\frac{\eta}{4D_z} \sum_{n=-\infty}^{\infty} e^{-j\beta z_d r_z} \left[2r_\rho p_4 - \beta r_\rho^2 p_5 \right] \quad (3.11)$$

$$E_z = -\frac{j\eta\beta}{4D_z} \sum_{n=-\infty}^{\infty} r_\rho r_z p_6 e^{-j\beta z_d r_z}, \quad (3.12)$$

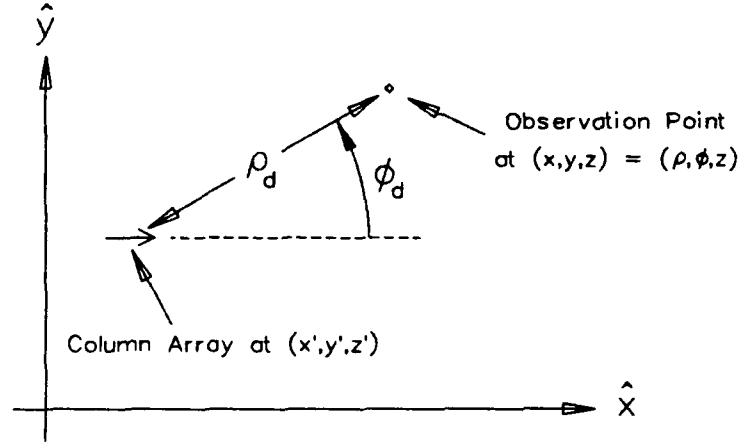


Figure 48: Top View of a Displaced \hat{x} -Directed Hertzian Dipole Array

where we have defined the following functions:

$$p_1 = \int_a^b I(x') H_0^{(2)}(\beta r_\rho \rho_d) dx' \quad (3.13)$$

$$p_2 = \int_a^b I(x') (\sin^2 \phi_d) H_0^{(2)}(\beta r_\rho \rho_d) dx' \quad (3.14)$$

$$p_3 = \int_a^b I(x') \frac{\cos 2\phi_d}{\rho_d} H_1^{(2)}(\beta r_\rho \rho_d) dx' \quad (3.15)$$

$$p_4 = \int_a^b I(x') \frac{\sin \phi_d \cos \phi_d}{\rho_d} H_1^{(2)}(\beta r_\rho \rho_d) dx' \quad (3.16)$$

$$p_5 = \int_a^b I(x') (\sin \phi_d \cos \phi_d) H_0^{(2)}(\beta r_\rho \rho_d) dx' \quad (3.17)$$

$$p_6 = \int_a^b I(x') (\cos \phi_d) H_1^{(2)}(\beta r_\rho \rho_d) dx'. \quad (3.18)$$

It should be noted that the current, $I(x')$, which is used in the integrals for p_1 through p_6 is the assumed current shape for the reference dipole of the infinite

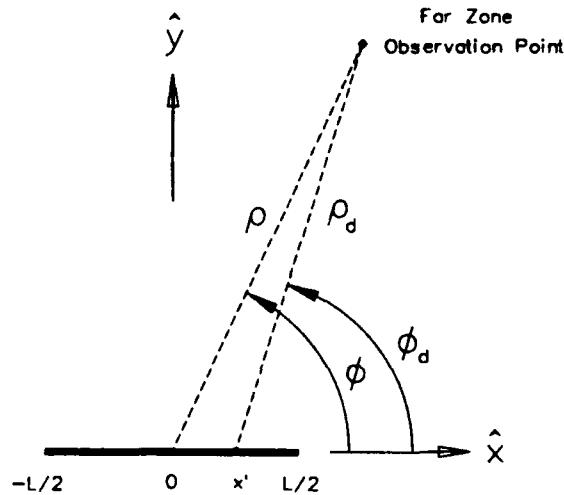


Figure 49: Top View of Far Zone Geometry for a Radiating Column of Periodic Transverse Dipoles

column array. Currents on all other elements are of the same form, with only a linear phase adjustment from Floquet's theorem.

The functions p_1 through p_6 are in a sense, pattern functions for the assumed current shape. Thus the motivation for designating them with the variable p . Unfortunately, field expressions cannot be derived with a single pattern function of the form used for the plane wave expansion from doubly-infinite arrays (ref. Equation (2.62)). Such expressions for singly-infinite modes can only be derived when the elements are aligned in the direction of the infinite direction (\hat{z}), which was the case with the axial slots in Chapter 2. Furthermore, the pattern functions p_1 through p_6 can only be found in closed form using far zone approximations, which are developed as follows.

Consider the far zone geometry of a radiating transverse dipole column array, as shown in Figure 49.

We use the leading term of the asymptotic series expansion for the Hankel functions of arbitrary order, which is [28]:

$$H_\nu^{(2)}(\beta r_{\rho\rho}) \sim \sqrt{\frac{j2}{\pi\beta r_{\rho\rho}}} j^\nu e^{-j\beta r_{\rho\rho}}. \quad (3.19)$$

For amplitude purposes, we make the approximations $\rho_d \approx \rho$ and $\phi_d \approx \phi$, for the entire length of the dipole mode. For phase purposes, we carry the slightly better approximation, $\rho_d \approx \rho - x' \cos \phi$. Using these far zone approximations in Equations (3.13) through (3.18), the pattern functions become:

$$p_1 \approx P_{fz} \cdot C \quad (3.20)$$

$$p_2 \approx P_{fz} \cdot C \cdot \sin^2 \phi \quad (3.21)$$

$$p_3 \approx P_{fz} \cdot C \cdot \frac{j \cos 2\phi}{\rho} \quad (3.22)$$

$$p_4 \approx P_{fz} \cdot C \cdot \frac{j \sin \phi \cos \phi}{\rho} \quad (3.23)$$

$$p_5 \approx P_{fz} \cdot C \cdot \sin \phi \cos \phi \quad (3.24)$$

$$p_6 \approx P_{fz} \cdot C \cdot j \cos \phi, \quad (3.25)$$

where the constant C is

$$C = \sqrt{\frac{j2}{\pi\beta r_{\rho\rho}}} e^{-j\beta r_{\rho\rho}}, \quad (3.26)$$

and the far zone pattern integral is

$$P_{fz} = \int_{-L/2}^{L/2} I(x') e^{j\beta r_{\rho} x' \cos \phi} dx'. \quad (3.27)$$

This pattern function is in agreement with the P^t function defined in Equation (2.62), thus it may be found in closed form for many common current shapes. For example, consider the piecewise sinusoidal current,

$$I(x') = \frac{\sin \left[\beta \left(\frac{L}{2} - |x'| \right) \right]}{\sin \left(\frac{\beta L}{2} \right)}. \quad (3.28)$$

The resulting far zone pattern function is

$$P_{fz}(PWS) = \frac{2}{\sin(\frac{\beta L}{2})} \left[\frac{\cos(\frac{\beta L}{2}) - \cos(\beta r_\rho \frac{L}{2} \cos \phi)}{\beta(r_\rho^2 \cos^2 \phi - 1)} \right]. \quad (3.29)$$

When $|r_\rho \cos \phi| = 1$, L'Hopital's Rule is used on Equation (3.29) to produce $P_{fz} = L/2$.

Finally, one should note that the asymptotic solution for the fields needs only to be carried for the propagating cylindrical wave modes of Equations (3.10) through (3.12). These modes are identified by having a real valued directional parameter, r_ρ . For most cases, this corresponds to only the $n = 0$ term.

A comparison was made of the asymptotic solution for the radiated electric field versus the more rigorous solution of numerically evaluating the p integrals and including enough evanescent cylindrical wave modes from Equations (3.10) through (3.12) for convergence. The numerical integration was performed with a 16 point Gaussian quadrature procedure [28]. A typical radiating transverse dipole mode was chosen with $L = \lambda/3$ and $D_z = \lambda/3$. The dipoles were \hat{x} -directed and the reference dipole was centered at the origin. A piecewise sinusoidal current was assumed on the dipole. In the solution comparisons, an error parameter was defined by

$$Error = \left| \frac{E_w^{asy} - E_w^{rig}}{E_w^{rig}} \right| \times 100\%, \quad (3.30)$$

where the subscript w denotes either an \hat{x} , \hat{y} , or \hat{z} field component. The computation time for each method was also noted.

Figure 50 shows the error in using the asymptotic solution for the \hat{x} component of the electric field from the example array, as seen along an observation path on the \hat{x} axis (at $z = 0$). As expected, the error decreases as the observation point moves away from the array. The ratio of CPU times for the methods is also plotted. Note that the asymptotic solution is generally about 40 times faster than the rigorous solution.

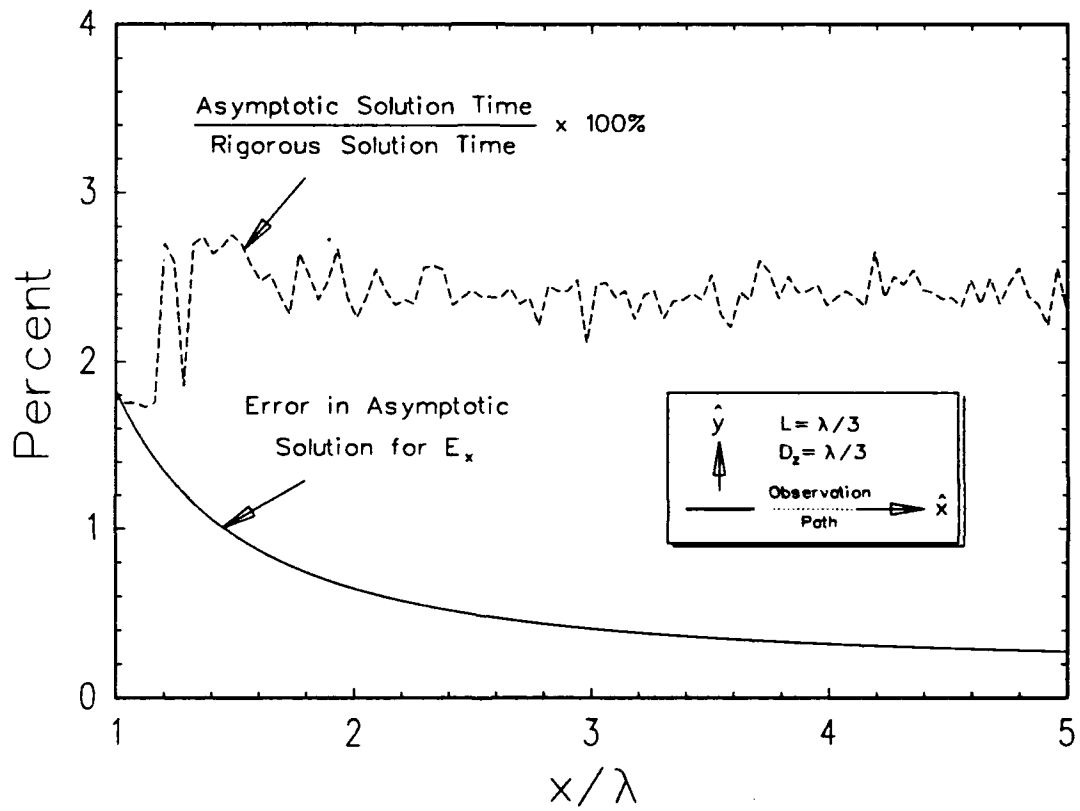


Figure 50: Error in Asymptotic Solution of E_x from Example Dipole Array in Free Space along an Axial Path - $L = D_z = \lambda/3$, $z = 0$, $s_z = 0$

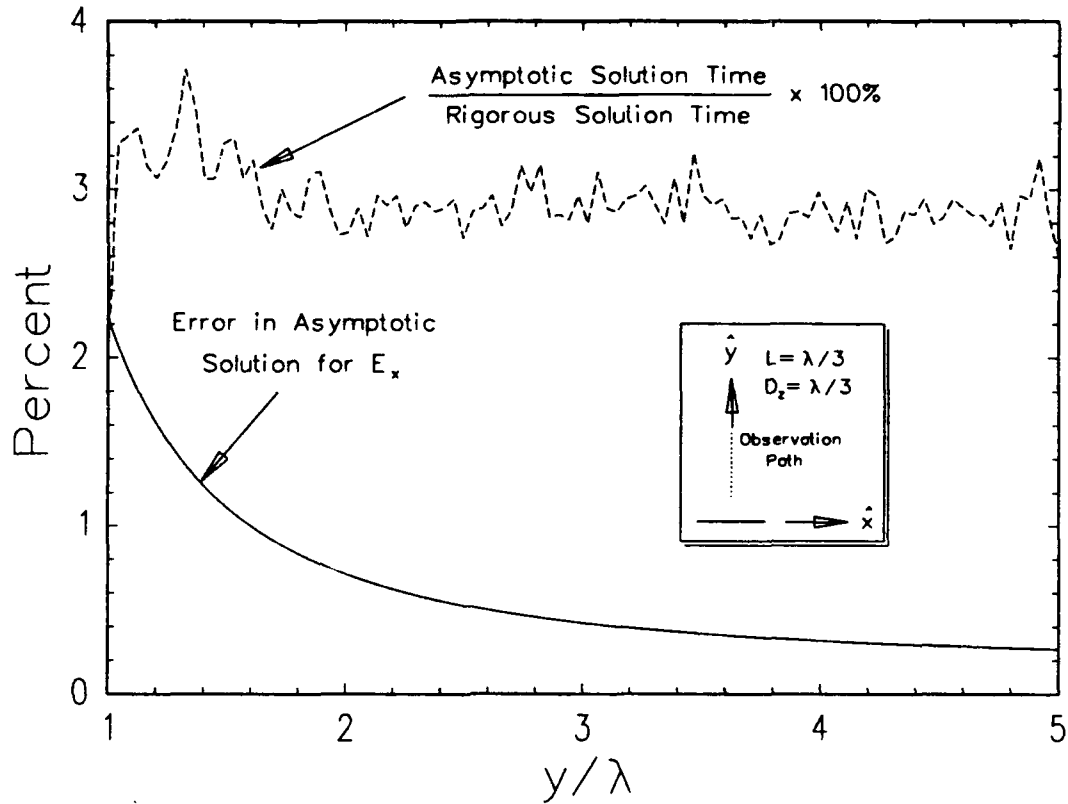


Figure 51: Error in Asymptotic Solution of E_x from Example Dipole Array in Free Space along a Transverse Path - $L = D_z = \lambda/3$, $z = 0$, $s_z = 0$

Figure 51 shows similar asymptotic error and time savings data for the example radiating dipole array along an observation path on the \hat{y} axis (at $z = 0$). Again, only the \hat{x} component of the field is used.

Based on Figures 50 and 51, one may be tempted to declare that a good rule of thumb is to use the asymptotic solution when the observation point is beyond about 2.5λ from the center of the radiating mode. To test this, both field components were found along a circumferential path at the radius of 2.5λ . The error in the asymptotic solution is plotted in Figure 52. Note that the error in E_x peaks at an angle between the \hat{x} and \hat{y} axes. The error in E_y is maximum on the \hat{x} axis, but this

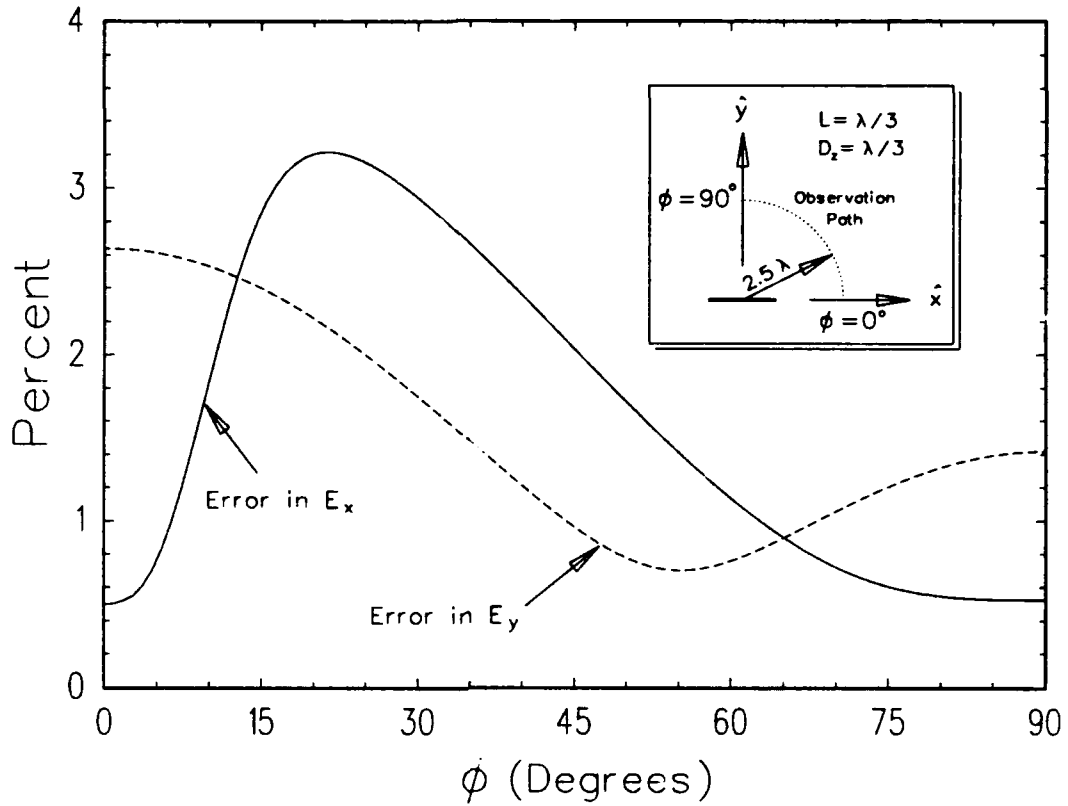


Figure 52: Error in Asymptotic Solution of E_x and E_y from Example Dipole Array in Free Space along a Circumferential Path at $\rho = 2.5\lambda$, $L = D_z = \lambda/3$, $z = 0$, $s_z = 0$

is of little concern since this field component is very small compared to the other at that location.

With the procedure to find the electric field in the spectral domain developed, the mutual impedance between two transverse dipole modes in a homogeneous medium may be expressed. Consider the geometry shown in Figure 53. Without loss of generality, it depicts an XY coordinate system which is centered with the center of the reference dipole in the transmitting array. The reference dipole in the transmitting array has a z coordinate of zero. The transmitting dipoles are aligned

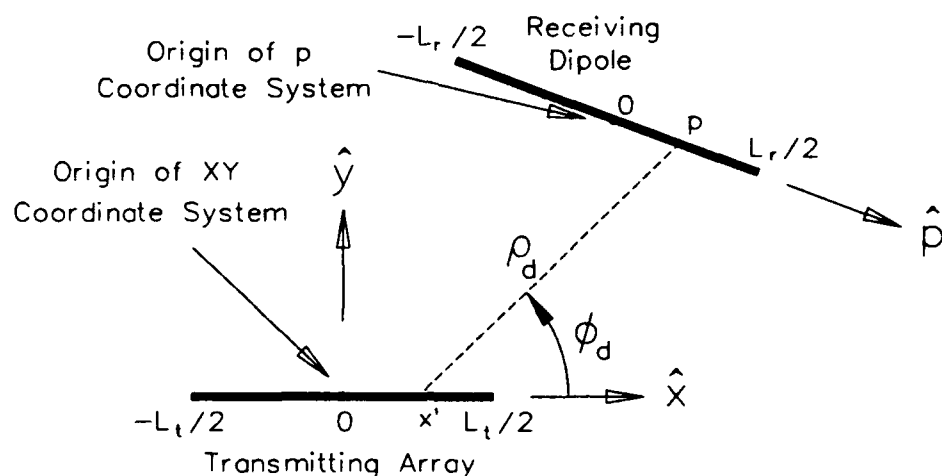


Figure 53: Transverse Dipole Array Coupling Geometry in Free Space

with \hat{x} and the receiving dipole (the reference element of its array) is \hat{p} oriented with an arbitrary location (including a possible non-zero z coordinate).

Substituting the spectral domain solution for the electric field into Equation (1.32), we get the following mutual impedance expression:

$$Z = \frac{\eta}{4D_z} \sum_{n=-\infty}^{\infty} e^{-j\beta z r_z} \cdot \int_{-L_r/2}^{L_r/2} [(\beta r_z^2 p_1 + \beta r_\rho^2 p_2 + r_\rho p_3)(\hat{x} \cdot \hat{p}) + (2r_\rho p_4 - \beta r_\rho^2 p_5)(\hat{y} \cdot \hat{p})] \cdot I^{test}(p) dp, \quad (3.31)$$

where p_1 through p_5 are the integrals defined in Equations (3.13) through (3.17) over the limits $-L_t/2$ to $L_t/2$. Note that the variables ρ_d and ϕ_d for the integrals are depicted in Figure 53. When the modes are spaced sufficiently far apart¹, the asymptotic expressions in Equations (3.20) through (3.24) may be used, along with a numerical integration along the testing filament using very few Gaussian quadrature

¹Sufficiently far apart is about 2.5λ center-to-center spacing along the \hat{x} or \hat{y} axes. For more general locations, a spacing of about 5λ is adequate.

points. The testing current, $I^{test}(p)$, is chosen for the receiving dipole, and is often of the same form as the transmitting current for that mode (i.e., the “quasi-Galerkin” method referred to in Chapter 1).

3.1.2 Spatial Domain Solution

When piecewise sinusoidal basis and testing functions are used, a practical spatial domain solution for the dipole column-to-column coupling can be formed. It is based on the closed form expressions for the fields (even in the near zone) radiated by a single dipole with such a current. These expressions were first derived by Carter [22] for a half wavelength dipole, and extended by Brown [23] for piecewise sinusoids of arbitrary length. From Brown’s solution, we can form the electric field from a single piecewise sinusoidal as the sum of weighted spherical wave contributions from the center and each endpoint of the dipole.

Consider the geometry depicted in Figure 54. It shows two single dipoles (no arrays) from the view of the $+\hat{z}$ axis. The transmitting dipole is centered on the origin and is \hat{x} -directed. The receiving dipole is arbitrarily located (including a possible non-zero z coordinate) and aligned in a direction \hat{p} which is some direction perpendicular to \hat{z} .

From Brown’s solution, the electric field at any point (x, y, z) from the transmitting piecewise sinusoidal electric current has the components:

$$E_x = -\frac{j\eta}{4\pi \sin(\frac{\beta L_t}{2})} \left[\frac{e^{-j\beta R_1}}{R_1} + \frac{e^{-j\beta R_2}}{R_2} - 2 \cos(\frac{\beta L_t}{2}) \frac{e^{-j\beta R}}{R} \right] \quad (3.32)$$

$$E_y = \frac{j\eta y}{4\pi(y^2 + z^2) \sin(\frac{\beta L_t}{2})} \left[\left(x - \frac{L_t}{2}\right) \frac{e^{-j\beta R_1}}{R_1} + \left(x + \frac{L_t}{2}\right) \frac{e^{-j\beta R_2}}{R_2} - 2x \cos(\frac{\beta L_t}{2}) \frac{e^{-j\beta R}}{R} \right] \quad (3.33)$$

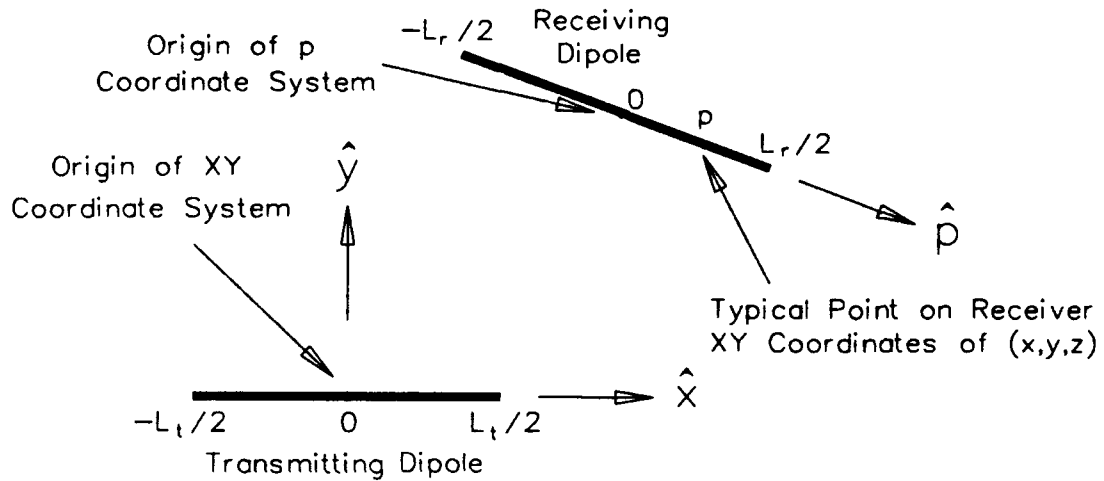


Figure 54: Single Dipole-to-Dipole Coupling Geometry - Top View

$$E_z = \frac{j\eta z}{4\pi(y^2 + z^2)\sin(\frac{\beta L_t}{2})} \left[\left(x - \frac{L_t}{2}\right) \frac{e^{-j\beta R_1}}{R_1} + \left(x + \frac{L_t}{2}\right) \frac{e^{-j\beta R_2}}{R_2} - 2x \cos\left(\frac{\beta L_t}{2}\right) \frac{e^{-j\beta R}}{R} \right] \quad (3.34)$$

where the distances are defined by

$$R = \sqrt{x^2 + y^2 + z^2} \quad (3.35)$$

$$R_1 = \sqrt{\left(x - \frac{L_t}{2}\right)^2 + y^2 + z^2} \quad (3.36)$$

$$R_2 = \sqrt{\left(x + \frac{L_t}{2}\right)^2 + y^2 + z^2} \quad (3.37)$$

The electric field components in Equations (3.32) through (3.34) are in units of volts/meter, with a hidden factor of 1 ampere accounting for the normalization of the piecewise sinusoidal current. Although the \hat{z} component of the electric field is not needed for the impedance calculations with $\hat{p} \perp \hat{z}$, it is presented in the above for completeness.

The mutual impedance between the two dipoles in Figure 54 is found by using the field components in Equations (3.32) and (3.33) in Equation (1.32). This gives

the following:

$$\begin{aligned}
Z_{d-d} = & \int_{-\frac{L_r}{2}}^{\frac{L_r}{2}} \left[\frac{j\eta}{4\pi \sin(\frac{\beta L_t}{2})} \left[\frac{e^{-j\beta R_1}}{R_1} + \frac{e^{-j\beta R_2}}{R_2} - 2 \cos\left(\frac{\beta L_t}{2}\right) \frac{e^{-j\beta R}}{R} \right] (\hat{x} \cdot \hat{p}) \right. \\
& - \frac{j\eta y}{4\pi(y^2 + z^2) \sin(\frac{\beta L_t}{2})} \left[\left(x - \frac{L_t}{2}\right) \frac{e^{-j\beta R_1}}{R_1} + \left(x + \frac{L_t}{2}\right) \frac{e^{-j\beta R_2}}{R_2} \right. \\
& \left. \left. - 2x \cos\left(\frac{\beta L_t}{2}\right) \frac{e^{-j\beta R}}{R} \right] (\hat{y} \cdot \hat{p}) \right] \cdot \frac{\sin[\beta(\frac{L_r}{2} - |p|)]}{\sin(\frac{\beta L_r}{2})} dp. \quad (3.38)
\end{aligned}$$

Note that this expression is not in the form of a nine term expansion of sine and cosine integrals as was used with slots in the spatial domain (ref. Equation (2.40)), because the dipoles are not necessarily parallel to each other.

To get the mutual impedance between column modes of periodic dipoles with inter-element spacings, D_z , one merely spatially adds the contributions of the infinite number of dipoles in the transmitting array to the same testing dipole (the reference element) in the receiving array. Suppose the transmitting dipole in Figure 54 is extended periodically in \hat{z} with D_z spacing and a Floquet phasing factor governed by a plane wave \hat{z} component of s_z (see Equation (2.4)). The mutual admittance between column modes of the transverse dipoles in a homogeneous medium with piecewise sinusoidal currents in the spatial domain is:

$$\begin{aligned}
Z = & \sum_{m=-\infty}^{\infty} e^{-j\beta m D_z s_z} \int_{-\frac{L_r}{2}}^{\frac{L_r}{2}} \left[\frac{j\eta}{4\pi \sin(\frac{\beta L_t}{2})} \left[\frac{e^{-j\beta R_{1m}}}{R_{1m}} + \frac{e^{-j\beta R_{2m}}}{R_{2m}} \right. \right. \\
& \left. \left. - 2 \cos\left(\frac{\beta L_t}{2}\right) \frac{e^{-j\beta R_{0m}}}{R_{0m}} \right] (\hat{x} \cdot \hat{p}) - \frac{j\eta y}{4\pi[y^2 + (z - m D_z)^2] \sin(\frac{\beta L_t}{2})} \right. \\
& \cdot \left[\left(x - \frac{L_t}{2}\right) \frac{e^{-j\beta R_{1m}}}{R_{1m}} + \left(x + \frac{L_t}{2}\right) \frac{e^{-j\beta R_{2m}}}{R_{2m}} - 2x \cos\left(\frac{\beta L_t}{2}\right) \frac{e^{-j\beta R_{0m}}}{R_{0m}} \right] (\hat{y} \cdot \hat{p}) \left. \right] \\
& \cdot \frac{\sin[\beta(\frac{L_r}{2} - |p|)]}{\sin(\frac{\beta L_r}{2})} dp, \quad (3.39)
\end{aligned}$$

where

$$R_{0m} = \sqrt{x^2 + y^2 + (z - mD_z)^2} \quad (3.40)$$

$$R_{1m} = \sqrt{\left(x - \frac{L_t}{2}\right)^2 + y^2 + (z - mD_z)^2} \quad (3.41)$$

$$R_{2m} = \sqrt{\left(x + \frac{L_t}{2}\right)^2 + y^2 + (z - mD_z)^2}. \quad (3.42)$$

The spatial sum in Equation (3.39) tends to oscillate about the convergence point as successive pairs of dipole terms (corresponding to $m = \pm$ some value) are added. The Fejer kernel, spiral average, and Shanks' transformations, which are described in Appendix A, may be applied to accelerate the convergence.

It is desirable to compare the convergence characteristics of the spectral and spatial domain solutions for the transverse dipole mode impedances derived in this and the previous section. Unfortunately, numerical integrations are required for the spectral domain solution and when $\hat{p} \neq \hat{x}$, for the spatial domain solution. Thus, in addition to the single infinite sum, a numerical integration must be performed at each sum index. This makes convergence a difficult quantity to define, since two dimensions of addition are in effect. Therefore, it is impossible to define a minimal "route" one can take in either domain until one reaches a desired accuracy, unlike the one dimensional closed form sums explored with the slots in Figure 7.

Although a rigorous convergence comparison cannot be made, a reasonable comparison can be made, by accepting some reasonable standards of numerical integration at each index of the summations, which should be very accurate. This was done for example arrays with dipole lengths of $L = \lambda/3$, inter-element spacings of $D_z = \lambda/3$, dipole radii of $L/40$, and no z offset between the reference element of the transmitting mode and the receiving element. The Floquet phase parameter, s_z , was also set to zero. The receiving element was aligned parallel to the transmitting element, and two pattern cuts were examined. The first cut used a separation in the

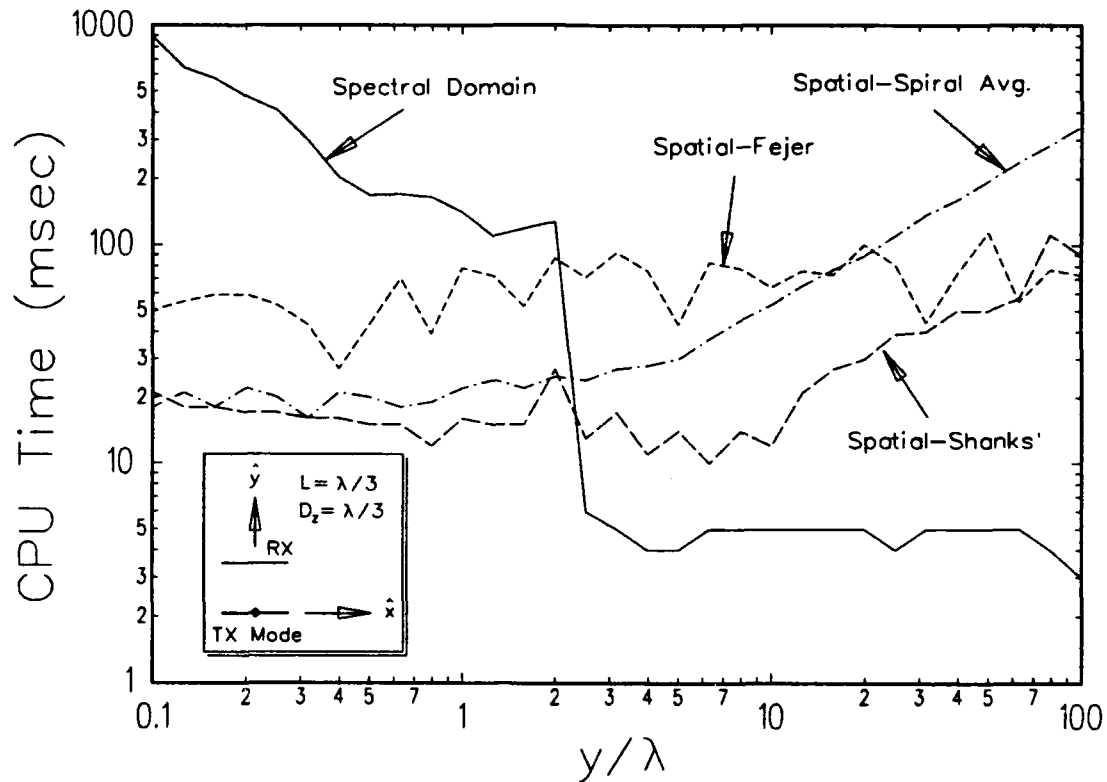


Figure 55: Comparison of Calculation Times by Four Solution Methods for Mutual Impedance versus Separation Distance y - Piecewise Sinusoidal Transverse Dipole Modes in Free Space with $L = D_z = \lambda/3$, $z = 0$, $s_z = 0$

\hat{y} direction. The CPU time to get "convergence" using the spectral domain solution and spatial domain solution (assisted by each acceleration technique) is plotted in Figure 55.

The sharp decrease in CPU time for the spectral domain beyond 2.5λ reflects the switch from the rigorous p integrals to the asymptotic closed form solution. It is only when that solution is used when the spectral domain becomes faster than the spatial domain. Note that the Shanks' transformation method is generally the best for the spatial domain.

The experiment was repeated for a pattern cut along the \hat{x} axis, using a wire radius separation in y . The results are plotted in Figure 56. Note that the spatial

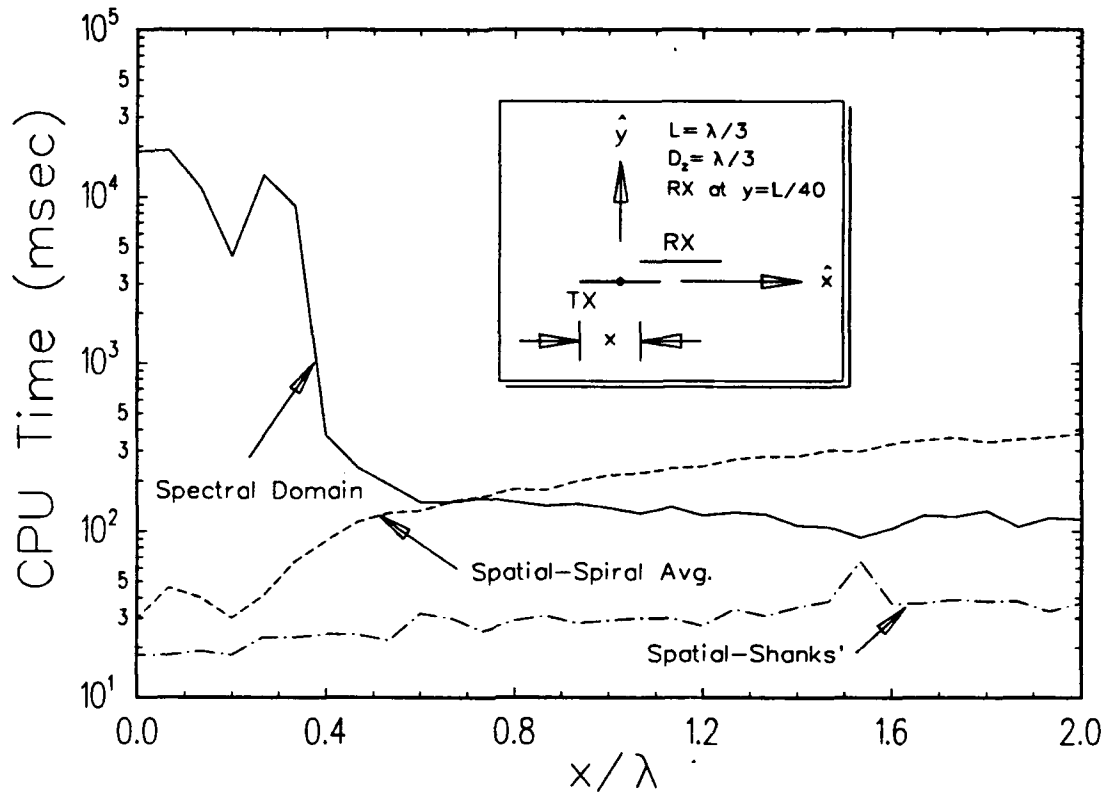


Figure 56: Comparison of Calculation Times by Four Solution Methods for Mutual Impedance versus Separation Distance x - Piecewise Sinusoidal Transverse Dipole Modes in Free Space with $L = D_z = \lambda/3$, $z = 0$, $y = L/40$, $s_z = 0$

domain with Shanks' transformation is superior, although the data does not extend to $x = 2.5\lambda$, where the asymptotic form of the spectral domain becomes extremely fast.

As a general rule of thumb, the spatial domain solution with the Shanks' transform acceleration is superior for all mutual impedance calculations involving center-to-center modal spacings of less than 2.5λ , and the asymptotic form of the spectral domain solution is superior for all other mutual impedance calculations in free space.

Next, we present the mutual impedance data associated with the observation paths used to produce the CPU data in Figures 55 and 56. Although the data from

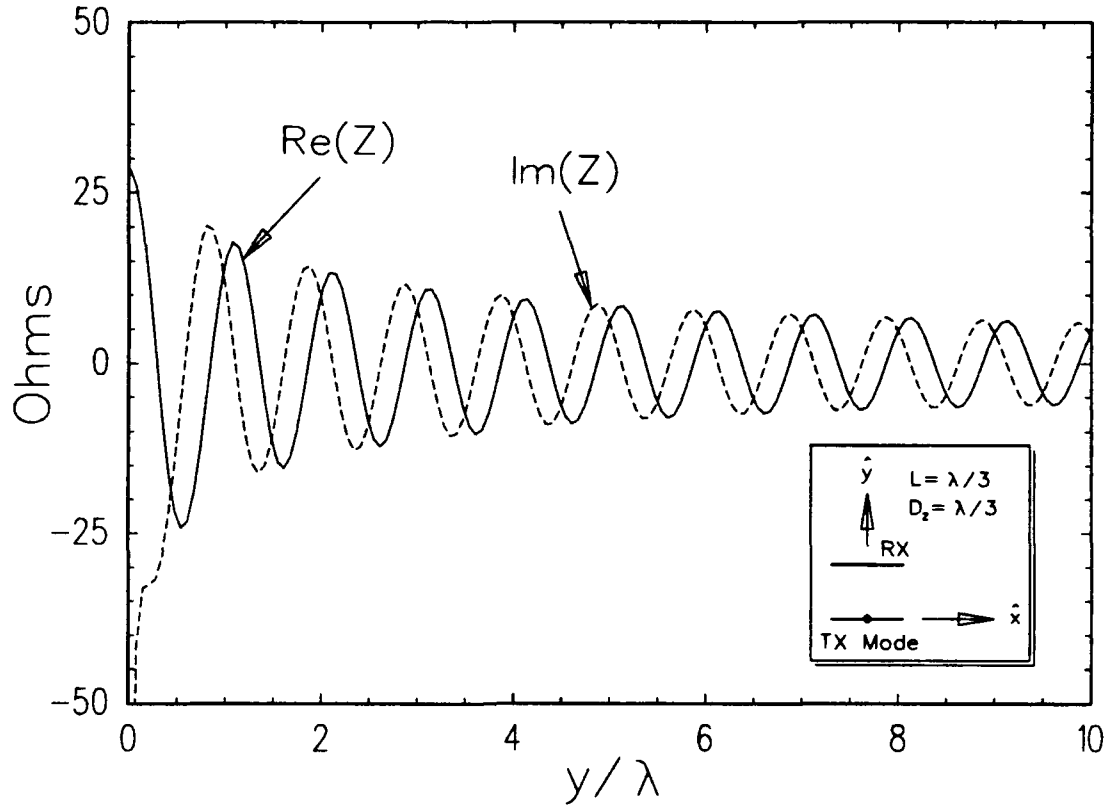


Figure 57: Mutual Impedance Between Piecewise Sinusoidal Transverse Dipole Modes in Free Space along a \hat{y} Axis Cut with $L = D_z = \lambda/3$, $z = 0$, $s_z = 0$

each of the methods is almost indistinguishable, we present the data from the spatial domain with Shanks' transformation. It is plotted in Figures 57 and 58. The data in the \hat{y} axis pattern cut tends to be sinusoidal with an amplitude which decays approximately as $1/\sqrt{y}$. This is as one expects with the asymptotic spectral domain solution predicting a single Hankel function dominance. The mutual reactance tends to go to $-\infty$ as y goes to zero, as one expects with the dipole lengths being shorter than that of primary resonance.

In Figure 58, we see the mutual impedance data (from the spatial-Shanks' method) along the \hat{x} axis pattern cut, with a wire radius ($= L/40$) of separation in y . Note the complicated behavior of the mutual reactance in the near zone as the

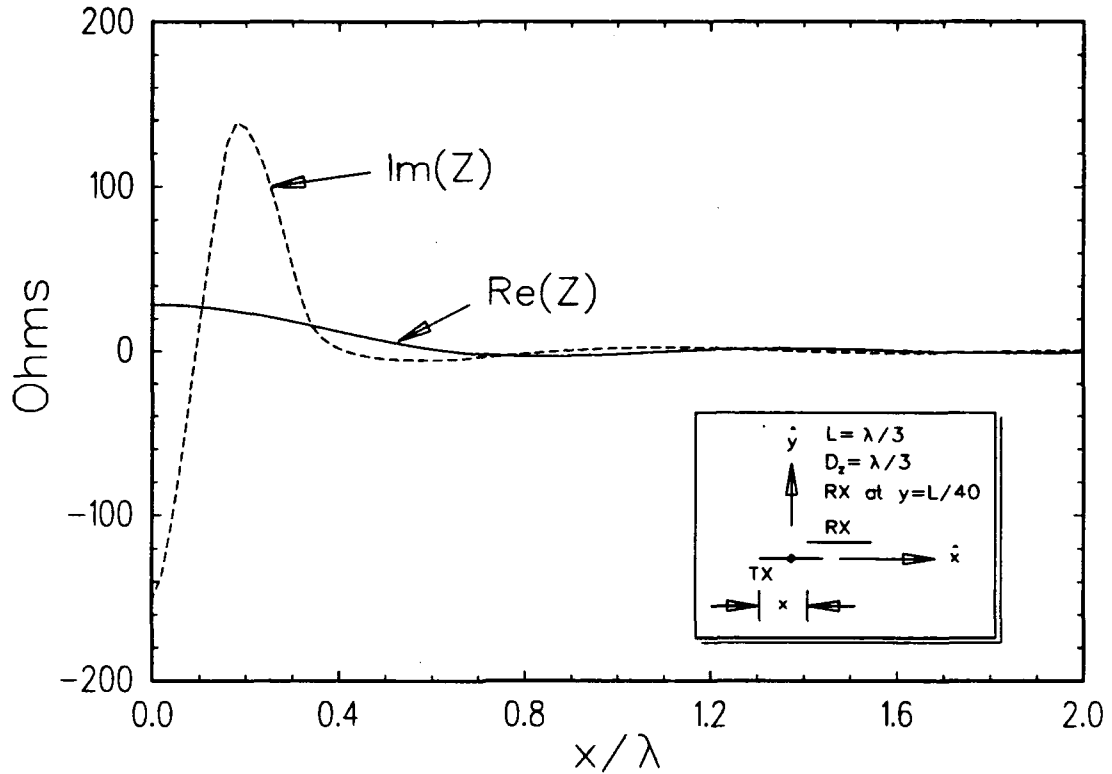


Figure 58: Mutual Impedance Between Piecewise Sinusoidal Transverse Dipole Modes in Free Space along an \hat{x} Axis Cut with $L = D_z = \lambda/3$, $z = 0$, $y = L/40$, $s_z = 0$

coupling changes from being highly capacitive to highly inductive. Beyond about 1λ , the data becomes sinusoidal with approximately a $1/\sqrt{x}$ decay. Although this data appears insignificant on the scale used in Figure 58, it is actually on the order of 1 ohm, which is not quite negligible for a good moment method solution.

To verify the accuracy of the methods used in this section, the self-impedance of a scanning non-skewed doubly-infinite array of dipoles was computed by spatially adding 101 column-to-column mutual impedances with a Floquet phasing factor and the Fejer kernel. The PMM code [3] was used for a reference data source. Since PMM is limited to use on planar arrays, the dipoles were all \hat{x} -directed with the array in the XZ plane. The dipole lengths and inter-element spacings in \hat{z} were each $\lambda/3$,

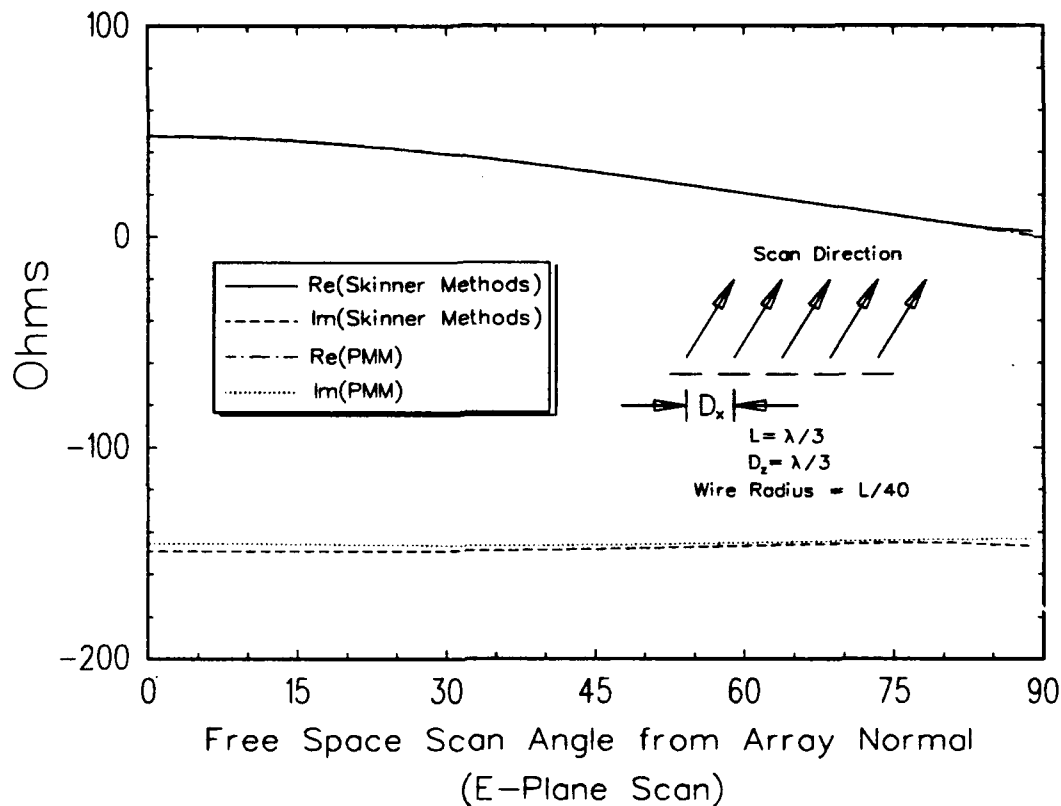


Figure 59: Scan Impedance of a Doubly-Infinite Array of \hat{x} -Directed Dipoles in Free Space - $L = D_z = \lambda/3$, $D_x = 0.4\lambda$, Wire Radius = $L/40$

the inter-column spacing was $D_x = 0.4\lambda$, and the wire radius was $L/40$. In Figure 59, we present the scan impedance data for this free space problem.

The data marked "Skinner Methods" in Figure 59 is computed by constructing the planar scan from column-to-column mutual impedances with the Floquet phasing factors and Fejer kernel. The column impedances are computed with the spatial domain method with Shanks' transformation for column separations in \hat{x} less than 2λ . From $2\lambda < x < 5\lambda$, the spectral domain solution is used. Beyond 5λ , the asymptotic pattern functions are used in the spectral domain solution. This produces scan impedance data which is very close to that predicted by PMM, except for a slight linear shift in the reactive term. This shift is most likely caused by PMM's method

of testing self-impedance, which places the testing filament exactly in the plane of the array for the propagating plane wave mode. With the "Skinner Methods" data, the testing filament was always placed a wire radius away from the plane of the array.

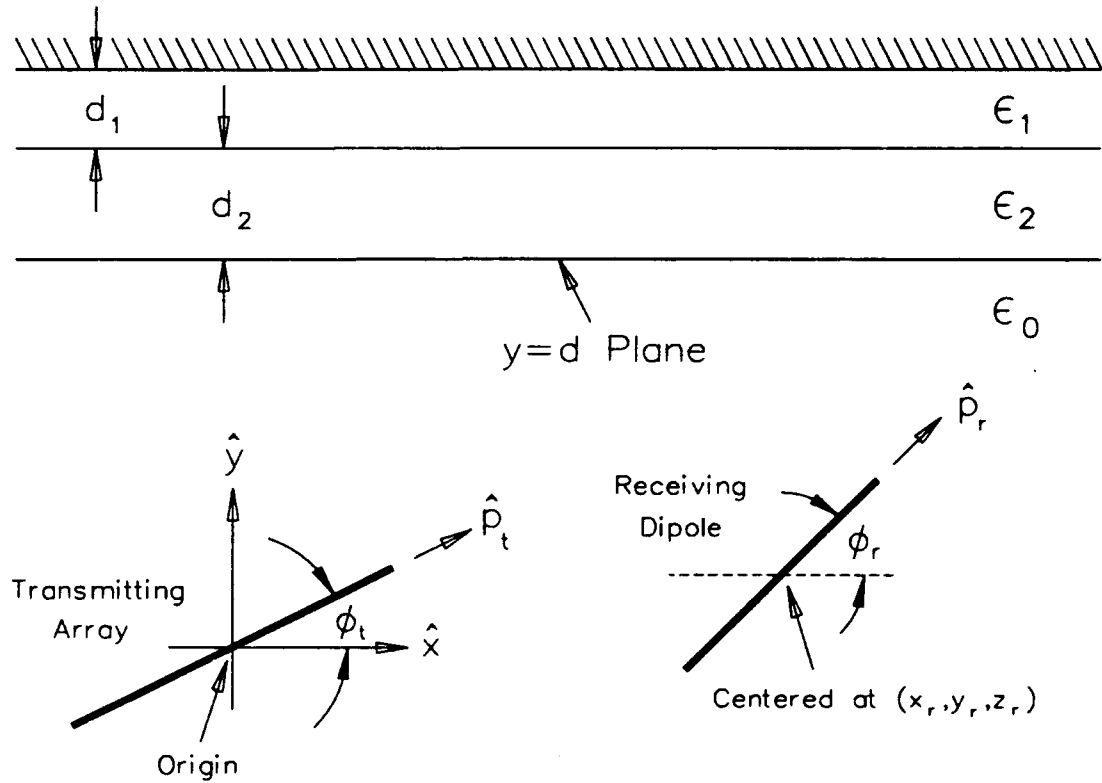


Figure 60: Geometry of Transverse Dipole Mode Coupling in the Vicinity of a Dielectric Clad Ground Plane

3.2 DIPOLES NEAR A DIELECTRIC CLAD GROUND PLANE

In this section, we consider the self and mutual impedances between transverse dipole modes which exist in the vicinity of a dielectric clad ground plane. The geometry is shown in Figure 60. Although it only depicts two dielectric layers on the ground plane, the number of such layers shall be considered arbitrary.

In Figure 60, the reference element of the transmitting array is centered at the origin, while the receiving element is centered at the coordinate (x_r, y_r, z_r) . Free space fills the half-space associated with $y < d$. Although not shown, the total lengths of the dipoles in the transmitting array are L_t and the total length of the receiving dipole is L_r .

The mutual coupling between the modes may be solved in several ways. For example, the Array Scanning Method (ASM) may be used, as it was in Chapter 2, with T factors describing the stratified media for the complete coupling. However, with both the dipole modes having arbitrary orientations (subject to $\hat{p} \perp \hat{z}$), the "artificial" doubly infinite arrays will be non-planar, and this solution will require nested double integrals, as noted by English [29]. Although Andre [30] developed an elegant method to overcome the need to evaluate such nested integrals in free space, his method cannot be applied with the dielectric clad ground plane.

To obviate the need to evaluate cumbersome nested integrals, the ASM may be applied here to only the component of the mutual impedance which arises from the reflections off the dielectric clad ground plane. That is, we can separate the mutual impedance into a direct (free space) component and a component encompassing all reflected energy. The techniques described in the previous section can be used to efficiently find the direct term (denoted Z_{dir}), while the ASM can be used to get the reflected term (denoted Z_{ref}).

By extension of Equation (B.9), the reflected term in the mutual impedance for the transverse dipole arrays in Figure 60 is:

$$Z_{ref} = \frac{D_x}{\lambda_0} \int_{-\frac{\lambda_0}{2D_x}}^{\frac{\lambda_0}{2D_x}} Z_{ref,A} ds_x, \quad (3.43)$$

where $Z_{ref,A}$ is the reflected impedance term from an "artificially created" doubly-infinite array of transmitting dipoles, as depicted in Figure 61². Note that the zero subscript on λ denotes that it is in free space. Also note that the outer dielectric

²Figure 61 depicts a portion of the receiving dipole inside the planes containing the transmitting dipoles. In general, the receiving dipole's position is completely arbitrary - it may be entirely on either side of the transmitting array, or straddling the array, as shown.

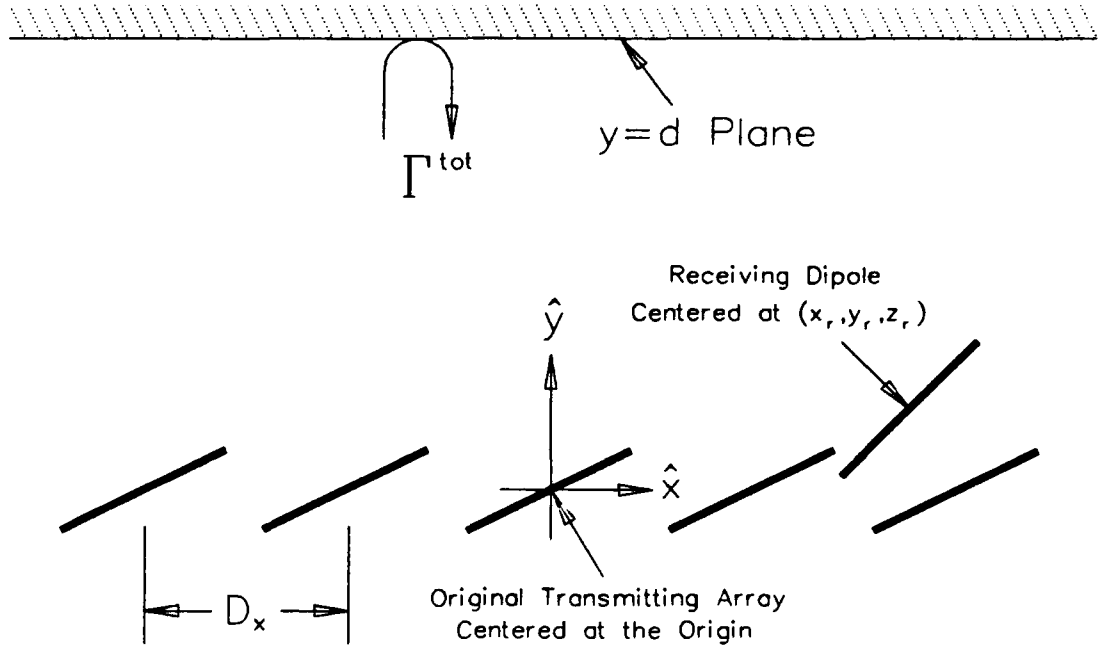


Figure 61: Geometry of "Artificially Created" Doubly-Infinite Array of Transverse Dipoles Used for the ASM Calculation of the Reflected Impedance Component near a Dielectric Clad Ground Plane

interface at $y = d$ in Figure 61 is shown as a surface with an effective reflection coefficient, which is denoted Γ^{tot} (for each polarization).

From the plane wave expansion of the fields from doubly-infinite array sources [1, 2], we express the ASM integrand as:

$$Z_{ref,A} = \frac{\eta_0}{2D_x D_z} \sum_{k=-\infty}^{\infty} \sum_{n=-\infty}^{\infty} \frac{e^{-j2d\beta_0 r_{y0}} e^{-j\beta_0 \bar{R}_r \cdot \hat{r}_{0,-}}}{r_{y0}} \cdot \left[P_{\perp}^{t,-} P_{\perp}^{r,-} \Gamma_{\perp}^{tot} + P_{\parallel}^{t,+} P_{\parallel}^{r,-} \Gamma_{\parallel}^{tot} \right]. \quad (3.44)$$

Several parameters in Equation (3.44) need explanation. The variables η_0 and β_0 refer to the intrinsic impedance and wavenumber of free space. The position vector \bar{R}_r refers to the coordinate of the center of the receive dipole, which is:

$$\bar{R}_r = x_r \hat{x} + y_r \hat{y} + z_r \hat{z}. \quad (3.45)$$

The unit vector $\hat{r}_{0,-}$ represents the direction of the plane waves in free space after they bounce off the outer dielectric surface, thus travelling with a component in the $-\hat{y}$ direction. This is given by

$$\hat{r}_{0,-} = (s_x + \frac{k\lambda_0}{D_x})\hat{x} - r_{y0}\hat{y} + \frac{n\lambda_0}{D_z}\hat{z}, \quad (3.46)$$

where r_{y0} normalizes the unit vector, and is chosen with the positive root for real values and the $-j$ root for evanescent plane waves. A similar direction $\hat{r}_{0,+}$ is defined by changing the sign on the \hat{y} component in Equation (3.46). The parameter s_x is the directional cosine which is used to steer the propagating plane waves, as noted in Chapter 2 and Appendix B.

The reflection coefficients Γ^{tot} are merely effective coefficients for the outer dielectric interface, as seen from a plane wave incident on the free space side. They are referenced to the electric field. The Fresnel forms of these coefficients, for reflection (into region 1) at the junction of two infinite half-spaces, are:

$$\Gamma_{12\perp} = \frac{\eta_2 r_{y1} - \eta_1 r_{y2}}{\eta_2 r_{y1} + \eta_1 r_{y2}} \quad (3.47)$$

and

$$\Gamma_{12\parallel} = \frac{\eta_2 r_{y2} - \eta_1 r_{y1}}{\eta_2 r_{y2} + \eta_1 r_{y1}}. \quad (3.48)$$

The Fresnel coefficient at the ground plane is -1 for each plane wave mode, angle, and polarization. The effective coefficients Γ_{\perp}^{tot} and Γ_{\parallel}^{tot} are then found by stepping through the dielectric layers from the ground plane to the outer interface, using the procedure defined by Equations (2.101) and (2.102).

The only remaining variables to explain in Equation (3.44) are the pattern factors, which unlike the planar slot array cases in Chapter 2, include superscripts designating $+$ and $-\hat{y}$ directional components. The basic reason for the chosen superscripts is that the reflected energy to be used in the computation comes from

the transmitting array launching plane wave in the $+\hat{y}$ direction and the receiving array sensing them from the $-\hat{y}$ direction. First, we define the total pattern factors, $P^{t,+}$ and $P^{r,-}$. They are:

$$P^{t,+} = \int_{-\frac{L_t}{2}}^{\frac{L_t}{2}} I(p_t) e^{+j\beta_0 p_t \hat{p}_t \cdot \hat{r}_{0,+}} dp_t \quad (3.49)$$

and

$$P^{r,-} = \int_{-\frac{L_r}{2}}^{\frac{L_r}{2}} I(p_r) e^{-j\beta_0 p_r \hat{p}_r \cdot \hat{r}_{0,-}} dp_r, \quad (3.50)$$

where $I(p_t)$ and $I(p_r)$ are the chosen basis and testing currents, respectively. To decompose these total pattern functions into polarization patterns, we use Equations (2.58) through (2.61). Using piecewise sinusoidal currents, and noting the geometry shown in Figure 60, we get:

$$P^{t,+} = \frac{2}{\beta_0 \sin(\frac{\beta_0 L_t}{2})} \frac{\cos(\frac{\beta_0 L_t \alpha_t}{2}) - \cos(\frac{\beta_0 L_t}{2})}{1 - \alpha_t^2}, \quad (3.51)$$

$$P^{r,-} = \frac{2}{\beta_0 \sin(\frac{\beta_0 L_r}{2})} \frac{\cos(\frac{\beta_0 L_r \alpha_r}{2}) - \cos(\frac{\beta_0 L_r}{2})}{1 - \alpha_r^2}, \quad (3.52)$$

$$P_{\perp}^{t,+} = -\frac{r_{z_0} \cos \phi_t}{\sqrt{r_{x_0}^2 + r_{z_0}^2}} \cdot P^{t,+}, \quad (3.53)$$

$$P_{\perp}^{r,-} = -\frac{r_{z_0} \cos \phi_r}{\sqrt{r_{x_0}^2 + r_{z_0}^2}} \cdot P^{r,-}, \quad (3.54)$$

$$P_{\parallel}^{t,+} = \frac{(r_{x_0}^2 + r_{z_0}^2) \sin \phi_t - r_{x_0} r_{y_0} \cos \phi_t}{\sqrt{r_{x_0}^2 + r_{z_0}^2}} \cdot P^{t,+}, \quad (3.55)$$

$$P_{\parallel}^{r,-} = -\frac{(r_{x_0}^2 + r_{z_0}^2) \sin \phi_r + r_{x_0} r_{y_0} \cos \phi_r}{\sqrt{r_{x_0}^2 + r_{z_0}^2}} \cdot P^{r,-}, \quad (3.56)$$

where we have defined

$$\alpha_t = r_{x_0} \cos \phi_t + r_{y_0} \sin \phi_t \quad (3.57)$$

and

$$\alpha_r = r_{x_0} \cos \phi_r - r_{y_0} \sin \phi_r \quad (3.58)$$

with r_{x_0} , r_{y_0} , and r_{z_0} being the \hat{x} , \hat{y} , and \hat{z} components of the plane wave directions in free space from Equation (3.46).

Unlike the case of slot-to-slot coupling, the dipole-to-dipole's reflection coupling calculations between various mode combinations may not be similar since the dipoles may be rotated with respect to each other and arbitrarily placed. With the slots, modes are confined to exist along a plane, which makes many of the ASM computations similar enough that Fast Fourier Transforms can speed the overall solution time. With the dipoles, there is no strong reason to use FFTs. Furthermore, as long as no dipole is within about $\lambda_0/4$ of the outer dielectric interface, only the propagating terms and neighboring evanescent modes in the plane wave expansion need to be considered. An inter-column spacing of $D_x = \lambda_0/2$ may be chosen for the "artificial array", as was done with the slot-to-slot applications. As long as $D_x < 1\lambda_0$, this makes only one propagating term. This means the ASM here is usually a simple numerical integration of only the $k = n = 0$ and $k = \pm 1/n = 0$ terms in Equation (3.44), as it is substituted into Equation (3.43). For these terms, $r_{z_0} = 0$, which eliminates the perpendicular polarization pattern factors, and simplifies the parallel factors to:

$$P_{||}^{t,+} = (r_{x_0} \sin \phi_t - r_{y_0} \cos \phi_t) P^{t,+} \quad (3.59)$$

and

$$P_{||}^{r,-} = -(r_{x_0} \sin \phi_r + r_{y_0} \cos \phi_r) P^{r,-}. \quad (3.60)$$

When evaluating the integrals in the ASM for the $k = -1, 0, 1/n = 0$ terms (assuming $D_x = \lambda_0/2$), singularities will occur as r_{y_0} approaches zero. Specifically, the singularities occur at $s_x = \pm 1$ for the $k = n = 0$ term, for $s_x = 1$ for the

$k = -1/n = 0$ term, and for $s_x = -1$ for the $k = 1/n = 0$ term. These singularities are similar to those which occurred with slots in a homogeneous half-space, and are not associated with any surface wave formations. As with the slot case (ref. Equations (2.87) through (2.89)), the singularities may be removed with an analytical approximation for a small neighborhood around the points. This gives:

$$\begin{aligned}
Z_{ref} \approx & \frac{\eta_0}{2\lambda_0 D_z} \left[\int_{-1}^{1-\Delta_1} \frac{e^{-j\beta_0 r_{z_0} x_r} e^{-j\beta_0 (2d-y_r) r_{y_0}}}{r_{y_0}} P_{\parallel}^{t,+} P_{\parallel}^{r,-} \Gamma_{\parallel}^{tot} \Big|_{k=-1/n=0} ds_x \right. \\
& + \int_{-1+\Delta_2}^{1-\Delta_3} \frac{e^{-j\beta_0 r_{z_0} x_r} e^{-j\beta_0 (2d-y_r) r_{y_0}}}{r_{y_0}} P_{\parallel}^{t,+} P_{\parallel}^{r,-} \Gamma_{\parallel}^{tot} \Big|_{k=n=0} ds_x \\
& + \int_{-1+\Delta_4}^1 \frac{e^{-j\beta_0 r_{z_0} x_r} e^{-j\beta_0 (2d-y_r) r_{y_0}}}{r_{y_0}} P_{\parallel}^{t,+} P_{\parallel}^{r,-} \Gamma_{\parallel}^{tot} \Big|_{k=1/n=0} ds_x \\
& + \left[\frac{\pi}{2} - \sin^{-1}(1 - \Delta_2) \right] e^{j\beta_0 x_r} P_{\parallel}^{t,+} P_{\parallel}^{r,-} \Gamma_{\parallel}^{tot} \Big|_{k=n=0, s_x=-1} \\
& + \left[\frac{\pi}{2} - \sin^{-1}(1 - \Delta_3) \right] e^{-j\beta_0 x_r} P_{\parallel}^{t,+} P_{\parallel}^{r,-} \Gamma_{\parallel}^{tot} \Big|_{k=n=0, s_x=1} \\
& + j e^{j\beta_0 x_r} \ln(1 + \Delta_1 + \sqrt{2\Delta_1 + \Delta_1^2}) P_{\parallel}^{t,+} P_{\parallel}^{r,-} \Gamma_{\parallel}^{tot} \Big|_{k=-1/n=0, s_x=1} \\
& \left. + j e^{-j\beta_0 x_r} \ln(1 + \Delta_4 + \sqrt{2\Delta_4 + \Delta_4^2}) P_{\parallel}^{t,+} P_{\parallel}^{r,-} \Gamma_{\parallel}^{tot} \Big|_{k=1/n=0, s_x=-1} \right] \quad (3.61)
\end{aligned}$$

The four Δ s are small positive numbers which define the neighborhoods in which the singularities are analytically removed. The remaining three integrals in Equation (3.61) are usually well behaved and may be evaluated fairly quickly by numerical methods. It should be noted that the product, $P_{\parallel}^{t,+} P_{\parallel}^{r,-} \Gamma_{\parallel}^{tot}$, is continuous across the singularities and thus its evaluation is equal under $k = -1/n = 0, s_x = 1$ and $k = n = 0, s_x = -1$, and also equal (but not to the previous pair) under $k = 1/n = 0, s_x = -1$ and $k = n = 0, s_x = 1$.

Again, it should be recalled that the formulation of the ASM in Equation (3.61) uses only one propagating term and two neighboring evanescent terms in the plane wave expansion. Therefore, it is only applicable to cases with $D_z < 1\lambda_0$ (i.e., no

other propagating modes - note that D_z was chosen to be $\lambda_0/2$) and $d > \lambda_0/4$. These conditions are typically met, though, which makes Equation (3.61) useful for most applications.

The reflected component of the self-impedance of a column of periodic transverse dipoles was tested by using the ASM. For an initial verification, cases were run with no dielectric coatings on the ground plane. In these cases, image theory can be used along with the methods for computing coupling in a homogeneous space described in the previous section as a check on the ASM computations.

The first case examined was that of the reflected term in the self-impedance of an \hat{x} -directed dipole array spaced an amount d from the ground plane. That is, $\phi_t = \phi_r = 0$. The lengths and inter-element spacing (D_z) of the array were $\lambda/3$ and piecewise sinusoidal currents were assumed. In Figure 62, the reflected impedance term is plotted as a function of the spacing from the ground plane. Since some of the data was computed extremely close to the ground plane, many more terms in kn space were used than the three given in Equation (3.61). Note that with the dipoles being \hat{x} -directed, the pattern factors become zero where r_{y_0} tends to approach zero, thus keeping the integrations in the ASM numerically stable without attempting to analytically remove any singularities.

By image theory, the data in Figure 62 should be an inversion of the data in Figure 57, with a compression of the horizontal axis by a factor of two, to account for the two-way reflection path. Such is the case, as seen in the two figures, which confirms that the ASM data for the reflection is accurate.

Another pattern using the ASM was computed for the reflected component of mutual impedance between two transverse piecewise sinusoidal dipole modes with $\phi_t = \phi_r = 0$ and a separation in \hat{x} . Again, the dipole lengths and inter-element spacings in \hat{z} were each $\lambda/3$, and $y_r = z_r = 0$. The pattern was taken as a function of

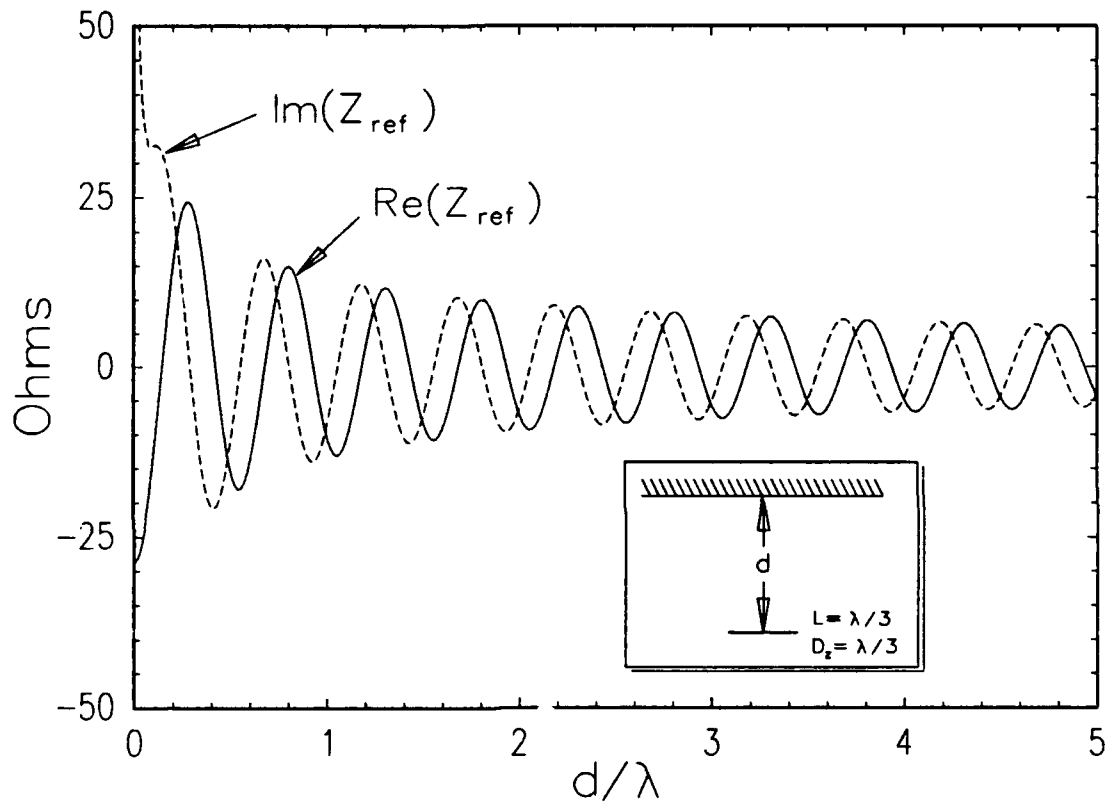


Figure 62: Reflected Component of Self-Impedance from a Bare Ground Plane using the ASM - $L = D_z = \lambda/3$, $\phi_t = \phi_r = 0$, $s_z = 0$

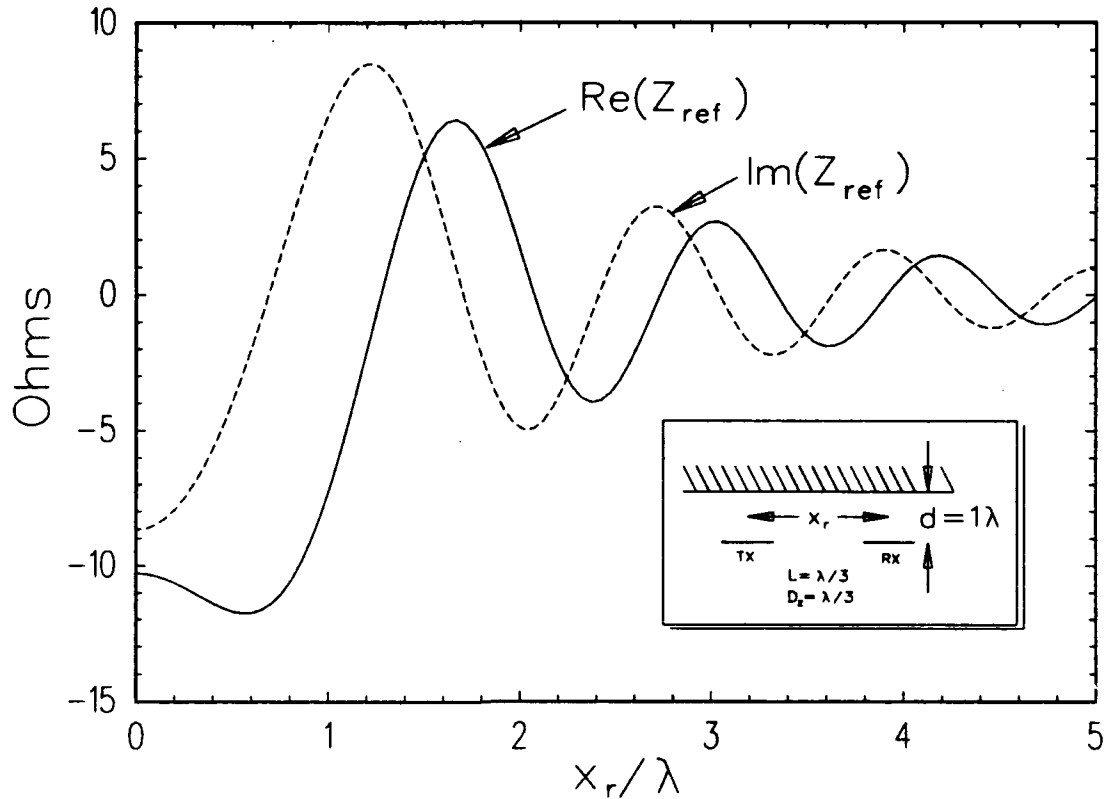


Figure 63: Reflected Component of Mutual Impedance from a Bare Ground Plane using the ASM - $L = D_z = \lambda/3$, $z = 0$, $\phi_t = \phi_r = 0$, $d = 1\lambda$, $s_z = 0$

the separation distance, x_r , at a fixed distance from the bare ground plane, $d = 1\lambda$. The results in Figure 63 are much stronger than the direct coupling component, which is in Figure 58, except for some very strong reactive coupling in the near zone for the direct case.

To test Equation (3.61), and in particular, the analytical removal of the singularities, the dipoles were rotated to $\phi_t = \phi_r = 30^\circ$. In this case, the pattern factors do not go to zero where the singularities occur, and Equation (3.61) is used with the restriction that $d > \lambda/4$. The ASM computed reflected component of the self-impedance (assuming piecewise sinusoidal currents) is compared with a computation from image sources, using the spectral domain solution for a homogeneous

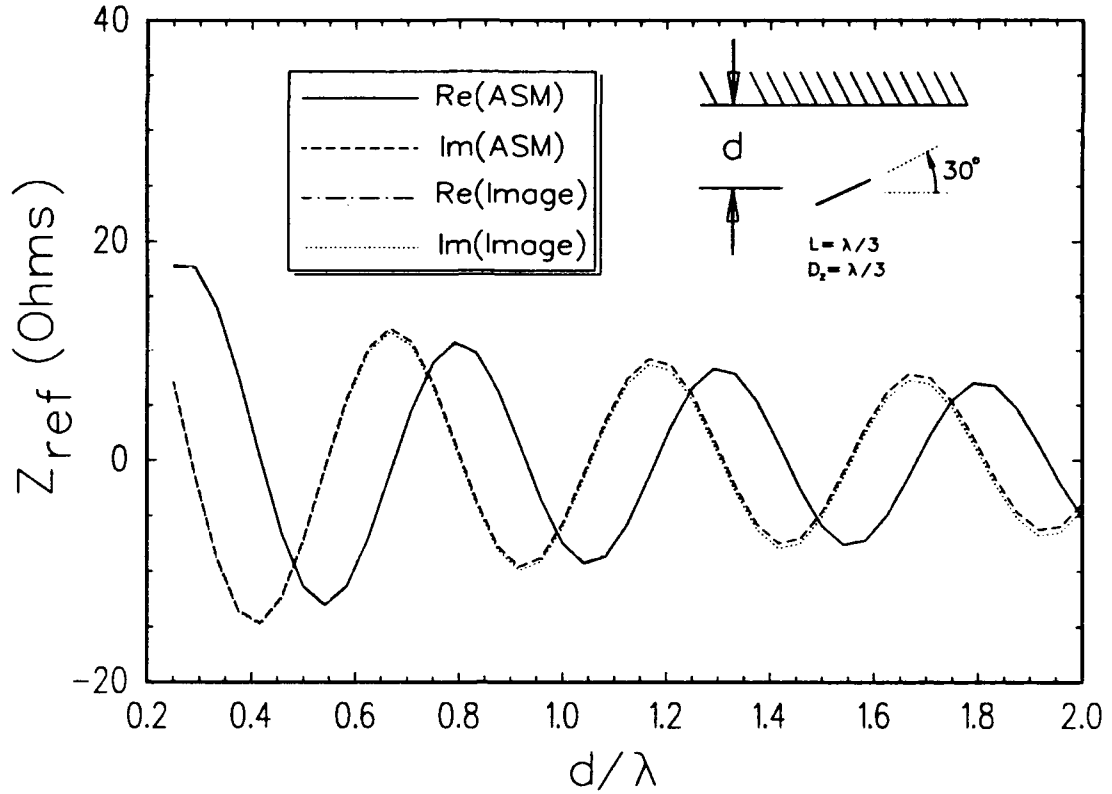


Figure 64: Reflected Component of Self-Impedance with a Bare Ground Plane using the ASM - $L = D_z = \lambda/3$, $\phi_t = \phi_r = 30^\circ$, $s_z = 0$

space (ref. Equation (3.31)). Impedance data is shown in Figure 64 as a function of spacing off the ground plane. Again, the dipole lengths and inter-element spacings are $\lambda/3$. Again, the agreement between the methods is excellent.

The integrands used in the three integrals in Equation (3.61) are now examined for the 30° tilted dipole array example just computed. In Figure 65, the integrand (multiplied by the leading $\eta_0/2\lambda_0 D_z$ coefficient) is plotted as a function of r_{x_0} , which is linearly related to s_x . Thus, the three integral regions are combined to form a single integration over $-3 < r_{x_0} < 3$. The three kn combination regions are identified below the r_{x_0} axis. For Figure 65, this integrand is shown as it exists when $d = \lambda/4$, which is the closest data point in Figure 64.

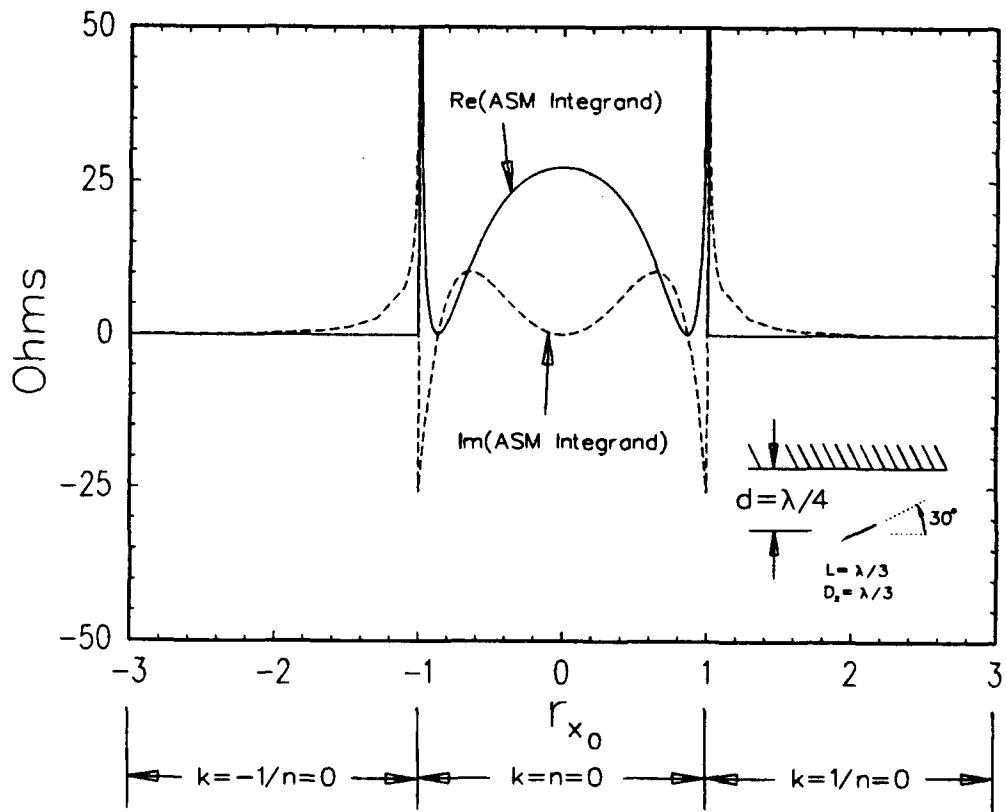


Figure 65: Integrand from the ASM Computation of the Reflected Component of Self-Impedance with a Bare Ground Plane - $L = D_z = \lambda/3$, $\phi_t = \phi_r = 30^\circ$, $d = \lambda/4$, $s_z = 0$

Several features in Figure 65 are important to note. The locations of the two singularities, which are at junctions of the three integral regions, are clearly evident. As r_{z_0} is "scanned" into the evanescent regions ($k = \pm 1$), the integrands become purely imaginary and decay rapidly. Finally, note that the integrand in Figure 65 is symmetric, which suggests that CPU time may easily be cut in half. This symmetry is a result of the ASM being used in a self-impedance application, and since the CPU time for the calculation is fairly fast (with only three terms in kn space), taking advantage of this symmetry does not make a noticeable improvement in the overall efficiency of a large moment method application.

A similar integrand plot at $d = 2\lambda$, which is the furthest data point in Figure 64, is given in Figure 66.

In Figure 66, the integrand contributions in the evanescent regions are much smaller than they were in Figure 65, which is expected with more propagation distance in \hat{y} for the evanescent decay. The integrand within the propagating region ($k = n = 0$) is much more oscillatory than it was when d was smaller, making the numerical integration more difficult. In fact, as d increases, these oscillations become worse until it an accurate numerical integration takes a large amount of CPU time. However, one may take notice that the curves in Figure 66 are similar to classical integrand curves on mathematical problems with stationary phase points. This suggests that instead of numerically evaluating the integral for large d , one may asymptotically find the reflected component of impedance by using the method of stationary phase.

Using the method of stationary phase to evaluate the $k = n = 0$ integral, and ignoring the remaining terms in Equation (3.61), the reflected impedance component becomes:

$$Z_{ref} \approx \frac{\eta_0}{2D_z} \sqrt{\frac{j}{\rho\lambda_0}} e^{-j\beta_0\rho} P_{||}^{t,+} P_{||}^{r,-} \Gamma_{||}^{tot} \Big|_{stat.pha.pt.} \quad (3.62)$$

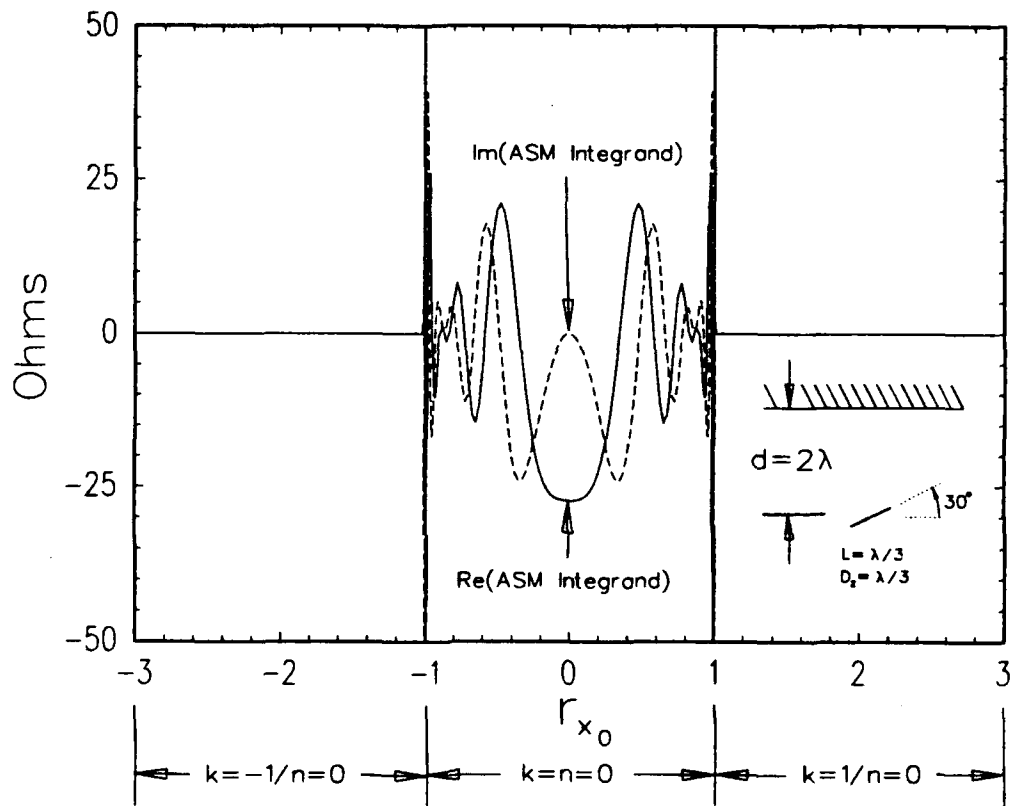


Figure 66: Integrand from the ASM Computation of the Reflected Component of Self-Impedance with a Bare Ground Plane - $L = D_z = \lambda/3$, $\phi_t = \phi_r = 30^\circ$, $d = 2\lambda$, $s_z = 0$

where

$$\rho = \sqrt{x_r^2 + (2d - y_r)^2}, \quad (3.63)$$

and the stationary phase point is designated by the scanning parameter

$$s_x = \frac{x_r}{\rho} \quad (3.64)$$

with $k = n = 0$. This stationary phase evaluation has the physical interpretation of a geometrical optics ray bounce off the outer dielectric interface, with the cylindrical wavefront reflecting according to an effective propagating plane wave coefficient for the incident ray angle. Note that ρ is the total bounce path (obeying the optical law of reflection) between the centers of the modes. It is also interesting to note that this stationary phase evaluation is equivalent to the homogeneous impedance solution in the spectral domain (Equation (3.31) with the asymptotic pattern integral expressions (Equations (3.20) through (3.24)) and ignoring higher order $1/\rho$ terms, and using an image source about the $y = d$ plane and the effective reflection coefficient. With this same expression derived in such different ways, each theory is further confirmed.

To test the stationary phase solution, the reflected component of the self-impedance of a tilted transverse dipole mode (piecewise sinusoidal currents) was computed in the vicinity of a dielectric coated ground plane. For the example, a single layer of dielectric was chosen with the dielectric constant at twice that of free space and a thickness of one-fifth of a wavelength in the material. The dipoles were tilted with $\phi_t = \phi_r = 30^\circ$, and again the lengths and inter-element spacings were chosen to be $\lambda/3$. Patterns of the reflected component of the self-impedance were taken as a function of the distance from the outer dielectric interface, using the numerically integrated solution of Equation (3.61) and the stationary phase point evaluation in Equation (3.62). The data is shown in Figure 67. It indicates excellent

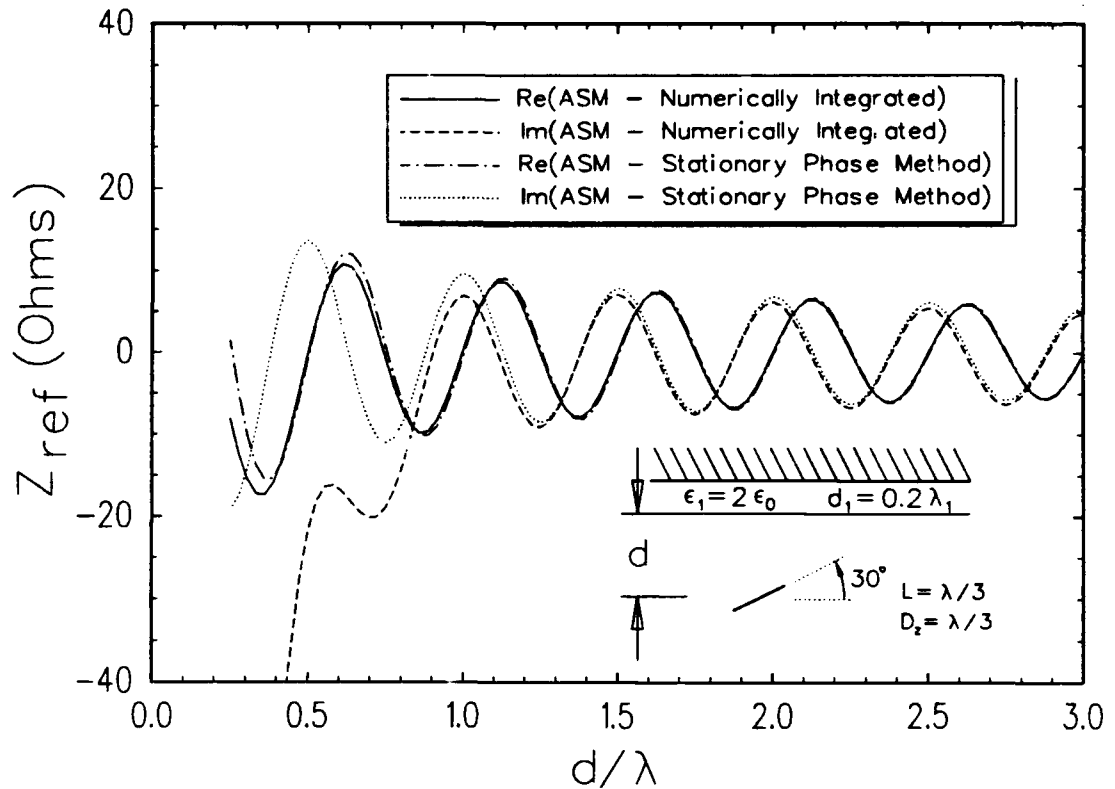


Figure 67: Comparison of Rigorous and Asymptotically Based ASM Solutions for Reflected Component of Self-Impedance from a Dielectric Coated Ground Plane - $L = D_z = \lambda/3$, $\phi_t = \phi_r = 30^\circ$, $s_z = 0$

agreement between the methods for separation distances of $d > 2\lambda$. Since a typical data point using Equation (3.61) takes about 0.5 CPU seconds and the single term asymptotic solution takes less than one millisecond, there is a strong preference to use the stationary phase solution for these larger separation distances.

It should be noted that the reflected impedance component for the dielectric coated ground plane (ref. Figure 67) is of the same order of magnitude as the impedance from a bare ground plane (ref. Figure 64). This is not unexpected since the lossless dielectric coating merely rotates the -1 reflection coefficient from the ground plane for the propagating plane wave term. Although surface waves can become excited in the dielectric, which would take energy away from the reflection,

they can only be excited by evanescent plane wave incidence from the free space region³. As long as the radiating dipole mode is spaced at least $\lambda/4$ from the outer dielectric interface, the energy in these evanescent plane waves which encounter the boundary will be insignificant.

To further verify the accuracy of the solutions developed in this section, we use an example problem where the PMM code [3] can provide a reference solution. The problem is to compute the reflected component of the scan impedance from a non-skewed doubly-infinite array of dipoles in the vicinity of a dielectric coated ground plane. For this example, the dipoles are all \hat{x} -directed (i.e., $\phi_t = \phi_r = 0$), which is required for use of the PMM code. The dipoles have lengths of $L = \lambda_0/3$, and spacings of $D_z = \lambda_0/3$ and $D_x = 0.4\lambda_0$. The wire radius is not important for the reflected component of impedance, but is specified as $L/40$ for future use. Two dielectric slabs coat the ground plane, with the $\epsilon_1 = 4\epsilon_0$, $\epsilon_2 = 2\epsilon_0$, $d_1 = 0.2\lambda_1$, and $d_2 = 0.2\lambda_2$ (see Figure 60). Finally, the dipole array is placed $d = \lambda_0/3$ away from the outer dielectric interface.

Column-to-column mutual impedances from 101 spatial terms are added spatially with Floquet phasing factors and a Fejer kernel. These mutual impedances are found by the Array Scanning Method using Equation (3.61) when $x_r < 5\lambda_0$ and the stationary phase solution in Equation (3.62) when $x_r > 5\lambda_0$. Since the dipoles are fairly close to the dielectrics, this stresses the accuracy of the stationary phase solution. The above method is labelled the ASM solution in Figure 68, which is compared with the reflected scan impedance data from the PMM code. The comparison is very good until extremely high scan angles are reached.

³These surface waves are signalled by a singularity in the effective reflection coefficient, Γ^{eff} . Such a singularity only occurs when evanescent plane waves exist in the free space region, since the slabs have dielectric constants greater than that of free space.

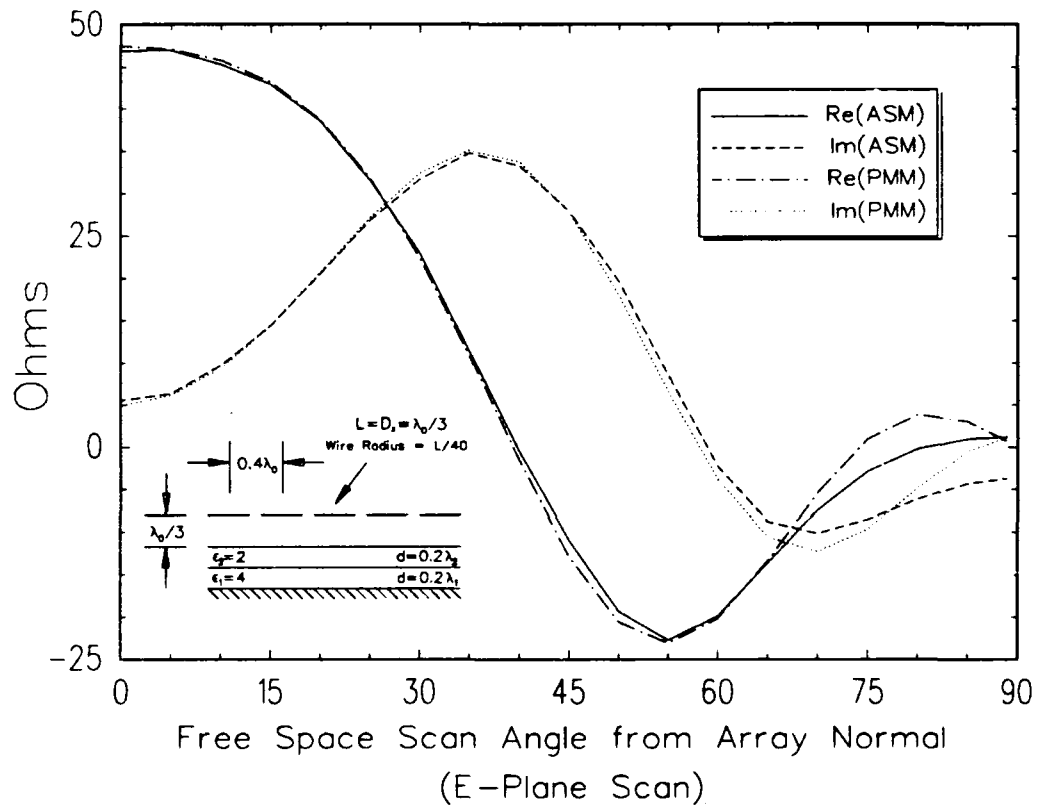


Figure 68: Reflected Component of Scan Impedance of a Doubly-Infinite Array of \hat{x} -Directed Dipoles near a Ground Plane Coated with Two Dielectrics

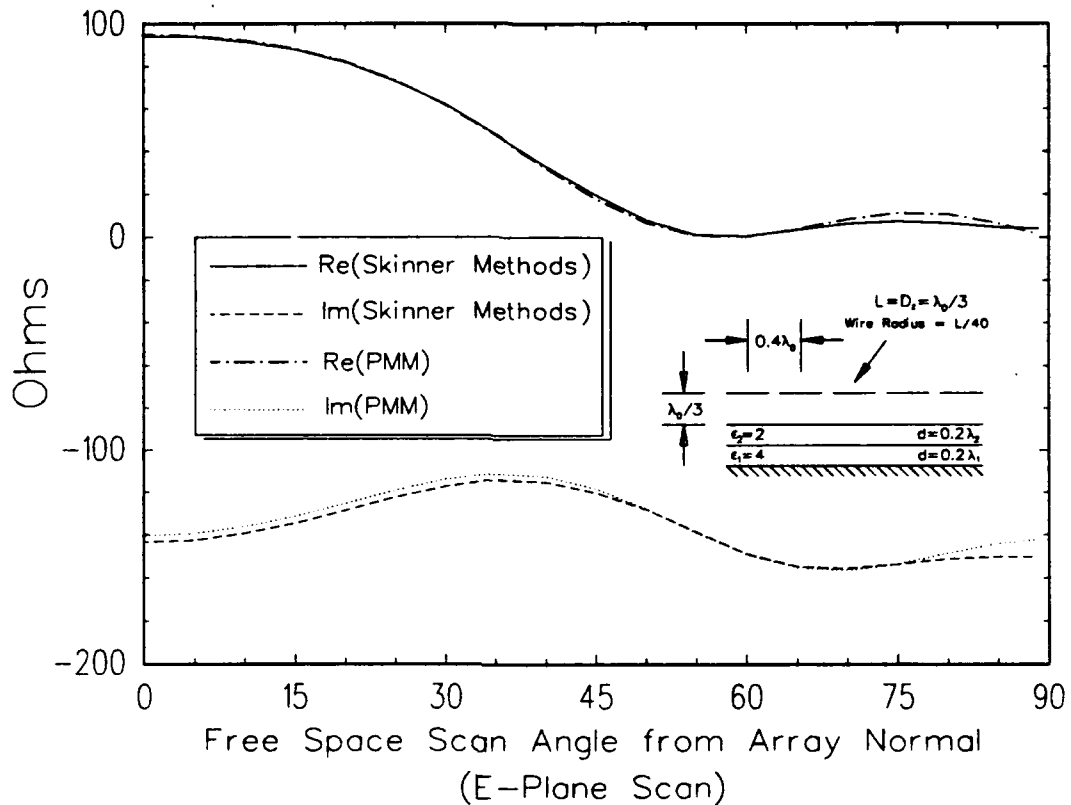


Figure 69: Total Scan Impedance of a Doubly-Infinite Array of \hat{z} -Directed Dipoles near a Ground Plane Coated with Two Dielectrics

Finally, we present the total scan impedance for the previous example geometry, which is the sum of the reflected component and a free space (direct) component, which was computed for Figure 59. The data is in Figure 69, which verifies that the methods used in this dissertation for computing column-to-column coupling work well compared to results predicted with the PMM code.

CHAPTER IV

DIPOLE-TO-SLOT COUPLING

In this chapter, we shall develop expressions for the voltage and current gains used in the coupling matrix in Equation (1.23). Specifically, we shall solve Equation (1.30) and (1.31) for transverse dipole and axial slot column modes, as they exist in Region III of Figure 4.

The Lorentz reciprocity theorem [14] is used to show that voltage gain calculations are the negative of the corresponding current gain calculations. Specifically, this theorem states that the fields radiated by an electric and magnetic current source obey the following equation:

$$\int \int \int (\bar{E}^a \cdot \bar{J}^b - \bar{H}^a \cdot \bar{M}^b) dv = \int \int \int (\bar{E}^b \cdot \bar{J}^a - \bar{H}^b \cdot \bar{M}^a) dv, \quad (4.1)$$

where the common superscripts denote a specific source and the fields radiated by that source. Assuming only the \bar{J}^a and \bar{M}^b sources exist, the reciprocity reduces to:

$$-\int \int \int \bar{H}^a \cdot \bar{M}^b dv = \int \int \int \bar{E}^b \cdot \bar{J}^a dv, \quad (4.2)$$

which shows that the applications of Equations (1.30) and (1.31) give the same answer except for a sign change when applied to the same dipole and slot modes, as long as the basis and testing currents are of the same form. Thus, it is only necessary to compute the coupling terms as either slot or dipole modes radiate to the other. The reciprocity can also show that slot-to-slot coupling and dipole-to-dipole coupling terms are symmetric without a sign change.

This chapter is divided into two main sections, which concentrate on solutions in a homogeneous space, and solutions for slot modes embedded in a near a dielectric coated ground plane.

4.1 COUPLING IN FREE SPACE

The dipole-to-slot coupling in free space will be developed from the viewpoint of a transverse electric current mode (dipole) radiating to an axial magnetic current mode (slot) which is on a ground plane. This corresponds to Equation (1.30), which is a current gain.

Using image theory, the ground plane may be removed and an image dipole source is added, as shown in Figure 70. The only pertinent effect of the image source for this application is to double the \hat{z} component of the radiated magnetic field. Without loss of generality, we define the center of the reference dipole to be at $z = 0$ and the center of the receiving slot to be at an arbitrary $z = z_c$. Although not depicted, the total length of the slots (which are into the paper) is L_r .

By translating the magnetic field radiated by a transverse Hertzian electric dipole mode (ref. Equation (3.4)), integrating over the finite dipole length, and including a factor of two to account for the image source, we get the total \hat{z} component of the magnetic field radiated by dipoles to be:

$$H_z = -\frac{j\beta}{2D_z} \sum_{n=-\infty}^{\infty} e^{-j\beta z r_z} r_\rho \int_{-\frac{L_d}{2}}^{\frac{L_d}{2}} I(p') (\sin \phi_d) H_1^{(2)}(\beta r_\rho \rho_d) dp', \quad (4.3)$$

where the variables ρ_d and ϕ_d are depicted in Figure 70 and r_z and r_ρ are defined in Equations (2.12) and (2.13). The function $I(p')$ is the chosen current shape for the radiating dipoles.

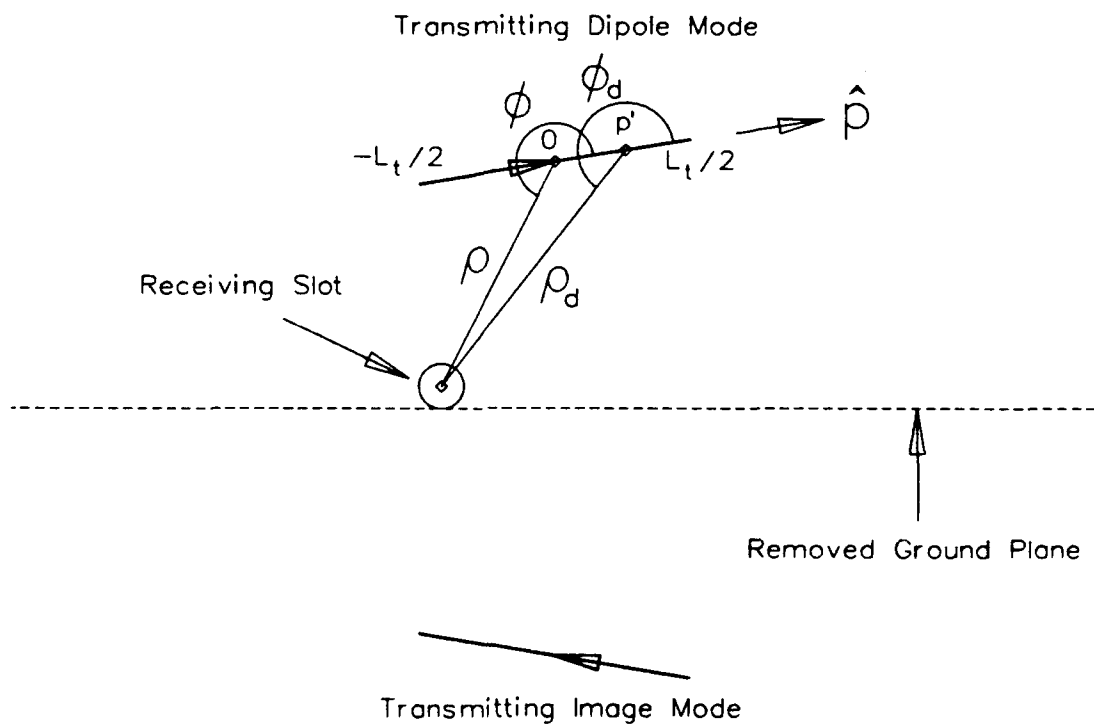


Figure 70: Geometry of Transverse Dipole Mode with Image Source Radiating to a Receive Axial Slot Mode in Free Space - Top View

The current gain is found by substituting Equation (4.3) into Equation (1.30). This yields:

$$G^{BC} = \frac{j\beta}{2D_z} \sum_{n=-\infty}^{\infty} r_\rho P^r \int_{-\frac{L_t}{2}}^{\frac{L_t}{2}} I(p') (\sin \phi_d) H_1^{(2)}(\beta r_\rho \rho_d) dp', \quad (4.4)$$

where P^r is the receiving slot pattern factor, given by:

$$P^r = \int_{z_c - \frac{L_r}{2}}^{z_c + \frac{L_r}{2}} I(z) e^{-j\beta z r_z} dz. \quad (4.5)$$

In the above pattern, the current $I(z)$ is the chosen testing function for the slot. This receive pattern definition is exactly the same as that used in Equation (2.25), which was for slot-to-slot coupling. Therefore, the closed form analytical evaluations in Equations (2.31) through (2.35) apply for several common testing functions.

The remaining integral in Equation (4.4) is a transmitting pattern factor for the dipoles. In general, it must be evaluated numerically. However, when the dipole mode is spaced far away from the receiving slot (i.e., ρ is electrically large), an asymptotic solution may be found, which simplifies the calculations. Using the large argument approximation of the Hankel function from Equation (3.19), and applying the far zone approximations that $\rho_d \approx \rho$ for amplitude purposes, $\rho_d \approx \rho - p' \cos \phi$ for phase purposes, and $\phi_d \approx \phi$ over the entire region of integration (see Figure 70), we get the following approximation for the current gain:

$$G^{BC} \approx -\frac{\sin \phi}{D_z} \sum_{n=-\infty}^{\infty} \sqrt{\frac{j r_\rho}{\rho \lambda}} P_{fz}^t P^r e^{-j\beta r_\rho \rho}, \quad (4.6)$$

where we have defined

$$P_{fz}^t = \int_{-\frac{L_t}{2}}^{\frac{L_t}{2}} I(p') e^{j\beta r_\rho p' \cos \phi} dp'. \quad (4.7)$$

This far zone transmitting pattern integral is the same as that defined in Equation (3.27). For many common current shapes, it may be found in closed form. For example, when a piecewise sinusoid is used for the transmitting dipole current, the result in Equation (3.29) is valid.

Note that although the summation in Equation (4.6) extends from $-\infty$ to ∞ , it only needs to be carried over the propagating modes for this far zone approximation, which are distinguished by r_ρ having real values.

The voltage gain from a slot mode radiating to a receiving dipole (Equation (1.31)) is found from the above by reciprocity. In general, it is:

$$G^{CB} = -\frac{j\beta}{2D_z} \sum_{n=-\infty}^{\infty} r_\rho P^t \int_{-\frac{L_r}{2}}^{\frac{L_r}{2}} I(p') (\sin \phi_d) H_1^{(2)}(\beta r_\rho \rho_d) dp', \quad (4.8)$$

where P^t is now the transmitting pattern factor for the slot mode (using Equation (4.5) except changing the sign to + in the exponential) and $I(p')$ is the testing current on the dipole. Similarly, when the modes are spread far apart, the asymptotic voltage gain is:

$$G^{CB} \approx \frac{\sin \phi}{D_z} \sum_{n=-\infty}^{\infty} \sqrt{\frac{j r_\rho}{\rho \lambda}} P_{fz}^r P^t e^{-j\beta r_\rho \rho}, \quad (4.9)$$

where P_{fz}^r is found from Equation (4.7) with $I(p')$ now being the testing current.

Note that when the testing current form for any current mode is of the same form as the radiating basis current, then the voltage gains are exactly the negative of the corresponding current gains. This is the result of reciprocity applied with the "quasi-Galerkin" form of testing in the moment method.

Now we wish to compare the rigorous solution for the current gain in Equation (4.4) with the asymptotic solution in Equation (4.6). By examining the equations, the contributing geometric factors include the distance between the modes and the relative angle between the dipoles' orientation and their "view" of the slot. That is,

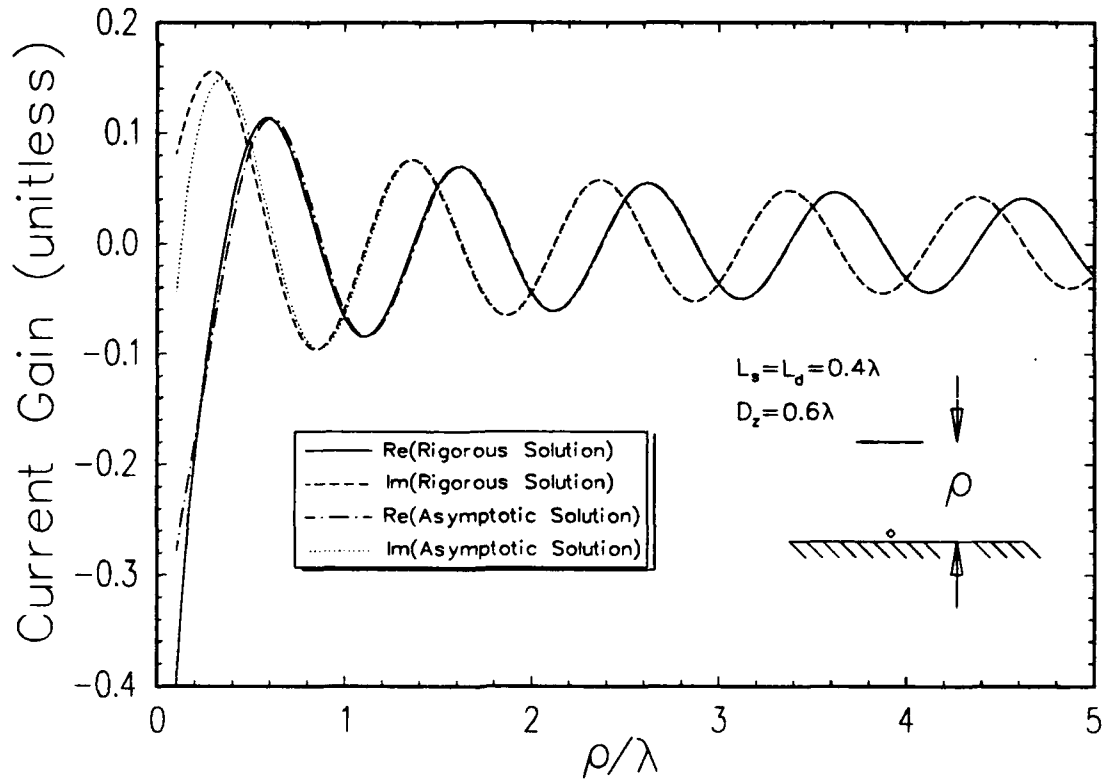


Figure 71: Dipole-to-Slot Coupling in Free Space with Dipoles Parallel to the Ground Plane - $L_s = L_d = 0.4\lambda$, $D_z = 0.6\lambda$, $z_c = 0$, $s_z = 0$

the dipoles' orientation with respect to the ground plane is of no consequence, as long as the center-to-center spacing ρ and the angle ϕ as depicted in Figure 70 are the same. Thus, we can form conclusions of the dipole-to-slot coupling by looking along a single observation path, which is along an axis perpendicular to the ground plane. This was done for three cases. Each case used slot and dipole lengths of 0.4λ , and inter-element spacings of $D_z = 0.6\lambda$ with piecewise sinusoidal currents. The slot center position was held at $z_c = 0$. To differentiate the three cases, the dipoles were first oriented parallel to the ground plane, then 45° away, and finally perpendicular to the ground plane. The results are plotted in Figures 71, 72, and 73, respectively.

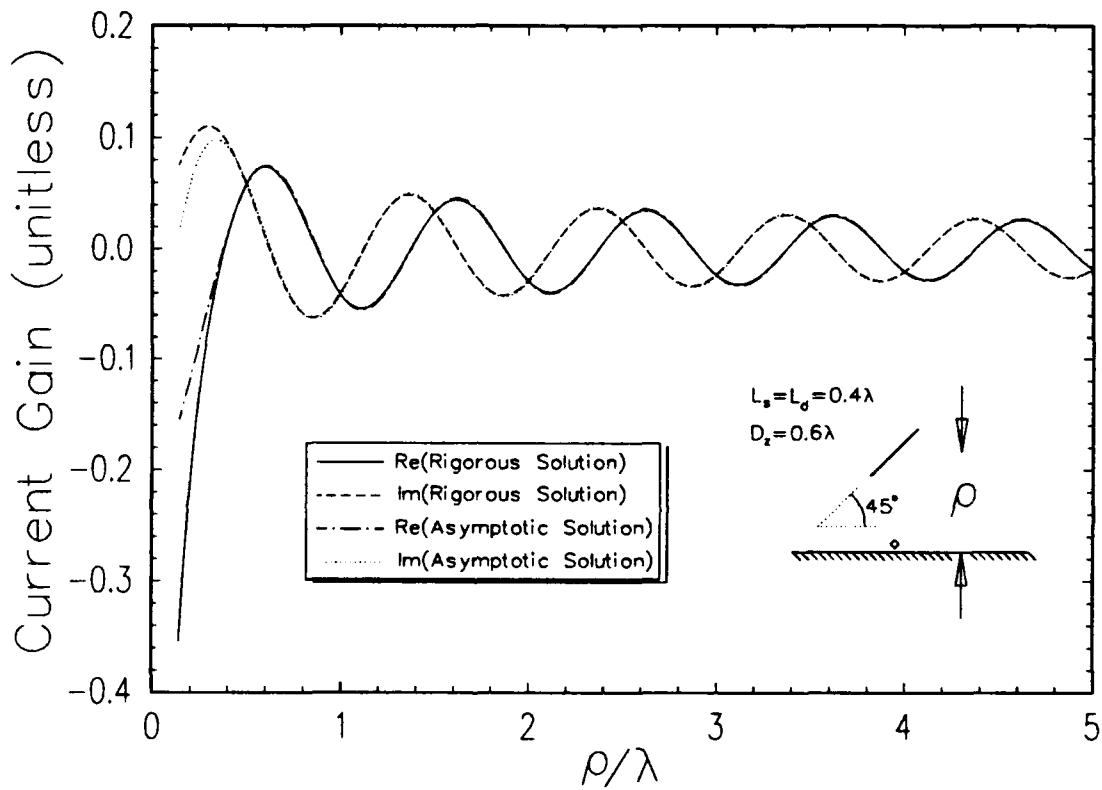


Figure 72: Dipole-to-Slot Coupling in Free Space with Dipoles 45° from Ground Plane - $L_s = L_d = 0.4\lambda$, $D_z = 0.6\lambda$, $z_c = 0$, $s_z = 0$

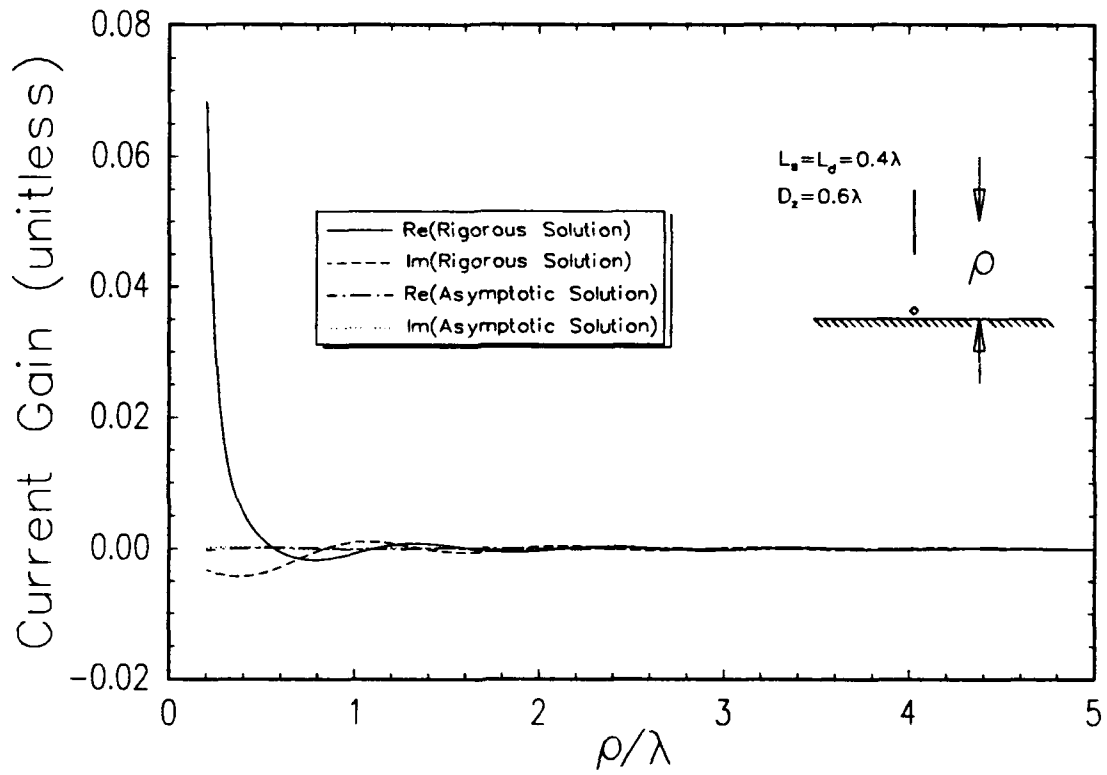


Figure 73: Dipole-to-Slot Coupling in Free Space with Dipoles Perpendicular to the Ground Plane - $L_s = L_d = 0.4\lambda$, $D_z = 0.6\lambda$, $z_c = 0$, $s_z = 0$

In Figures 71 and 72, the asymptotic solution converges to the rigorous solution when $\rho > 1\lambda$. The error in the asymptotic solution at $\rho = 1\lambda$ in Figure 73 is fairly large in a percentage sense, but since the numbers are so small, it is inconsequential. Therefore, as a general rule of thumb, the asymptotic solution is acceptable whenever $\rho > 1\lambda$. Note that the coupling between the dipole and slot modes decreases as the slot's position becomes closer to end-fire to the dipoles. This is not surprising from a spatial domain perspective, with the pattern of the dipoles having a null at end-fire.

To test the accuracy of the rigorous and asymptotic solutions, a simulation was devised for the scanning current gain between a transmitting doubly-infinite array of dipoles and a receiving slot. Using the PMM code for a reference [3], the doubly-infinite dipole array must be a planar array. That is, each dipole must be oriented parallel to the ground plane. Piecewise sinusoidal currents were used on dipoles and the slot, both of which having lengths of 0.4λ , and inter-element spacings were chosen at $D_x = D_z = 0.6\lambda$. The transverse components (i.e., x and z) of the centers of the reference dipole in the "central" column corresponded with the same components for the center of the slot. The dipole array plane was spaced at $y = 0.1\lambda$ away from the ground plane containing the slot, which was chosen to be small to stress the accuracy of the column-to-column current gain solutions.

The results of the scanning current gain are in Figure 74. The data marked as the "Skinner" method comes from adding 101 column-to-column current gains with a Floquet phasing factor and a Fejer kernel. The column-to-column data was derived from Equation (4.4) when the spacing between the dipole column (center) and slot was less than 1λ , and from the asymptotic solution in Equation (4.6) for larger spacings. The disagreements between this method and the PMM code data are almost indistinguishable, giving great confidence in the solutions derived in this section.

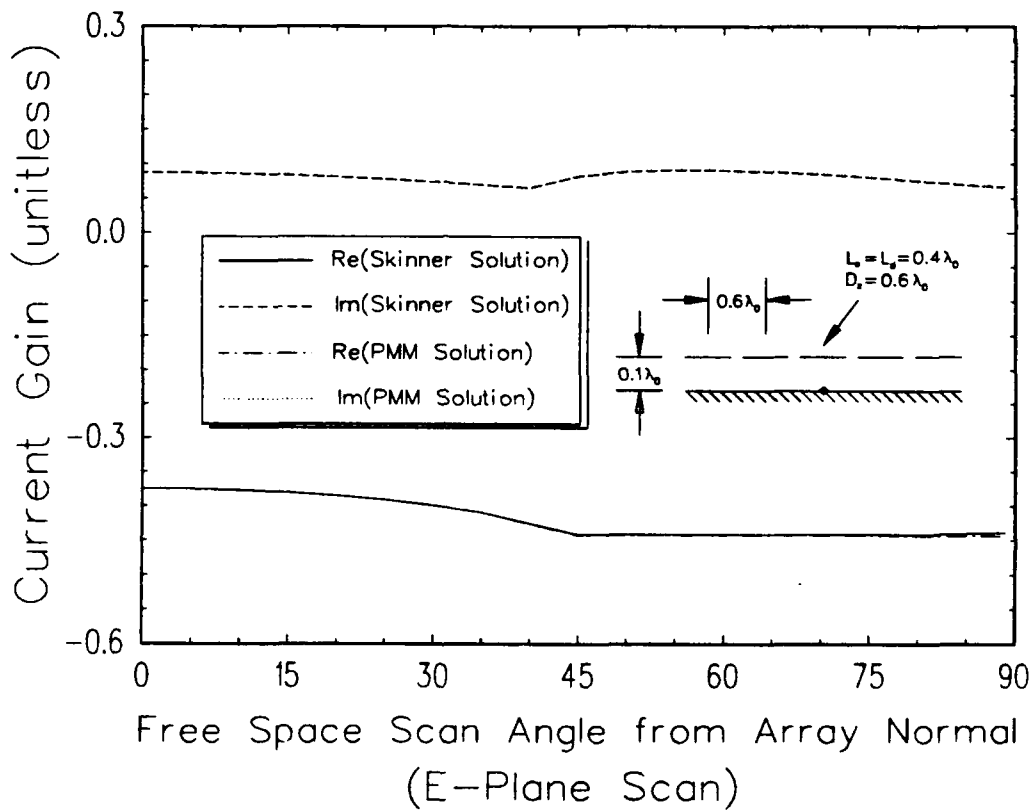


Figure 74: Scanning Current Gain between a Doubly-Infinite Array of Transmitting Dipoles and a Receiving Slot Spaced 0.1λ Away - Skinner Solution Overlays PMM Solution Almost Perfectly

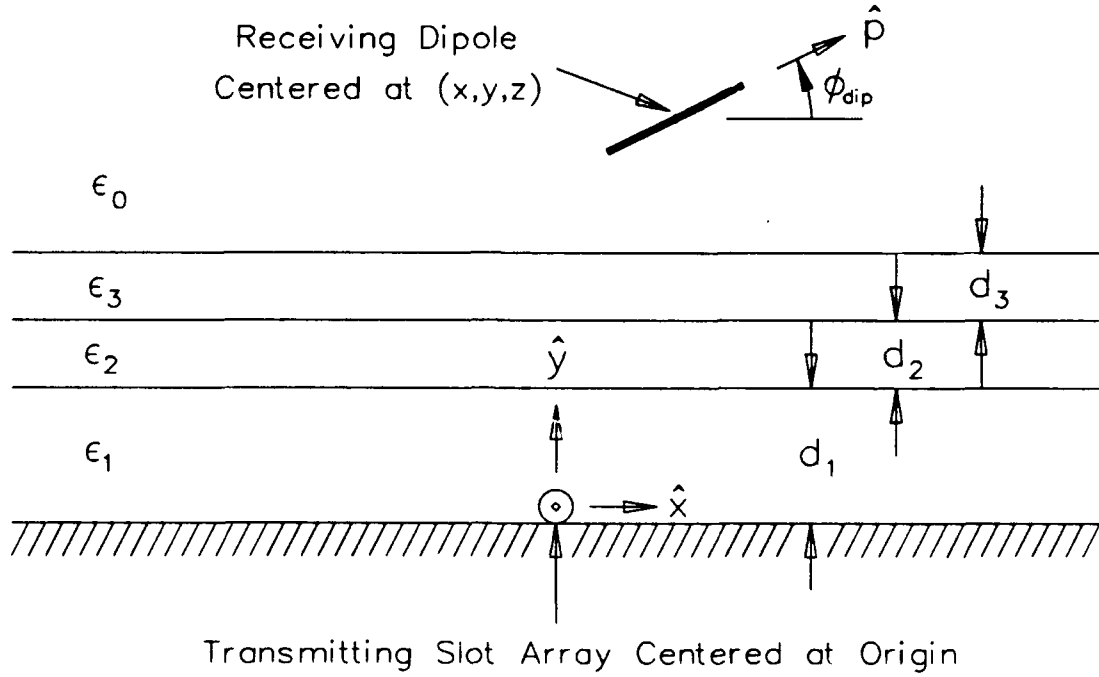


Figure 75: Geometry of Slot-to-Dipole Coupling through a Stratified Medium

4.2 COUPLING THROUGH A STRATIFIED MEDIA

In this section, we consider the coupling between slot and dipole column modes which exist between a set of infinite dielectric slabs. The solution will first be derived in terms of the slot mode radiating to a receiving dipole, which is the voltage gain in Equation (1.31). The geometry is shown in Figure 75. Although it depicts only three dielectric layers with an infinite half-space of free space, the analysis will be developed in terms of an arbitrary m number of slabs. The dipoles' orientation is in some transverse direction (i.e., $\hat{p} \perp \hat{z}$), with ϕ_{dip} designating the orientation angle with respect to \hat{x} .

The mutual coupling between the modes will be found using the Array Scanning Method (ASM). The derivation of the solution follows similarly to that of the Case

B slot-to-slot coupling (i.e., on different ground planes) through a stratified medium, except the testing with the receiving dipole's current must now be done with the electric field radiated by the slot mode.

As with other ASM applications in this dissertation, we begin by extending Equation (B.9) to the problem at hand. For the voltage gain, we construct an "artificial" doubly-infinite array of transmitting magnetic currents on the ground plane, and integrate out the scan as follows:

$$G^{CB} = \frac{D_x}{\lambda_1} \int_{-\frac{\lambda_1}{2D_x}}^{\frac{\lambda_1}{2D_x}} G_A^{CB} ds_x, \quad (4.10)$$

where G_A^{CB} is the voltage gain associated with the full doubly-infinite array of slots radiating to the receiving dipole. Again, choosing the inter-column spacing of $D_x = \lambda_1/2$ for the "artificial" array, we get:

$$G^{CB} = \frac{1}{2} \int_{-1}^1 G_A^{CB} ds_x. \quad (4.11)$$

The voltage gain between a doubly-infinite array of slots and a receiving dipole has been derived by Henderson [31]. This derivation uses the fact that the pattern factors for electric and magnetic fields from both slot and dipole sources are related by $\pm\eta$ factors, with the sign depending on the polarization and direction of propagation. His result is easily extended to the geometry shown in Figure 75, in which the receiving dipole is not necessarily oriented in some direction parallel to the XZ plane. From this, we get:

$$G_A^{CB} = \frac{1}{2D_x D_z} \sum_{k=-\infty}^{\infty} \sum_{n=-\infty}^{\infty} \frac{e^{-j\beta_0(\bar{R}_{dip} - \hat{y}d_{tot}) \cdot \hat{r}_{0,+}}}{r_{y1}} \phi_{1m} \cdot \left[P_{\parallel}^t P_{\perp}^{r,-} T_{\perp}^{HE} - \frac{r_{y1}}{r_{y0}} P_{\perp}^t P_{\parallel}^{r,-} T_{\parallel}^{HE} \right]. \quad (4.12)$$

In the above, we have defined

$$\bar{R}_{dip} = x\hat{x} + y\hat{y} + z\hat{z}, \quad (4.13)$$

which is a position vector to the center of the receiving dipole. The quantity d_{tot} represents the sum of the thicknesses of all the dielectric slabs. The unit vector $\hat{r}_{0,+}$ represents the direction of plane waves in free space after emerging from all the dielectric layers into free space. It is found by first identifying the plane wave directions in the dielectric slab nearest to the ground plane, which is:

$$\hat{r}_1 = (s_x + \frac{k\lambda_1}{D_x})\hat{x} + r_{y_1}\hat{y} + (s_{z_1} + \frac{n\lambda_1}{D_z})\hat{z}, \quad (4.14)$$

where r_{y_1} is chosen to normalize the vector with the positive root chosen for real values and the $-j$ root chosen for evanescent modes. This is the same r_{y_1} which is explicitly written twice in Equation (4.12). In the above, s_{z_1} is determined by a parameter s_{z_0} from an excitation source, as discussed in Chapter 5. In the remainder of this chapter, we shall assume $s_{z_1} = 0$.

To find $\hat{r}_{0,+}$, we step through the layers, applying the phase matching conditions in Equations (2.76) and (2.77) to get the \hat{x} and \hat{z} components of the plane wave directions in each material, then find the \hat{y} component by normalizing the unit vectors with either the positive real root or the $-j$ imaginary root for the $+\hat{y}$ direction convention (which is implied in the subscript in $\hat{r}_{0,+}$). The quantity ϕ_{1m} in Equation (4.12) is the same total phase delay factor through the dielectrics which is defined in Equation (2.106).

To complete the discussion of Equation (4.12), we must define the pattern and T factors. The pattern factors for the transmitting slot are related to the magnetic field that they radiate. They are the same as those defined by Equations (2.62) through (2.64), with the evaluations of the basic pattern integral performed for the

first dielectric slab's wavenumber, β_1 . With the possibility that piecewise sinusoidal or cosinusoidal currents may be defined with effective dielectric constants for the slots, the transmitting pattern factors (using the + exponential) in Equations (2.70) and (2.71) are appropriate.

The receiving pattern factors for the dipole are designated with a negative superscript to indicate that it applies to an incoming wave from the $-\hat{y}$ direction. These patterns are referenced to the electric field that the dipole receives. They are described by Equations (3.50), (3.54), and (3.56), with the simple replacement of the negative of ϕ_{dip} from Figure 75 for the variable, ϕ_r . Equation (3.52) may be used for the basic receive pattern factor when a piecewise sinusoidal testing current is assumed.

The T factors in Equation (4.12) carry the HE superscript to remind us that they "transform" the magnetic field radiated by the slot source into an electric field which is sensed by the dipole receiver. These T factors are:

$$T^{HE} = \frac{2 \tau_{m,0} \prod_{i=1}^{m-1} [1 + \Gamma_{i,i+1}]}{\prod_{i=1}^m [1 - \Gamma_{i,i-1} \Gamma_{i,i+1}^e e^{-j2\beta_i d_i r_{y_i}}]}. \quad (4.15)$$

In the above,

$$\tau_{m,0} = 1 + \Gamma_{m,0}, \quad (4.16)$$

which is a Fresnel transmission coefficient from the last dielectric slab to the free space. It was separated from the other transmission coefficients in the numerator product to avoid any confusion since the material index increases from 1 to m , then goes to 0. Equation (4.15) applies to both the parallel and perpendicular polarization terms used in Equation (4.12), with the common subscripts deleted from each coefficient in Equation (4.15) for convenience. The Γ^e quantity in the denominator is an effective reflection coefficient, which is found by successive applications of Equations

(2.101) and (2.102), starting with the Fresnel coefficient $\Gamma_{m,0}$ and working inward to the 1,2 interface. Finally, it must be noted that all coefficients in Equation (4.15) are related to the electric field, thus the appropriate Fresnel reflection coefficients are in Equations (3.47) and (3.48).

The terms indexed by the material i in the denominators of the T factors may go to zero at certain scan directions. This is again an indication of the resonant excitation of a surface wave in the i th medium. These singularities may be integrated around numerically by introducing a slight loss in the \hat{y} -directed propagation exponential in the denominator of Equation (4.15). This is the same approach adopted with multiple dielectric slabs for the Case B slot-to-slot coupling (i.e., slots on different ground planes), which we have dubbed the “numerically integrated version of the ASM”.

The implementation of the plane wave expansion for the integrand used in the ASM may be truncated to including only the propagating plane wave modes launched by the slot array in the first dielectric slab. Since ϵ_1 has to be greater than or equal to the dielectric constant of free space, no propagating plane waves will enter free space from evanescent modes launched by the slot array source. In addition, any plane waves launched as evanescent modes should be of negligible strength upon reaching the dipole, especially if the dipole is reasonably spaced from the outer dielectric interface (i.e., at least about $\lambda_0/4$).

Several experiments were performed using the ASM solution of Equation (4.11) with the integrand being only the propagating modes in Equation (4.12). The first experiment consisted of a slot in a ground plane coated by a thin layer of styrofoam. The styrofoam was modelled with a relative dielectric constant of 1.05 and a thickness of $\lambda_0/30$. The slot and dipole lengths were both $0.4\lambda_0$ and the inter-element spacing was $D_z = 0.6\lambda_0$. An effective dielectric constant of the free space constant was used

for defining piecewise sinusoidal current shapes for both the slots and dipole. The dipole was oriented along \hat{x} , which corresponds to $\phi_{dip} = 0$. In this and all examples used in this chapter, the center of the dipole was always at $z = 0$. To create a pattern, the total distance y from the dipole to the ground plane (not just to the styrofoam) was varied.

This example case is similar to the case used in creating Figure 71, with the exceptions that a thin layer of styrofoam is now present and the voltage gain is to be determined instead of the current gain (from the dipole mode radiating to the slot). However, intuition and experience suggest that the styrofoam should have little effect, and with the "quasi-Galerkin" approach of having the same current forms for transmitting and testing, the voltage gain should be the exact negative of the current gain. Therefore, the rigorously integrated data from Figure 71 may be inverted and compared with the ASM calculated data with the styrofoam slab present. This was done, and the results are plotted in Figure 76.

The ASM computed data compares extremely well with the direct free space calculations (using Equation (4.8)), confirming the validity of the ASM solution. Only a slight discrepancy exists when the dipole is less than $1\lambda_0$ from the ground plane. This discrepancy is caused by a combination of the near zone effect of the styrofoam and the neglecting of evanescent terms in the ASM calculations.

A second example was formed with the same styrofoam coated ground plane. All parameters in this example remained the same as before, except the dipoles were rotated 45° from the ground plane. This example is similar to the free space example in Figure 72, so the "rigorous solution" data from this figure was inverted (to convert current gain into voltage gain) and compared with ASM based calculations using the styrofoam. The results are plotted in Figure 77. Again, the ASM data compares favorably with the free space calculations.

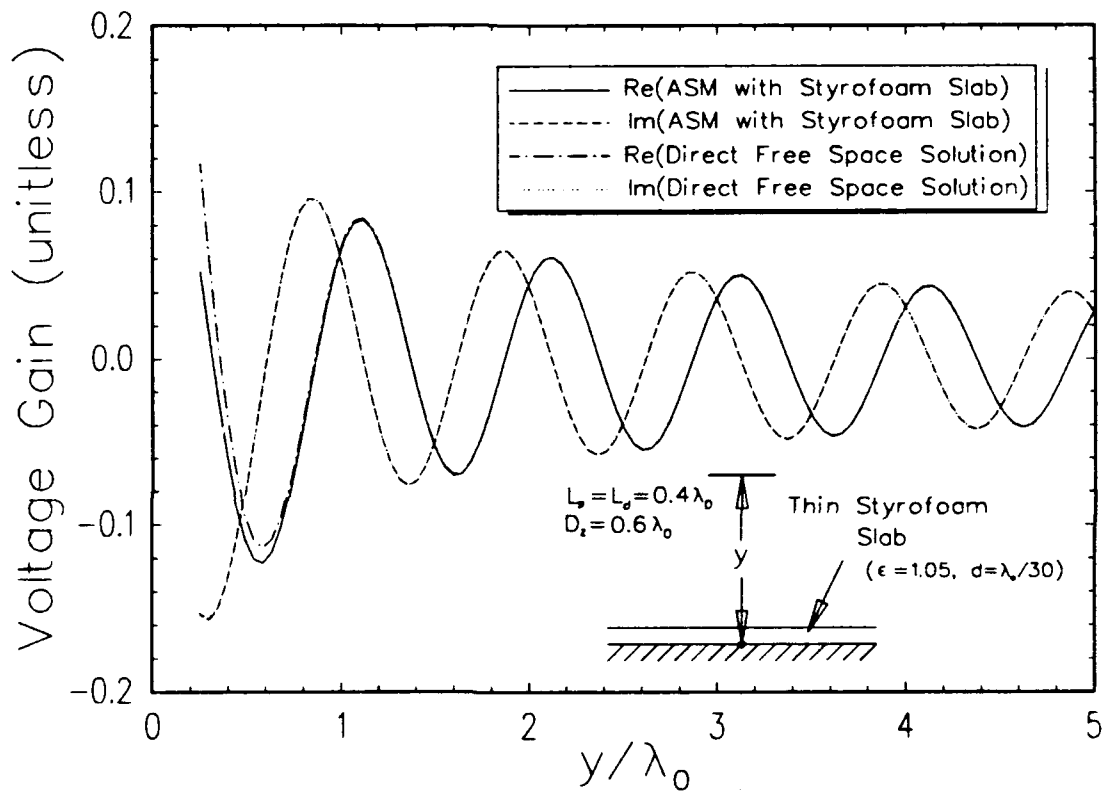


Figure 76: Slot-to-Dipole Coupling with the Dipole Parallel to a Styrofoam Coated Ground Plane - $L_s = L_d = 0.4\lambda_0$, $D_z = 0.6\lambda_0$, $s_z = 0$, $d_1 = \lambda_0/30$, $\epsilon_1 = 1.05\epsilon_0$

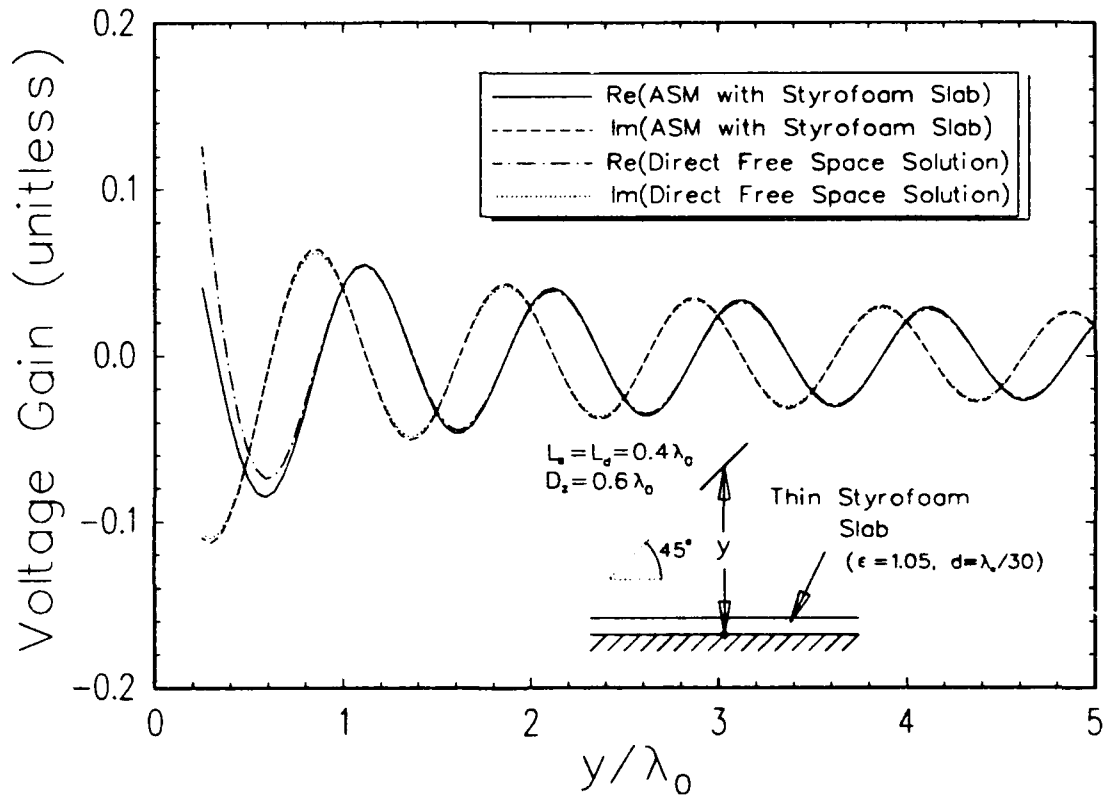


Figure 77: Slot-to-Dipole Coupling with the Dipole 45° to a Styrofoam Coated Ground Plane - $L_s = L_d = 0.4\lambda_0$, $D_z = 0.6\lambda_0$, $s_z = 0$, $d_1 = \lambda_0/30$, $\epsilon_{1r} = 1.05$

The third example for the ASM uses two dielectric slabs on the ground plane. The dielectric nearest the ground plane has a permittivity of 4 times that of free space and the outer slab has a permittivity of 2 times that of free space. Both slabs are one-fifth of a wavelength thick for their respective wavelengths. A single column of slots are cut into the ground plane with lengths of $\lambda_1/2$ and inter-element spacings of $D_z = 3\lambda_1/4$. An effective dielectric constant of $4\epsilon_0$ is used to define the piecewise sinusoidal current shape used for the slots. The receiving dipole tests with a piecewise sinusoidal current and is tilted to 45° from \hat{x} and located at a distance of $y - d_{tot} = 1\lambda_0$ from the outer dielectric interface. To create a pattern, the x position of the dipole relative to the slot was varied from $-2\lambda_0$ to $+2\lambda_0$. The ASM computed data is shown in Figure 78.

In addition to the real and imaginary components of the coupling being plotted in Figure 78, the total magnitude of the complex voltage gain is also shown. This magnitude is asymmetric about x , which is explained by the pattern factor of the receiving dipole. By a simple geometrical optics argument with the known pattern of a dipole, the maximum should occur in the neighborhood of $x = -1\lambda_0$, which is where the dipole is fully "broadside" to the slot. Similarly, a minimum should occur at about $x = +1\lambda_0$, where the dipole is "end-fire" to the slot. The precise maximum and minimum locations get distorted, though, by both a refraction effect and a spatial decay factor. However, the data in Figure 78 closely supports the intuition from geometrical optics, further confirming the validity of the ASM solution for the coupling.

Next, we show what happens to the coupling when the dipoles remain parallel to the double-slab coated ground plane (see insert in Figure 79). In this case, all parameters are the same as the previous example, except now the dipole angle is $\phi_{dip} = 0$ and the dipoles are brought to only $y - d_{tot} = 0.2\lambda_0$ from the outer dielectric

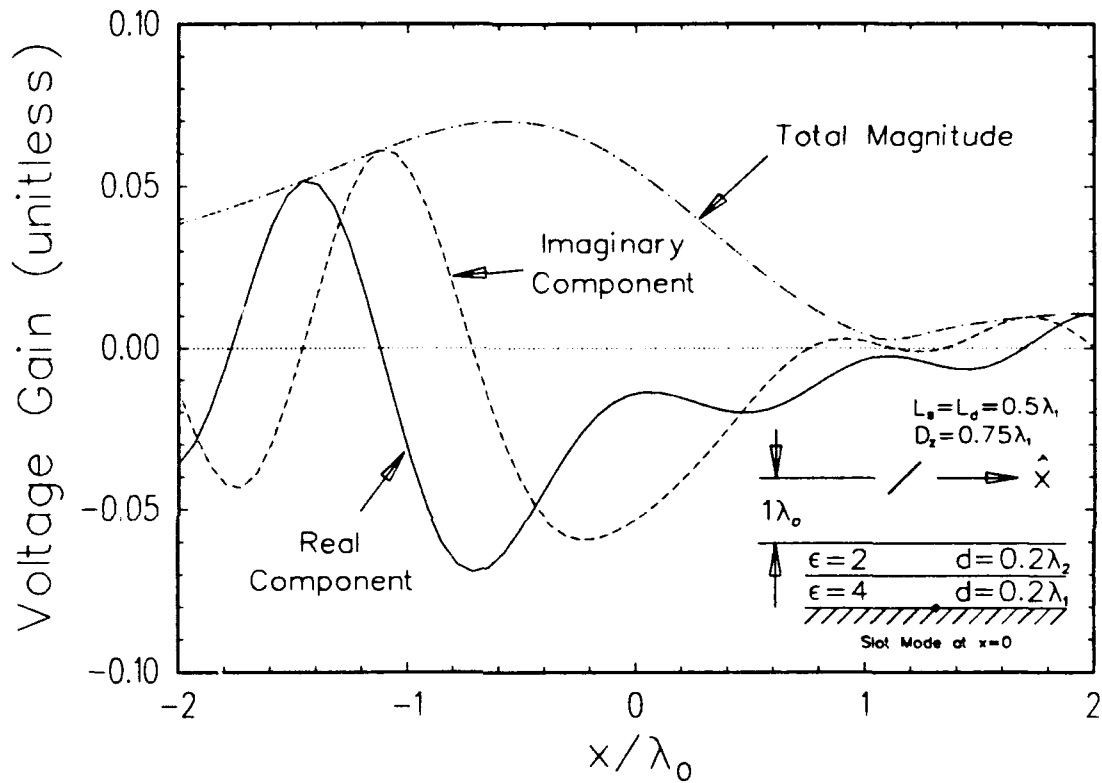


Figure 78: Slot-to-Dipole Coupling with the Double Slab Example Geometry and Dipoles Tilted to 45° from \hat{x} , $y-d_{tot} = 1\lambda_0$, $\epsilon_{1r} = 4$, $\epsilon_{2r} = 2$, $d_1 = 0.2\lambda_1$, $d_2 = 0.2\lambda_2$, $L_s = L_d = 0.5\lambda_1$, $D_z = 0.75\lambda_1$, $s_z = 0$

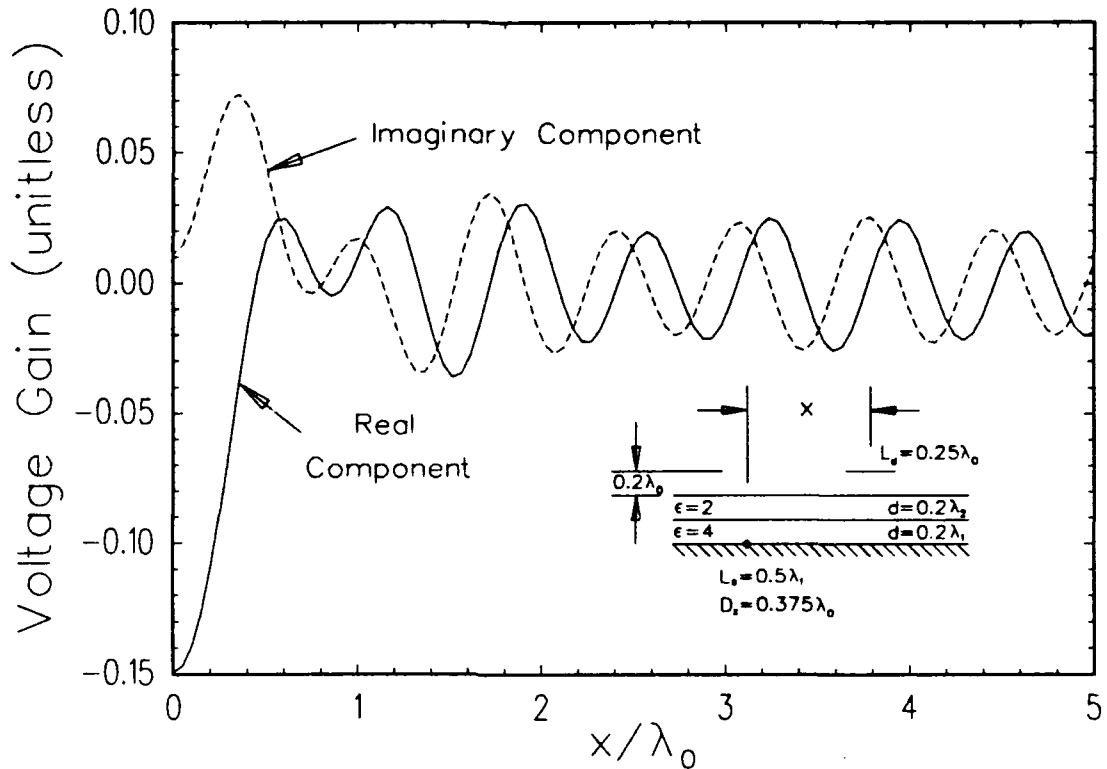


Figure 79: Slot-to-Dipole Coupling with the Double Slab Example Geometry and Dipoles Parallel to the Ground Plane, $y - d_{tot} = 0.2\lambda_0$

interface. The ASM solution for the voltage gain between the column modes was used as the x position of the dipole varied with respect to the slots. The results are plotted in Figure 79.

Beyond $x > 2\lambda_0$, the data in Figure 79 appears as nearly a constant sinusoid for both the real and imaginary components of gain. The period of this sinusoid is shorter than a free space wavelength. This suggests a surface wave is dominating the data at this point. Indeed, although any surface wave must be trapped inside the dielectric slabs, their effects can dominate the voltage gain data as it is evanescently coupled through the $0.2\lambda_0$ layer of free space to the receiving dipole.

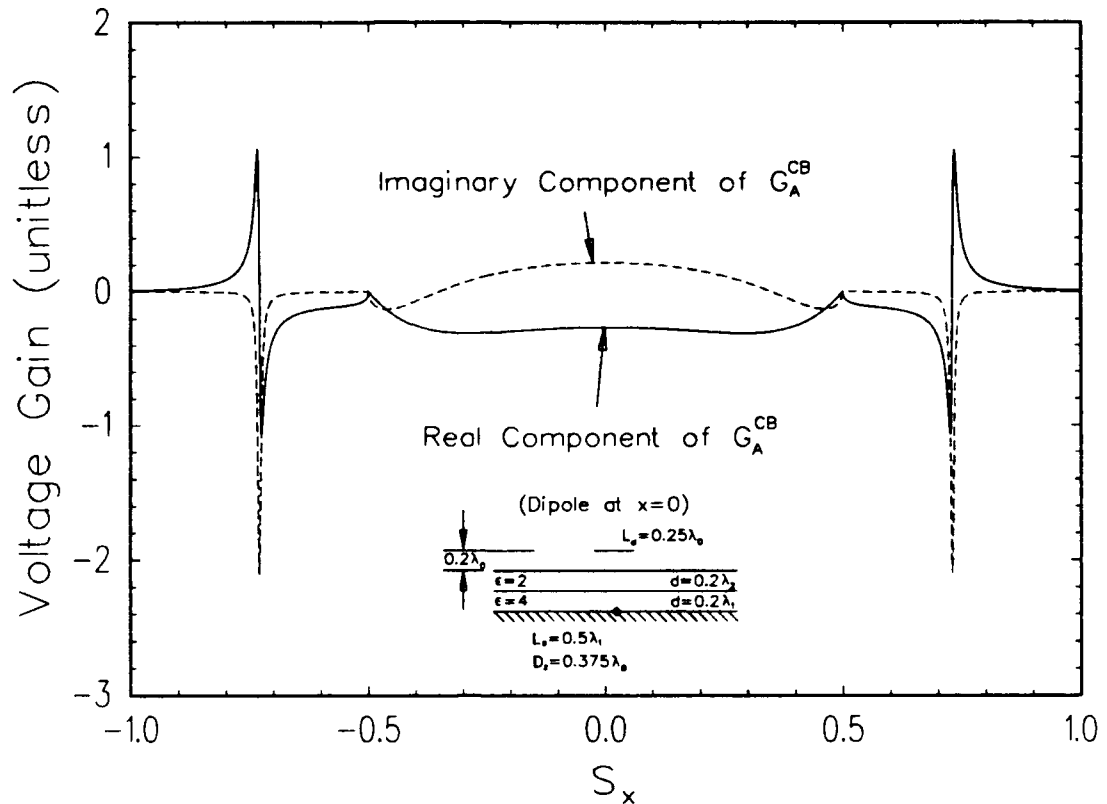


Figure 80: Integrand for Previous ASM Solution at $x = 0$

The relatively strong surface wave phenomena is evident in Figure 80, which depicts the integrand used in this ASM application for the position $x = 0$. At the scan position of $s_x = \pm 0.5$, a critical angle is established where no propagation can emerge into the free space region. At about $s_x = 0.73$, the resonant excitation of a strong surface wave is clearly evident. This surface wave is actually excited in the first dielectric slab (nearest the ground plane), which can be seen by examining the factors of the denominator of $T_{||}^{HE}$ for each dielectric layer (ref. Equation (4.15)). No surface wave is excited in the second dielectric layer for the full scan range in the first material. Note that a loss tangent of 0.02 was used to eliminate the true surface wave singularity for this plot.

Figure 80 is essentially an inverse Fourier transform of the data in Figure 79. In fact, for this example, the data in Figure 80 could have been run through a Fast Fourier Transform algorithm to speed up the production of the data in Figure 79, as is done with the slot-to-slot coupling with stratified media. However, for most moment method problems, the geometry of the dipoles in relation to the slots will not be a simple periodicity in x only with y and z held constant. Therefore, in general, the application of an FFT for this coupling is not as beneficial as it is for slot-to-slot coupling.

Since this surface wave coupling should become weaker as the dipole moves further from the outer dielectric interface, an experiment was performed to see what the coupling would be under the same conditions used to produce Figure 79, except changing $y - d_{tot}$ from $0.2\lambda_0$ to $0.7\lambda_0$. The ASM computed result is plotted in Figure 81. Note that the scales in this figure are the same as those in Figure 79, and that the amplitudes of what may be surface waves is much smaller than before.

In Figure 82, we plot the ASM integrand used to produce Figure 81¹. The scales are the same as those used in Figure 80. Note that the surface waves are barely evident at $s_x \approx \pm 0.73$, and that the coupling before the critical angle is of the same order of magnitude as with the closer spaced case in Figure 80.

Finally, we wish to validate the ASM produced slot-to-voltage coupling data by spatially adding 101 column-to-column terms with a Floquet phasing factor and Fejer kernel to simulate the scanning voltage gain between two doubly-infinite arrays. This data may be compared with voltage gain data used by the PMM code [3]. With the double slab geometry used in producing Figure 79 (along with the same element lengths and directions, D_z and current shapes - note that $y - d_{tot} = 0.2\lambda_0$), we simulate this scanning voltage gain for a column-to-column spacing of

¹Again, loss tangents of 0.02 are used for each slab.

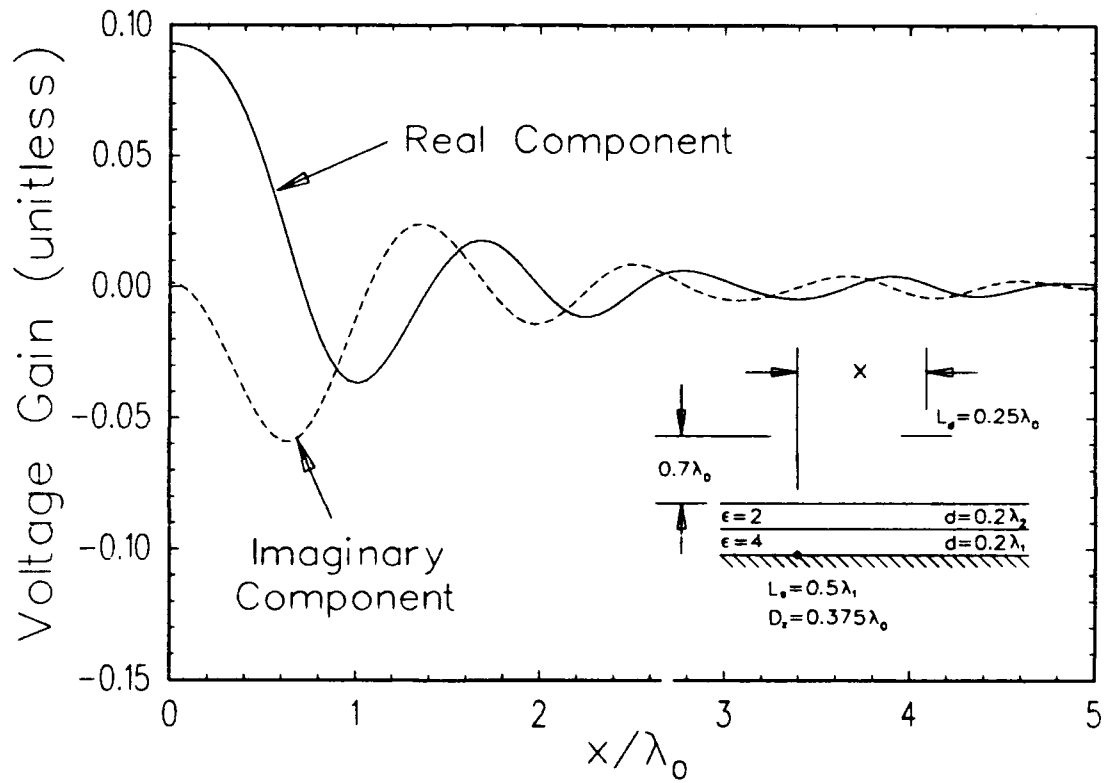


Figure 81: Slot-to-Dipole Coupling with the Double Slab Example Geometry and Dipoles Parallel to the Ground Plane, $y - d_{tot} = 0.7\lambda_0$

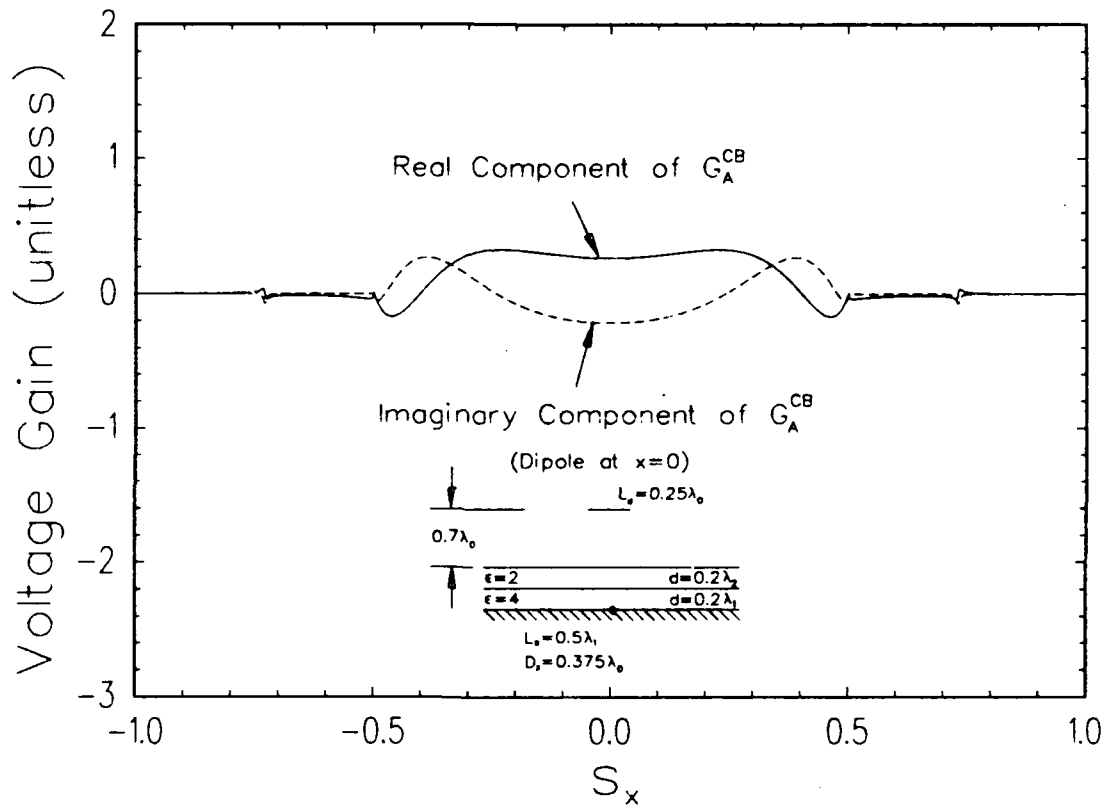


Figure 82: Integrand for Previous ASM Solution at $x = 0$

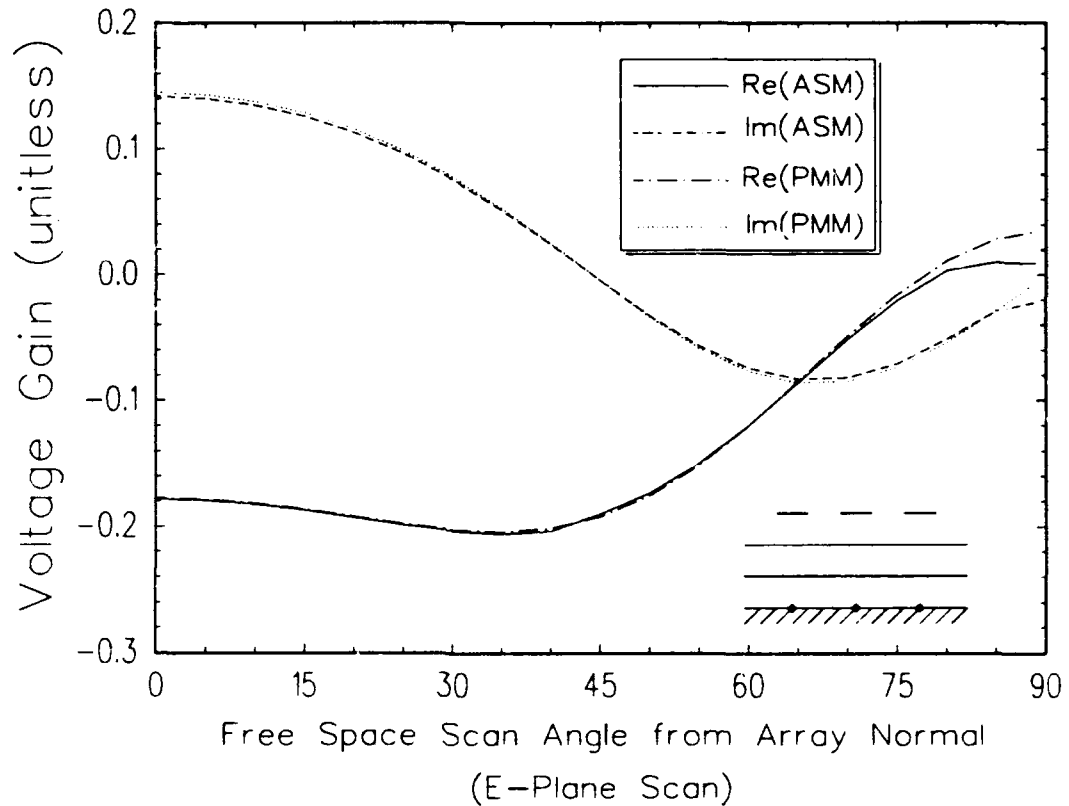


Figure 83: Scanning Voltage Gain between a Doubly-Infinite Array of Transmitting Slots and a Receiving Dipole with the Double Slab Example Geometry - $y - d_{tot} = 0.2\lambda_0$

$D_x = 0.375\lambda_0 = 0.75\lambda_1$. The simulated scanning voltage gain from the ASM data is plotted in Figure 83, along with the reference data from the PMM code. The agreement between the curves is excellent until very high scan angles are reached, which is attributed to the Fejer kernel addition. This demonstrates that the data in Figure 79 is probably accurate, even though the ASM implementation ignored all evanescent wave excitations within the first dielectric slab².

Now consider what happens when the transmitting slot mode and receiving dipole are spaced far apart. Using the previously described double slab geometry,

²In this example, the only term used for the ASM integrand was the $k = n = 0$ term.

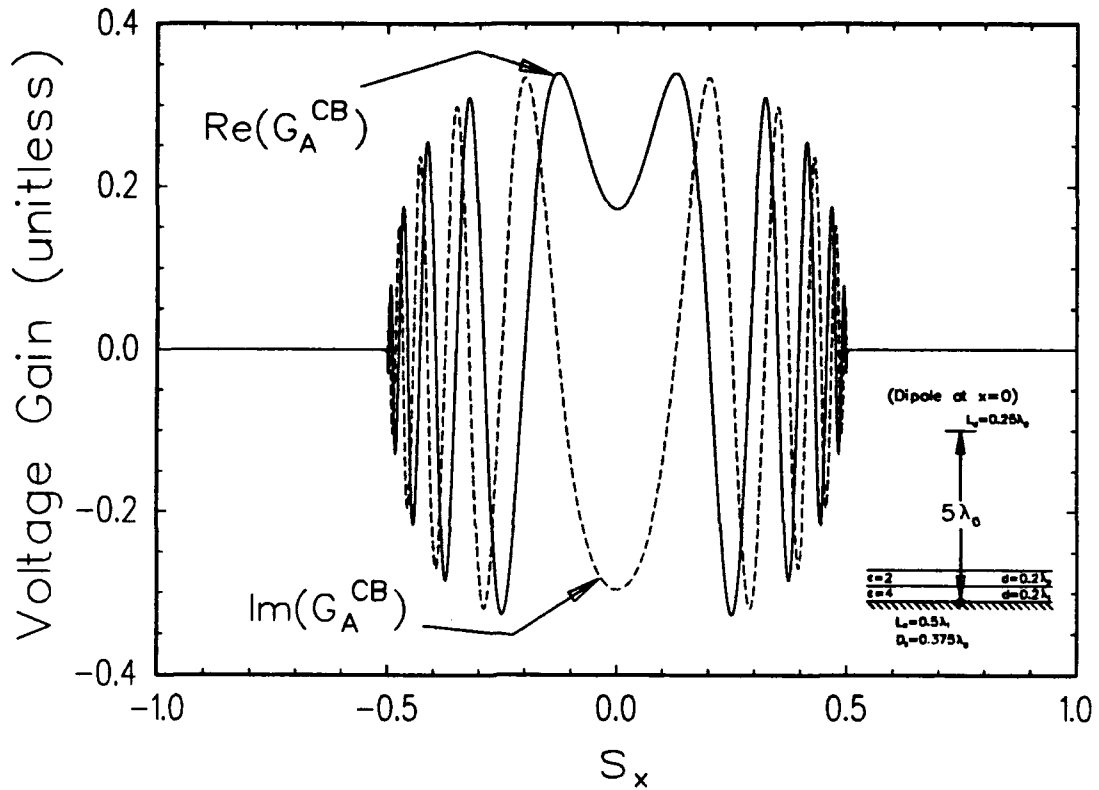


Figure 84: Integrand for ASM Solution with the Double Slab Geometry and the Dipole at $(0, 5\lambda_0, 0)$

we examine the integrand for the ASM when the dipole is centered at $x = z = 0$ and $y = 5\lambda_0$. This integrand is plotted in Figure 84.

As seen in Figure 84, as the modes become widely spaced, the integrand becomes very oscillatory and therefore more difficult to numerically integrate. However, a stationary phase evaluation may be made, similar to that performed for the reflected component of dipole-to-dipole impedance in Chapter 3.

The stationary phase point is identified by the s_x parameter which solves the following equation:

$$x = d_1 \frac{s_x}{\sqrt{1 - s_x^2}} + d_2 \frac{\left(\frac{\beta_1 s_x}{\beta_2}\right)}{\sqrt{1 - \left(\frac{\beta_1 s_x}{\beta_2}\right)^2}} + \dots$$

$$+ d_m \frac{\left(\frac{\beta_1 s_x}{\beta_m}\right)}{\sqrt{1 - \left(\frac{\beta_1 s_x}{\beta_m}\right)^2}} + (y - d_{tot}) \frac{\left(\frac{\beta_1 s_x}{\beta_0}\right)}{\sqrt{1 - \left(\frac{\beta_1 s_x}{\beta_0}\right)^2}}, \quad (4.17)$$

where x and y are the coordinates of the center of the dipole and the slot is centered at the origin. A quick numerical search may be made to find the value of s_x which solves Equation (4.17), which corresponds to the scanning direction which guides a ray through the dielectrics (at the plane wave refracting angles) and into the free space region from the slot mode to the center of the receiving dipole.

Once the stationary phase point is located, the stationary phase approximation to the ASM integral is:

$$G^{CB} \approx -\frac{1}{2D_z} \sqrt{\frac{j}{\rho\lambda_0}} e^{-j\beta_0\rho} \phi_{1m} P_{\perp}^t P_{\parallel}^r, -T_{\parallel}^{HE} \Big|_{stat.pha.pt.} \quad (4.18)$$

where

$$\rho = \sqrt{x^2 + (y - d_{tot})^2}. \quad (4.19)$$

To test the stationary phase evaluation, we compared it with the numerically integrated ASM solution for the double slab example geometry with the same slot and dipole mode types previously described. First, we kept the x coordinate of the receiving dipole at zero and varied the y coordinate from just "above" the outer dielectric interface until $y = 3\lambda_0$. This comparison is shown in Figure 85. The data shows that the stationary phase evaluation is surprisingly good at very low values of y , and very accurate when $y > 2\lambda_0$.

In Figure 86, we compare the numerically integrated ASM solution with the stationary phase solution with the same geometry except fixing y at $2\lambda_0$ and varying x . In this data, the stationary phase point drifts from $s_x = 0$. Thus, the excellent agreement in this figure demonstrates that the stationary phase point is being accurately tracked. It also demonstrates that the stationary phase solution is generally good as long as $\rho > 2\lambda_0$.

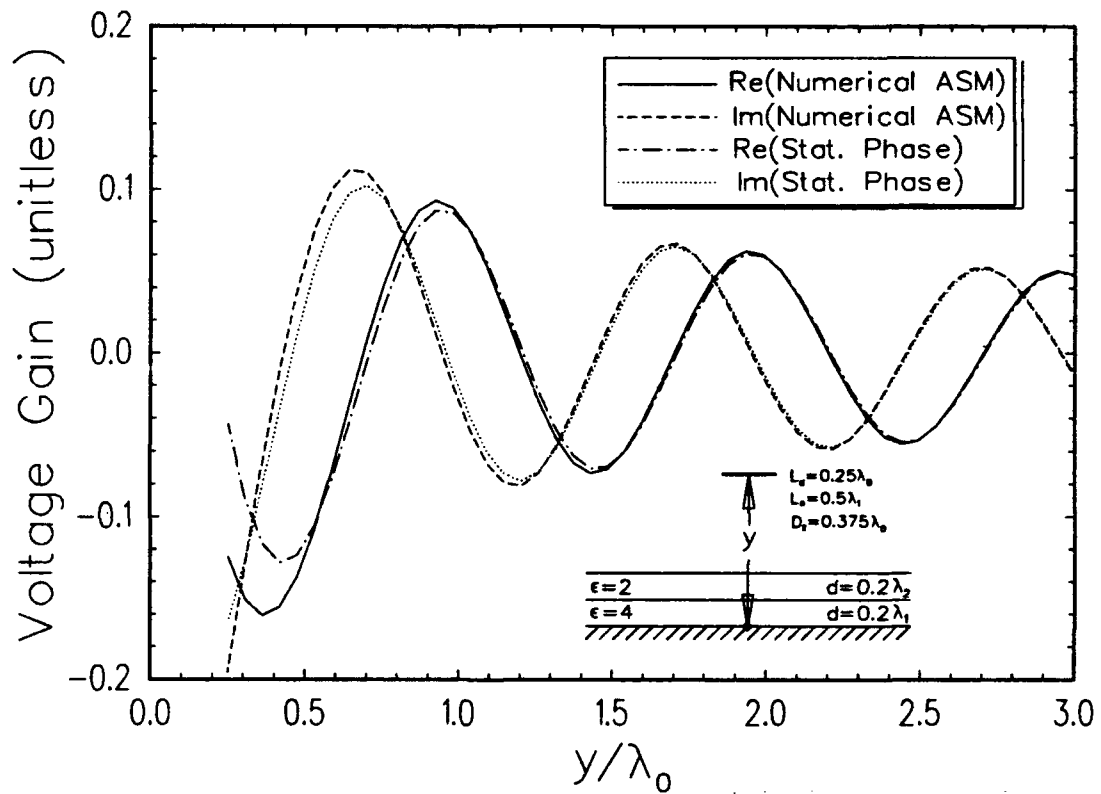


Figure 85: Comparison of Numerically Integrated ASM Solution and Stationary Phase Solution for Slot-to-Dipole Coupling with the Double Slab Example Geometry vs. y at $x = z = 0$

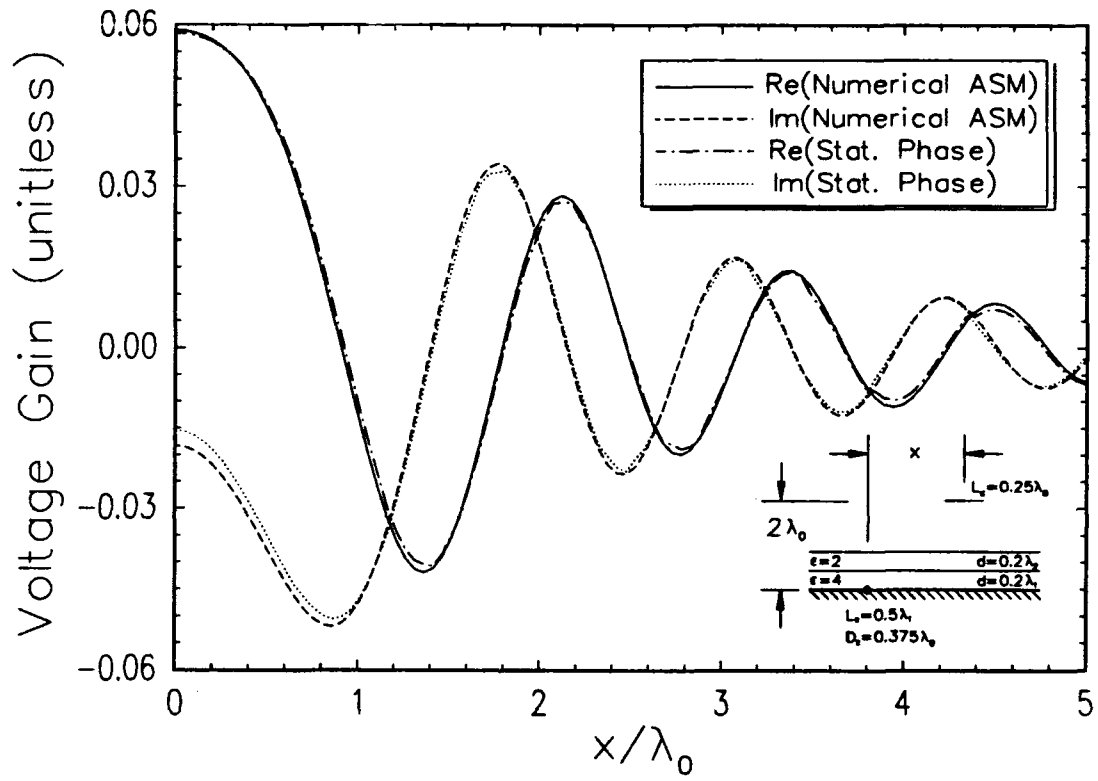


Figure 86: Comparison of Numerically Integrated ASM Solution and Stationary Phase Solution for Slot-to-Dipole Coupling with the Double Slab Example Geometry vs. x at $y = 2\lambda_0$ and $z = 0$

To conclude this chapter, we present the ASM formulation for the current gain between a transmitting column of periodic dipoles and a receiving slot with a dielectric coated ground plane. Applying the Lorentz reciprocity to Equations (4.10) and (4.12), it is simply:

$$G^{BC} = -\frac{D_x}{\lambda_0} \int_{-\frac{\lambda_0}{2D_x}}^{\frac{\lambda_0}{2D_x}} \left[\frac{1}{2D_x D_z} \sum_{k=-\infty}^{\infty} \sum_{n=-\infty}^{\infty} \frac{e^{-j\beta_0(\bar{R}_{dip} - \hat{y}d_{tot}) \cdot \hat{r}_{0,+}}}{r_{y1}} \cdot \phi_{1m} \left[P_{\parallel}^r P_{\perp}^{t,-} T_{\perp}^{HE} - \frac{r_{y1}}{r_{y0}} P_{\perp}^r P_{\parallel}^{t,-} T_{\parallel}^{HE} \right] \right] ds_x, \quad (4.20)$$

where all variables are defined the same as with the ASM solution for the voltage gain with the geometry shown in Figure 75, except for the pattern factors. The transmitting pattern factors in the above refer to the electric field emitted from the dipoles. The basic transmitting pattern factor is:

$$P^{t,-} = \int_{-\frac{L_{dip}}{2}}^{\frac{L_{dip}}{2}} I(p) e^{+j\beta_0 p \hat{p} \cdot \hat{r}_{0,-}} dp. \quad (4.21)$$

The polarization components of this factor are found by applying Equations (3.54) and (3.56) to $P^{t,-}$, with the substitution of the negative of ϕ_{dip} for ϕ_r .

The receiving pattern factors for the current gain apply to the magnetic field sensed by the slots, and is the same as those defined in Equations (2.62) through (2.64).

Finally, it should be noted that when the "quasi-Galerkin" approach of having a testing current of the same form of the transmitting current for each mode, the calculation of the current gain is not necessary, sense it will be the exact negative of the corresponding voltage gain.

CHAPTER V

EXCITATION SOURCES AND FAR ZONE FIELDS

In this chapter, we shall develop expressions for the excitation vector and we shall show how to obtain far zone scattered fields from the magnetic slot currents to complete the moment method solution developed in the previous four chapters.

Two types of excitation sources may be considered. The first, and simplest, is a direct excitation of some or all of the dipole modes by delta gap generators. Such an excitation is discussed by Thiele [18], and is trivial to implement in the excitation vector. This kind of excitation will be used when antenna radiation patterns are to be generated. Since this excitation is relatively easy to use and understand, no further discussion of it will be given in this dissertation.

The second excitation source to be considered is from an external plane wave. With the constraint that such a plane wave exists only in Region I (ref. Figure 4), this source only directly excites a set of currents for the slot modes on the ground plane between Regions I and II (i.e., the "type A" slots). This excited current is discussed in the first section of this chapter.

The last section of this chapter devotes itself to the solution of the far zone scattered fields which are radiated by the equivalent scattering currents.

5.1 INDUCED CURRENT IN A SLOT FROM AN EXTERNAL PLANE WAVE SOURCE

This section develops solutions for the current which is excited in the slots of the first ground plane in a scattering problem. This current, unlike the equivalent magnetic scattering currents for the slots¹, has units of electric amperes. To eliminate confusion, it is reasonable to think of this excited current as a "magnetic voltage".

Regardless of the nomenclature adopted, the excitation current from an external source is defined by Equation (1.33). Recall that the integral in this equation is only over the length of the reference slot for a particular mode.

Consider the geometry shown in Figure 87. It shows a view from the $-\hat{z}$ axis (i.e., the "bottom view") of a magnetic testing current for a reference slot on a dielectric coated ground plane. Note that the center of the \hat{z} -directed slot current is arbitrarily positioned with the constraint that it lies on the ground plane. Although only three dielectric slabs are depicted on the ground plane, the number of slabs is arbitrary with a material index running from 1 (nearest the ground plane) to m . The infinite half space is free space.

The direction of incidence and a pair of orthogonal polarization states for the propagating plane wave source are depicted in Figure 88.

In Figure 88, the direction of incidence (in medium "0") may be defined as:

$$\hat{s}_0 = s_{x_0}\hat{x} + s_{y_0}\hat{y} + s_{z_0}\hat{z}, \quad (5.1)$$

where the directional components are:

$$s_{x_0} = -\cos \alpha \sin \eta \quad (5.2)$$

$$s_{y_0} = \cos \eta \quad (5.3)$$

¹Recall that the equivalent magnetic currents, which have units of volts, are the unknowns in the moment method problem.

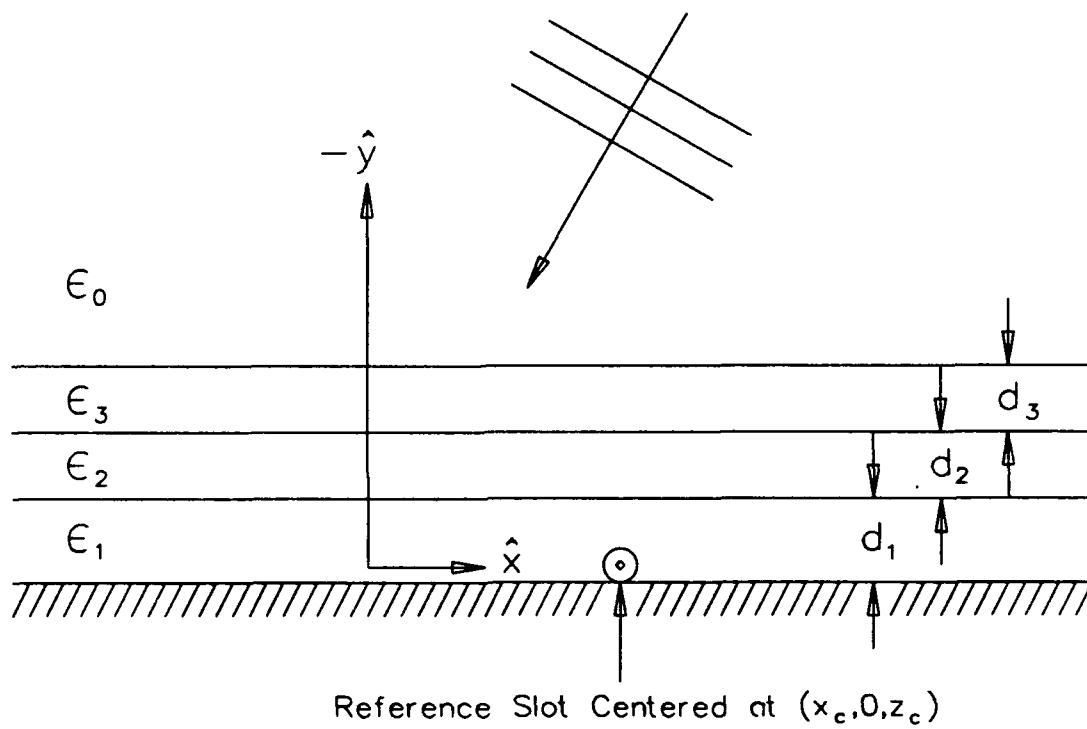


Figure 87: Bottom View of Plane Wave Excitation of a Slot

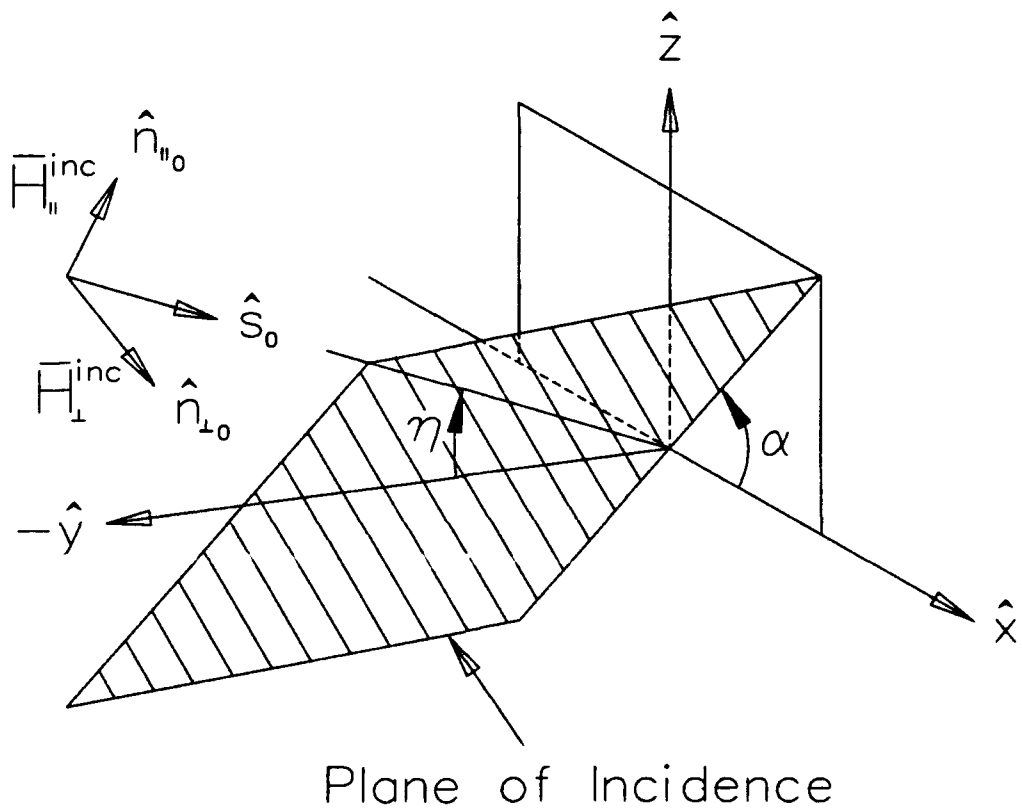


Figure 88: Propagation Direction and Orthogonal Polarization States for an Incident Plane Wave

$$s_{z_0} = -\sin \alpha \sin \eta, \quad (5.4)$$

and the angle of incidence is such that $0 \leq \alpha \leq 180^\circ$ and $-90^\circ \leq \eta \leq 90^\circ$. These α and η angles always refer to the incident propagation direction in free space.

No matter what polarization is used in the incident wave, it may be decomposed into the two depicted linear polarizations from Figure 88, such that

$$\overline{H}^{inc} = C_{\parallel} \overline{H}_{\parallel}^{inc} + C_{\perp} \overline{H}_{\perp}^{inc}, \quad (5.5)$$

where C_{\parallel} and C_{\perp} are complex constants. The magnetic fields for these linear polarizations are in the directions $\hat{n}_{\parallel 0} = \hat{\eta}$ and $\hat{n}_{\perp 0} = -\hat{\alpha}$, respectively. These directions are given by:

$$\hat{n}_{\perp 0} = -\frac{\hat{y} \times \hat{s}_0}{|\hat{y} \times \hat{s}_0|} \quad (5.6)$$

and

$$\hat{n}_{\parallel 0} = \frac{\hat{n}_{\perp 0} \times \hat{s}_0}{|\hat{n}_{\perp 0} \times \hat{s}_0|}. \quad (5.7)$$

Substituting Equation (5.1) into (5.6) and (5.7), we get:

$$\hat{n}_{\perp 0} = \frac{-s_{z_0} \hat{x} + s_{x_0} \hat{z}}{\sqrt{s_{x_0}^2 + s_{z_0}^2}} \quad (5.8)$$

and

$$\hat{n}_{\parallel 0} = \frac{-s_{x_0} s_{y_0} \hat{x} + (s_{x_0}^2 + s_{z_0}^2) \hat{y} - s_{y_0} s_{z_0} \hat{z}}{\sqrt{s_{x_0}^2 + s_{z_0}^2}}. \quad (5.9)$$

As the incident plane wave enters the various dielectric slabs, its propagation direction refracts and the polarization vectors change. The transverse propagation direction components in the i th material are:

$$s_{x_i} = s_{x_0} \frac{\beta_0}{\beta_i} \quad (5.10)$$

and

$$s_{z_i} = s_{z_0} \frac{\beta_0}{\beta_i}. \quad (5.11)$$

The \hat{y} component of the plane wave direction in the i th material is

$$s_{y_i} = \sqrt{1 - s_{x_i}^2 - s_{z_i}^2}, \quad (5.12)$$

with the positive real root taken².

The polarization directions in the i th material are found by using Equations (5.8) and (5.9), with the substitution of s_{x_i} , s_{y_i} , and s_{z_i} for s_{x_0} , s_{y_0} , and s_{z_0} , respectively. Note that $\hat{n}_{\perp i} = \hat{n}_{\perp 0}$ for any material i , but in general, $\hat{n}_{\parallel i} \neq \hat{n}_{\parallel 0}$.

In order to evaluate the excitation current, we need to know the total magnetic field at the testing element due only to the presence of the excitation plane wave. This field is the "generalized incident" field used in Equation (1.33). Consider some point on the slot current at the ground plane, designated by the position vector

$$\bar{R} = x_c \hat{x} + z \hat{z}. \quad (5.13)$$

Applying duality to electric field expressions derived by Munk [1, 2], the total magnetic field created by the incident plane wave may be found anywhere in the geometry shown in Figure 87. At the position \bar{R} , the generalized incident magnetic field is:

$$\begin{aligned} \bar{H}^{ginc}(\bar{R}) = & \phi_{m1} e^{-j\beta_1 \bar{R} \cdot \hat{s}_1} \left[[\bar{H}^{inc}(0, -d_{tot}, 0) \cdot \hat{n}_{\perp 0}] T_{\parallel}^{HE} \hat{n}_{\perp 1} \right. \\ & \left. + [\bar{H}^{inc}(0, -d_{tot}, 0) \cdot \hat{n}_{\parallel 0}] \frac{s_{y_0}}{s_{y_1}} T_{\perp}^{HE} [\hat{n}_{\parallel 1} - \hat{y}(\hat{y} \cdot \hat{n}_{\parallel 1})] \right]. \quad (5.14) \end{aligned}$$

The field $\bar{H}^{inc}(0, -d_{tot}, 0)$ is the magnetic field of the incident plane wave evaluated at a point on the outer dielectric interface "above" the origin. The function ϕ_{m1} represents a phase delay from this point to the origin on the ground plane, which is

$$\phi_{m1} = \prod_{i=1}^m \phi_i = \prod_{i=1}^m e^{-j\beta_i d_i s_{y_i}}. \quad (5.15)$$

²Note that evanescent waves can never be formed inside the dielectric slabs from the propagating wave in free space since $\epsilon_i \geq \epsilon_0$.

Finally, the T^{HE} functions give the effective transmission from the free space region through the dielectric layers into the layer nearest the ground plane. These functions are given in Equation (4.15), with electric field reflection coefficients used as they were done in Chapter 4.

The expression for the generalized incident field in Equation (5.14) may now be substituted into Equation (1.33) to get the excitation current. Noting that the receiving slot is \hat{z} oriented, this becomes:

$$I^A = \int_{z_c - \frac{L}{2}}^{z_c + \frac{L}{2}} \phi_{m1} e^{-j\beta_1 \bar{R} \cdot \hat{s}_1} \left[[\bar{H}^{inc}(0, -d_{tot}, 0) \cdot \hat{n}_{\perp 0}] T_{\parallel}^{HE} \frac{s_{z_1}}{\sqrt{s_{x_1}^2 + s_{z_1}^2}} - [\bar{H}^{inc}(0, -d_{tot}, 0) \cdot \hat{n}_{\parallel 0}] T_{\perp}^{HE} \frac{s_{y_0} s_{z_1}}{\sqrt{s_{x_1}^2 + s_{z_1}^2}} \right] I^{test}(z) dz. \quad (5.16)$$

In the above, $I^{test}(z)$ is the magnetic testing current associated with the slot mode. This is the same testing current for this mode which is used in finding entries for the coupling matrix.

The excitation current expression in Equation (5.16) may be simplified by adopting some pattern factor definitions which are similar to those used elsewhere in this dissertation. The compact expression is:

$$I^A = \phi_{m1} e^{-j\beta_1 \bar{R}_c \cdot \hat{s}_1} \left[[\bar{H}^{inc}(0, -d_{tot}, 0) \cdot \hat{n}_{\perp 0}] T_{\parallel}^{HE} P_{\perp,1}^r + [\bar{H}^{inc}(0, -d_{tot}, 0) \cdot \hat{n}_{\parallel 0}] T_{\perp}^{HE} \frac{s_{y_0}}{s_{y_1}} P_{\parallel,1}^r \right], \quad (5.17)$$

where

$$\bar{R}_c = x_c \hat{x} + z_c \hat{z}, \quad (5.18)$$

which is the position of the center of the slot, and

$$P_{\perp,1}^r = \hat{z} \cdot \hat{n}_{\perp 1} P_1^r \quad (5.19)$$

$$P_{\parallel,1}^r = \hat{z} \cdot \hat{n}_{\parallel 1} P_1^r \quad (5.20)$$

with the total pattern factor defined by

$$P_1^r = \int_{-\frac{L}{2}}^{\frac{L}{2}} I^{test}(z') e^{-j\beta_1 z' s_{z1}} dz' \quad (5.21)$$

In this basic pattern factor, the variable $z' = z - z_c$, which shifts the integration of the slot current so that it is centered at the origin.

Two cases often occur where the expression in Equation (5.17) is furthered simplified. The first is when the no dielectric slabs are placed on the ground plane, so that the incident plane wave is only in free space. In this case, the excitation current is:

$$\begin{aligned} I^A(\text{free space}) &= 2e^{-j\beta_0 \bar{R}_c \cdot \hat{s}_0} \left[[\bar{H}^{inc}(0,0,0) \cdot \hat{n}_{\perp 0}] P_{\perp,0}^r \right. \\ &\quad \left. + [\bar{H}^{inc}(0,0,0) \cdot \hat{n}_{\parallel 0}] P_{\parallel,0}^r \right], \end{aligned} \quad (5.22)$$

where $P_{\perp,0}^r$ and $P_{\parallel,0}^r$ are defined by Equations (5.19) through (5.21) with the substitute of the zero subscript for the one subscript throughout.

The second frequently occurring case is when $\alpha = 0$ (ref. Figure 88) and the polarization is such that the magnetic field in the incident wave is purely \hat{z} -directed. By Harrington's convention [14], this polarization is denoted the TE_z case (meaning no electric field component in \hat{z}). Referring to the axis of infinite periodicity (\hat{z}) as being vertical, this case can be called the horizontal polarization (referenced to the electric field). In this case, the \hat{z} component of the propagation directions in any material (s_{z_i}) is zero. Furthermore, the perpendicular polarization state vector becomes $\hat{n}_{\perp i} = \hat{z}$ and the parallel polarization state contains no \hat{z} component. Therefore, the excitation current expression in Equation (5.17) reduces to:

$$I^A(\alpha = 0, TE_z) = \phi_{m1} e^{j\beta_0 z_c \sin \eta} H^{inc}(0, -d_{tot}, 0) T_{\parallel}^{HE} P_1^r. \quad (5.23)$$

Using

$$\overline{H}^{inc}(x, y, z) = \hat{z} e^{-j\beta_0(\overline{R} + \hat{y}d_{tot}) \cdot \hat{s}_0}, \quad (5.24)$$

which is a phasor representation of the time harmonic incident magnetic field (suppressing the $e^{j\omega t}$ time convention), Equation (5.23) becomes:

$$I^A(\alpha = 0, TE_z) = \phi_{m1} e^{j\beta_0 x_c \sin \eta} T_{\parallel}^{HE} P_1^r. \quad (5.25)$$

Note that this expression corresponds to excitation from a plane wave source with magnetic field strength of 1 ampere/meter (or electric field strength of 120π volts/meter).

Finally, when the plane wave source is directed with $\alpha = 0$ and is TE_z polarized, and the ground plane is not coated with any dielectrics, the excitation current reduces to:

$$I^A(\alpha = 0, TE_z, freespace) = 2 e^{j\beta_0 x_c \sin \eta} P_1^r. \quad (5.26)$$

Now some example calculations will be presented. The first example is for a 1 cm long slot in a ground plane with no dielectrics. Using a frequency of 10 GHz (i.e., $L = \lambda_0/3$), and centering the slot at the origin, the excitation current using a piecewise sinusoidal testing current is computed to be $0.011027 + j0$ amperes at all η angles³. This value is constant because the \hat{z} -directed slot has a pattern which is omni-directional in η . Furthermore, it is interesting to note that the precise value is nearly equal to the 1 Amp/meter plane wave source times the 0.01 meter slot length. In fact, the ground plane doubles the incident field at the slot, but the assumed testing current shape enters a factor for its average level, which for the piecewise sinusoid is slightly over one half. Using a piecewise sinusoid at a lower frequency

³This agrees with results given by the PMM code, when one multiplies the PMM result by 3.77.

This factor comes from PMM using a 100 volt/ meter plane wave source and this dissertation using a 377 volt/meter source.

should approximate a triangular current distribution, which has an average level of exactly one half. Indeed, computing the 1 cm long slot's excited current at 1 GHz produced a value of $0.010009 + j0$ amperes, which is much closer to the expected value. Using a constant testing current shape, which has an average level of one, the excited current for the 1 cm long slot becomes exactly $0.02 + j0$ amperes, at all frequencies. Finally, all of the above examples were repeated for 10 cm long slots at frequencies scaled down by factors of 10, and the results were simply that the excited current values increased by factors of 10. Thus, the induced current for the slot centered at the origin with no dielectrics is easily guessed by the assumed testing current shape and the slot's length.

Now we examine what happens when the 1 cm long slot (at 10 GHz) is moved to a value of $x_c = 5\lambda_0$ onto the ground plane in free space. Using the same excitation plane wave from Equation (5.24), the excited current has a magnitude of 0.011027 amperes as before, but is rotated in phase as the η angle varies. This is shown in Figure 89, which shows the real and imaginary components of this current as a function of η . Thus, similar slots located at different positions on the ground plane get excitation currents of the same magnitude, but different phases, as expected from Floquet's theorem.

The next example contains two dielectric slabs over the ground plane. The first slab (closest to the ground plane) has a relative dielectric constant of 4 and a thickness of $0.2\lambda_1$. The second slab has a relative dielectric constant of 2 and a thickness of $0.2\lambda_2$. Operating at 10 GHz, the slot is $\lambda_1/2$ long ($= 0.75$ cm) and centered at the origin. Its testing current is defined by a piecewise sinusoid with an effective dielectric constant of 4. The computed excitation current as a function of η is shown in Figure 90. Note that although the slot's pattern is omni-directional in η , the T factor causes a variation in the induced current with the refraction effects.

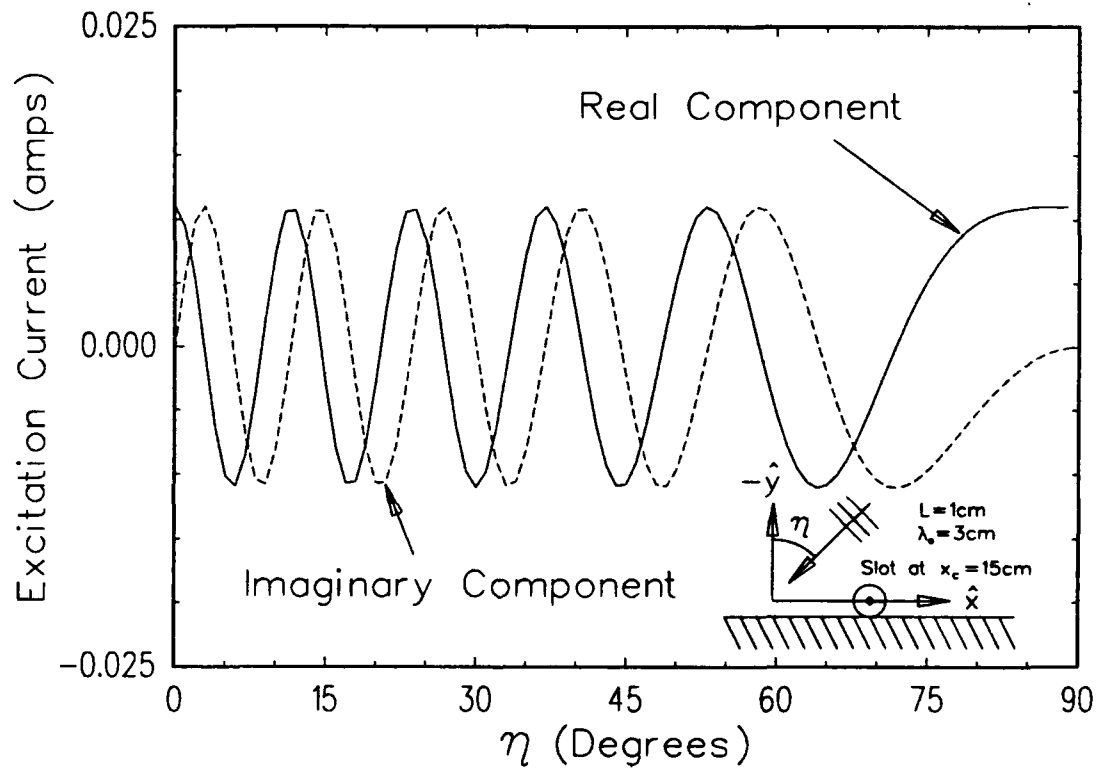


Figure 89: Excitation Current for a Slot in a Ground Plane with No Dielectrics - $L = 1\text{cm}$, $\lambda_0 = 3\text{cm}$, $x_c = 15\text{cm}$, $\alpha = 0$, TE_z source

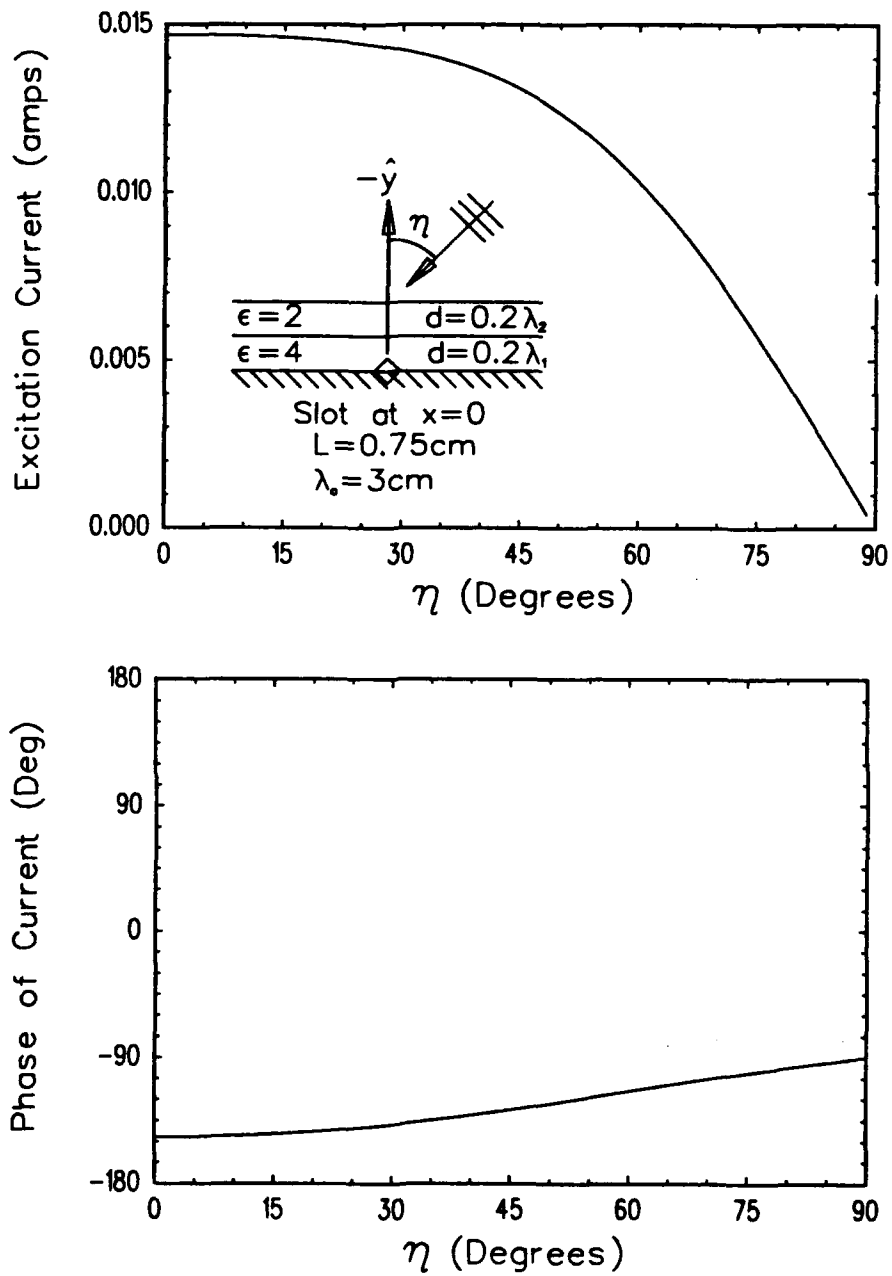


Figure 90: Excitation Current for a Slot at the Origin in a Double Slab Coated Ground Plane - $f = 10\text{GHz}$, $L = 0.75\text{cm}$, $\epsilon_e = \epsilon_1 = 4\epsilon_0$, $\epsilon_2 = 2\epsilon_0$, $d_1 = 0.2\lambda_1$, $d_2 = 0.2\lambda_2$, $\alpha = 0$, TE_z source

For a final example, we repeat the last example except we translate the slot to a location of $x_c = 5\lambda_0 = 10\lambda_1$. The computed excitation current is plotted in Figure 91. Note that it contains the same magnitudes as the currents plotted in Figure 90, but with a phase rotation similar to that shown in Figure 89.

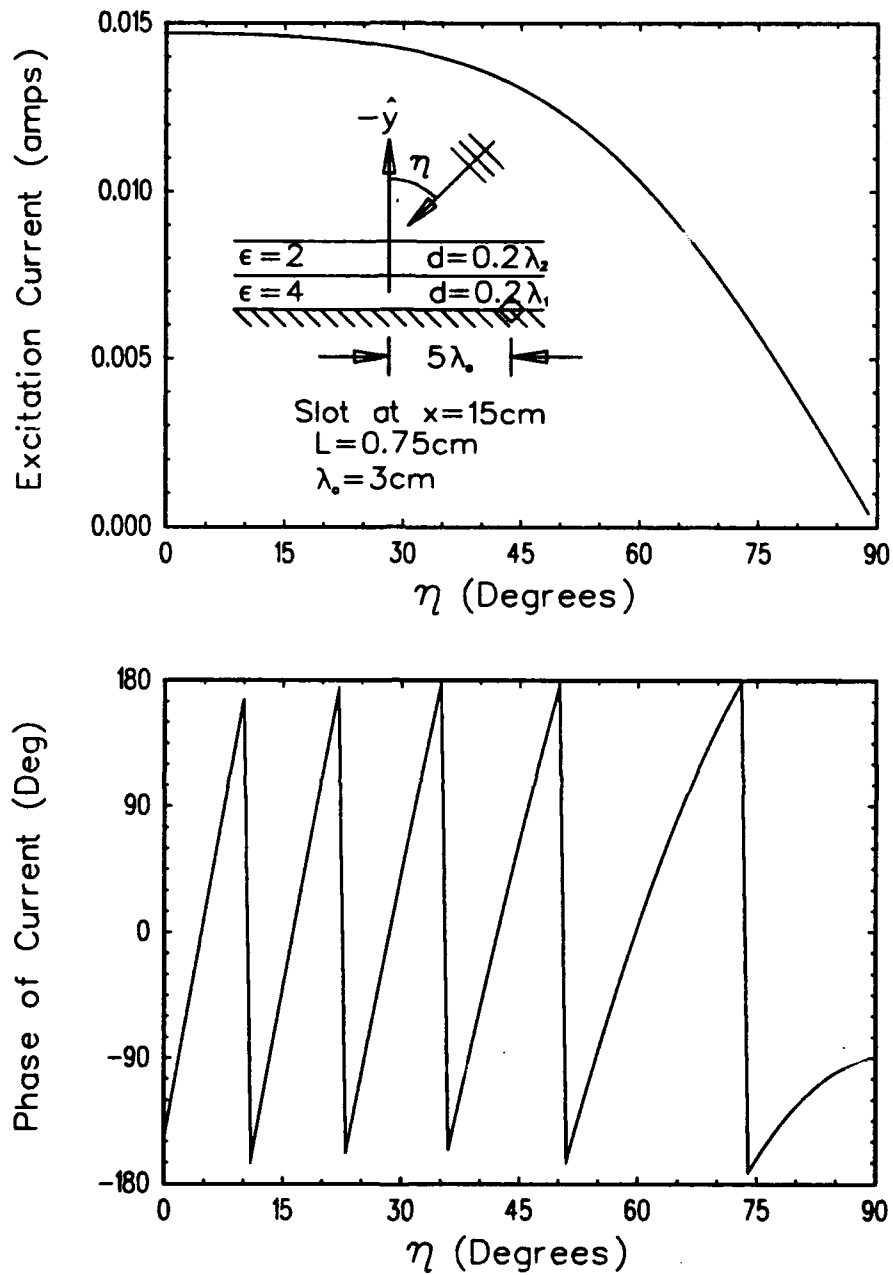


Figure 91: Excitation Current for a Slot at $x_c = 15\text{cm}$ in a Double Slab Coated Ground Plane - $f = 10\text{GHz}$, $L = 0.75\text{cm}$, $\epsilon_e = \epsilon_1 = 4\epsilon_0$, $\epsilon_2 = 2\epsilon_0$, $d_1 = 0.2\lambda_1$, $d_2 = 0.2\lambda_2$, $\alpha = 0$, TE_z source

5.2 FAR ZONE SCATTERED FIELDS

In this section, we complete the overall moment method solution by deriving the far zone scattered field expressions that the equivalent magnetic scattering currents for the slots radiate into Region I (ref. Figure 4). This will be done for both a slotted ground plane in free space and one with dielectric coatings.

Consider the scattering problem from an incident plane wave propagating in the direction \hat{s}_0 , as depicted in Figures 88 and 92. This incident direction defines a quantity s_{z_0} , from Equation (5.1). The s_{z_0} parameter is then used to set up the Floquet based phasing between the elements in each infinite column mode for the slots and dipoles. In other words, s_{z_0} is fixed by the chosen incident direction and the resulting periodic basis functions and moment method solution is specific to that value of s_{z_0} .

The scattered field expressions may only be evaluated with the same s_{z_0} parameter which is used to define the periodic modes. Therefore, the far zone scattered fields may only be evaluated for directions corresponding to:

$$\hat{s}^{scat} = s_x^{scat} \hat{x} + s_y^{scat} \hat{y} + s_{z_0} \hat{z}, \quad (5.27)$$

where s_x^{scat} and s_y^{scat} are arbitrary, as long as they are real valued and satisfy the normalization of \hat{s}^{scat} . The complete set of suitable \hat{s}^{scat} directions forms a cone of bistatic scattering⁴, as shown in Figure 92. This cone is analogous to the "Keller Cone of Diffraction" from an infinite diffracting wedge [18]. This is not to say that fields may not be evaluated at any point in space, but rather, in the asymptotic limit

⁴Other "grating lobe" bistatic cones are also possible, but usually not present when $D_z < 1\lambda$, and definitely not present when $D_z < \lambda_0/2$. These grating lobes occur for values of $-1 < r_z < 1$ where $r_z = s_z + n\lambda_0/D_z$.

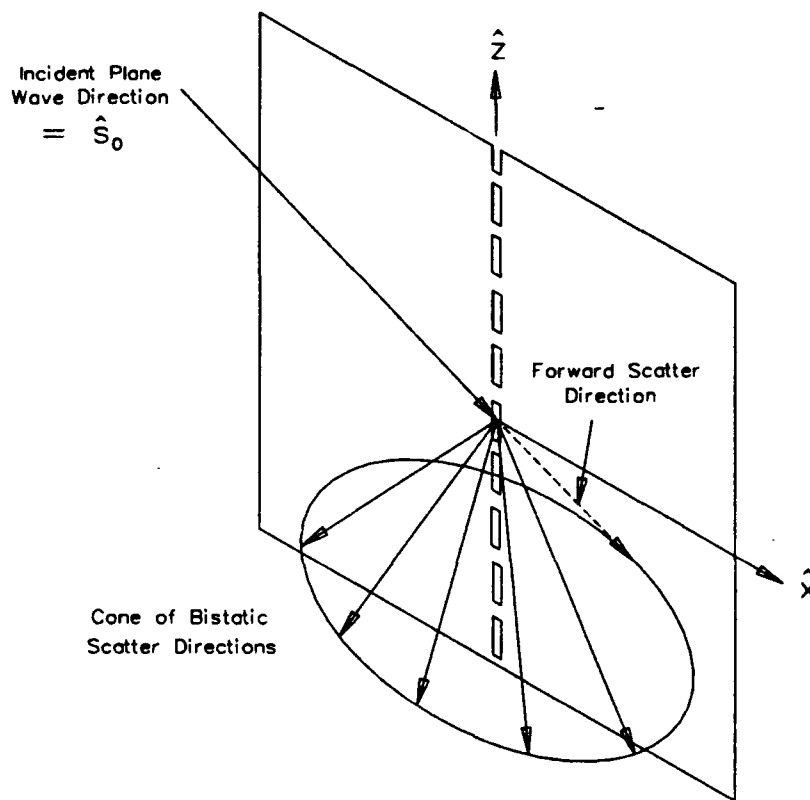


Figure 92: Cone of Bistatic Scatter Directions for a Periodic Column of Slots Illuminated at an Arbitrary Incident Angle

of the extreme far zone, only the fields propagating in the directions found in this cone are applicable.

The only true monostatic problem occurs when $s_{z0} = 0$, in which case it is possible to choose $\hat{s}^{scat} = -\hat{s}_0$. For non-zero values of s_{z0} , the closest direction to monostatic possible is to choose $s_x^{scat} = -s_{x0}$ and $s_y^{scat} = -s_{y0}$, which corresponds to the one direction (other than the forward scatter direction) in the bistatic cone which lies in the plane of incidence (ref. Figure 88). Using the α, η angle pair shown in Figure 88, this occurs by having the scattering direction with the same α angle as the incident direction, but with the opposite η angle.

Now we shall find the far zone scattered field for a single periodic axial slot mode on a ground plane with no dielectrics. Either the electric or magnetic field may be obtained, but since we know in the far zone that they are orthogonal and are related in magnitude by the free space intrinsic impedance, it is only necessary to explicitly find one of the fields. The electric field is chosen for convenience since its components are confined to the cylindrical ϕ direction.

Suppose M slot modes exist on the outer ground plane with no dielectrics. Assume the reference element for the m th slot mode is centered at

$$\bar{R}_m = x_m \hat{x} + z_m \hat{z} \quad (5.28)$$

and that the ground plane is at the XZ plane with the illumination region (i. e., Region I from Figure 4) is in the $y < 0$ half-space. By extension of Equation (2.19), the electric field radiated by the m th slot mode (including image sources) is:

$$\bar{E}_m = -\hat{\phi}_m \frac{V_m^A \beta_0}{j2D_z} \sum_{n=-\infty}^{\infty} e^{-j\beta_0 z r_z} r_\rho P^n H_1^{(2)}(\beta_0 r_\rho \rho_m), \quad (5.29)$$

where V_m^A is the coefficient in the solution vector for the strength of the scattering current (with units of volts assuming the magnetic current mode is unitless - see Equation (1.23)). The pattern factor is the same as that defined in Equation (2.21), which is found in closed form for many common current shapes. The r_ρ and r_z quantities define cylindrical wave directions, and are defined in Equations (2.12) and (2.13). In Equation (5.29), a localized cylindrical coordinate system of (ρ_m, ϕ_m, z) is assumed which originates at the m th slot mode, which is possibly displaced from the true origin.

In the far zone, $\hat{\phi}_m \approx \hat{\phi}$, the true cylindrical circumferential vector, and $\rho_m \approx \rho$ for amplitude purposes and $\rho_m \approx \rho + x_m \cos \alpha \sin \eta$ for phase purposes (see Figure 88). Using the large argument approximation of the Hankel function from Equation

(3.19), one gets:

$$\bar{E}_{m,fz} \approx -\hat{\phi} \frac{V_m^A}{D_z} r_\rho P^t \sqrt{\frac{j}{r_{\rho\rho}\lambda_0}} e^{-j\beta_0 z r_z} e^{-j\beta_0 r_\rho(\rho+x_m \cos \alpha \sin \eta)}, \quad (5.30)$$

where the values of r_z , r_ρ , and P^t are evaluated only for the s_z parameter from the incident wave which defines the cone of scattering⁵. Note that using the cone of scattering truncates the infinite sum in near zone expression in Equation (5.29) to a single term - even when more than one propagating cylindrical wave mode exists (ala grating lobes)!

Equation (5.30) may be written more compactly by using the scattering direction definition from Equation (5.27) and the modal placement definition from Equation (5.28). The compact form is:

$$\bar{E}_{m,fz} \approx -\hat{\phi} \frac{V_m^A}{D_z} r_\rho P^t \sqrt{\frac{j}{r_{\rho\rho}\lambda_0}} e^{-j\beta_0 r_{\rho\rho}} e^{j\beta_0 \bar{R}_m \cdot \hat{s}^{scat}}, \quad (5.31)$$

where now we are defining the pattern factor integral such that the \hat{z} -directed current is centered at the origin (i.e., the z displacement is now accounted in \bar{R}_m in the exponential). Note that in the above,

$$r_\rho = \sqrt{s_x^{scat^2} + s_y^{scat^2}}. \quad (5.32)$$

The total scattered field in the far zone from the direction \hat{s}^{scat} is found by simple addition of the fields from the M slot modes. The complex V_m^A coefficients (found in the moment method) and the exponential involving $\bar{R}_m \cdot \hat{s}^{scat}$ take care of the necessary amplitude and phase factors between the field terms. Thus, the total far zone field is:

$$\bar{E}_{fz} \approx -\hat{\phi} \frac{e^{-j\beta_0 r_{\rho\rho}}}{D_z} \sqrt{\frac{j}{r_{\rho\rho}\lambda_0}} \sum_{m=1}^M P^t V_m^A e^{j\beta_0 \bar{R}_m \cdot \hat{s}^{scat}}. \quad (5.33)$$

⁵Or the r_z corresponding to a desired grating lobe direction in the far zone.

The pattern factors may vary between the modes since all modes are not necessarily of the same element length.

When a plane wave illuminates the slots, an often desirable quantity is the radar echo width. It is found using the well known formula [32],

$$\sigma = \lim_{\rho \rightarrow \infty} 2\pi\rho \frac{|\overline{E}^{scat}|^2}{|\overline{E}^{inc}|^2}. \quad (5.34)$$

Since the excitation vector entries in the previous section of this chapter were defined from a plane wave source with magnetic field strength of 1 ampere/ meter, the magnitude of the incident electric field is 120π volts/meter. With the physical dimensions in Equation (5.33) defined in meters, the resulting scattered electric field is also in units of volts/meter. Therefore, the echo width is:

$$\sigma_{freespace} = \frac{1}{7200\pi r_\rho D_z^2 \lambda_0} \left| \sum_{m=1}^M P^t V_m^A e^{j\beta_0 \overline{R}_m \cdot \hat{s}^{scat}} \right|^2, \quad (5.35)$$

which, despite appearances, results in dimensions of meters with the 7200π factor containing a hidden dimension of volts squared per meter squared.

Now we consider the scattering from slot modes in a dielectric coated ground plane. These fields may be found anywhere in space (including in the dielectrics) using the Array Scanning Method (ASM). We desire only the far zone fields, though, which exist only in the free space volume beyond the dielectric slabs.

For the dielectric coated ground plane, we use the geometry shown in Figure 87. Again, we assume the m th mode is centered at \overline{R}_m , which is defined in Equation (5.28). By extension of Equation (B.9), the field radiated by the m th mode is:

$$\overline{E}_m = \frac{D_x}{\lambda_1} \int_{-\frac{\lambda_1}{2D_x}}^{\frac{\lambda_1}{2D_x}} \overline{E}_{m,A} ds_{x_1}, \quad (5.36)$$

where the radiation from an artificially created doubly-infinite array of slots (with inter-column spacing D_x) is $\overline{E}_{m,A}$. This integrand is found by the methods of Munk

[1, 2]. It is:

$$\begin{aligned} \bar{E}_{m,A} = & - \frac{V_m^A}{2D_x D_z} \sum_{k=-\infty}^{\infty} \sum_{n=-\infty}^{\infty} \frac{e^{-j\beta_0(\bar{R}-\bar{R}_m+\hat{y}d_{tot})\cdot\hat{r}_r}}{r_{y_1}} \phi_{1m} \\ & \cdot \left[P_{\parallel}^t T_{\perp}^{HE} \hat{n}_{\perp 0} - \frac{r_{y_1}}{r_{y_0}} P_{\perp}^t T_{\parallel}^{HE} \hat{n}_{\parallel 0} \right]. \end{aligned} \quad (5.37)$$

This equation is almost drawn from inspection of Equation (4.12) with the elimination of the pattern factor for the testing dipole.

Several parameters in Equation (5.37) require explanation. The vector \bar{R} describes the position of the field observation point in free space. The coefficient V_m^A (in units of volts) is the scattering magnetic current coefficient which was solved in the moment method. As before, d_{tot} is the total thickness of the dielectric layers. The ϕ_{1m} factor is the phase delay of propagation through the layers which is given in Equation (2.106). Plane wave directions in the first dielectric slab are defined by

$$\hat{r}_{1,-} = (s_{x_1} + \frac{k\lambda_1}{D_x})\hat{x} - r_{y_1}\hat{y} + (s_{z_1} + \frac{n\lambda_1}{D_z})\hat{z} \quad (5.38)$$

where r_{y_1} is formed to normalize the unit vector with the positive root chosen for propagating waves and the $-j$ root chosen for evanescent waves. Plane wave directions in the other layers and free space are of similar form to Equation (5.38), with the refracted \hat{x} and \hat{z} components following Equations (2.76) and (2.77). Finally, the s_{z_1} parameter is determined from the s_{z_0} free space parameter using Equation (2.77). The s_{z_0} parameter is set by the excitation source.

The pattern factors in Equation (5.37) are for the magnetic fields radiated by the transmitting slots in the first dielectric slab. They are the same as those defined by Equations (2.62) through (2.64). The T factors in Equation (5.37) are exactly the same as those defined in Equation (4.15), with electric field reflection coefficients used as done in the application in Chapter 4. Finally, the polarization state vectors

are:

$$\begin{aligned}\hat{n}_{\perp 0} &= -\frac{\hat{y} \times \hat{r}_{0,-}}{|\hat{y} \times \hat{r}_{0,-}|} \\ &= \frac{-r_{z_0} \hat{x} + r_{x_0} \hat{z}}{\sqrt{r_{x_0}^2 + r_{z_0}^2}}\end{aligned}\quad (5.39)$$

and

$$\begin{aligned}\hat{n}_{\parallel 0} &= -\hat{n}_{\perp 0} \times \hat{r}_{0,-} \\ &= \frac{-r_{x_0} r_{y_0} \hat{x} - (r_{x_0}^2 + r_{z_0}^2) \hat{y} - r_{y_0} r_{z_0} \hat{z}}{\sqrt{r_{x_0}^2 + r_{z_0}^2}}.\end{aligned}\quad (5.40)$$

Equation (5.36) with the integrand given in Equation (5.37) can be used to find the scattered electric field from the m th slot mode anywhere in the free space volume. We are interested, though, in only finding the far zone fields. As a result, only modes corresponding to plane wave propagation in free space from the doubly-infinite sum in Equation (5.37) are important. Furthermore, only the particular plane waves with r_{z_0} equal to the incident s_{z_0} of the excitation source⁶ is to be counted. Furthermore, when D_x is chosen to be $\lambda_1/2$, no "azimuthal" grating lobes can exist in the free space region, so the only relevant plane wave term is the $k = n = 0$ term in Equation (5.37). Therefore, using this choice for D_x , the far zone field from the m th slot mode is:

$$\begin{aligned}\bar{E}_{m,fz} &= -\frac{V_m^A}{2\lambda_1 D_x} \int_{-1}^1 \frac{e^{-j\beta_0(\bar{R} - \bar{R}_m + \hat{y}d_{tot}) \cdot \hat{r}_{0,-}}}{r_{y_1}} \phi_{1m} \\ &\quad \cdot \left[P_{\parallel}^t T_{\perp}^{HE} \hat{n}_{\perp 0} - \frac{r_{y_1}}{r_{y_0}} P_{\perp}^t T_{\parallel}^{HE} \hat{n}_{\parallel 0} \right] ds_{x_1},\end{aligned}\quad (5.41)$$

where all terms in the integrand are evaluated for the $k = n = 0$ condition only.

As mentioned in the section on the induced current on the slots, a common form of excitation is from a plane wave with the direction angle $\alpha = 0$ (see Figure

⁶Or a single desired "elevation" grating lobe direction, if one exists.

88). For the scattered fields in the direction with $\alpha = 0$, the parameter $s_{z_0} = 0$. Therefore, $\hat{n}_\perp = \hat{z}$ for each media and \hat{n}_\parallel has no \hat{z} component⁷. This makes $P_\parallel^t = 0$ and $P_\perp^t = P^t$. Therefore, for this excitation, Equation (5.41) reduces to:

$$\bar{E}_{m,fz}(\alpha = 0) = -\hat{\phi} \frac{V_m^A P^t}{2\lambda_1 D_z} \int_{-1}^1 \frac{e^{-j\beta_0(\bar{R} - \bar{R}_m + \hat{y}d_{tot}) \cdot \hat{r}_{0,-}}}{r_{y_0}} \phi_{1m} T_{\parallel}^{HE} ds_{x_1}. \quad (5.42)$$

Note that since P^t is independent of s_{x_1} for the axial slots, it is pulled out of the integrand in Equation (5.42).

Although Equation (5.42) expresses the ASM solution for the radiated electric field from a slot mode in the $\alpha = 0$ plane (i.e., the XY plane), it is difficult to perform the numerical integration for observation points which are far away from the slots. As an example, consider the double slab example geometry which was used to produce the excitation current data in Figure 90. Keeping the same geometry with the reference slot centered at the origin and choosing an inter-element spacing of $D_z = 0.75\lambda_1$, the integrand for the ASM solution in Equation (5.42) is computed for an observation point at $\bar{R} = -20\lambda_0\hat{y}$. This unitless integrand is plotted in Figure 93.

As seen by the plotted integrand in Figure 93, thousands of numerical samples are required to accurately produce the numerical integral for Equation (5.42) at this observation distance of just 20 wavelengths from the slot mode. As the observation distance is brought further away, the sampling problem gets even worse. Clearly, for the desired far zone field patterns, the numerical implementation of Equation (5.42) is impractical.

To form a practical far zone field solution, an asymptotic evaluation of the integral in Equation (5.42) may be made by the method of stationary phase. By

⁷In fact, $\hat{n}_\parallel = -r_{y_0}\hat{x} - r_{x_0}\hat{y} = -\hat{\phi}$ at this condition.

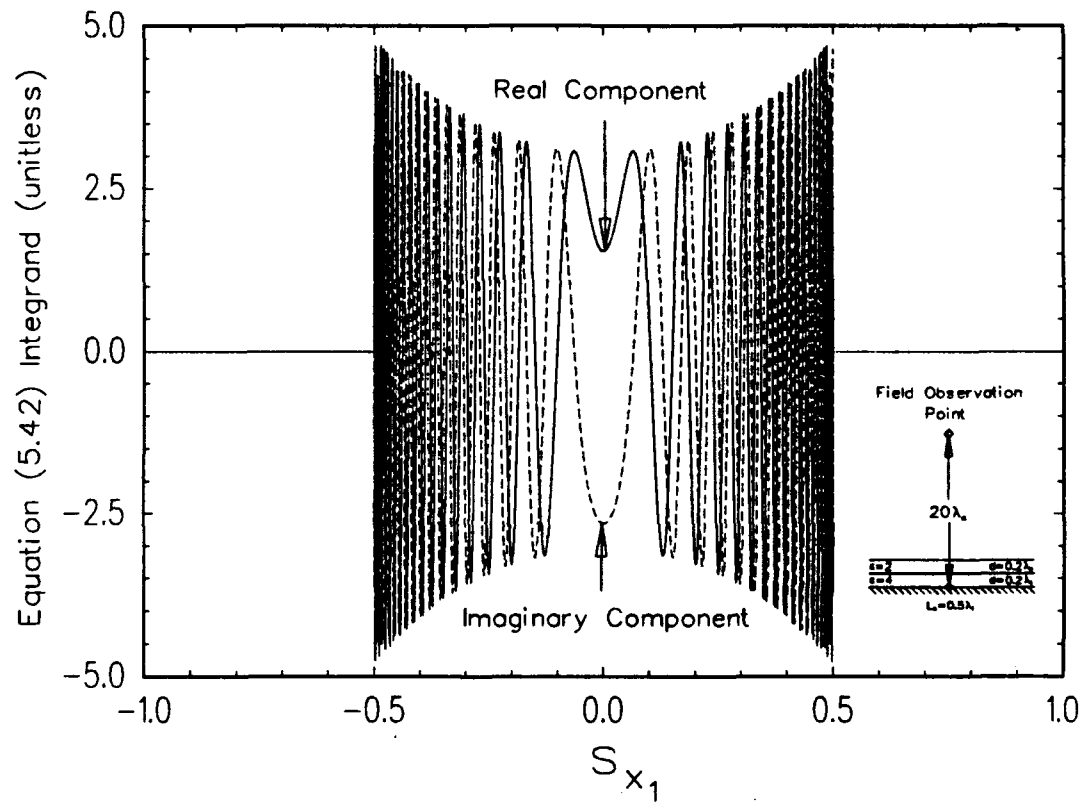


Figure 93: Integrand from ASM Solution for Fields from a Slot Mode in the Double Slab Example Geometry - $\bar{R} = -20\lambda_0\hat{y}$, $\bar{R}_m = 0$

this method, Equation (5.42) becomes:

$$\bar{E}_{m,fz}(\alpha = 0) \approx -\hat{\phi} \frac{V_m^A P t}{2D_z} \sqrt{\frac{j}{\rho \lambda_0}} e^{-j\beta_0 \rho} e^{j\beta_0 \bar{R}_m \cdot \hat{s}^{scat}} \phi_{1m} T_{||}^{HE} \Big|_{stat.pha.pt.} \quad (5.43)$$

where

$$\rho = \sqrt{x^2 + (y + d_{tot})^2}. \quad (5.44)$$

The stationary phase condition may be defined by Equation (4.17), but since the observation point will only be considered to be very far away, the following simple approximation may be made:

$$s_{x_1}(stat.pha.pt.) \approx \frac{\beta_0}{\beta_1} \sin \eta, \quad (5.45)$$

where η is the angle defined in Figure 88.

A numerical experiment was made to compare the results of Equations (5.42) and (5.43) with the same example double slab geometry used to generate Figure 90. For this case, the slots were centered at the origin with spacing $D_z = 0.75\lambda_1$. A "quasi-far zone" pattern was formed at a constant radius of $10\lambda_0$ from the origin. The radiating slot mode was excited with $V_m^A = 1$ volt, and the resulting field patterns are plotted in Figure 94.

The excellent comparison between the fields computed with Equations (5.42) and (5.43) in Figure 94 indicate that the stationary phase evaluation has been implemented correctly. The only place where the data is in disagreement is near $\eta = 90^\circ$, where a numerical problem in making the integration in Equation (5.42) causes a problem⁸.

Now consider the free space case, again. We note that when the dielectrics are removed, $\phi_{1m} = 1$ and $T_{||}^{HE} = 2$. Also, note that with $\alpha = 0$, the r_ρ parameter in Equation (5.31) is equal to one. Therefore, for the free space case, Equations (5.43)

⁸This numerical problem may be alleviated by sampling the integrand in finer increments.

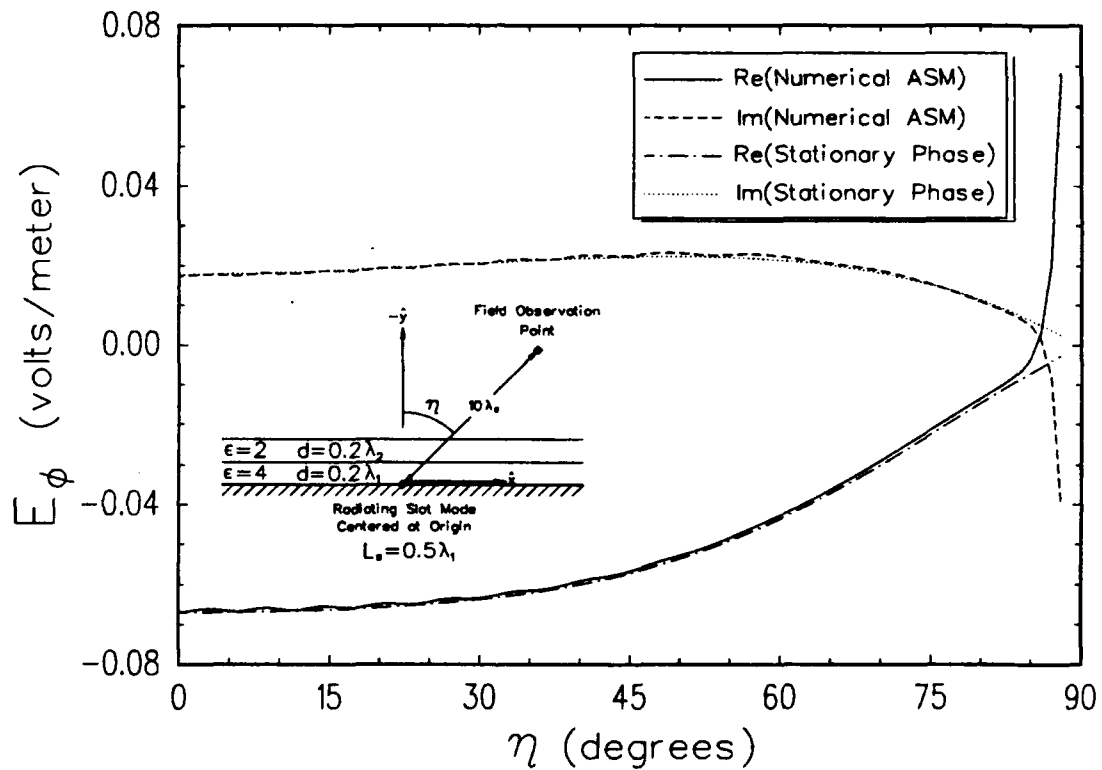


Figure 94: Electric Fields Radiated by a Single Slot Mode in the Example Double Slab Geometry at an Observation Radius of $10\lambda_0$

and (5.31) are in complete agreement, which is remarkable since they were derived in vastly different ways. This provides further evidence to support both the ASM solution set-up and the stationary phase evaluation.

To conclude this chapter, we present the radar echo width from a collection of slot modes in a stratified media, whose voltages were determined by the moment method procedure described in this dissertation. Adding the fields from M modes using Equation (5.43), and substituting into Equation (5.34), we get:

$$\sigma(\alpha = 0) = \frac{|\phi_{1m} T_{||}^{HE}|_{stat. pha. pt.}^2}{28800\pi D_z^2 \lambda_0} \left| \sum_{m=1}^M P^t V_m^A e^{j\beta_0 \bar{R}_m \cdot \hat{s}^{scat}} \right|^2. \quad (5.46)$$

Again, the radar echo width in Equation (5.46) is in units of meters, with the 28800π factor containing a hidden unit of volts squared per meter squared.

CHAPTER VI

RESULTS

In this chapter, we present the total moment method solutions for "finite by infinite" axial slot and transverse dipole geometries. Using the tools developed in Chapters 2 through 5, the moment method procedure described in Chapter 1 is implemented.

Two major categories of geometries are considered in this chapter. The first is that of a finite width radome, which is composed of a finite number of periodic slot columns in two infinite parallel ground planes surrounded by infinite dielectric slabs (e.g., see Figures 96 and 97). For this category, some of the most important results to be computed are the transmitted fields through the finite periodic surface caused by an incident plane wave.

The second major category is that of a phased array antenna in the presence of a finite width radome. For this category, we will determine the radiated field patterns through the radome and the input impedances of various elements in the transmitting array.

All results shown in this chapter are for the $\alpha = 0$ plane (see Figure 88). Furthermore, only the TE_z (electric field being "horizontal" with " \hat{z} = vertical") is considered. Piecewise sinusoidal basis and testing functions are used.

Finally, the reader should be cautioned that the main purpose of this dissertation has been to create and validate an analysis procedure for electromagnetic

scattering from geometries of the type in Figure 1. The data presented in this chapter is calculated to provide confidence in the moment method solutions and show the usefulness of having such an analysis procedure. No major attempts have been made to develop an optimized design for either the radome or radome/antenna examples shown in this chapter.

6.1 RADOME EXAMPLES

A good radome design using periodic surfaces often requires a stabilized frequency response for a wide range of angles of incidence. Such a design can be found with the array coupling terms exhibiting "scan independence", which can be achieved with a proper dielectric profile [27].

In this section, we shall present a radome design which approximates the "scan independence" goal, but which is designed without any particular attention to materials with available dielectric constants or with the necessary mechanical and environmental properties required for many practical applications.

As noted in the discussion in Chapter 2 on Figure 35, scan independence in the E-plane is approximated over a wide range of incidence angles for the "one sided outer zone" scan admittance of a doubly-infinite (non-skewed) array of slots embedded in a double slab geometry with the following parameters (see Figure 18): $\epsilon_1 = 4\epsilon_0$, $\epsilon_2 = 2\epsilon_0$, $\epsilon_e = \epsilon_1$, $d_1 = 0.4\lambda_1$, $d_2 = 0.3\lambda_2$, $L_s = 0.5\lambda_1$, $W = L_s/10$, $D_x = 0.45\lambda_1$, and $D_z = 0.75\lambda_1$. To simplify the radome design, this lattice and dielectric profile geometry was selected for both Regions I and III (see Figure 4), with the goal of keeping the entire radome design symmetric.

To complete the design, a dielectric profile for Region II needs to be found, which is compatible with the chosen slot sizes and spacings, and for which the "one

sided inner zone" self scan admittance and mutual scan admittance (between the ground planes) are approximately scan independent. Using the PMM code [3], such conditions were found with the following symmetric inner zone profile: $\epsilon_1 = 4\epsilon_0$, $\epsilon_2 = 2\epsilon_0$, $\epsilon_3 = 4\epsilon_0$, $d_1 = 0.0667\lambda_1$, $d_2 = 0.2357\lambda_2$, and $d_3 = 0.0667\lambda_3$.

To demonstrate that the chosen radome profile and slot geometries are reasonably scan independent, calculations were run on the PMM code for doubly-infinite arrays of the slots on each ground plane. In these calculations, a single piecewise sinusoid mode (and testing function) was used for each doubly-infinite array. The radome design was scaled for the above parameters at 10 GHz, with the goal that the arrays should resonate and be transmissive at this frequency. Transmission of the fields from three discrete incident plane wave directions in the $\alpha = 0$ plane (see Figure 88) were found over a band of frequencies, and the resulting data is plotted in Figure 95. Indeed, the data demonstrates that the infinite radome is fairly transparent at 10 GHz for normal through 60° incidence, with similar passbands for each direction.

The doubly-infinite array examined by the PMM code was truncated so that only 21 columns of periodic slots would exist on each ground plane. This corresponds to an aperture of about 4.5 wavelengths in free space. The ground planes and dielectrics, however, remained infinite in extent. The slots also remained infinitely periodic in \hat{z} . A view from the infinite axis ($+\hat{z}$) of this geometry is shown in Figure 96. In this figure, asterisks are put on the ground plane to designate the locations of the slots. The dimensions for this geometry are again scaled for the radome to be transparent at 10 GHz. Note the thin layers of $\epsilon_r = 4$ dielectric in between the ground planes. A front view (i.e., normal to the radome) of the 21 columns is given in Figure 97, which shows the lattice and shapes of the slots (drawn to scale), as they exist on each of the two ground planes.

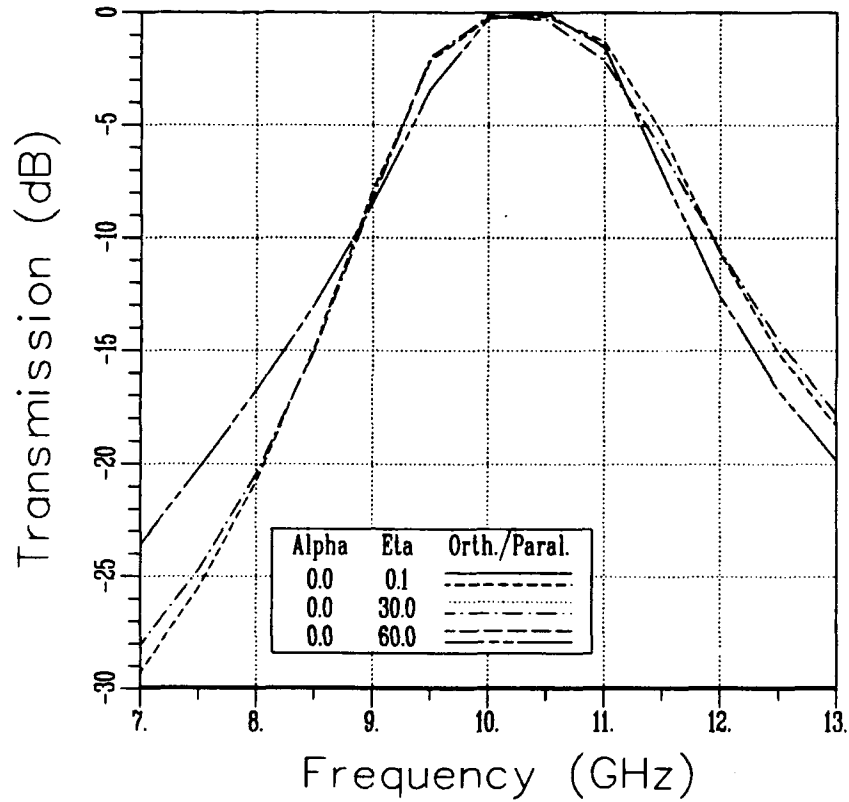


Figure 95: Transmission Through a Radome Composed of Doubly-Infinite Slot Arrays Embedded in Dielectrics which Give Near Scan Independence using the PMM Code

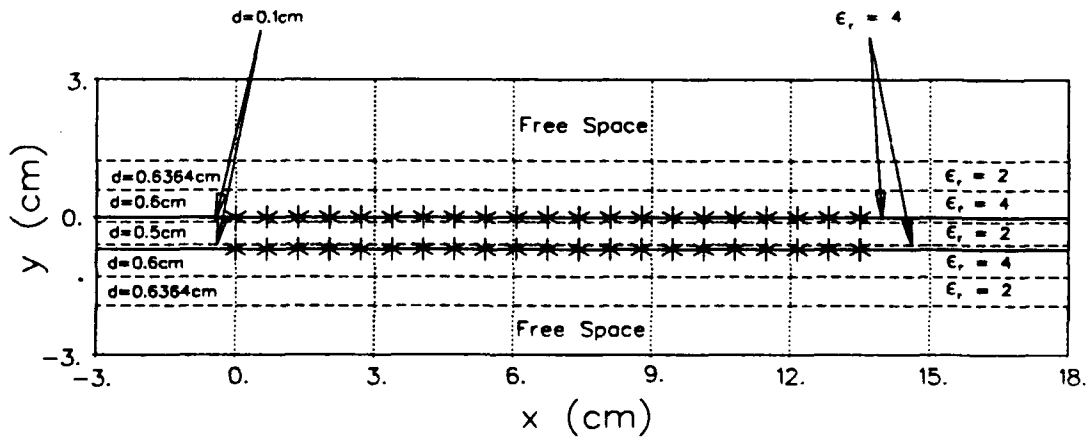


Figure 96: Top View of the Truncated Hybrid Radome - 21 Columns of Slots on Each Infinite Ground Plane with Infinite Dielectrics - Asterisks Designate Each Column of Periodic Slots

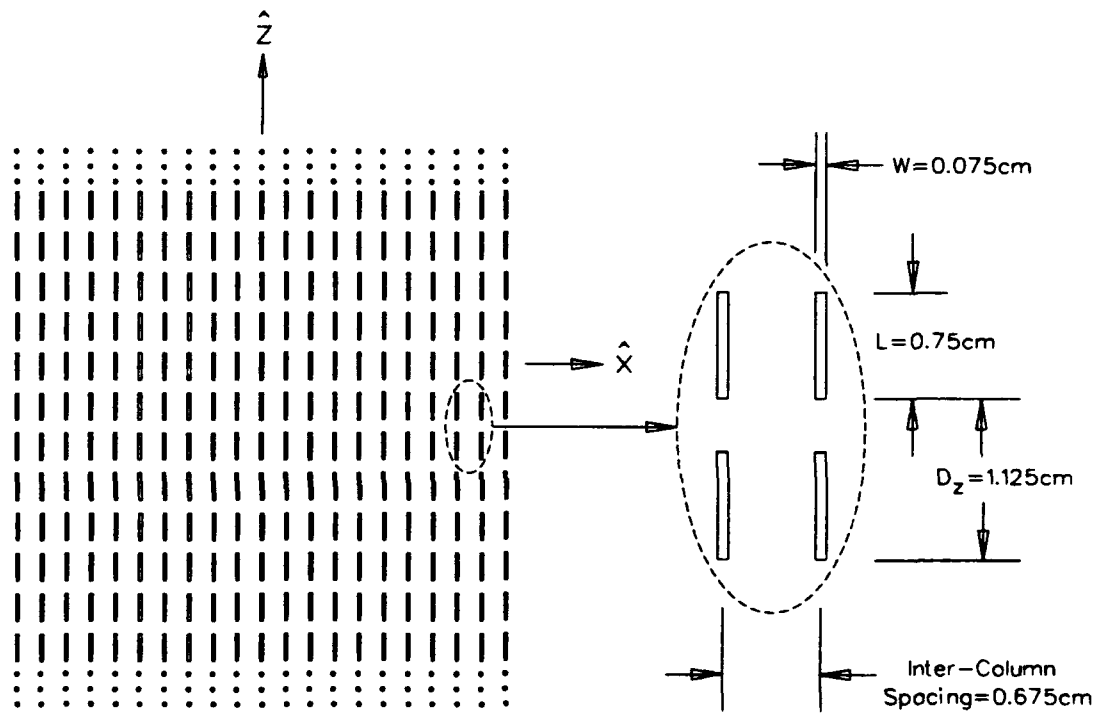


Figure 97: Front View of the Truncated Hybrid Radome - 21 Columns of Slots on Each Infinite Ground Plane

To verify the accuracy of the moment method procedure in this dissertation, the equivalent magnetic scattering currents for the geometry in Figures 96 and 97 were computed for the excitation of a plane wave at normal incidence with electric field magnitude of 100 volts/meter at 10 GHz. These currents were calculated by the present methods with one periodic piecewise sinusoidal mode for each slot column and with piecewise sinusoidal testing currents. As a reference for comparison, the PMM code was used to find the currents for the infinite radome using a single piecewise sinusoidal mode for each ground plane of slots under similar excitation. The resulting magnetic current coefficients are plotted in Figure 98.

The data from the present methods and the PMM code in Figure 98 is in general agreement, except for a slight discrepancy on the levels of the current magnitudes for the slots on "Ground Plane B" (i.e., modes 22 through 42). This encouraging result demonstrates that the methods in this dissertation are generally good, though some numerical errors are possibly occurring. The ripples in the currents for the finite radome are expected, though, as edge effects cause the currents not to be completely uniform across the aperture.

To compute the scattering current data for the 42 mode radome in Figure 98, approximately 50 minutes of CPU time on a VAX 8550 machine was used. Over 99% of this time was used to compute the coupling matrix for the basic geometry, which is independent of the excitation source¹. Once this coupling matrix is computed, though, it may easily be stored and quickly recalled for other calculations. This was done, and the remaining data shown in this dissertation for the 21 column truncated radome were calculated in just a few CPU seconds.

A backscatter pattern was calculated for the 21 column truncated hybrid radome. It is shown in Figure 99. The results are given in dB compared to a

¹As long as s_z and the frequency remain the same. All results in this dissertation use $s_z = 0$.

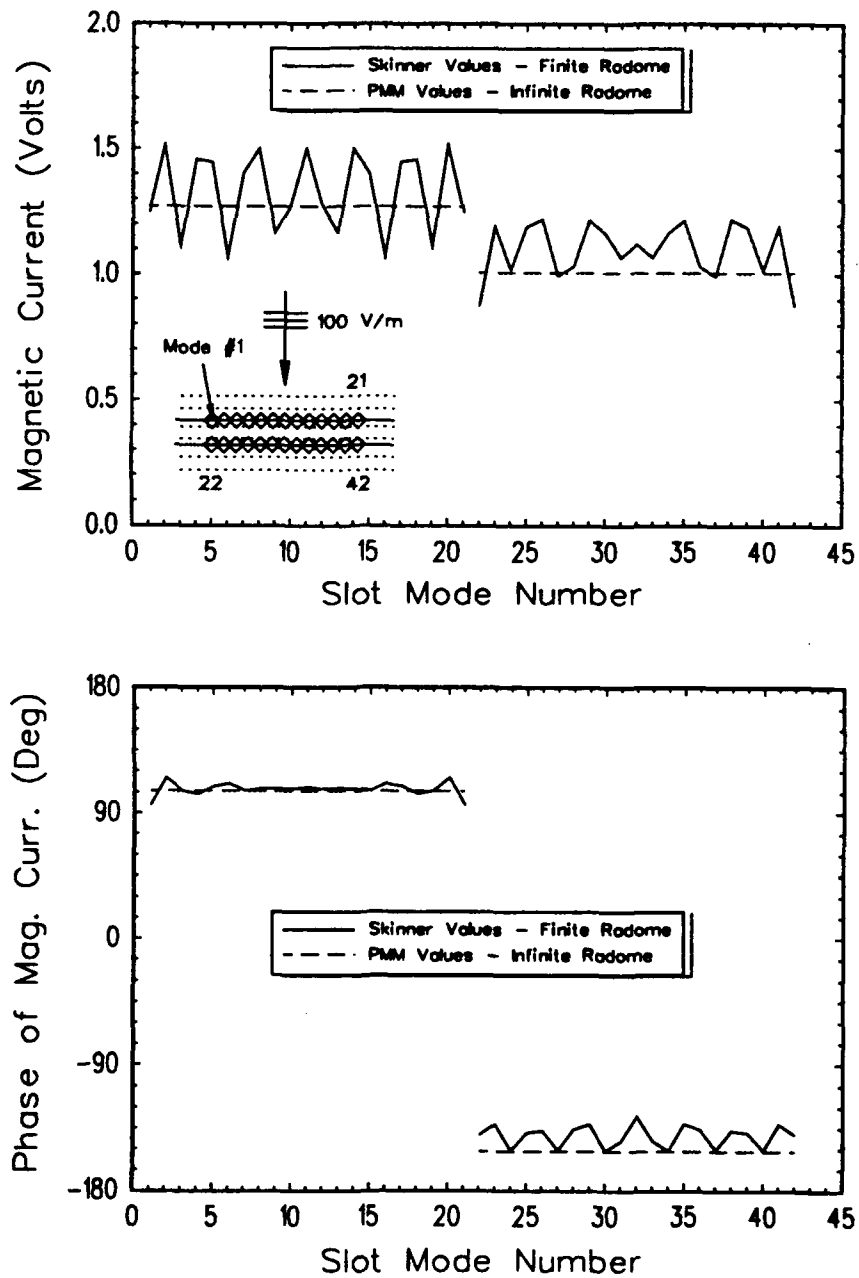


Figure 98: Currents on the 21 Column Truncated Hybrid Radome vs. Currents on an Infinite Radome - 100 V/m Normal Incidence Source, TE_z , 10 GHz

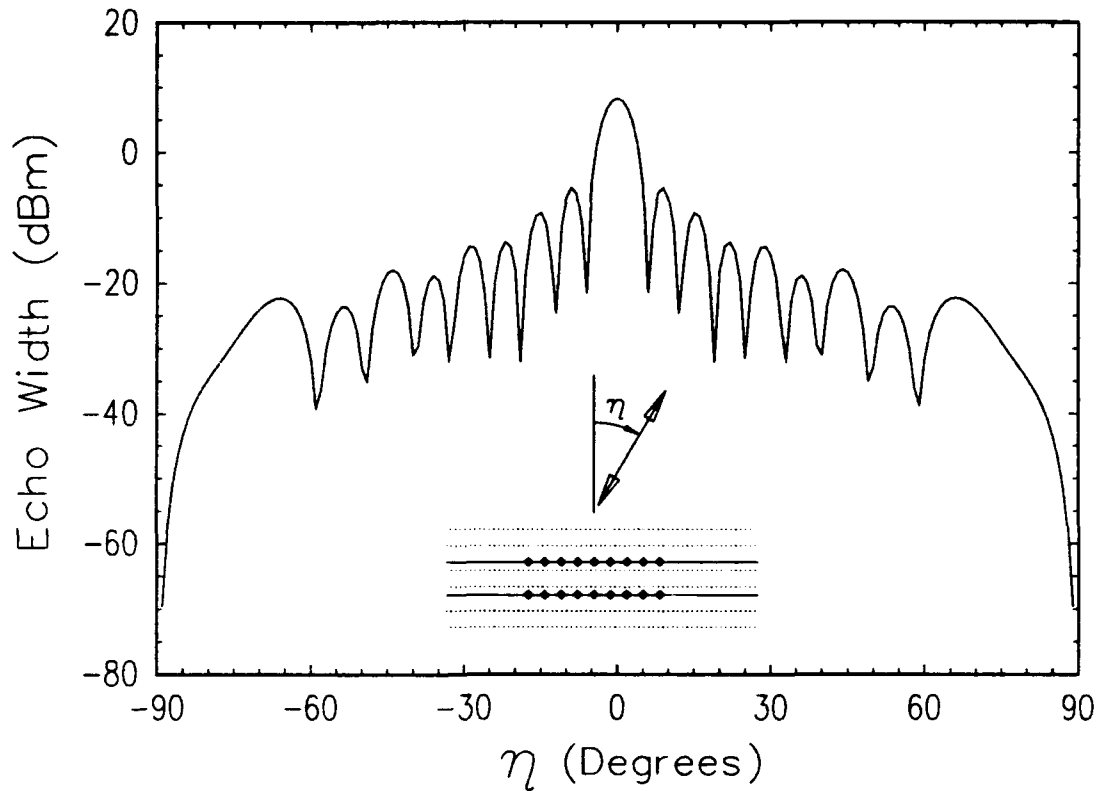


Figure 99: Backscatter from 21 Column Truncated Hybrid Radome at 10 GHz, TE_z

meter. Note that the far sidelobes in this pattern are much higher than the drop-off that a simple physical optics solution would predict.

One of the interesting qualities of a truncated radome is its transmission pattern. In this dissertation, the “bistatic” transmission was computed for fixed directions of plane wave incidence. A normalization of the resulting transmitted field data at a certain far zone radius was performed by comparing the fields with those radiated by physical optics currents for the physical aperture excited by the incident plane wave. The physical aperture, in this case, is assumed to be the number of slot columns times the inter-column spacing times $\cos \eta$ (for the angular projection)².

²This physical aperture is therefore based on the “cell size”, which goes 1/2 the inter-column spacing beyond the last slots on each end.

The normalized bistatic transmission patterns for the 21 column truncated hybrid radome were computed at 10 GHz for plane wave incidence at $\eta = 0$ (i.e., normal), $\eta = 30^\circ$, and $\eta = 60^\circ$. These patterns are given in Figures 100, 101, and 102, respectively. Recall that the PMM predictions for the infinite hybrid radome (Figure 95) were for almost perfect transparency at each of the angles of incidence. Indeed, the main lobes transmitted in each pattern in Figures 100 through 102 are at nearly 0 dB, normalized to the physical optics from the physical apertures. Actually, the main lobe in Figure 100 comes up to +0.3 dB. This overshoot may be partially due to some inaccuracy in assuming the effective aperture is the physical aperture. Most of the discrepancy, however, is probably due to the minor inaccuracy of the currents noted in Figure 98.

To further validate the accuracy of the code created for this dissertation, a less transparent radome was examined. For this radome, the lattice spacing consisted of $D_x = 0.675\text{cm}$ and $D_z = 2.0\text{cm}$ with no grid skewing. The axial slot elements were 1.5cm long and 0.75mm wide. Twenty one columns of these slots existed on each ground plane with a layer of 1cm of air between the planes. No dielectrics were used, so that the transmissivity would change as a function of angle of incidence.

The poorer radome was examined at 8 GHz (which is below the first resonance of the slots) for plane wave incidence at $\eta = 0$ (i.e., normal) and $\eta = 60^\circ$ in the TE_z polarization. By the PMM code, an infinite radome of such slots would have a transmission of -12.3 dB at normal incidence and -5.8 dB at 60° . The normalized³ transmission from the 21 column truncated radome at normal and 60° incidence are shown in Figures 103 and 104.

The peak level of the main beam in Figure 103 is at -12.6 dB, which is only 0.3 dB lower than the PMM value. The peak level in Figure 104 is at -6.7 dB (0.9

³By the physical optics level from the physical aperture

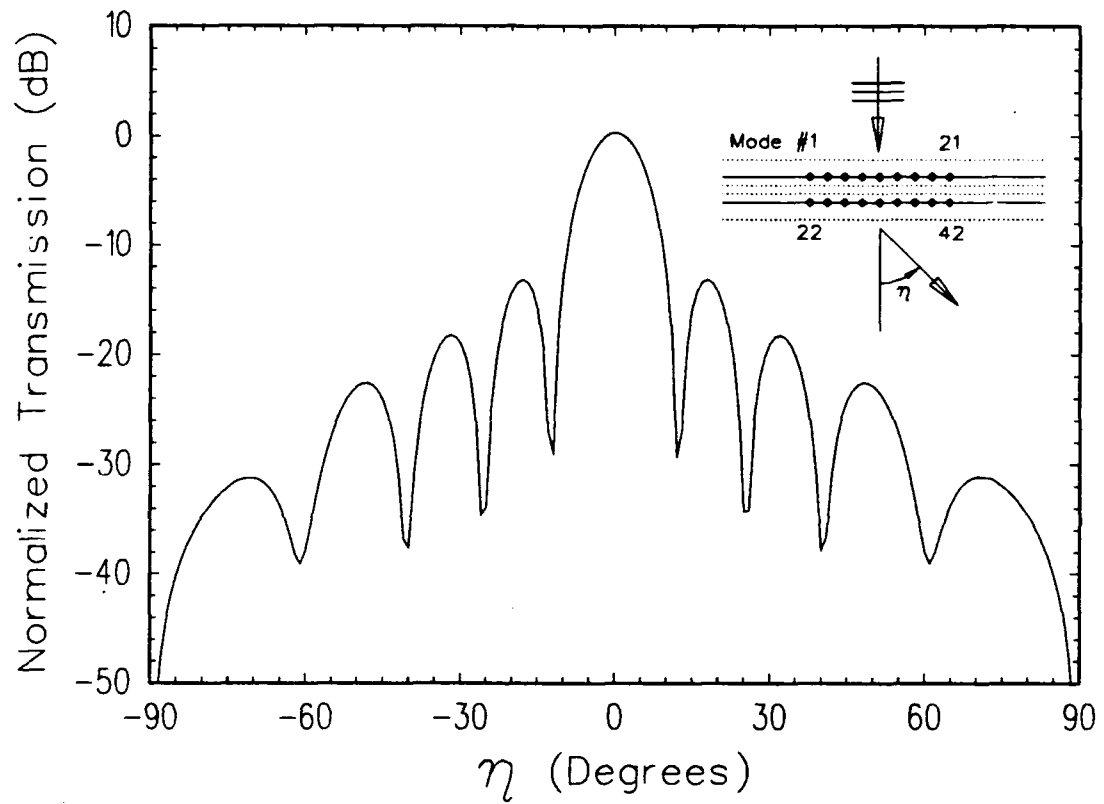


Figure 100: Bistatic Transmission Pattern of 21 Column Truncated Hybrid Radome at 10 GHz, TE_z , Normal Incidence - Data Normalized to Physical Optics

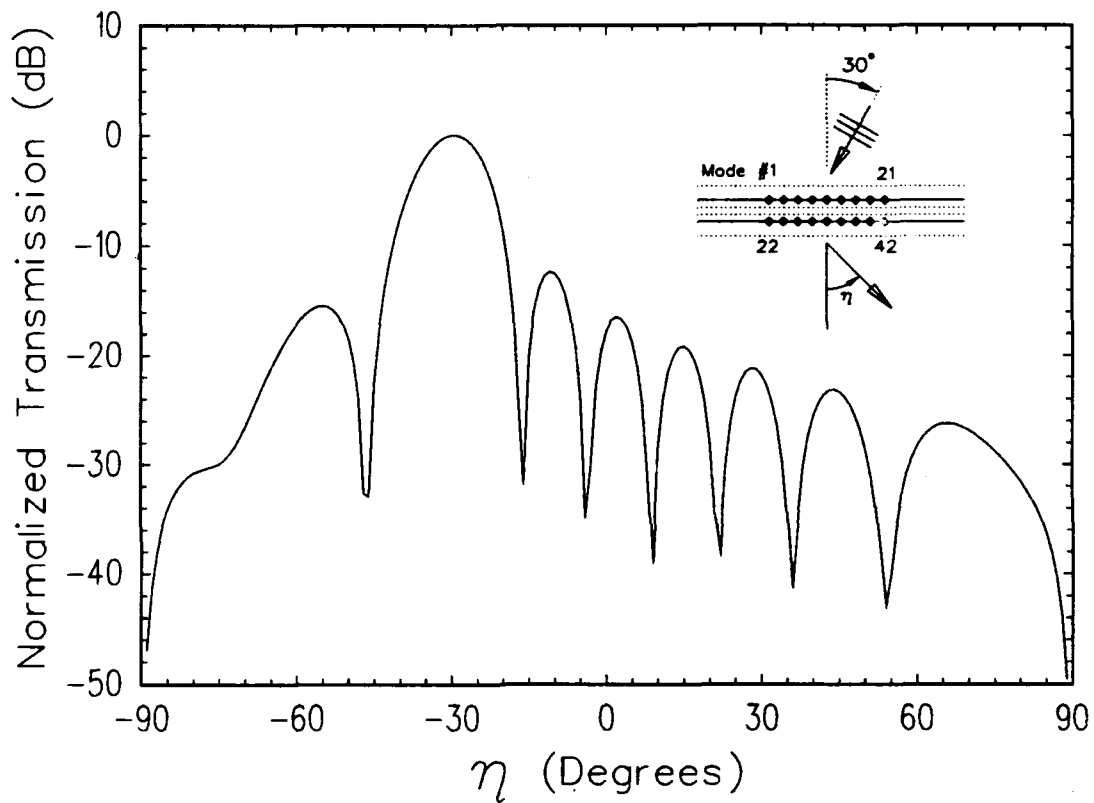


Figure 101: Bistatic Transmission Pattern of 21 Column Truncated Hybrid Radome at 10 GHz, TE_z , $\eta = 30^\circ$ Incidence - Data Normalized to Physical Optics

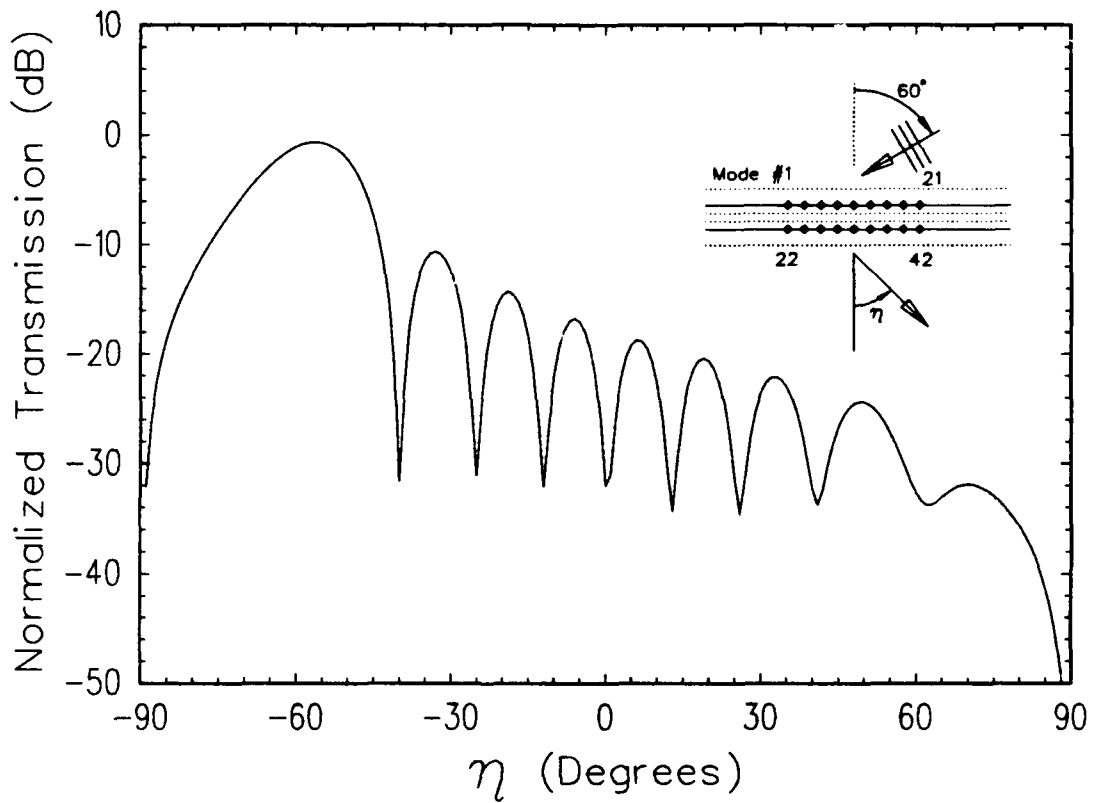


Figure 102: Bistatic Transmission Pattern of 21 Column Truncated Hybrid Radome at 10 GHz, TE_z , $\eta = 60^\circ$ Incidence - Data Normalized to Physical Optics

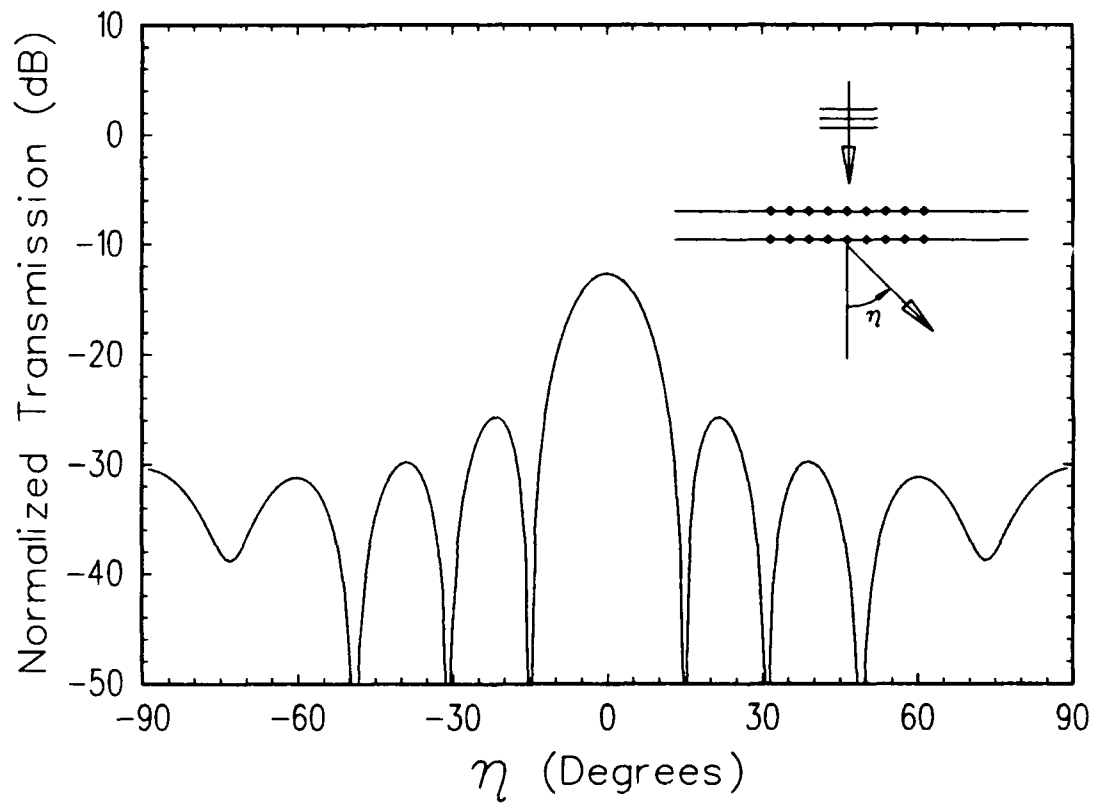


Figure 103: Bistatic Transmission Pattern of 21 Column Truncated Metal Radome (No Dielectrics) at 8 GHz, TE_z , Normal Incidence - Data Normalized to Physical Optics

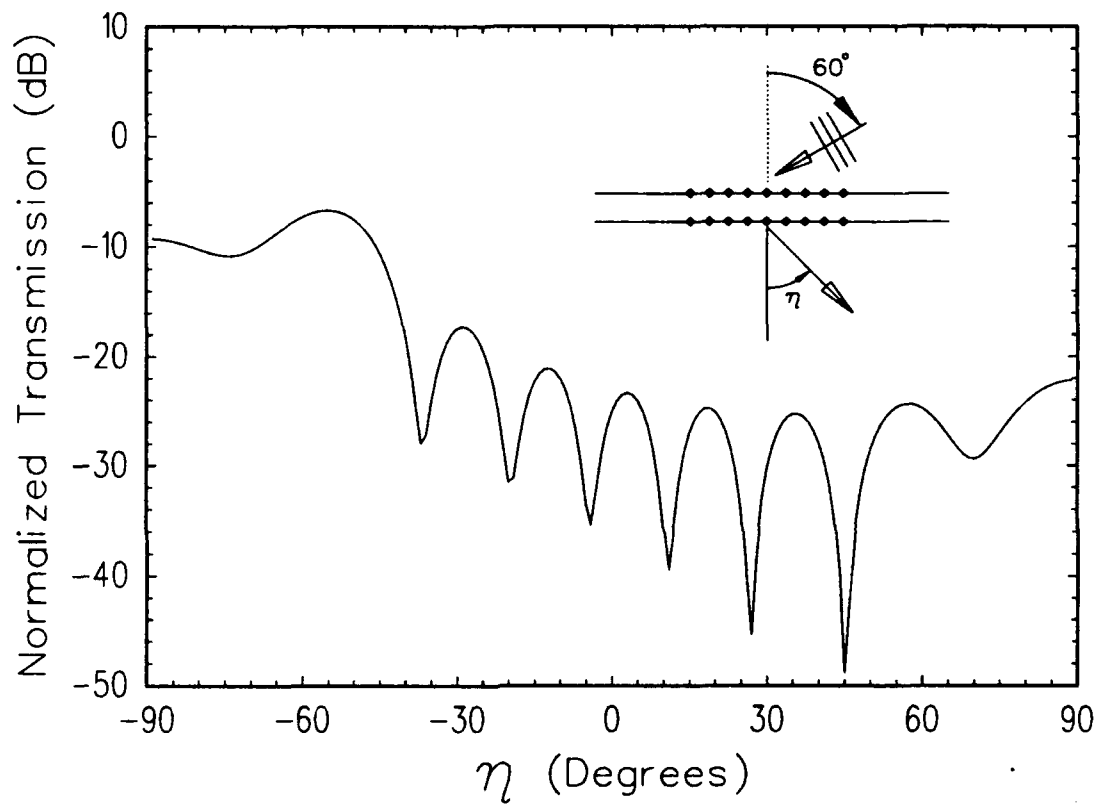


Figure 104: Bistatic Transmission Pattern of 21 Column Truncated Metal Radome (No Dielectrics) at 8 GHz, TE_z , $\eta = 60^\circ$ Incidence - Data Normalized to Physical Optics

dB off the PMM value), and is located at $\eta = -55^\circ$. These discrepancies are most likely due to the small physical aperture (only 1.8 free space wavelengths) at 60° incidence.

To conclude this section, we present a larger version of the truncated hybrid radome, which was transparent at 10 GHz for a wide range of scan angles. The 21 column slot arrays embedded in the 7 dielectric layers were extended to a total of 41 columns for each ground plane. The same lattice spacings and element types were used, as well as the same dielectrics, with the geometry scaled for the resonance at 10 GHz. The new 41 column wide aperture now extends to about 9 wavelengths of aperture (at normal incidence) in free space.

The first data collected on the larger truncated hybrid radome was the magnetic scattering current coefficients (using piecewise sinusoidal basis and testing functions) for the modes, as excited by a 100 volt/meter plane wave source at 10 GHz and normal incidence. These data, along with the PMM currents for the infinite radome, are plotted in Figure 105.

Note that the magnitude of the ripples in the currents across the aperture are smaller on the "first" ground plane (i.e., nearest the excitation plane wave) for the 41 column case than the 21 column case (see Figure 98). The ripples on the "back" ground plane currents exhibit the opposite trend with the growing aperture. One might expect that some ripples in the currents would occur near the edges of the aperture, but would die out in the center. This is clearly not happening, as the ripples are of near equal amplitude (with respect to other ripples on the same ground plane) across the entire aperture. One explanation for this phenomena is that these ripples are primarily the product of the surface waves in the dielectrics, and that the "net" result of the surface waves excited is smaller for the front ground plane (and interestingly, larger for the back ground plane) as the number of slot columns

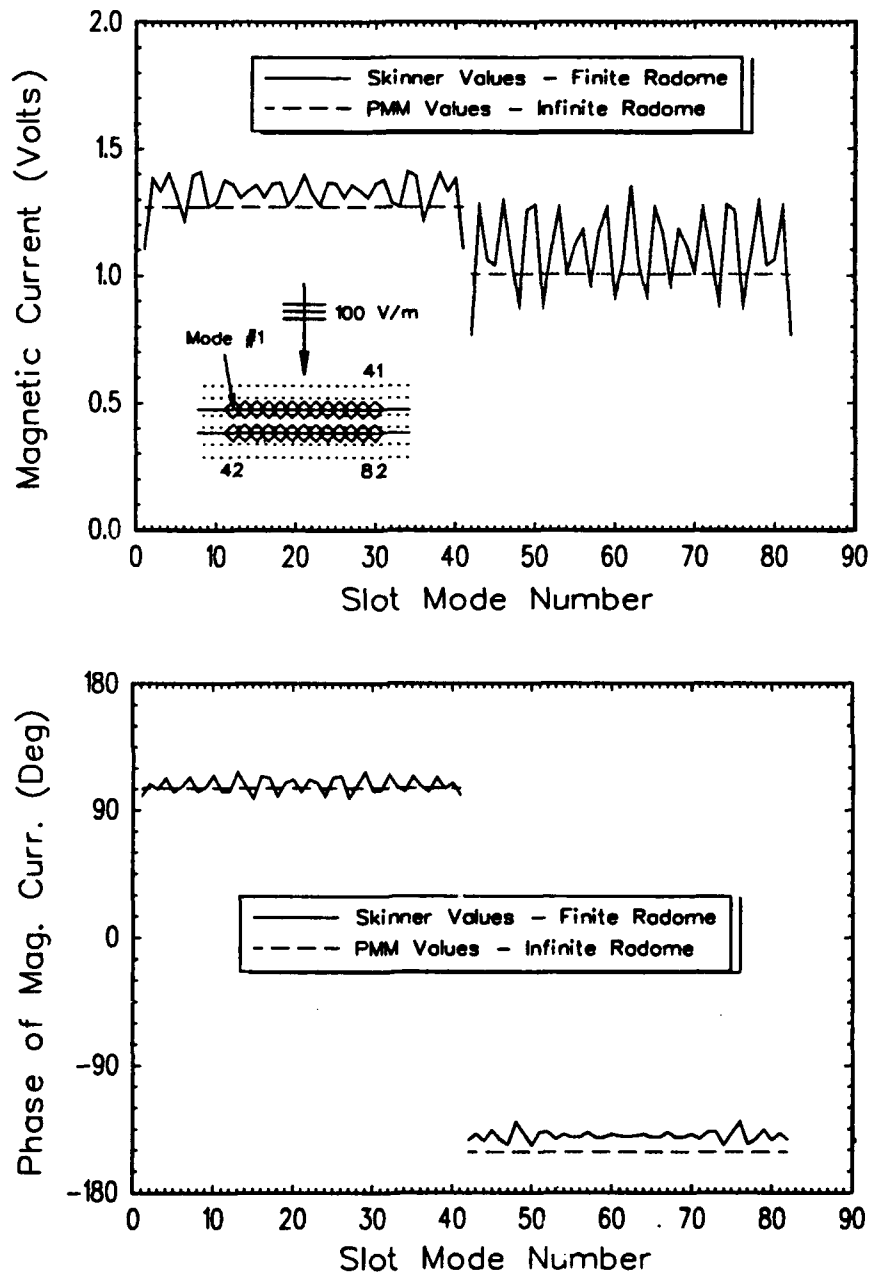


Figure 105: Currents on the 41 Column Truncated Hybrid Radome vs. Currents on an Infinite Radome - 100 V/m Normal Incidence Source, 10 GHz, TE_z

grows⁴, and that this "net" surface wave exists without decay with respect to \hat{x} (i.e., across the transverse dimension of the aperture), causing ripples of constant amplitude.

It may also be noted in Figure 105 that the currents for the back ground plane in the truncated radome are not converging perfectly with the corresponding calculation from the infinite radome. Again, this is an indication that the numerical implementation of the moment method solution used in this dissertation may have some minor errors, but that the general solution is fairly good.

The creation of the coupling matrix for the 41 column (total of 82 modes) truncated hybrid radome took slightly over 3 hours of CPU time on a VAX 8550 machine. This matrix was stored, though, and subsequent data runs for this geometry at 10 GHz were run in a matter of a few CPU seconds.

The next calculation performed on the 41 column truncated hybrid radome was a backscatter pattern. It is shown in Figure 106. Although the main beam is higher than that shown in Figure 99, the far sidelobes follow approximately the same envelope, indicating that they may be dominated by edge scattering effects.

The transmission through the 41 column truncated hybrid radome was also examined at 10 GHz for $\eta = 0$ (i.e., normal), $\eta = 30^\circ$, and $\eta = 60^\circ$ incidence. The resulting bistatic field patterns were normalized to the field from physical optics from an open physical aperture (in the main beam direction). The resulting data is plotted in Figures 107 through 109. As with the 21 column case (see Figure 100), the normal incidence transmission peaks at about +0.3 dB, which indicates the solution currents for the slots are not absolutely perfect, as noted in the discussion of Figure 105. Also note that the main beam peak in Figure 109 is closer to 0 dB and more

⁴It may be hypothesized that the "net" surface wave excited in an infinite radome is exactly zero!

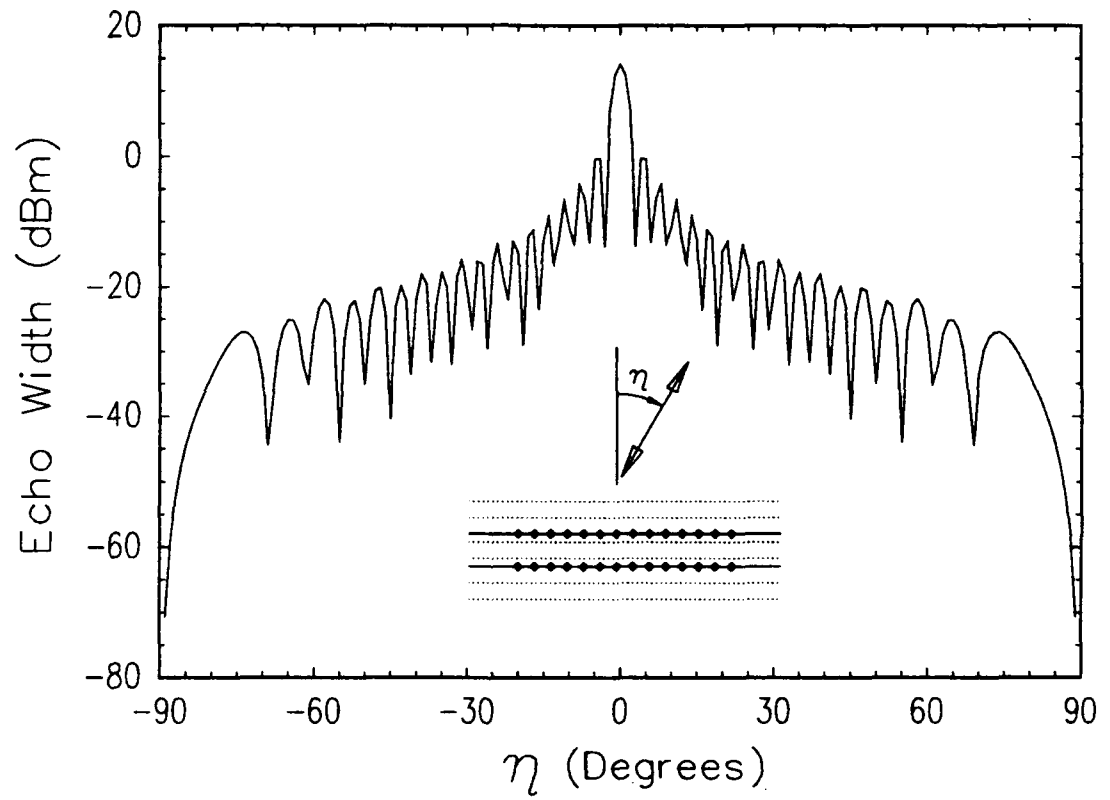


Figure 106: Backscatter from 41 Column Truncated Hybrid Radome at 10 GHz, TE_z

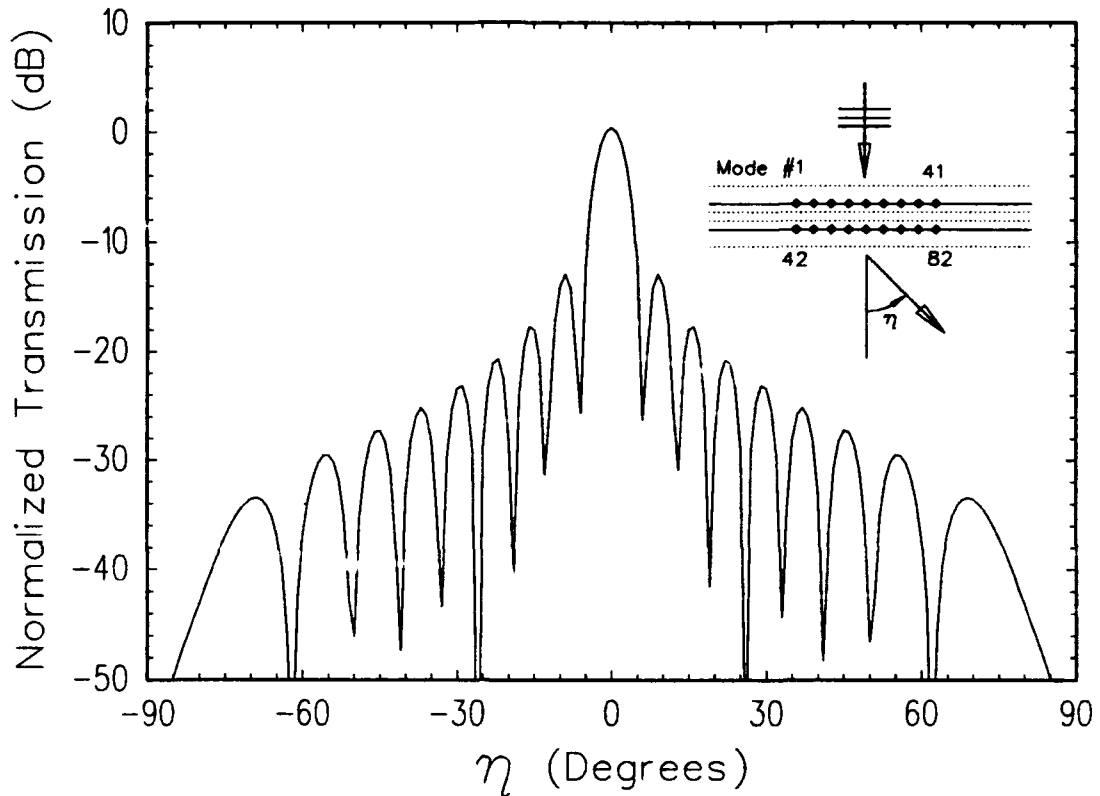


Figure 107: Bistatic Transmission Pattern of 41 Column Truncated Hybrid Radome at 10 GHz, TE_z , Normal Incidence - Data Normalized to Physical Optics

accurately at $\eta = -60^\circ$ that the result plotted in Figure 102. This is simply the result of the larger aperture.

Finally, to demonstrate the usefulness of the analysis developed in this research, an attempt was made to lower the transmitted bistatic sidelobes through the 41 column truncated hybrid radome. This was done by loading the slots near the edges of the radome with shunt admittances across the centers of the slots, which add directly to the self admittances in the coupling matrix. With the stored coupling matrix computed from the "untreated" radome, design analysis with different slot loadings can be done very quickly, as long as the slot and dielectric geometries remain unchanged.

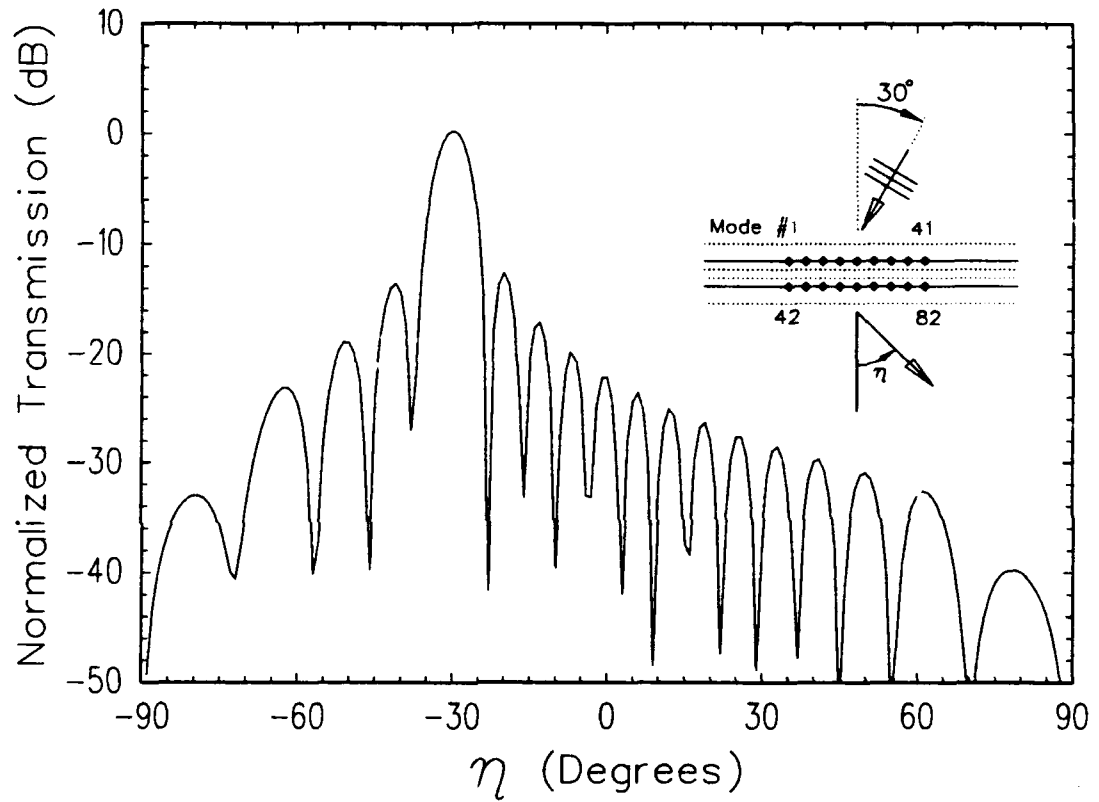


Figure 108: Bistatic Transmission Pattern of 41 Column Truncated Hybrid Radome at 10 GHz, TE_z , $\eta = 30^\circ$ Incidence - Data Normalized to Physical Optics

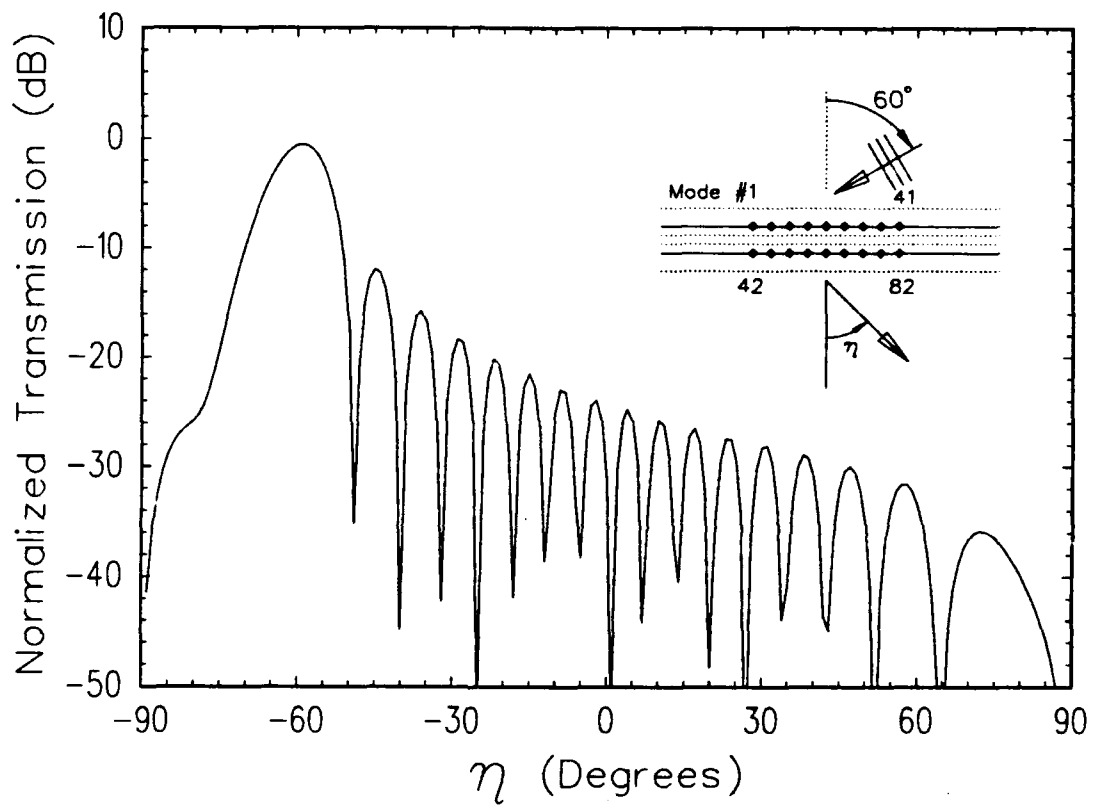
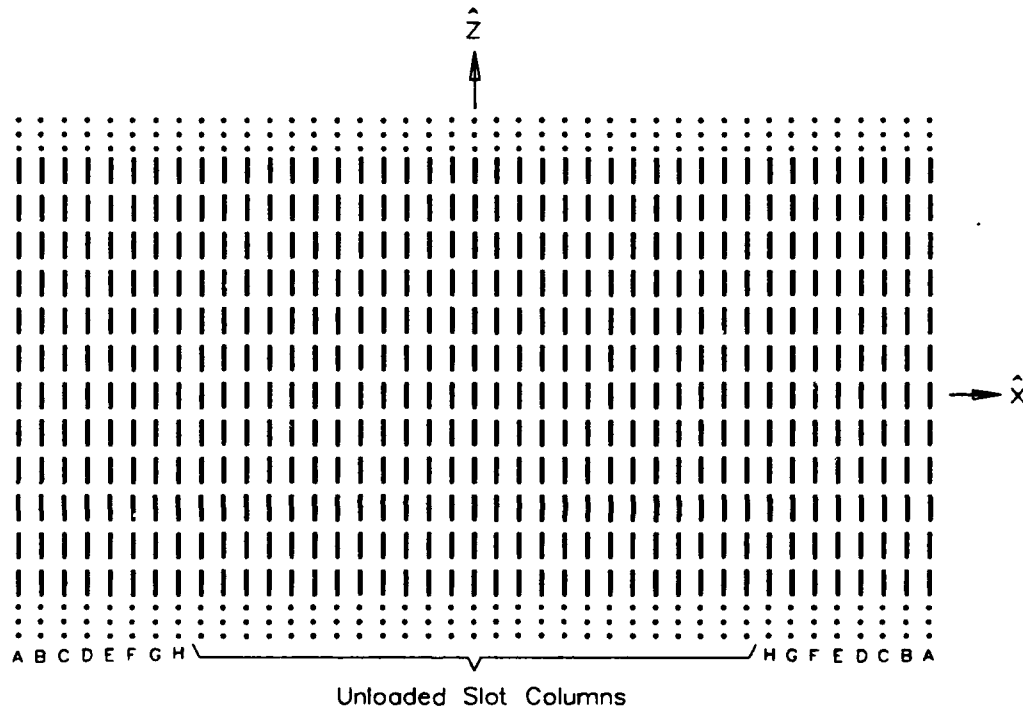


Figure 109: Bistatic Transmission Pattern of 41 Column Truncated Hybrid Radome at 10 GHz, TE_z , $\eta = 60^\circ$ Incidence - Data Normalized to Physical Optics

To lower the 41 column hybrid radome used in this section, the slots in the first 8 columns nearest each edge in each ground plane were loaded in a symmetric fashion⁵. Each slot in the first column (the edge - i.e., modes number 1, 41, 42, and 82) were loaded with 100Ω resistances. Heading inward, the slot columns were loaded with 200Ω , 400Ω , 800Ω , 1600Ω , 3200Ω , 6400Ω , and 12800Ω shunt resistances. Such a loading was created to taper the currents around the edges of the aperture, which should reduce the bistatic sidelobes transmitted through the radome. A front view (normal to the radome) of the 41 column of slots, showing the lattice (drawn to scale) and the shunt resistors, is given in Figure 110. Note that a similar set of slots with the same edge loadings exists on each ground plane.

The edge loaded 41 column hybrid radome was illuminated at normal incidence (10 GHz). The resulting normalized transmission pattern is given in Figure 111, with the plot from the untreated radome shown for reference. The edge treatment does significantly reduce the bistatic sidelobes, but also reduces the main beam of transmission by 1.6 dB. Recall that roughly 40% of the aperture has some degree of resistive loading, which undoubtedly was the reason for this high main beam loss. It is suspected that a similar 8 column edge treatment would reduce the sidelobes well on larger truncated radomes of the same lattice, but with much smaller losses in the main beam.

⁵Note that this is merely a simple trial design, with no attempt of optimization.



Slot Shunt Resistance Loads: A=100 Ω , B=200 Ω , C=400 Ω ,
 D=800 Ω , E=1600 Ω , F=3200 Ω , G=6400 Ω , and H=12,800 Ω

Figure 110: Front View of 41 Column of Slots with Edge Loadings Provided by Shunt Resistances

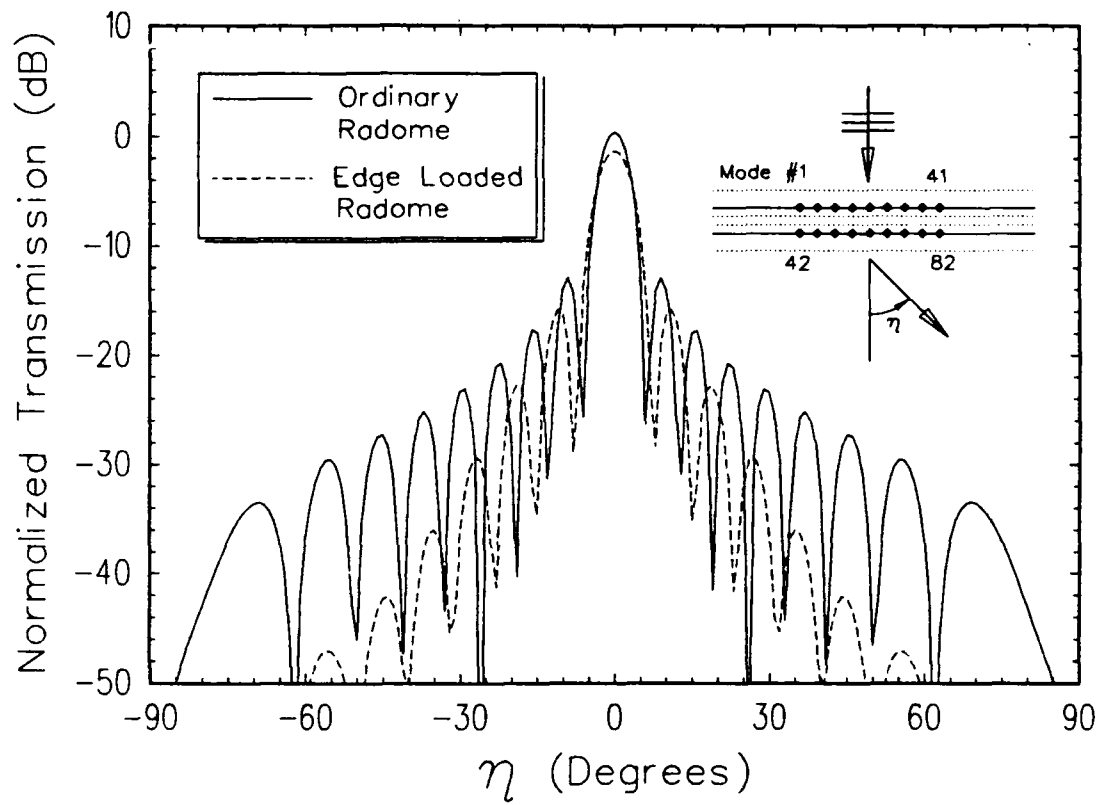


Figure 111: Bistatic Transmission Pattern of Edge Treated and Ordinary Truncated 41 Column Hybrid Radomes at 10 GHz, TE_z , Normal Incidence - Data Normalized to Physical Optics

6.2 ANTENNA WITH RADOME EXAMPLES

Now consider the radiation and scattering from a phased array antenna composed of a finite number of periodic transverse dipole elements in the presence of a truncated radome (e.g., see Figure 113). The phased array is backed by a finite width ground plane which is infinite in \hat{z} . This ground plane needs to be modeled with equivalent electric scattering currents, to be consistent with the Green's functions used in the moment method solution in this dissertation.

A finite width ground plane may be simulated for the TE_z polarization at a given frequency by a finite number of transverse dipole column arrays which are resonating passive scatterers. A similar technique was successfully used by Strickler [11] for modeling a finite width ground plane in the TM_z polarization. The transverse dipole columns are chosen as a truncated version of a doubly-infinite array of perfectly reflecting resonant dipoles, which may be found with the PMM code [3].

In this section, we will show the effects of a phased array antenna in the presence of the 21 column truncated hybrid radome, which was discussed in the previous section. Recalling that this radome was designed to be transparent at 10 GHz, we choose the radiating phased array antenna to operate at the same frequency. Therefore, the finite width ground plane must be designed to reflect perfectly at 10 GHz, normal incidence, with the hope that it is also highly reflective at other angles of incidence at the same frequency. The dipole elements in this ground plane must be chosen at the same D_z (or a submultiple thereof) as the slots in radome, which was 1.125cm.

We choose the dipole lengths in the simulated ground plane to be 1cm, the radii to be 0.2mm, and an inter-column spacing of $D_x = 1.35\text{cm}$ ⁶. A non-skewed grid is

⁶The inter-column spacing is chosen to be less than $\lambda_0/2$ at the resonant frequency to avoid any grating lobe scattering.

selected and the inter-element spacing is $D_z = 1.125\text{cm}$. Using the PMM code, a load of $j161.8\Omega$ (which is 2.575nH at 10 GHz) is needed at the dipole terminals to bring a doubly-infinite array of such dipoles to resonance. With these loads inserted, the PMM code was used to calculate the transmission through the doubly-infinite array of passive dipoles near 10 GHz for normal incidence, $\eta = 30^\circ$, and $\eta = 60^\circ$ (all at $\alpha = 0$). Single piecewise sinusoidal basis and testing functions were used for each element. The results are plotted in Figure 112. A small picture of the normal view of a section of the dipole array is also included. Noting that no loss mechanisms exist, this doubly-infinite array does an excellent job of providing perfect reflection at normal incidence and near perfect reflection at the other angles. Therefore, a truncated version of this array should provide a good job of simulating a finite width ground plane at 10 GHz .

Nine columns of periodic transverse dipoles with the inductive loads were selected for the finite width ground plane simulation. A similar set of dipoles (except being unloaded) were spaced 0.75cm off the "ground plane", which corresponds to $\lambda_0/4$ at the operating frequency. The finite width phased array antenna was placed parallel to the radome and centered in the radome's aperture. The antenna face was brought to $0.5875\lambda_0$ from the outer dielectric interface. This combined antenna and radome geometry is shown in Figure 113, with the view from the infinite $(+\hat{z})$ axis. Note that the truncated hybrid radome is exactly the same as that shown in Figure 96.

The elements of the antenna face were uniformly excited (and in-phase for normal direction beam steering) with one volt delta gap generators, and allowed to radiate. The simulated ground plane elements and slot modes remained passive scatterers. The resulting transmission through the radome is plotted in Figure 114, along with a reference pattern for the antenna and ground plane dipoles without

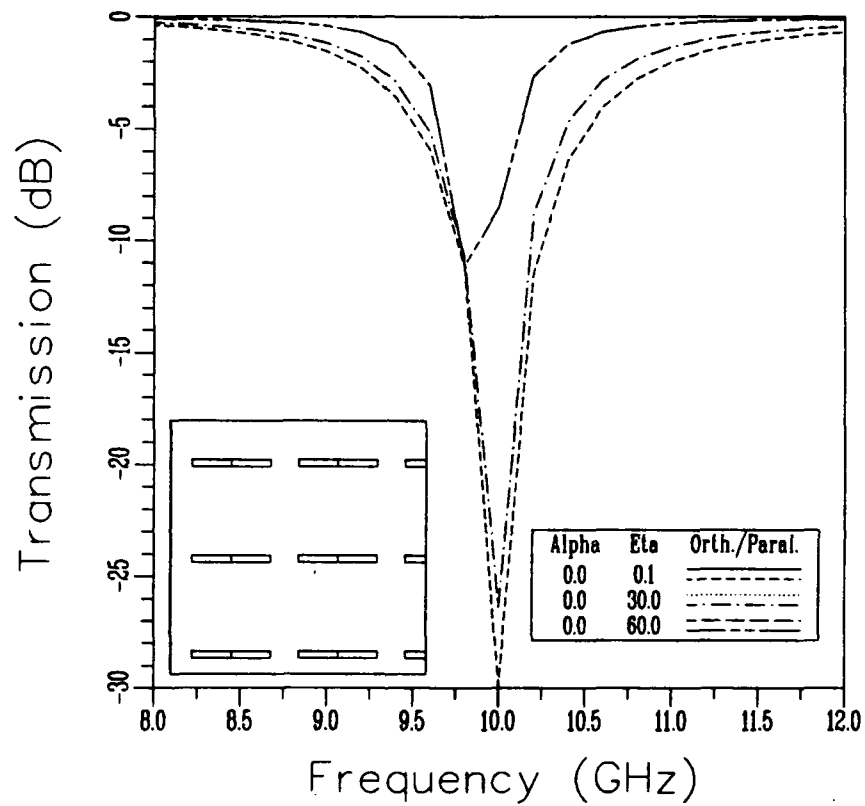


Figure 112: Transmission Through a Doubly-Infinite Array of Passive Inductively Loaded Dipoles in Resonance from the PMM Code

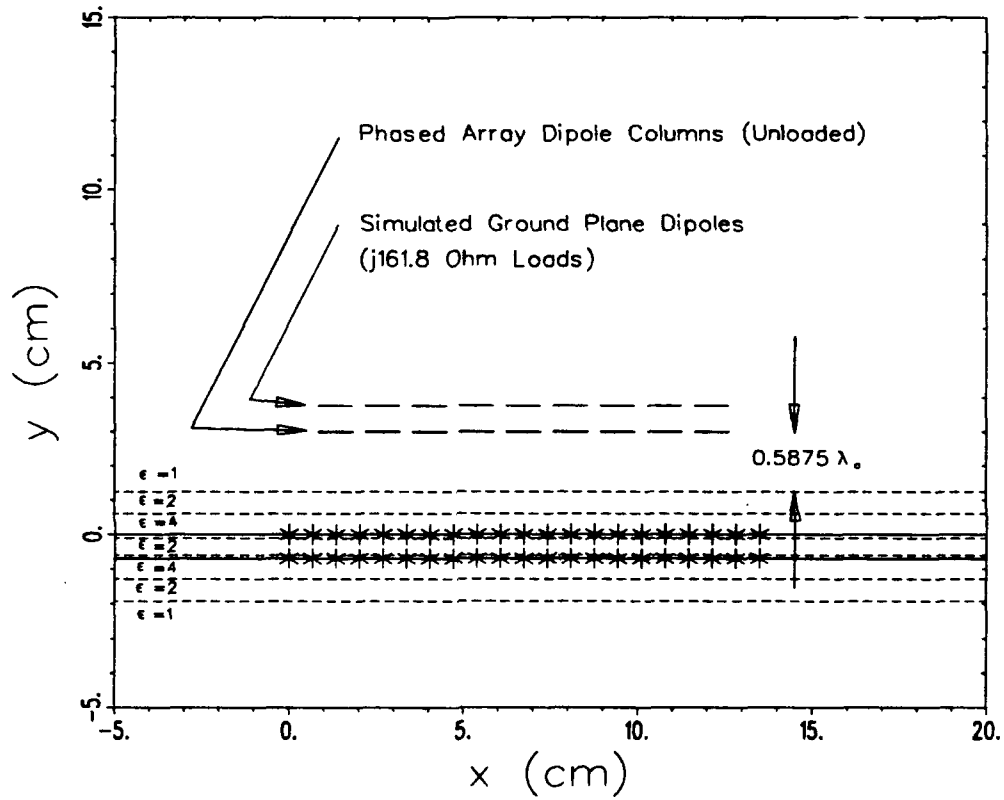


Figure 113: Top View of Finite Phased Array Antenna Near the 21 Column Truncated Hybrid Radome - Antenna to Radome Space = $0.5875\lambda_0$

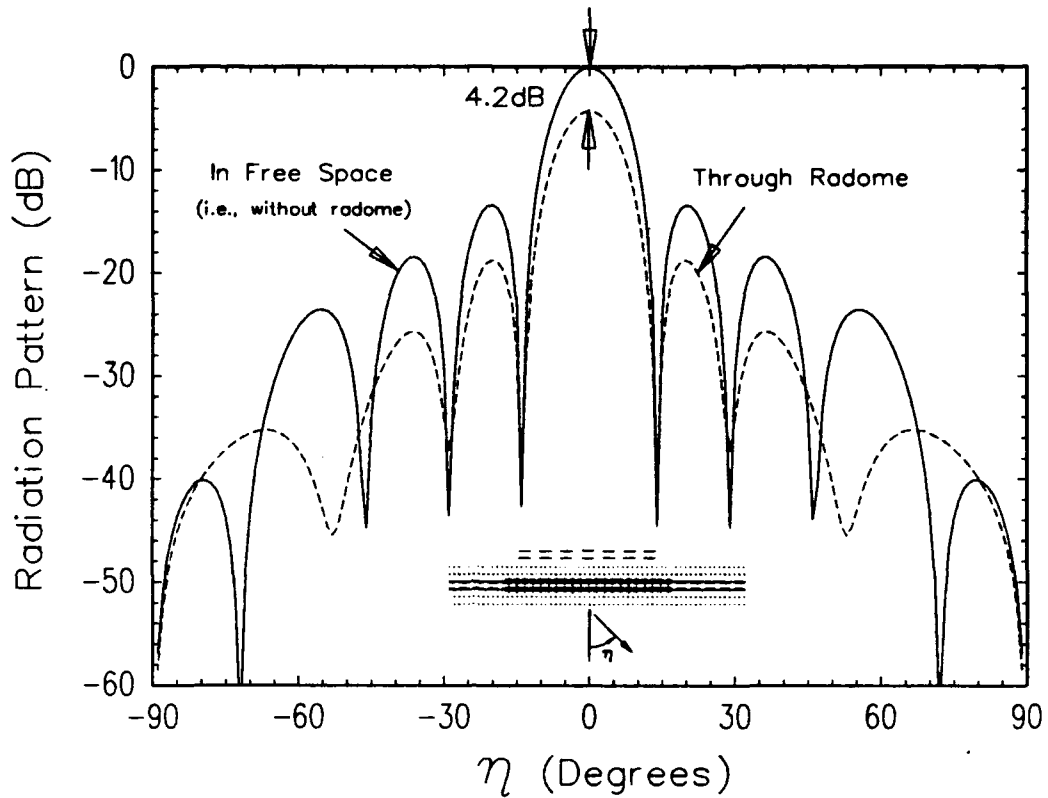


Figure 114: Transmission Patterns for the Antenna/Radome Geometry in Figure 113 and the Antenna in Free Space with Uniform In-Phase Excitation, 10 GHz, TE_z

the radome. The free space main beam provides a normalization for both patterns. Note that the main beam of the antenna through the radome is about 4 dB lower than the main beam in free space.

The apparent loss of 4 dB of transmission through the radome is puzzling, especially with the excellent transmission result (normalized to the fields expected by physical optics) the same radome demonstrated in Figure 100. To see why it occurred, some numerical experiments were created.

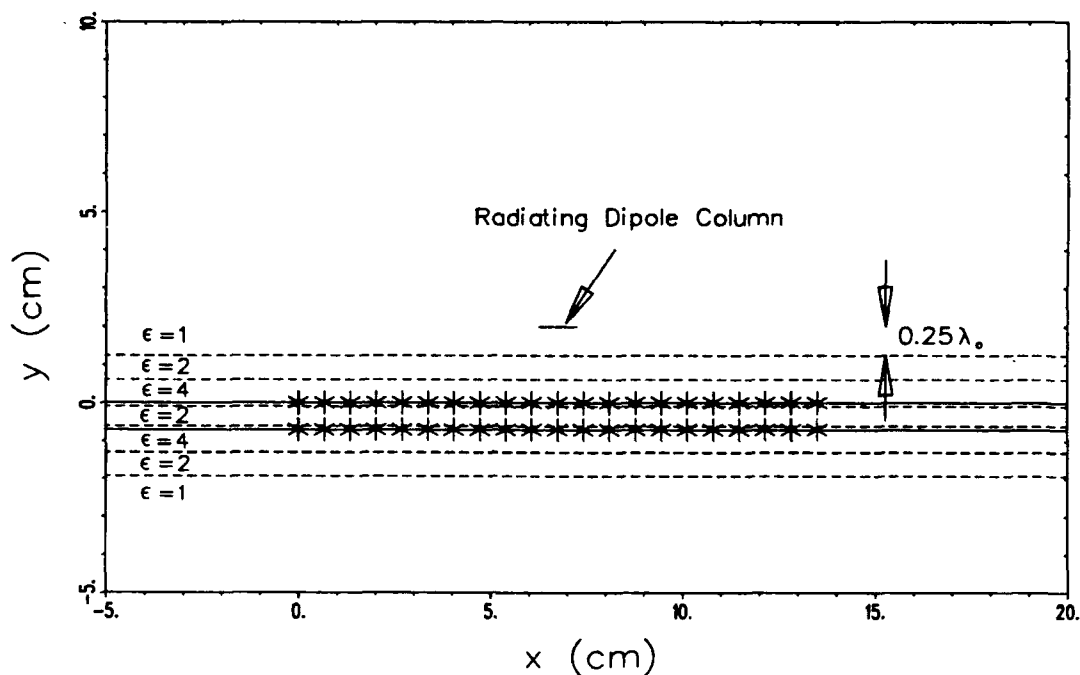


Figure 115: Top View of Test Geometry with One Radiating Column of Transverse Dipoles placed $\lambda_0/4$ from the 21 Column Truncated Hybrid Radome

The first experiment consisting of one column of radiating periodic transverse dipoles⁷ placed $\lambda_0/4$ away from the outer dielectric surface of the 21 column truncated hybrid radome, and centered in the radome's aperture. A top view of this geometry is shown in Figure 115.

The resulting radiation of the dipole column from Figure 115, both through the radome and without the radome, are plotted in Figure 116. Note that the apparent loss through the radome is almost 4 dB. This loss is probably not solely due to edge effects from the radome, since from the single dipole column's perspective, the radome should appear very wide.

Another experiment was conducted by moving the single radiating dipole column further from the radome, with the hypothesis that some near zone effects were

⁷Again, with $L = 1\text{cm}$, $D_z = 1.125\text{cm}$, wire radius = 0.2mm, and unloaded.

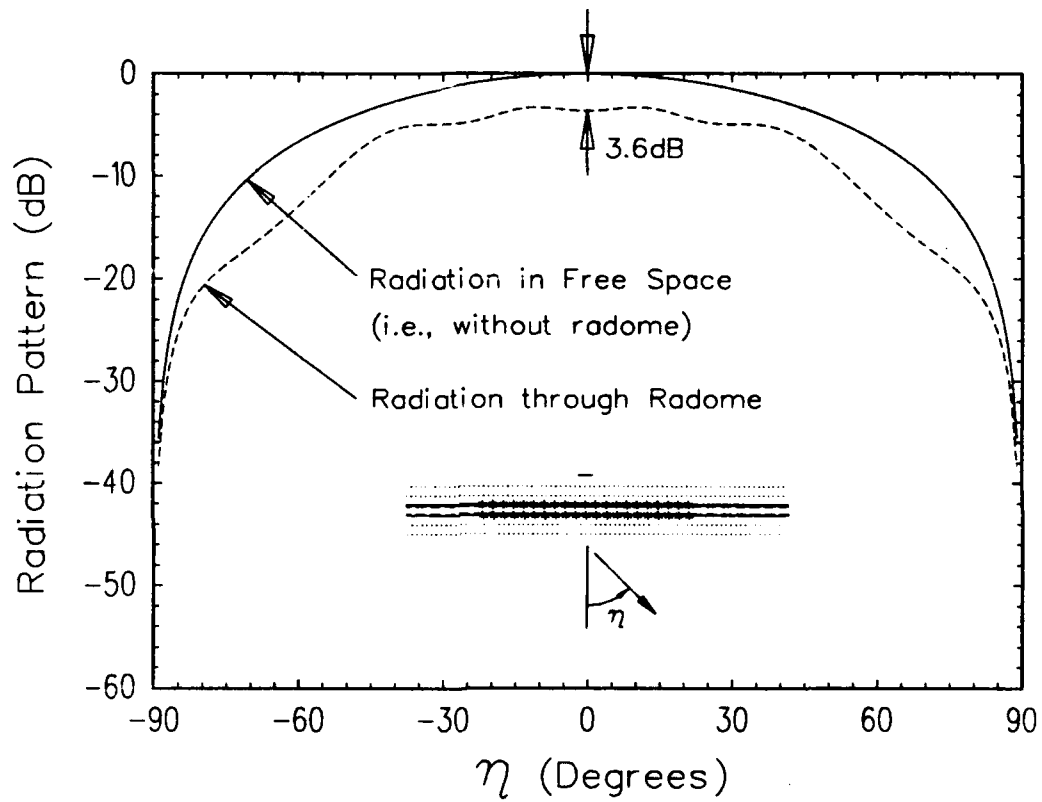


Figure 116: Transmission Patterns for the Single Dipole Column in Figure 115 both Through the Radome and Without the Radome, 10 GHz, TE_z

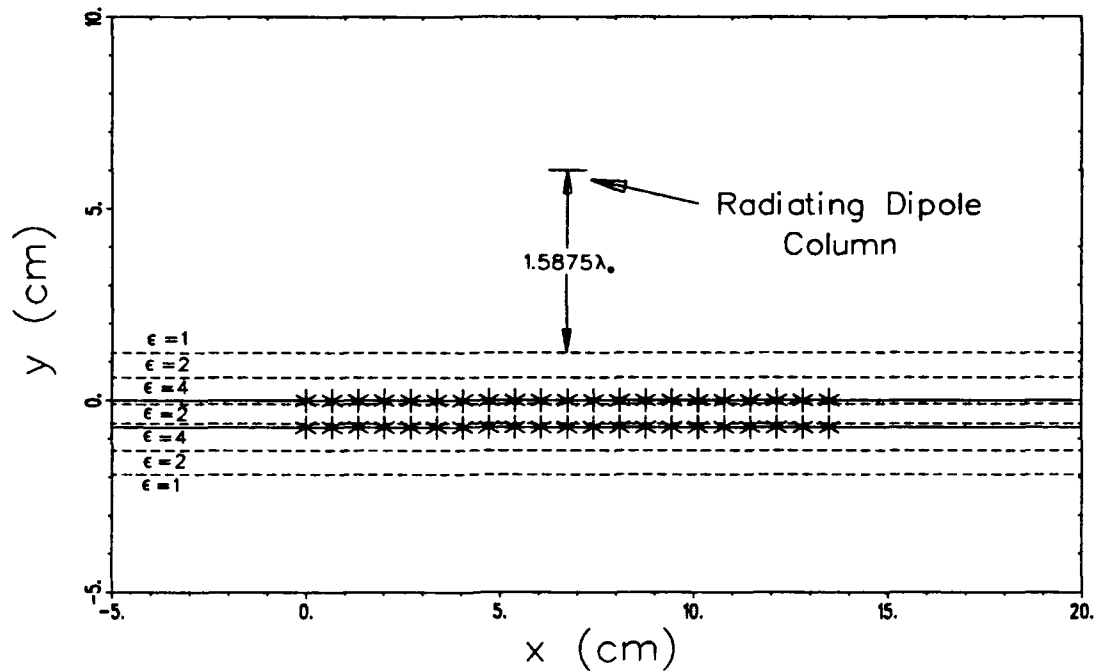


Figure 117: Top View of Test Geometry with One Radiating Column of Transverse Dipoles placed $1.5875\lambda_0$ from the 21 Column Truncated Hybrid Radome

making the radome incapable of perfect transmission in the previous cases. The new distance between the dipoles and the outer dielectric surface was $1.5875\lambda_0$. A top view of this geometry is shown in Figure 117.

The resulting transmission patterns for the dipole column from Figure 117 in free space and through the radome are plotted in Figure 118. This time, the drop in transmission through the radome at the normal direction is only 0.25 dB. This provides some confirmation that a near zone problem may have appeared to make the radome less transmissive than it is. Also note that the edges of the radome create some rippling and shadow effects in the transmission pattern.

The apparent loss through the radome when radiating dipoles are placed close to the radome may be caused by many effects. Two major effects were contemplated by the researcher. The first is the simple fact that the dipoles radiating near the

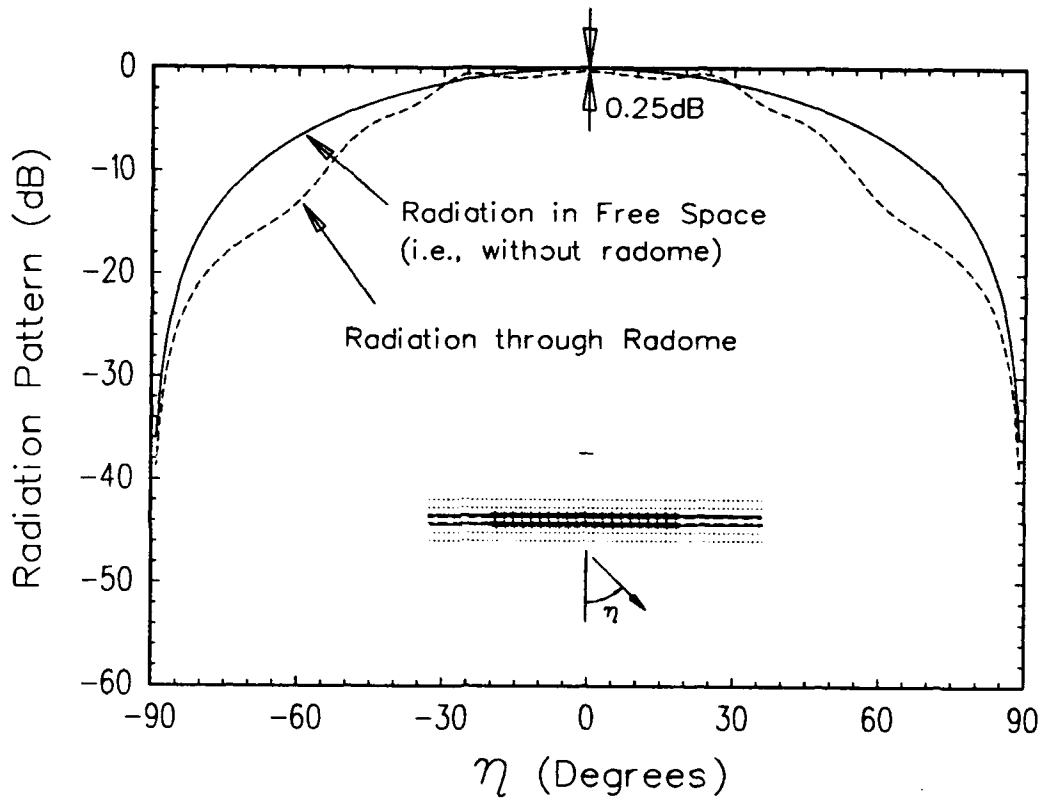


Figure 118: Transmission Patterns for the Single Dipole Column in Figure 117 both Through the Radome and Without the Radome

radome introduce cylindrical wavefronts, which cannot be approximated as a simple plane wave⁸ However, any cylindrical wavefront may be decomposed into a bundle of plane waves, and since the radome is supposed to be transmissive for most angles of plane wave incidence, it seems highly unlikely that a cylindrical wavefront should be reflected or attenuated by 4 dB.

A second theory is that the near zone presence of the dielectric coated radome provides a de-tuning effect on the radiating dipoles. Recalling that the radome's presence provides a reflected component in the self-impedance term, it is possible that a large reflected component could change the input impedance of the dipoles enough so that they radiate with much lower currents than they would in free space under the same impressed one volt delta gap generators.

To test this theory, the input impedances for the antenna array columns from the geometry in Figure 113 were calculated and plotted. These calculations were made by dividing the one volt impressed sources on each column mode by the solution current coefficients, found in the moment method. The input impedance data is shown in Figure 119, along with similar input impedance data for the 9 column phased array in free space.

The input impedances in Figure 119 for each column in free space is nearly constant, and also very near the value of $87 - j162\Omega$ predicted for each column in the PMM code (not plotted). The input impedances for the columns near the radome, though, vary greatly, and are on the average much higher in magnitude than their free space counterparts. This provides some confirmation that the antenna is radiating less efficiently in this position very near the radome.

As a final test, the 9 column phased array antenna was moved back to a distance of $2.5875\lambda_0$ from the radome. This geometry is shown in Figure 120.

⁸Recall that the radome was designed to be perfectly transmissive for plane wave incidence.

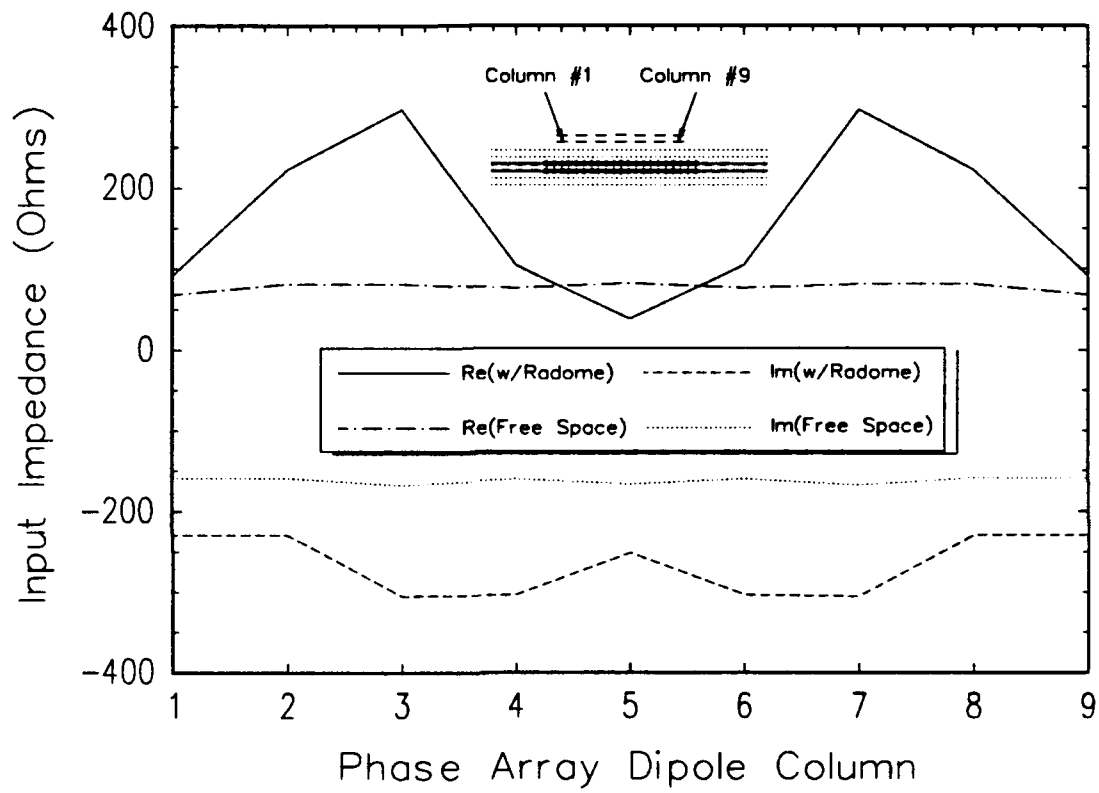


Figure 119: Input Impedances for Each Column in the Dipole Antenna Array in Figure 113 along with Similar Input Impedances for the Antenna in Free Space, 10 GHz

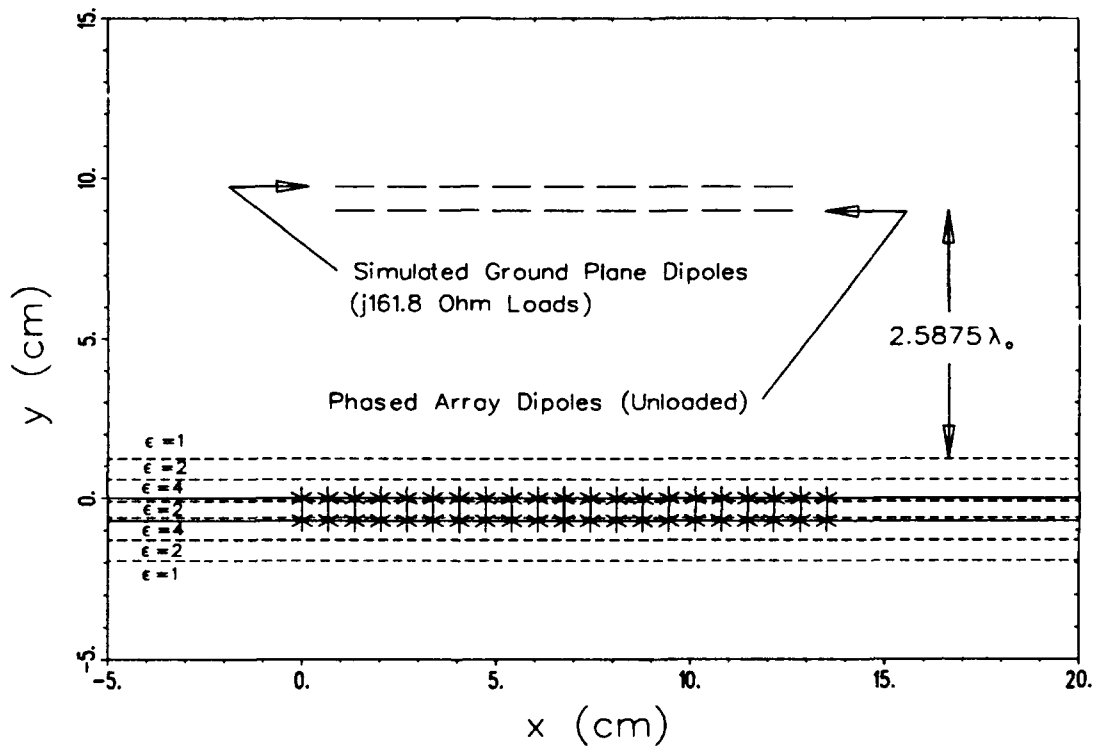


Figure 120: Top View of Finite Phased Array Antenna Near the 21 Column Truncated Hybrid Radome - Antenna to Radome Space = $2.5875\lambda_0$

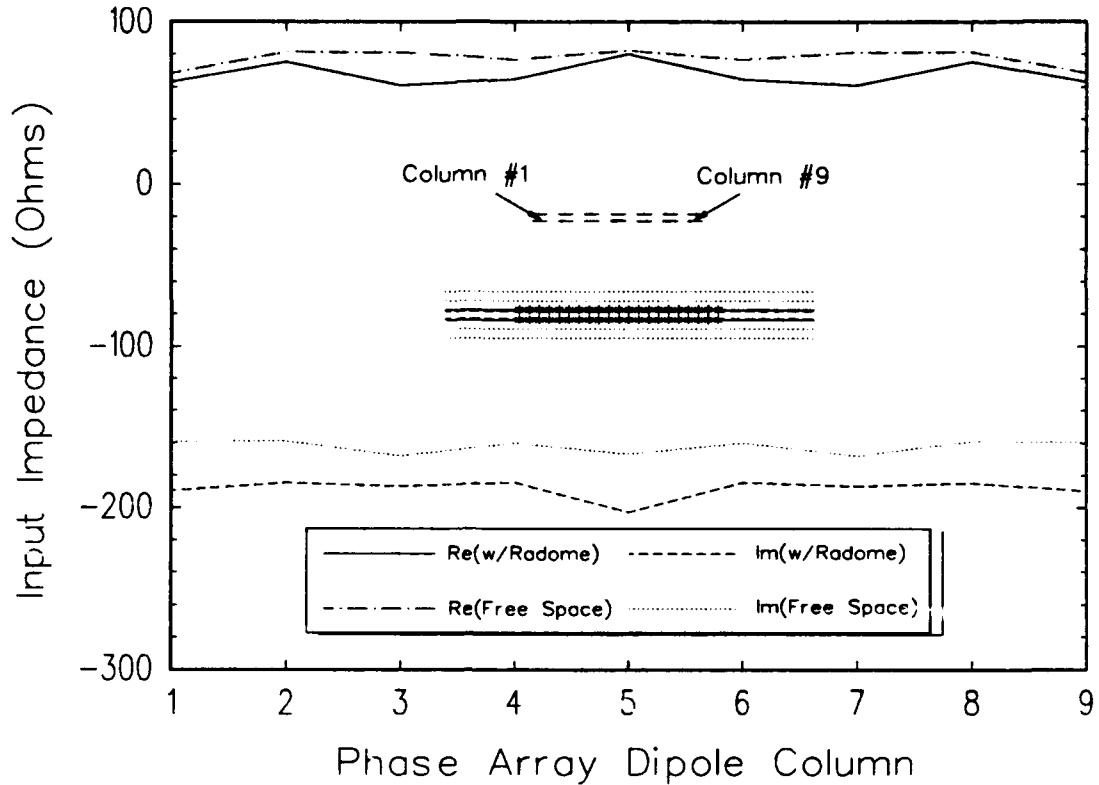


Figure 121: Input Impedances for Each Column in the Antenna Array in Figure 120 along with Similar Input Impedances for the Antenna in Free Space, 10 GHz

The antenna was again excited uniformly with 1 volt delta gap generators (in-phase) and allowed to radiate both in free space and through the radome. First, however, the input impedances were calculated. They are plotted in Figure 121. Note that the impedances with the radome are much better behaved, and nearer the magnitudes of the free space input impedances than those shown in Figure 119.

Finally, the transmitted field patterns for the antenna shown in Figure 120 were calculated and are shown in Figure 122. Note that now the apparent transmission loss is only 1.4 dB, which may be largely due to the fact that the radome's aperture is not large enough for this antenna at this distance from the radome.

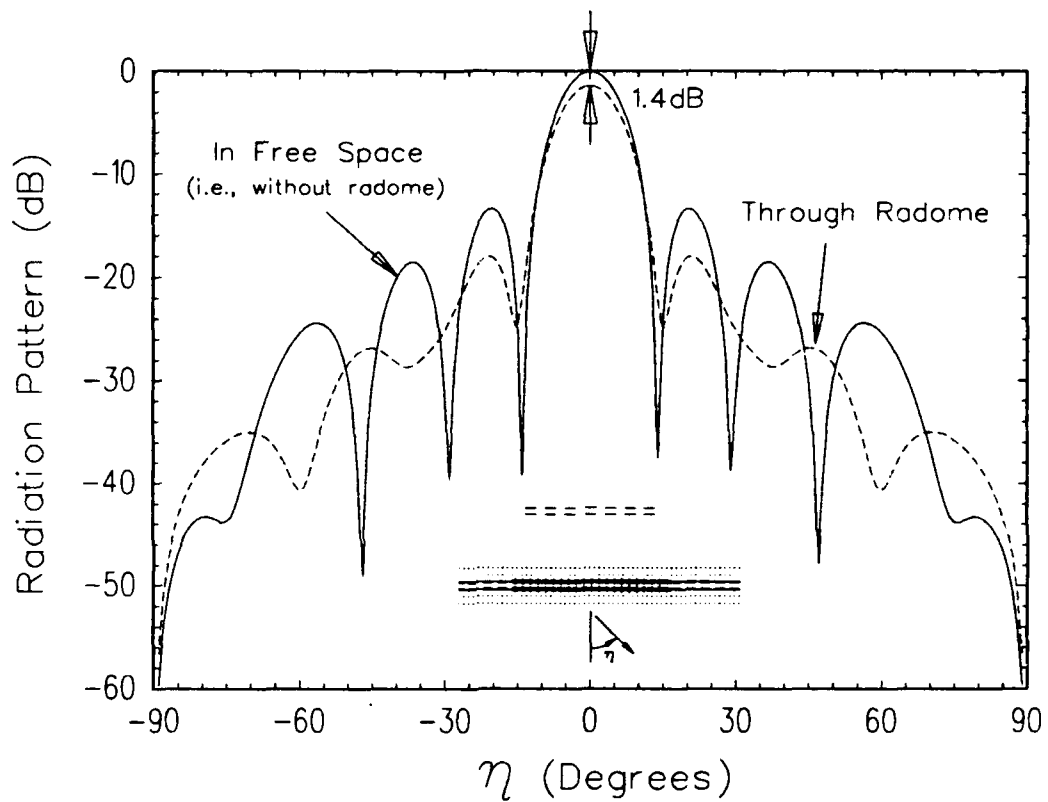


Figure 122: Transmission Patterns for the Antenna/Radome Geometry in Figure 120 and the Antenna in Free Space with Uniform In-Phase Excitation, 10 GHz, TE_z

CHAPTER VII

CONCLUSIONS

This dissertation describes the development of a moment method based solution for the electromagnetic radiation and scattering from geometries composed of a finite collection of transverse dipole column arrays and a finite collection of axial slot arrays, as possibly buried within a stratified medium, as shown in Figures 1 and 2. These geometries form a subset of the general class of "finite by infinite" periodic surfaces, which are of growing interest.

A coupling matrix for the geometry is developed with 9 sub-blocks, representing mutual admittances, mutual impedances, unitless voltage gains, and unitless current gains. Efficient methods for calculating the entries of the coupling matrix were developed, using both spatial and spectral domain methods in free space, and using the Array Scanning Method (ASM) to circumvent the application of Sommerfeld integrals with planar dielectric interfaces. Asymptotic approximations were also explored, with convergence tests made to test the accuracy of such methods, as compared to more rigorous solutions.

Throughout the dissertation, coupling matrix calculations were compared with those from the PMM code [3], by spatially constructing doubly-infinite array coupling with many column-to-column coupling terms. Excellent agreement with the PMM solutions provides confidence in each "piece" of the moment method solution.

Finally, the complete moment method procedure was applied to finite width radome and radome/antenna geometries, with results in specular scattering directions coming very close to those predicted by a simple combination of using PMM data and physical optics. Scattering from these geometries in non-specular directions, however, could not be accurately predicted by methods previous to this research.

Future research may be made in extending the methods used in this dissertation for wire and slot elements of more general shapes and orientations. Truncations in the dielectric sandwich in which the arrays are embedded may be approached with diffraction methods. In addition, now that the analysis method has been developed (though it may certainly be refined for better efficiency and accuracy), a new class of antenna and radome designs may be explored, with treatments of edge scattering effects better understood than from the experimental "trial and error" approach of the past.

APPENDIX A

CONVERGENCE ACCELERATION OF INFINITE SUMS

Many attempts have been made at accelerating the numerical evaluation of infinite sums associated with the radiation of periodic sources [33, 34, 35]. Most published efforts involve only the acceleration of a periodic Green's function, which does not contain a pattern factor to assist the convergence.

Most acceleration attempts involve the Poisson sum formula [20] to convert spatial domain expressions to spectral domain expressions (or vice versa). Some attempts also use the Kummer's transformation [28] to split a single domain sum into a combination of spectral and spatial domain sums. While there are isolated cases where this is beneficial, they occur infrequently and thus the Kummer's transformation is not used in this study.

Some acceleration techniques can be applied after the Poisson sum transformation to either spatial or spectral domain sums. These techniques can involve windowing, as in the Fejer kernel. Weighted windowing can produce poor results at high scan angles, but with s_z constrained to zero, this is not a concern for the one-dimensional sums for this class of problems. In addition to windowing methods, other "piggyback" forms of acceleration can be applied. They include the spiral average method and the Shanks' transformation. These methods are described as follows.

Examples given in this appendix do not involve the pattern factors associated with axial slots and transverse dipoles. The effect that these pattern factors make on convergence is discussed in the main body of this dissertation.

A.1 THE FEJER KERNEL

The Fejer kernel is a simple triangular windowing function, which when multiplied to certain series terms, enhances summation convergence [36]. The implementation of the Fejer kernel is simply to make the following approximation:

$$\sum_{m=-\infty}^{\infty} f(m) \approx \sum_{m=-M}^M w(m) f(m), \quad (\text{A.1})$$

where the Fejer kernel weights given by

$$w(m) = 1 - \frac{|m|}{M+1}. \quad (\text{A.2})$$

When applying the Fejer kernel to a series, apriori knowledge of what integer M leads to good accuracy is usually not available. Therefore, the strategy for obtaining convergence is to incrementally adjust M from 1 up to whatever is required, applying the M dependent Fejer kernel at each iteration, and compare successive iterations until very small changes in the sum are detected. Since the shape of the Fejer kernel (or any windowing function) changes with each increment, an unavoidable "overhead" in computation time is formed when a good value for M is not known apriori.

The Fejer kernel is particularly effective for series of which successive partial summations tend to oscillate about the convergent solution.

A.2 THE SPIRAL AVERAGE METHOD

The spiral average method is a technique to enhance the convergence of singly infinite spatial domain sums occurring from periodic sources. The method is based on the fact that no matter where a field observation point is located (with respect to a radiating column array) the difference in spatial slant distances between successive sources and the observation point will asymptotically approach the inter-element spacing (D_z) as the spatial index is increased. That is, the series of slant distances, which from the Pythagorean theorem is non-linear, asymptotically approaches a linear condition.

When summing spatially on an index of $-\infty$ to ∞ , it is convenient to locate the zero index source as near to the observation point as possible, then add pairs of terms associated with \pm the next integer index. When successive pairs of spatial domain quantities are added, whether they are fields, induced voltages, or impedances, they tend to spiral about the convergence point in the complex plane.

To illustrate the spiral average method, the following example is used. Suppose we wish to calculate the free space periodic Green's function from an array of simple point sources, as depicted in Figure 123.

The Green's function is

$$G = \sum_{m=-\infty}^{\infty} \frac{e^{-j\beta R_m}}{4\pi R_m}. \quad (\text{A.3})$$

Now suppose the inter-element spacing, D_z , is $\lambda/3$. Then by the spiral average method, exactly 3 pairs of successive partial sums should form one revolution in the spiral. Therefore, we may truncate the sum at some value $m = M$ where $M \geq 3$ and average the last three partial sums. The series of partial sums and the effect of the spiral average is shown in Figure 124, which shows the calculation for an observation point at $\rho = 0.2\lambda$ and $z = 0.1\lambda$.

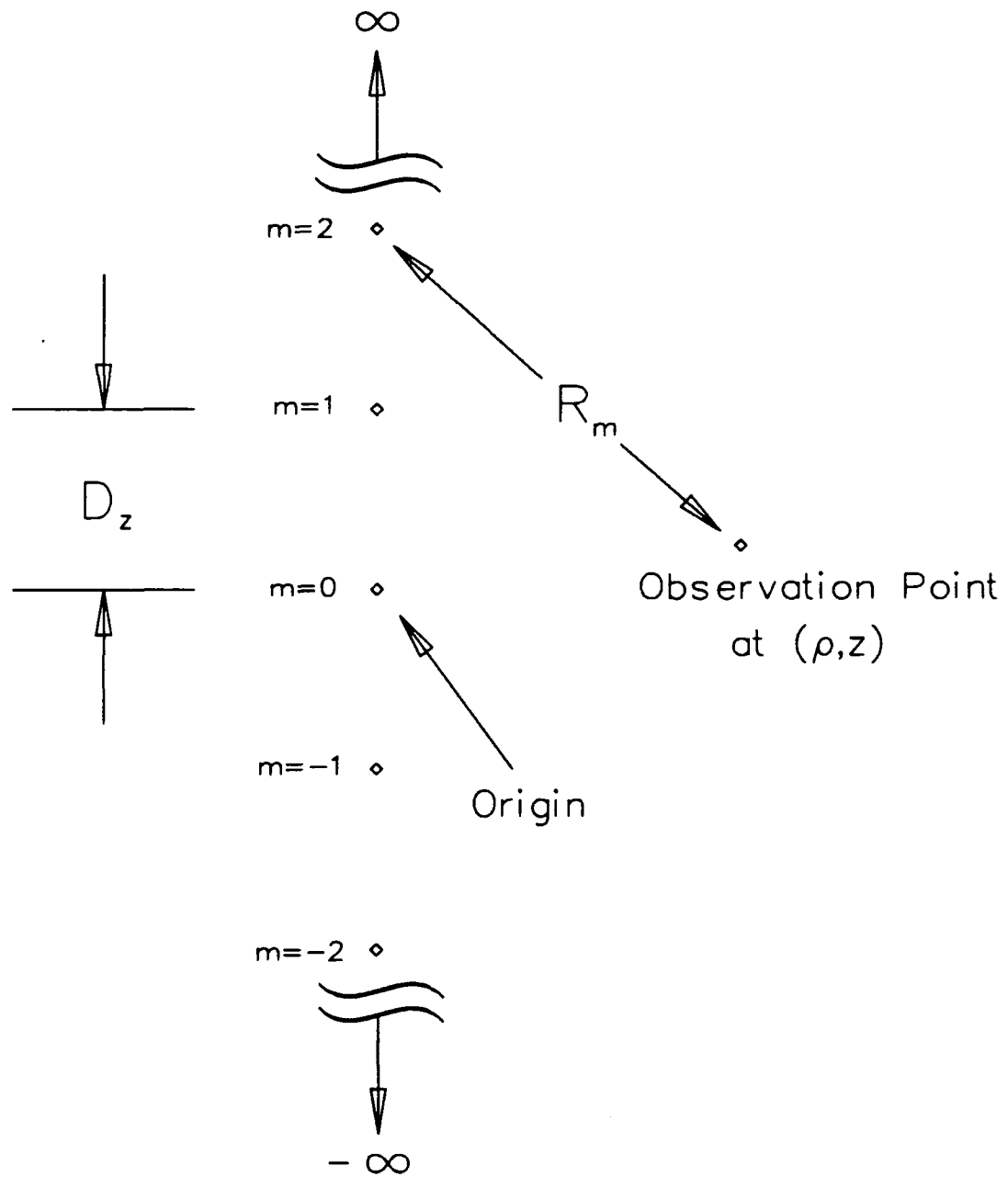


Figure 123: Array of Point Sources

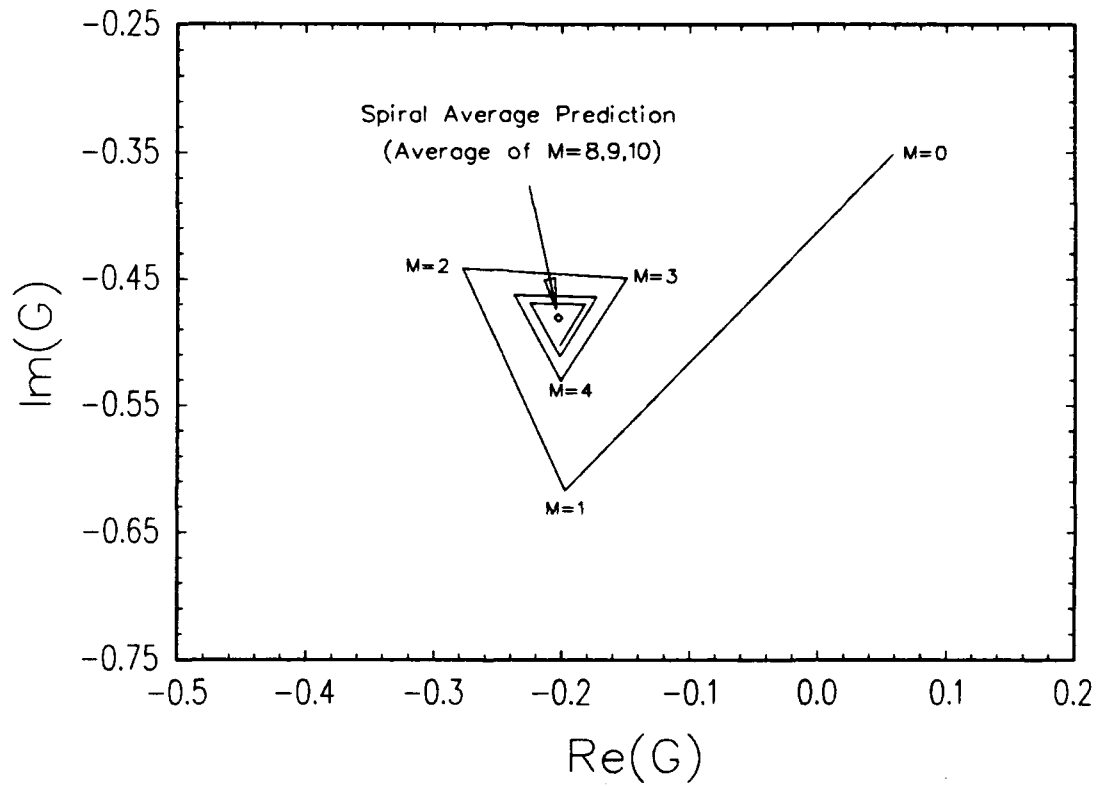


Figure 124: Spiral Average Method for Free Space Periodic Green's Function - $D_z = \lambda/3$, $\rho = 0.2\lambda$, $z = 0.1\lambda$

For the example chosen, the inter-element spacing of $\lambda/3$ makes one revolution in the spiral occur in exactly three successive terms. Thus, the spiral appears to be approximately of the form of equilateral triangles. Had the inter-element spacing been $\lambda/4$, the spiral would look like a set of squares. For a spacing of $D_z = 2\lambda/3$, three successive terms would be used in the spiral average, which would correspond to two revolutions in the spiral. In general, the rule is that the number of terms in one revolution is

$$N = \lambda/D_z. \quad (\text{A.4})$$

Often, the inter-element spacing will be an irrational number which does not lead to an exact number of revolutions to average. In this case, an error parameter must be chosen and a search must be made until the number of terms in the spiral is within the error percentage of an integral number of revolutions.

As with the Fejer kernel method, the spiral average method must be iterated with increases in the maximum M until convergence is found. Unlike the Fejer kernel method, though, the past history of computations may be saved in the spiral average. For example, consider the case plotted in Figure 124. The present spiral average computation involved averaging the partial sums at $M = 8, 9$, and 10 . To reach the next prediction, add the pair of terms to get $M = 11$, then divide it by 3 , add this to the prediction, and subtract out the $M = 8$ partial sum divided by 3 . This process takes much less time than the complete change of weights associated with the Fejer kernel.

Had the observation distance, ρ , been far from the array axis, more terms would have to be included to make the series approach a well behaved spiral. This is a simple consequence of the non-linear phase change between terms in the series. As a result, the spiral average method works quicker for closer observation points.

A.3 SHANKS' TRANSFORMATION

Shanks' transformation is an algorithm which converts an infinite summation into a "pyramid" of numbers, the cornerstone of which is a prediction of the infinite sum. It is based on the assumption that the partial sums (i.e., summed from $m = -M$ to $+M$, as M increases) form a mathematical transient [37]. The transient for the partial sums up to order N are assumed to behave according to a $(N + 1)$ th order finite difference equation. The Shanks' algorithm is used to predict the final convergent sum, using all of the partial sums up to order N . Shanks' algorithm was recently used by Singh [35] for electromagnetic applications involving infinite arrays.

The pyramid formed with Shanks' transformation are numbers denoted by the function, $e_m(S_n)$, where m designates the column of the entry and n represents the row. Furthermore, S_n is the partial sum of order n . Thus, e_m is a function which operates on the partial sums. The subscript m can range from zero to the highest order of the partial sums used. To generate the pyramid, the algorithm is defined by the following equations:

$$e_0(S_n) = S_n, \quad (\text{A.5})$$

$$e_1(S_n) = \frac{1}{[e_0(S_{n+1}) - e_0(S_n)]}, \quad (\text{A.6})$$

$$e_{m+1}(S_n) = e_{m-1}(S_{n+1}) + \frac{1}{[e_m(S_{n+1}) - e_m(S_n)]}, \quad (\text{A.7})$$

where the last equation is valid for $m = 1, 2, 3, \dots$

A particularly powerful application of Shanks' transformation is on the Leibnitz series for π . The series is

$$\pi = \sum_{n=0}^{\infty} \frac{4(-1)^n}{2n+1}. \quad (\text{A.8})$$

With the help of Shanks' transformation, only the first 8 terms of the series are needed to calculate π correctly to eight significant figures. Direct addition of the

series requires approximately 40 million terms for the same accuracy! Truncating the series at $N = 4$, the pyramid formed by Shanks' algorithm is as follows:

n	e0 = S _n	e1	e2	e3	e4
0	4.00000	-0.75	3.16667	-28.753	3.14235
1	2.66667	1.25	3.13334	82.284	--
2	3.46667	-1.75	3.14524	--	--
3	2.89524	2.25	--	--	--
4	3.33968	--	--	--	--

As seen in the above data, the predicted value of π using the Shanks' algorithm on the first five partial sums is 3.14235, which is at the $e_4(S_0)$ slot (the "cornerstone"). The e_{odd} columns are intermediary steps which must be filled to generate the pyramid. The next best prediction requires two additional terms, which puts the cornerstone at the $e_6(S_0)$ slot.

Shanks' transformation tends to work better on series which oscillate about the convergence point. For the infinite array problems in electromagnetics, oscillations (or in the complex plane, spiraling) occurs in spatial domain expressions, while spectral domain sums approach the convergence point in a monotonic manner. Shanks' algorithm may be used to decrease the number of spectral domain terms for a given accuracy, but the overhead associated with building the pyramid of numbers makes it no faster than just adding the raw spectral domain series. In the spatial domain, however, Shanks' transformation can reduce computation time due to the dramatic reduction in the number of terms required.

APPENDIX B
THE ARRAY SCANNING METHOD FOR A SINGLE COLUMN OF PERIODIC SOURCES

Consider a doubly infinite array of electric Hertzian dipoles on the XZ plane in free space, as depicted in Figure 125. The elements are indexed spatially with the subscripts qm , which denote the X and Z lattice positions, respectively. Note that the reference element, denoted by $q = m = 0$, is located at the origin, and that all dipoles are oriented in some common direction \hat{p} . The magnetic vector potential from a typical element at an observation point, (x, y, z) , is [14]:

$$d\bar{A}_{qm} = \hat{p} \frac{\mu I_{qm} dl}{4\pi} \frac{e^{-j\beta R_{qm}}}{R_{qm}}, \quad (\text{B.1})$$

where the spatial distance is

$$R_{qm} = \sqrt{(qD_x - x)^2 + y^2 + (mD_z - z)^2}. \quad (\text{B.2})$$

Assume that the currents for the Hertzian array obey Floquet's theorem for some propagation in the direction

$$\hat{s} = \hat{x}s_x + \hat{y}s_y + \hat{z}s_z. \quad (\text{B.3})$$

By Floquet's theorem [19], the current on a typical element is of the form

$$I_{qm} = I e^{-j\beta q D_x s_x} e^{-j\beta m D_z s_z}. \quad (\text{B.4})$$

Now consider the total vector potential at the observation point, given by the superposition of all of the sources as

$$d\bar{A} = \sum_{q=-\infty}^{\infty} e^{-j\beta q D_x s_x} \left[\hat{p} \frac{\mu I dl}{4\pi} \sum_{m=-\infty}^{\infty} \frac{e^{-j\beta R_{qm}}}{R_{qm}} e^{-j\beta m D_z s_z} \right]. \quad (\text{B.5})$$

in a Fourier series, one can use the Fourier method. That is, the coefficients can be found by

$$d\bar{A}_q = \frac{1}{T} \int_{-T/2}^{T/2} (d\bar{A}) e^{-jq\omega_0 t} dt, \quad (\text{B.7})$$

where the Fourier series period is

$$T = \frac{2\pi}{|\omega_0|} = \frac{\lambda}{D_x}. \quad (\text{B.8})$$

Thus comes the result that the vector potential from the single column of sources including the reference element is

$$d\bar{A}_0 = \frac{D_x}{\lambda} \int_{-\frac{\lambda}{2D_x}}^{\frac{\lambda}{2D_x}} (d\bar{A}) ds_x. \quad (\text{B.9})$$

Note that the integrand in Equation (B.9) represents the total vector potential from the complete doubly infinite array of sources in Figure 125. Also note that the variable s_x is merely the sine of the scan direction (relative to the \hat{y} axis, as projected in the XY plane) caused by the phasing of the elements. Thus, Equation (B.9) may be interpreted as finding the weighted average of the total vector potential over some range of scan angles. Thus, finding the vector potential from this equation is dubbed the array scanning method (ASM).

The array scanning method in Equation (B.9) may easily be extended to find the fields, induced voltages, or mutual impedances for columns of periodic elements (dipoles or slots) of finite length and arbitrary shape. This extension comes from spatial derivatives and integrals, and does not affect the integration on s_x . Equation (B.9) may also be extended to include any stratified media which is infinite in \hat{x} and \hat{z} . Such a media will not disturb the Floquet phasing between the currents in the doubly infinite array, which is essential in the derivation of the ASM.

The array scanning method suggests that if one desires the effect of a single column of sources, one can "artificially" construct a doubly infinite array around the single column, and apply the form of Equation (B.9). The user has freedom over the inter-column spacing D_x in this "artificial" array. If one chooses $D_x = \lambda/2$, then the limits of integration go from -1 to $+1$, which corresponds to scanning over the entire XY plane in real space. This is often the most convenient choice in that it forces the occurrence of surface wave singularities (for stratified media) to occur only in the central term of the plane wave expansion.

BIBLIOGRAPHY

- [1] B. A. Munk, G. A. Burrell, and T. W. Kornbau, *A General Theory of Periodic Surfaces in Stratified Dielectric Media*, Technical Report 784346-1, ElectroScience Laboratory, Ohio State University, generated under contract F33615-76-C-1024, for Avionics Laboratory, Air Force Wright Aeronautical Laboratories, Wright-Patterson AFB, Ohio, November 1977.
- [2] B. A. Munk, *A General Theory of Periodic Surfaces in a Stratified Dielectric Medium*, Technical Report 715582-4, ElectroScience Laboratory, Ohio State University, generated under contract F33615-83-C-1013, for Avionics Laboratory, Air Force Wright Aeronautical Laboratories, Wright-Patterson AFB, Ohio, February 1986.
- [3] L. W. Henderson, *Introduction to PMM*, Technical Report 715582-5, ElectroScience Laboratory, Ohio State University, generated under contract F33615-83-C-1024, for Avionics Laboratory, Air Force Wright Aeronautical Laboratories, Wright-Patterson AFB, Ohio, February 1986.
- [4] S. W. Schneider, *The Design and Construction of Two Low VSWR Broadband Arrays*, M. S. Thesis, Ohio State University, 1988.
- [5] T. Cwik, R. Mittra, K. C. Lang, and T. K. Wu, *Frequency Selective Screens*, feature article for the IEEE Antennas and Propagation Society Newsletter, Vol. 29, No. 2, April 1987.
- [6] K. A. Shubert, *Impedance Properties of Large Finite Dielectric Covered Phased Arrays*, Ph.D. Dissertation, Ohio State University, 1980.
- [7] R. Kastner and R. Mittra, *A Combination of the Spectral-Iterative Technique and the Conjugate Gradient Method for Analyzing Finite-Sized Frequency Selective Surfaces with Rectangular Patches*, in 1984 IEEE Antennas and Propagation Soc. Int. Symp. Dig., Boston, Massachusetts, pp. 925-928, June 1984.
- [8] T. Cwik and R. Mittra, *The Effects of the Truncation and Curvature of Periodic Surfaces: A Strip Grating*, IEEE Transactions on Antennas and Propagation, Vol. AP-36, No. 5, pp. 612-622, May 1988.
- [9] J. A. Hughes, *Impedance Properties of Cylindrical Arrays and Finite Planar Arrays*, M.S. Thesis, Ohio State University, 1988.
- [10] J. I. Simon, *Impedance Properties of Periodic Linear Arrays Conformal to a Dielectric-Clad Infinite PEC Cylinder*, Ph.D. Dissertation, Ohio State University, 1989.
- [11] K. A. Strickler, *Impedance Properties of Singly Infinite Periodic Surfaces Composed of Azially Oriented Dipoles*, M.S. Thesis, Ohio State University, 1989.

- [12] G. J. Hayes, *Mutual Impedance Properties of an Infinite Line Array of Dipoles with Transverse Elements*, M.S. Thesis, Ohio State University, 1989.
- [13] R. F. Harrington, *Field Computations by Moment Methods*, Krieger Publishing Co., Malabar, Florida, 1968.
- [14] R. F. Harrington, *Time-Harmonic Electromagnetic Fields*, McGraw-Hill, 1961.
- [15] C. A. Balanis, *Antenna Theory, Analysis and Design*, John Wiley and Sons, New York, 1982, p. 338.
- [16] C. T. Tai, *Dyadic Green's Functions in Electromagnetic Theory*, Intext, 1971.
- [17] S. A. Schelkunoff and H. T. Friis, *Antenna Theory and Practice*, John Wiley and Sons, 1952.
- [18] W. L. Stutzman and G. A. Thiele, *Antenna Theory and Design*, John Wiley and Sons, 1981.
- [19] L. Brillouin, *Wave Propagation in Periodic Structures*, Dover, 2nd Edition, 1953.
- [20] A. Papoulis, *The Fourier Integral and Its Applications*, McGraw-Hill, 1962.
- [21] H. Bateman, *Table of Integral Transforms*, Volume I, McGraw-Hill, 1954.
- [22] P. S. Carter, *Circuit Relations in Radiating Systems and Applications to Antenna Problems*, Proceedings of the IRE, Vol. 20, pp. 1004-1041, June 1932.
- [23] G. H. Brown, *Directional Antennas*, Proceedings of the IRE, Vol. 25, pp. 79-145, January 1937.
- [24] B. A. Munk and G. A. Burrell, *Plane-Wave Expansion for Arrays of Arbitrarily Oriented Piecewise Linear Elements and Its Application in Determining the Impedance of a Single Linear Antenna in a Lossy Half-Space*, IEEE Transactions on Antennas and Propagation, Vol. AP-27, No. 3, pp. 331-343, May 1979.
- [25] T. W. Kornbau, *Analysis of Periodic Arrays of Rotated Linear Dipoles, Rotated Crossed Dipoles, and of Biplanar Dipole Arrays in Dielectric*, Ph.D. Dissertation, Ohio State University, 1984.
- [26] F. B. Hildebrand, *Introduction to Numerical Analysis*, McGraw-Hill, New York, 1956.
- [27] B. A. Munk, T. W. Kornbau, and R. D. Fulton, *Scan Independent Phase Arrays*, Radio Science, Vol. 14, No. 6, pp. 979-990, Nov-Dec 1979.
- [28] M. Abramowitz and I. E. Stegun, editors, *Handbook of Mathematical Functions with Formulas, Graphs, and Mathematical Tables*, National Bureau of Standards, U. S. Government Printing Office, 1964.
- [29] E. K. English, *Electromagnetic Scattering from Infinite Periodic Arrays of Arbitrarily Oriented Dipole Elements Imbedded in a General Stratified Medium*, Ph.D. Dissertation, Ohio State University, 1983.

- [30] R. Andre, *An Analysis Method for Double Periodic Nonplanar Antenna Arrays*, M.S. Thesis, Ohio State University, 1985.
- [31] L. W. Henderson, *The Scattering of Planar Arrays of Arbitrarily Shaped Slot and/or Wire Elements in a Stratified Dielectric Medium*, Ph.D. Dissertation, Ohio State University, 1983.
- [32] J. J. Bowman, T. B. A. Senior, and P. L. E. Uslenghi, *Electromagnetic and Acoustic Scattering by Simple Shapes*, Hemisphere Publishing Corp., New York, 1969.
- [33] R. Lampe, P. Klock, and P. Mayes, *Integral Transforms Useful for the Accelerated Summation of Periodic, Free-Space Green's Functions*, IEEE Transactions on Microwave Theory and Techniques, Vol. MTT-33, No. 8, pp. 734-736, August 1985.
- [34] R. E. Jorgenson and R. Mittra, *Efficient Calculation of the Free-Space Periodic Green's Function*, IEEE Transactions on Antennas and Propagation, Vol. AP-38, No. 5, pp. 633-642, May 1990.
- [35] S. Singh, W. Richards, J. Zinecker, and D. Wilton, *Accelerating the Convergence of Series Representing the Free Space Periodic Green's Function*, IEEE Transactions on Antennas and Propagation, Vol. AP-38, No. 12, pp. 1958-1962, December 1990.
- [36] C. Lanczos, *Applied Analysis*, Prentice-Hall, 1964.
- [37] D. Shanks, *Non-Linear Transformations of Divergent and Slowly Convergent Sequences*, J. Math. Phys., Vol. 34, 1955.